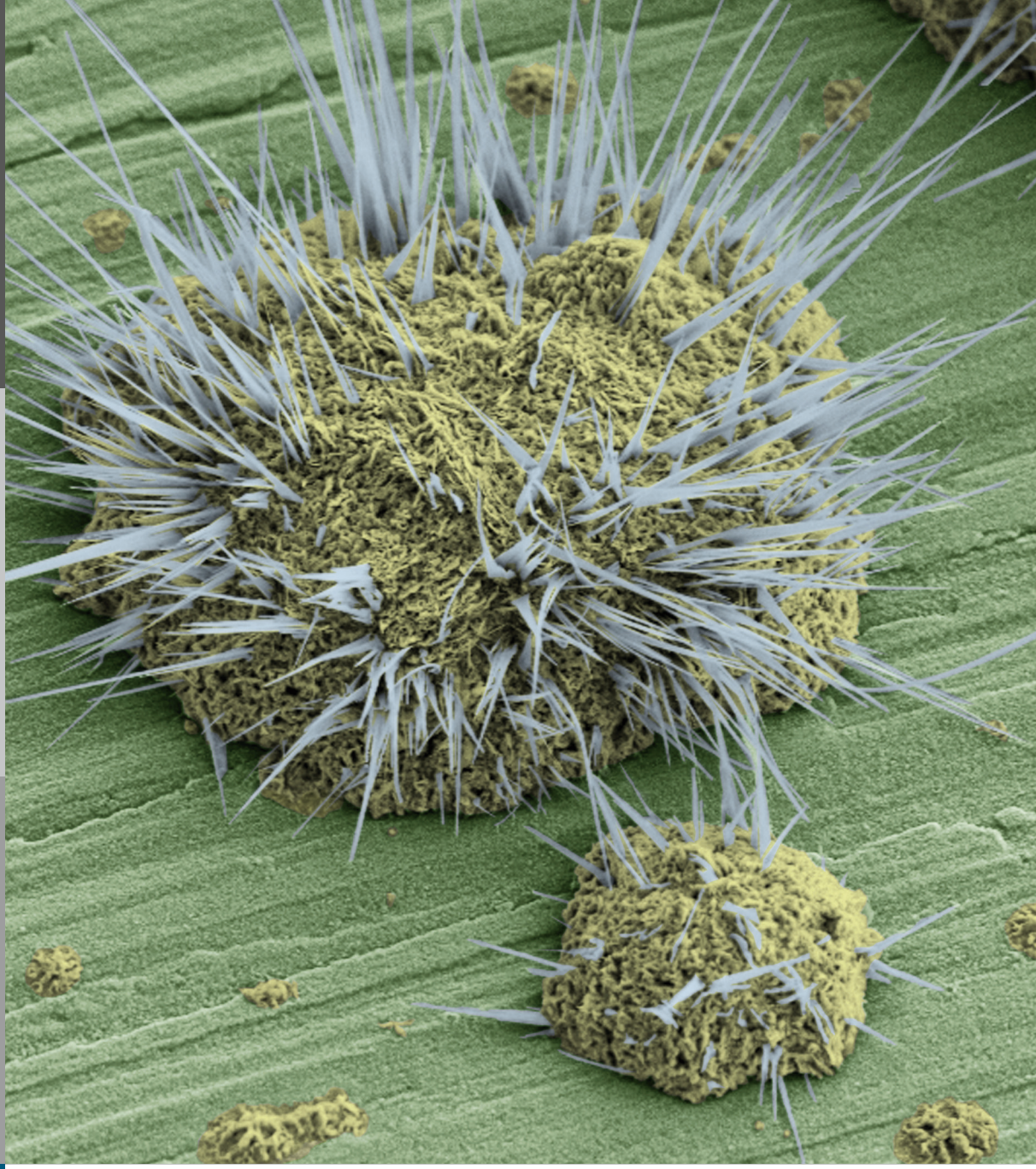

Oxidation Mechanisms of Materials for Heat Exchanging Components in CO_2/H_2O-containing Gases Relevant to Oxy-fuel Environments

Tomasz Olszewski

JÜLICH
FORSCHUNGSZENTRUM

Member of the Helmholtz Association

Schriften des Forschungszentrums Jülich
Reihe Energie & Umwelt / Energy & Environment Band / Volume 159

Forschungszentrum Jülich GmbH
Institute of Energy and Climate Research (IEK)
Microstructure and Properties of Materials (IEK-2)

Oxidation Mechanisms of Materials for Heat Exchanging Components in CO_2/H_2O-containing Gases Relevant to Oxy-fuel Environments

Tomasz Olszewski

Schriften des Forschungszentrums Jülich
Reihe Energie & Umwelt / Energy & Environment Band / Volume 159

ISSN 1866-1793 ISBN 978-3-89336-837-2

Bibliographic information published by the Deutsche Nationalbibliothek.
The Deutsche Nationalbibliothek lists this publication in the Deutsche Nationalbibliografie; detailed bibliographic data are available in the Internet at http://dnb.d-nb.de.

Publisher and Distributor:	Forschungszentrum Jülich GmbH Zentralbibliothek 52425 Jülich Phone +49 (0) 24 61 61-53 68 · Fax +49 (0) 24 61 61-61 03 e-mail: zb-publikation@fz-juelich.de Internet: http://www.fz-juelich.de/zb
Cover Design:	Grafische Medien, Forschungszentrum Jülich GmbH
Printer:	Grafische Medien, Forschungszentrum Jülich GmbH
Copyright:	Forschungszentrum Jülich 2012

Schriften des Forschungszentrums Jülich
Reihe Energie & Umwelt / Energy & Environment Band / Volume 159

D 82 (Diss., RWTH Aachen University, 2012)

ISSN 1866-1793
ISBN 978-3-89336-837-2

The complete volume is freely available on the Internet on the Jülicher Open Access Server (JUWEL) at http://www.fz-juelich.de/zb/juwel

Abstract

In the context of CO_2 emission reduction, the oxy-fuel technology provides a promising option applicable in centralized energy production. This technology is based on pulverized coal combustion with pure oxygen instead of air. Different from the conventional systems, metallic heat exchanging components in the oxy-fuel plants will be subjected to service environments containing high amounts of CO_2 and H_2O.

In the present study the oxidation behaviour of selected ferritic/martensitic and austenitic steels as well as Ni-base alloys, which are candidate materials for heat exchanging components, was investigated in model gas mixtures containing high amounts of CO_2 and/or H_2O at temperatures in the range of 550 to 700°C and times ranging from a few up to 1000 hours. The results obtained after oxidation in the simulated oxy-fuel environments were compared with the behaviour in air, Ar/CO_2 and Ar/H_2O gases. For studying the effect of oxygen present in the real oxy-fuel atmosphere, Ar/CO_2 gas was mixed additionally with different amounts of O_2.

It was found that in the CO_2 and/or H_2O-rich gases, the ferritic/martensitic steels tended to form Fe-rich oxide scales with significantly higher growth rates than the Cr-rich surface scales formed during air exposure. The Fe-rich scales were formed as a result of a decreased flux of chromium in the bulk alloy toward the surface because of enhanced internal oxidation of chromium in the H_2O-containing gases and carbide formation in the CO_2-rich gases. It was observed, however, that martensitic steels with higher initial Cr concentration had a stronger tendency to form protective Cr-base oxide scales when 1 or 3% of oxygen was added to the Ar/CO_2 gas mixture. The oxide scale formation was affected by minor alloying additions, especially silicon.

The poorly protective Fe-base oxide scales formed during exposure of the ferritic/martensitic steels to simulated oxy-fuel environments appeared to be permeable to CO_2 molecules resulting in carburization of the steels whereby the extent was reduced by increasing water vapour content in the gas mixture. Carburization of 9-12% Cr martensitic steels was also found to be significantly reduced when 0.5 vol.% of SO_2 were added to oxidizing CO_2-rich environments.

The oxidation behaviour of the austenitic steels strongly depended on the detailed alloy composition. At 550°C all austenitic steels exhibited very slow scale growth rates, however, at and above 600°C steels with lower Cr content (17-20wt.%) started to form multi-layered, Fe-rich oxide scales whereby the outer oxide layer was prone to spalling upon thermal cycling. For the 25% Cr austenitic steel and the Ni-base alloys much lower oxidation rates were observed, however, presence of water vapour in combination with intentionally added oxygen in the test atmosphere resulted in formation of volatile chromium species.

The effect of surface modification was studied in the case of the 9-12% Cr and the austenitic steels with lower Cr content. At higher temperatures (650-700°C) a significant improvement in oxidation resistance was observed for austenitic steels when cold work was applied to the surface prior to exposure in CO_2/H_2O-rich atmospheres.

Zusammenfassung

Eine vielversprechende Möglichkeit, die CO_2-Emissionen in großtechnischen Anlagen zur Stormerzeugung zu senken, besteht in der Anwendung des Oxy-Fuel-Verfahrens. Diese Technologie beruht auf der Verbrennung von Kohlepulver in reinem Sauerstoff anstatt in Luft. Im Gegensatz zu herkömmlichen Verbrennungsanlagen werden beim Oxy-Fuel-Verfahren die metallischen Wärmetauscher Betriebsmedien mit hohen CO_2- und H_2O-Gehalten ausgesetzt.

In der vorliegenden Arbeit wurde das Oxidationsverhalten ausgewählter ferritisch/ martensitischer und austenitischer Stähle sowie von Ni-Basislegierungen untersucht. Diese Werkstoffe sind potentiell geeignet als Konstruktionswerkstoffe für Wärmetauscher. Das Oxidationsverhalten wurde in Testgasen mit hohen CO_2- und/oder H_2O-Gehalten, im Temperaturbereich von 550 bis 700°C, für bis zu 1000h untersucht. Die Ergebnisse, die unter simulierten Oxy-Fuel-Bedingungen erzielt wurden, wurden anschließend mit Ergebnissen von Oxidationsversuchen in Luft, Ar/CO_2 und Ar/H_2O verglichen. Um den Einfluß von Sauerstoff in realen Oxy-Fuel-Atmosphären zu untersuchen, wurden dem Ar/CO_2-Gemisch zusätzlich verschiedene Mengen O_2 beigemischt.

In CO_2- und/oder H_2O-reichen Atmosphären zeigte sich, dass die ferritsch/martensitischen Stähle Fe-reiche Oxidschichten ausbilden. Diese Oxidschichten zeigten signifikant höhere Wachstumsraten als die Cr-reichen Schichten, die sich auf diesen Werkstoffen während der Hochtemperaturauslagerung in Luft bildeten. Die Fe-reichen Oxidschichten bildeten sich aufgrund verminderter Cr-Diffusion vom Inneren des Substratmaterials zu dessen Oberfläche. Grund hierfür ist verstärkte innere Oxidation von Chrom in H_2O-haltigen Gasen, bzw Karbidbildung im Falle CO_2-haltiger Gase. Bei martensitischen Stählen mit höherem Cr-Gehalt wurde eine verstärkte Tendenz zur Bildung schützender Cr-reicher Oxidschichten beobachtet, wenn der Ar/CO_2-Atmosphäre 1 oder 3% Sauerstoff beigemischt wurden. Die Oxidschichtbildung wurde von Begleitelementen, besonders Si, beeinflusst.

Die Fe-reichen Oxidschichten die sich auf den martensitischen Stählen unter simulierten Oxy-Fuel-Bedingungen bildeten, scheinen für CO_2-Moleküle durchlässig zu sein. Dies führt zu erheblicher Aufkohlung der Stähle, wobei dieser Effekt durch Erhöhung des H_2O-Gehaltes in der Versuchsatmosphäre reduziert wird. Die Aufkohlung der martensitischen Stähle mit 9-12% Cr wurde ebenfalls signifikant reduziert, wenn dem oxidierenden CO_2-reichen Gasgemisch geringe Mengen SO_2 zugegeben wurden.

Das Oxidationsverhalten der austenitischen Stähle war stark von der genauen Zusammensetzung der Werkstoffe abhängig. Bei 550°C zeigten alle austenitischen Stähle ein sehr geringes Oxidschichtwachstum. Ab 600°C bildete sich auf Stählen mit geringem Cr-Gehalt (17-20 wt.%) eine mehrlagige, Fe-reiche Oxidschicht, wobei der äußere Teil der Schicht beim thermischen Zyklieren zum Abplatzen neigte. Austenitische Stähle mit hohem Cr-Gehalt und Ni-Basislegierungen wiesen deutlich geringere Oxidationsraten auf. Hierbei ist jedoch zu beachten, dass das Vorhandensein von H_2O in der Versuchsatmosphäre, in Kombination mit bewust zugemischtem Sauerstoff, zur Bildung flüchtiger Cr-Verbindungen führte.

An Stählen mit 9-12% Cr und austenitischen Stählen mit geringem Cr-Gehalt wurden die Auswirkungen einer Oberflächenbehandlung untersucht. Nach Kaltverformung der Oberfläche zeigten die austenitischen Stähle eine signifikante Verbesserung ihres Hochtemperatur-oxidationsverhaltens in CO_2/H_2O-reichen Gasen.

Table of contents

1. Introduction

1.1 Energy conversion systems with CO_2 sequestration

The anthropogenic CO_2 emission from stationary sources originates mostly from combustion systems such as power plants, cement kilns, furnaces in industries and iron/steel production plants. In these processes the direct firing of fuel with air is the most economic technology to extract and use the energy contained in the fossil fuels [1]. It is estimated that about 30 percent of all CO_2 emissions due to human activities come from fossil fuels used for generating electricity [2].

The energy demand is expected to increase globally due to population increase and higher energy consumption. At present, fossil fuels are the dominant source to fulfill the global primary energy demand and it is expected that it will likely remain supplying over 85% of all primary energy for the rest of the century [3]. Therefore, it is obvious that in the future fossil fuels (coal, oil and gas) will still be the major sources for electricity production even with a projected increase in alternate renewable sources [4].

Several possibilities are considered to reduce CO_2 emissions from coal-fired power plant [5, 6]:

- increasing the fuel conversion efficiency in conventional boilers
- a further increase in efficiency by introduction of combined cycles (IGCC)
- switching to a fuel with a lower fossil carbon content

However, to achieve the global target reduction in CO_2 emissions of approximately 60% by 2050 [7], carbon dioxide capture and permanent underground storage will be necessary. Carbon abated clean coal technologies will be required for retrofitting existing power plants and installation on new power plants [8]. Therefore substantial efforts have been made in recent years to develop technologies enabling the production of electricity with so-called “zero CO_2 emissions”.

Capturing and sequestration of carbon dioxide is the only way to achieve the decrease in CO_2 emissions required by international regulations (Kyoto protocol and Intergovernmental Panel on Climate Change) decreasing in CO_2 emission [1].

Currently, three main approaches are discussed for capturing CO_2 from the exhaust gas of fossil fuel fired power plants allowing “near zero CO_2 emission”:

- post-combustion capture
- pre-combustion capture
- oxy-fuel combustion

1.2 Post-combustion

Post-combustion systems separate CO_2 from the flue gases produced by the air combustion of the primary fuel. In principle this system can be applied to flue gases produced from the combustion of any type of fuel. During post-combustion a liquid solvent is typically used to capture a small fraction of CO_2 (typically 3-15% by volume) present in a flue gas stream in which the main constituent is nitrogen. For a modern pulverized coal power plant or a natural gas combined cycle power plant, current post-combustion capture systems employ an organic solvent such as monoethanolamine and other primary amines including the newly developed hindered amines [9]. Recently efforts have been undertaken worldwide to develop more efficient and lower cost post-combustion systems, following all possible approaches for the CO_2 separation steps using sorbents, membranes or cryogenics [1]. The post-combustion concept requires large scale equipment for the CO_2 removal and the handling of the chemicals. It also consumes process heat and leads to additional exhaust gas pressure losses, meaning that the thermal efficiency is significantly reduced [10].

1.3 Pre-combustion

In this concept, the fuel is first converted to H_2 and CO by gasification or reforming and then to H_2 and CO_2 by the water shift reaction (Eq. 1.1). Afterwards the CO_2 is removed and the H_2 is fed as fuel into a power plant with nearly no CO_2 in the exhaust gas [11]. CO_2 and H_2-rich gas can be produced through, e.g., partial oxidation, methane-steam reforming or auto-thermal reforming with a subsequent water-gas shift reaction [10].

$$CO + H_2O = CO_2 + H_2 \qquad \text{(Eq. 1.1)}$$

The resulting mixture of hydrogen and carbon dioxide from the above equation can be separated into a CO_2 and H_2 stream. CO_2 is typically removed through scrubbing with physical or chemical solvents. The difference between this scrubbing and the one employed in post combustion is that here the gas pressure and the CO_2 concentration are much higher, thus the size of the required equipment is substantially smaller [10]. Other techniques allowing CO_2 removal from the flue gas stream in pre-combustion systems are based on pressure swing adsorption onto adsorbents such as zeolites which act as molecular sieves or cryogenic separation where CO_2 is separated from the syngas by a condensation process whereby liquid CO_2 is produced. Membrane separation is also commercially applied for hydrogen separation but selectivity of commercially available membranes for CO_2/H_2 separation is still quite low [12].

Hydrogen obtained after CO_2 removal is a carbon-free energy carrier and therefore can be used in many applications such as boilers, furnaces, gas turbines, engines and fuel cells. Although the initial fuel conversion steps are more elaborate and costly than those in post-combustion systems, the high concentrations of CO_2 produced by the shift reactor (typically 15 to 60% by volume on a dry basis) and the high pressures often encountered in these applications are more favourable for CO_2 separation. Pre-combustion would be used at power plants that employ integrated gasification combined cycle (IGCC) technology [1].

1.4 Oxy-fuel combustion

Conventional coal-fired boilers use air for combustion of the fossil fuel. During this process nitrogen from the air dilutes the CO_2 concentration in the flue gas. The capture of CO_2 from such dilute mixtures using amine stripping is relatively expensive. During oxy-fuel combustion, a combination of high purity oxygen and recycled flue gas is used for combustion of the fuel. By recycling the exhaust gases, a gas mixture mainly consisting of CO_2 and water vapour is generated. The latter can be easily removed from the flue gas by cooling and compressing the gas stream instead of using chemicals [5]. The general idea of the oxy-fuel concept compared with the pre- and post-combustion is presented in Fig. 1.1. Additionally, a more detailed representation of the oxy-fuel technology is demonstrated in Fig. 1.2.

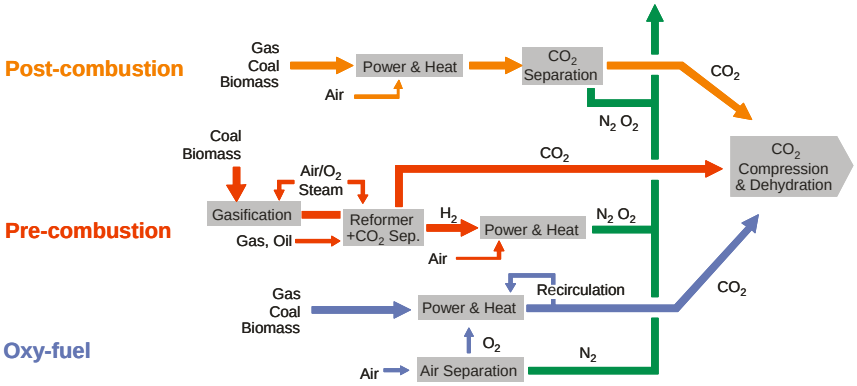

Figure 1.1: Schematic representation of the oxy-fuel, pre- and post-combustion concepts. Based on [1]

Current methods of oxygen production by air separation comprise cryogenic distillation, adsorption using multi-bed pressure swing units and polymeric or ceramic membranes. However, the only technology currently available for very large plants is the cryogenic air separation [1, 12]. Oxygen purity from an existing air separation units ranges from 95 to 99.99% [13]. The cryogenic air separation process consumes energy thus some loss of the overall plant efficiency is unavoidable. It is envisaged that the total energy required for the air separation unit and for CO_2 compression decreases the efficiency of the power plant by about 9% (absolute value), but the capital and operation cost is substantially less than that for a standard plant with chemical absorption for CO_2 recovery [5].

Combustion of a fuel with pure oxygen has a combustion temperature of about 3500°C which is far too high for typical combustion parts. The combustion temperature is therefore reduced by the proportion of flue gas and gaseous or liquid water recycled back to the combustion chamber. Increase of the oxygen fraction in the oxidizer results in higher gas emissivity but decreases the total amount of flue gases. Thus, the participation of convective heat transfer in the total heat transfer mechanism is slightly reduced in comparison with air combustion. However, due to partially looping of the flue gases back to the combustion chamber the overall heat transfer can be improved in oxy-fuel firing. This is because of the higher emissivity of the CO_2/H_2O gas mixture compared to that of nitrogen which is the main constituent of the flue gases during air firing. The improvement of boiler efficiency and steam generation was reported to be approximately 5% [1, 14].

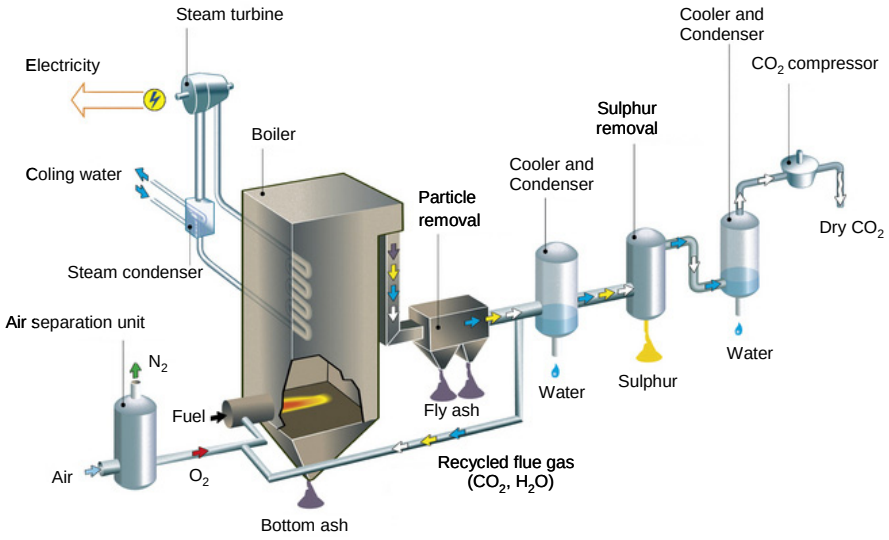

Figure 1.2: Schematic representation of the oxy-fuel concept. Reproduced from Vattenfal

One of the major advantages of oxy-fuel combustion compared to the pre- and post-combustion systems (Fig. 1.1) is very high CO_2 capture efficiency reported to be close to 100%. Depending on the fuel used and the particular oxy-fuel combustion process the net flue gas, after cooling to condense the water vapour, contains 80 to 98% pure CO_2 (the rest being excess O_2, NO_x, SO_x and Ar). Some studies have demonstrated that the level of NO_x reduction can be up to 75% compared to coal burning in air [15]. A problem area identified in the oxy-fuel process is air leakage, which is already known in conventional boilers but has no major impact on the process there. In the oxy-fuel process, however, the CO_2 purity in the flue gas influences the energy demand of the CO_2 separation and therefore the presence of air in the combustion chamber has a detrimental effect on the overall CO_2 separation efficiency [16]. Depending on the air leakage, the resulting flue gas can have a CO_2 purity ranging from 80% to 95% (in volume) [13].

The oxy-fuel technology can be applied successfully as a retrofit to a wide range of already existing boilers and furnace systems. Therefore, it is necessary to investigate whether the currently used boiler construction materials (mainly heat exchanging components) are suitable for power plants with oxy-fuel combustion.

The composition of flue gases during oxy-fuel firing differs slightly depending on the type of used fuel and other parameters such as oxygen excess and oxygen purity. The literature data

presented in Tab. 1.1 clearly indicate much higher concentrations of CO_2 and H_2O in the flue gases compared to those in air-firing in which the nitrogen is the major flue gas constituent.

Flue gas composition in vol.% (except E)

	Air-firing			Oxy-fuel firing		
	A	B	C	D	E (wt.%)	F
Ar	0.8	-	0.8 - 0.9	2.1	8.29*	0.21
N_2	71.3	76.4	67 - 74	4.8		4.20
O_2	2.5	2.8	5 - 6	1.9	1.28	3.00
H_2O	10.0	5.9	8 - 15	31.8	18.8	18.92
CO_2	15.3	14.7	11 - 12	58.9	65.96	73.55
SO_2	0.13	0.04	400-2300**	0.49	0.80	0.12

* values for Ar and N_2 are given as total sum
** ppm

Table 1.1: Flue gas composition during air firing A-C and oxy-firing D-F. Source of data: A,D [11]; B [18]; C [17]; E [3]; F [13]

As oxy-fuel combustion combined with sequestration must provide power for several significant unit operations such as flue gas compression, which are not required in a conventional plant without sequestration, oxy-fuel combustion/sequestration is less efficient per unit of electricity produced than the air-fired process. However, it is more efficient than a conventional plant with CO_2 sequestration due to the significant energy required for scrubbing a dilute gas stream prior to compression [5]. This explains why the oxy-fuel technology is so attractive for utilities which must be currently adapted to the new situation on the energy market due to existing regulations for limitations of green house gas emissions.

2. Aim of the present study

Increase of atmospheric greenhouse gas concentrations is believed to result in a potentially hazardous global change of climatic conditions. Carbon dioxide was recognized as one of the major contributors to the global warming effect. Therefore, CO_2 capture and storage is gradually becoming an important concept to reduce greenhouse gas emissions. Oxy-fuel combustion offers the possibility of significant reduction in CO_2 emission and is considered as a promising option for the decrease in greenhouse gases emission required by international regulations.

During oxy-fuel firing the heat exchanging components will be exposed to a flue gas composed mainly of CO_2 and H_2O. In most power plants the boiler construction materials are low alloy steels, while for higher operation temperatures, ferritic/martensitic steels, austenitic steels and even Ni-base alloys are in use to fulfill the requirement for higher creep strength.

A number of papers are dealing with the behaviour of such materials in combustion gases of conventional power plants, in water vapour or CO_2. However, the studies are very rare regarding the oxidation resistance of metallic components exposed to the CO_2- and H_2O-rich gases prevailing under oxy-fuel conditions. Therefore, the aim of the present study is to investigate the behaviour of selected candidate construction materials for heat exchanging components in atmospheres containing high concentrations of CO_2 and H_2O.

The present study mainly focuses on better understanding of the effect of variation in CO_2, H_2O and O_2 content in the oxidizing atmosphere as well as the effect of alloy composition on oxidation behaviour of commercially available materials. A large part of the present investigation is devoted to elucidate the interaction between the various gas species and how this interaction affects the material performance. For this purpose, exposures of the selected materials are carried out in which a stepwise variation in concentrations of the relevant gas species (CO_2, H_2O, O_2, SO_2) is followed.

In this way the results of this study contribute to the understanding of the fundamentals of scale formation mechanisms prevailing during service of construction materials in oxy-fuel relevant, CO_2- and H_2O-rich gases.

3. Oxidation of metallic materials

3.1 Thermodynamic considerations

Oxidation is the most frequently encountered high temperature corrosion reaction. Metallic construction materials are oxidized when heated to elevated temperatures in environments containing oxygen at sufficiently high level, e.g., air, steam, combustion atmospheres, etc. However, oxidation can also take place in environments with low oxygen activity [19].

The oxidation process can be described as a chemical reaction between metal and oxygen:

$$M + O_2 = MO_2 \qquad \text{(Eq. 3.1)}$$

The prediction of the spontaneous occurrence of such a reaction can be derived from the second law of thermodynamics. Under conditions that both temperature and pressure are constant, the second law of thermodynamics can be expressed as [20]:

$$\Delta G = \Delta H - T\Delta S \qquad \text{(Eq. 3.2)}$$

where ΔG is the change in Gibbs free energy; ΔH the difference in enthalpy; T the temperature and ΔS the entropy change.

Under these conditions the second law states that the Gibbs free energy change can be as follows:

$\Delta G < 0$: spontaneous reaction expected
$\Delta G > 0$: thermodynamically possible if additional energy is added
$\Delta G = 0$: reaction in equilibrium

With the approximation for ideal gas where the oxygen activity is identical with its partial pressure, the Gibbs free energy for the oxidation reaction described in Eq. 3.1 can be written as:

$$\Delta G = \Delta G^\circ + RT \ln\left(\frac{a_{MO_2}}{a_M \, p_{O_2}}\right) \qquad \text{(Eq. 3.3)}$$

where ΔG° is the standard Gibbs free energy; R the gas constant; T the temperature; p_{O_2} the oxygen partial pressure; $a_{M_xO_y}$ and a_M the oxide and metal activities which describe the deviation from the standard state for the respective given species.

The equation can be subsequently simplified by setting the activities of pure solids to unity. For the case of equilibrium ($\Delta G = 0$), the above equation can then be expressed in the following way:

$$\Delta G^\circ = -RT \ln p_{O_2} \qquad \text{(Eq. 3.4)}$$

Transformation of Eq. 3.4 leads to:

$$p_{O_2} = \exp\left(\frac{-\Delta G^\circ}{RT}\right) \qquad \text{(Eq. 3.5)}$$

Equation 3.5 allows to calculate the dissociation pressure of a given oxide as a function of temperature. This value can easily be derived from the Ellingham-Richardson diagram (Fig. 3.1). In this figure the standard Gibbs free energy of formation versus temperature for many simple oxides is plotted. This diagram provides the opportunity to compare the thermodynamic stability of different oxides. The lower the position of the line in the diagram, the more stable the oxide is. Another important observation which can be made from the Ellingham-Richardson diagram is that with increasing temperature metal oxides become thermodynamically less stable.

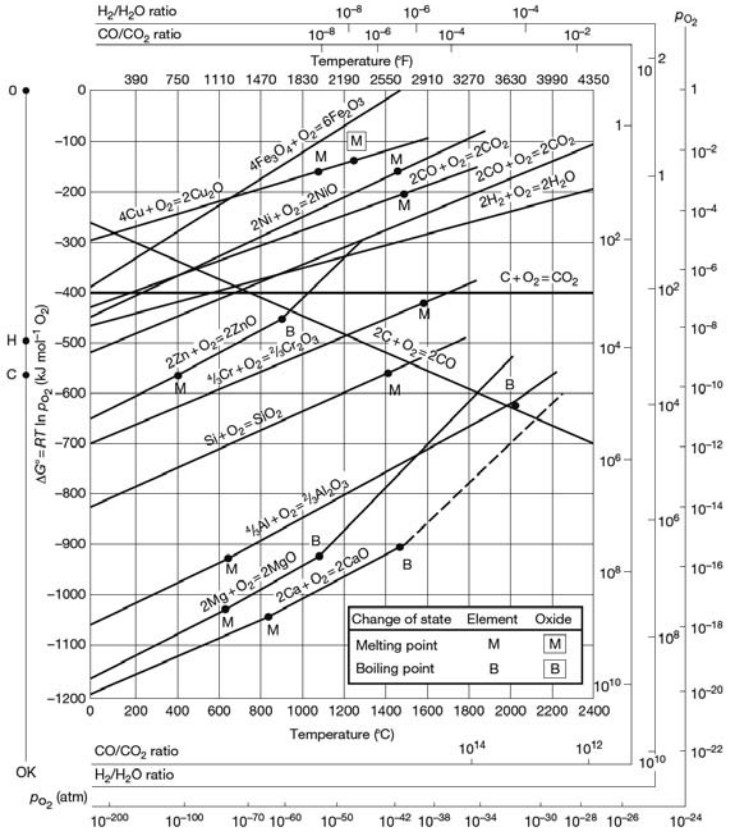

Figure 3.1: Ellingham-Richardson diagram showing the standard Gibbs free energies of formation of selected oxides as a function of temperature [21]

3.2 Kinetics of oxidation

The thermodynamic approach described in the previous section allows to derive under which conditions a metal can oxidize. However, it does not allow to derive the actual occurring reaction steps during the oxidation process. Fig. 3.2 describes possible stages occurring during the reaction between a metallic surface and oxygen at high temperature.

The initial step in the metal-oxygen reaction involves the adsorption of atomic oxygen on the metal surface (t_1). Oxide nucleates at favorable sites and most commonly grows laterally while atomic oxygen may dissolve in the metal (t_2). The first two stages depend significantly on the surface orientation, crystallographic structure as well as the number and type of defects of the metal surface. As the layer thickens it provides a protective scale barrier to shield the metal from

the gas. When a continuous film covers the surface, the reaction can proceed only through solid-state diffusion of the reactants through the oxide film, i.e. for further scale growth electrons must move through the oxide to reach the oxygen atoms adsorbed on the surface, while oxygen ions, metal ions, or both must move through the oxide layer. Additionally oxygen atoms may diffuse into the metal (t_3). Growth stresses in the scale may create cavities, pores, micro-cracks or other defects, modifying the oxidation mechanism. In this situation the oxide scale no longer constitutes a perfect diffusion barrier which avoids the gas penetration to the metal (t_4). Furthermore, formation of large macro-cracks, volatile or liquid compounds is also possible thus acceleration in oxide scale deterioration may be observed in such a situation (t_5) [19, 22, 23].

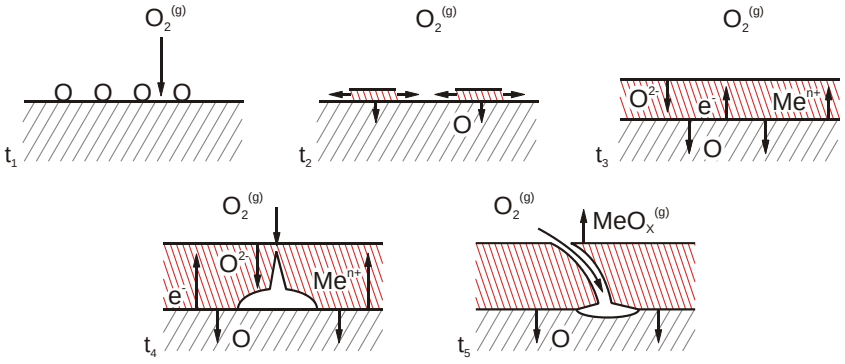

Figure 3.2: Schematic representation of the reaction between a metallic surface and oxygen during high temperature exposure. Description in the text. Adapted from [23]

In the case that a gas tight oxide scale prevails, thermodynamic equilibrium is attained at the metal/scale and the scale/gas interfaces and the oxide growth is determined by the diffusion of the reactants through the scale. Gradients of metal activity and oxygen partial pressure are established across the scale as presented in Fig. 3.3. Metal cations and oxygen anions will tend to migrate across the scale in opposite directions [24].

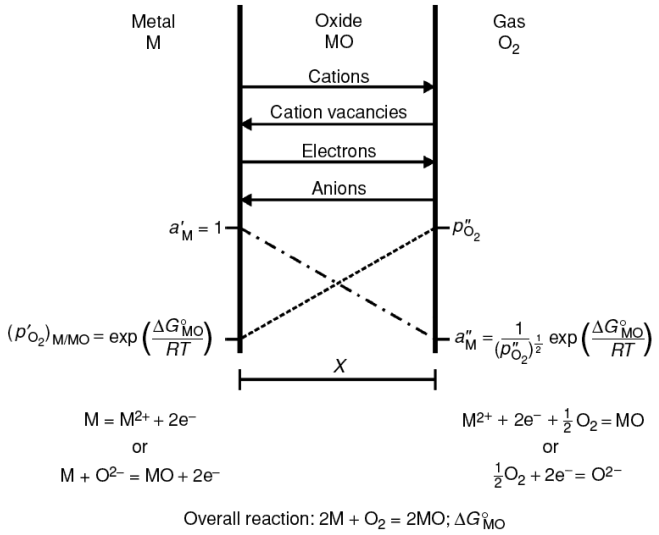

Figure 3.3: Diagram of scale formation according to Wagner's model [20]

For a dense oxide scale which is adherent to the metal substrate cation transport across the growing oxide layer controls in many cases the rate of the scaling rate. Therefore, the outward cation flux $j_{M^{2+}}$ is equal and opposite to the inward flux of cation defects j_{V_M} :

$$j_{M^{2+}} = -j_{V_M} = D_{V_M} \frac{C''_{V_M} - C'_{V_M}}{x} \qquad \text{(Eq. 3.6)}$$

where D_{V_M} is the diffusion coefficient of cation vacancies; C''_{V_M} and C'_{V_M} are the vacancy concentrations at the scale/gas and scale/metal interface, respectively, and x is the thickness of the oxide.

Since there is thermodynamic equilibrium attained at each interface, the value of $(C''_{V_M} - C'_{V_M})$ is constant:

$$j_{M^{2+}} = \frac{1}{V_{OX}} \frac{dx}{dt} = D_{V_M} \frac{C''_{V_M} - C'_{V_M}}{x} \qquad \text{(Eq. 3.7)}$$

where V_{OX} is the molar volume of the oxide. Therefore, the rate of oxide thickening is given as:

$$\frac{dx}{dt} = \frac{k'}{x} \text{ where } k' = D_{V_M} V_{OX} (C''_{V_M} - C'_{V_M}) \quad \text{(Eq. 3.8)}$$

Integrating and noting that $x = 0$ at $t = 0$ the following equation can be obtained:

$$x^2 = 2k' \cdot t \quad \text{(Eq. 3.9)}$$

which is commonly known as the parabolic rate law frequently observed during oxidation of metals and alloys at elevated temperatures [20].

3.3 Rates of oxidation

The kinetics of oxidation of metals and alloys do not in all cases follow a parabolic rate. Some reactions follow a linear rate or other reaction kinetics which may include logarithmic or inverse logarithmic rates. These reactions kinetics are schematically illustrated in Fig. 3.4.

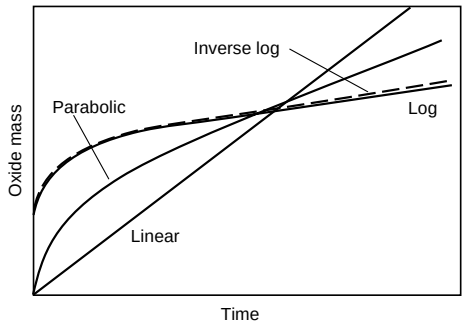

Figure 3.4: Different oxidation kinetics observed during the oxidation of metals. Reproduced from [25]

3.3.1 Parabolic oxidation kinetics

In the case of the situation that the oxidation reaction is controlled by the diffusion of ions through the oxide scale the observed kinetics follow a parabolic rate law as described in section 3.2. The driving force for a parabolic growth of oxide scale is governed by the chemical potential gradient across the oxide scale. As the oxide grows thicker, the diffusion distance between oxide/metal and oxide/gas interfaces increases, and the oxidation rate slows down. It can be expressed as:

$$x^2 = k_r \cdot t \qquad \text{(Eq. 3.10)}$$

where x is the oxide scale thickness; k_r the parabolic rate constant; t the exposure time.

Oxidation rates are frequently determined by measurement of the oxygen uptake, i.e., the weight gain occurring as a result of the oxidation process. Therefore, the parabolic rate law is frequently given as:

$$\left(\frac{\Delta m}{A}\right)^2 = k_p \cdot t \qquad \text{(Eq. 3.11)}$$

where $\left(\frac{\Delta m}{A}\right)$ is the mass gain (Δm) per unit area (A).

3.3.2 Linear oxidation kinetics

If the metal surface is not protected by a barrier of dense, adherent oxide, the oxidation rate may remain constant with time, and one of the other steps in the oxidation reaction is rate controlling rather than the transport processes in the scale. Linear kinetics are expected to occur when for instance a porous oxide layer is formed. The oxidation rate does not slow down after longer times resulting in a rapid oxidation of the metal [19]. The linear oxidation kinetic rate can be expressed by:

$$x = k_l \cdot t \qquad \text{(Eq. 3.12)}$$

where x is the thickness of the oxide; k_l is linear rate constant.

3.3.3 Other reaction rate equations

At very low temperatures when thin oxide films form on the metal surface (usually less than 100nm), the oxidation rate usually follows either a logarithmic or inverse logarithmic rate.

The driving force for the oxidation is the electric field across the oxide film. The logarithmic rate can be expressed by:

$$x = k_e \log(a \cdot t + 1) \qquad \text{(Eq. 3.13)}$$

while the inverse logarithmic equation can be written as:

$$\frac{1}{x} = b - k_i \log t \qquad \text{(Eq. 3.14)}$$

where a, b, k_e and k_i are constants.

In practical applications it is nearly impossible to distinguish between logarithmic and inverse logarithmic kinetics due to large difficulties in measurements of such thin oxide scales.

A number of other kinetic equations have been reported in literature, e.g., cubic, asymptotic, sub-parabolic and para-linear [20, 25-27]. Those are, however, assumed to describe the combination of the simple reactions presented above rather than new oxidation mechanisms. For instance, para-linear oxidation was found to describe the oxidation process if, e.g., a competition between the parabolic growth of a chromium oxide scale and the vaporization of volatile Cr-species simultaneously occurred [28, 29, 30].

Many oxidation tests of commercial alloys are carried out in complex atmospheres. Long term exposures are usually conducted under non-isothermal conditions. The oxidation behaviour and therefore the overall kinetics of metallic components are frequently affected by scale cracking, delamination or spalling. The initially formed protective oxide scale can break down locally during the oxidation process, e.g., as a result of growth or thermally induced stress. Due to these factors in many cases the obtained oxidation curves cannot be described by any of the kinetics equations presented above. Some of the most frequently encountered oxidation behaviours during high temperature exposures are schematically depicted in Fig. 3.5.

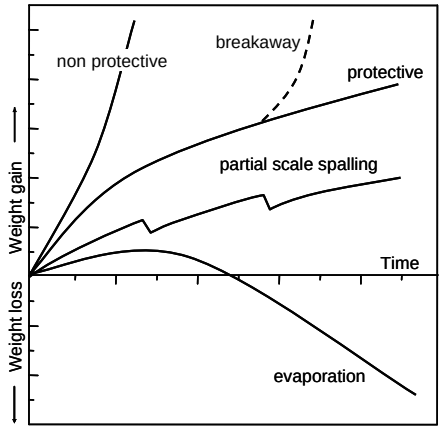

Figure 3.5: Different oxidation kinetics frequently encountered in real metal and alloy systems, especially occurring during long term, discontinuous oxidation. Based on [19, 22]

3.4 Oxidation of iron

Iron is the most commonly used metallic construction material. However, pure iron is hardly used for high temperature applications because of its very high reactivity even at ambient conditions and relatively poor mechanical properties. The rate of oxidation of iron is governed by the stabilities of the various oxide phases which are in turn a function of the temperature and oxygen partial pressure of the environment. When iron oxidizes in air at temperatures above 570°C, it grows a layered scale consisting of FeO (wustite), Fe_3O_4 (magnetite), and Fe_2O_3 (hematite). Since the FeO phase is not stable below 570°C, Fe oxidized below this temperature would be expected to form a two-layered scale of Fe_3O_4 and Fe_2O_3 with the Fe_3O_4 next to the metal [20, 23, 31].

The oxide scale formation mechanism on iron involves the ionization of Fe at the interface with metal according to the reaction A in Fig. 3.6. The iron ions and electrons migrate outward through the FeO layer via iron vacancies and electron holes, respectively. At the wustite/magnetite interface magnetite is reduced by iron ions and electrons (reaction B). Iron ions and surplus electrons to this reaction proceed outward through the magnetite layer, over iron ion vacancies and over electron holes and excess electrons. At the magnetite/hematite interface, magnetite is formed according to reaction C. If iron ions are mobile in the hematite they will migrate through this phase over iron ion vacancies together with electrons and new hematite will form at the Fe_2O_3/gas interface according to reaction D. At the interface with the atmosphere

oxygen can be ionized as well. If oxygen ions are mobile in the hematite layer, the iron ions and electrons, in excess of requirements for the reduction of hematite to magnetite, will react with oxygen ions diffusing inwards through the Fe_2O_3 layer via oxygen vacancies forming new Fe_2O_3 [20].

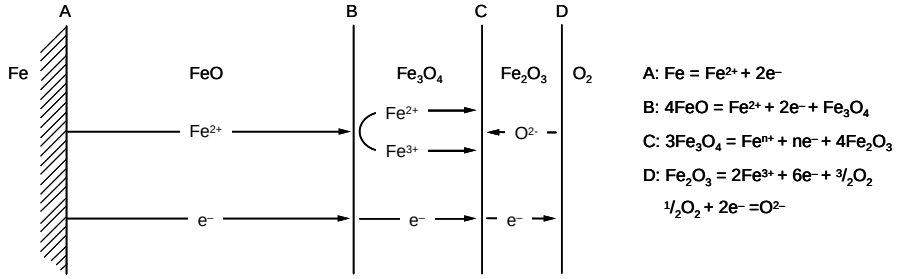

Figure 3.6: Schematic illustration of the oxide layers formed during iron oxidation above 570°C in a high pO_2 gas and the dominant diffusing species through each oxide layer. The reactions that take place at each interface are presented on the right side. Based on [20, 32]

3.5 Oxidation of Fe-Cr alloys

From all the alloying elements added to steels, Cr is most frequently used for improving the oxidation properties. The addition of only 1wt.% of chromium to iron results in a significant improvement in oxidation resistance. At low Cr content the decrease in the scaling rate is mainly related to the formation of Fe/Cr-rich spinel and suppression of the wustite phase. Upon increasing the Cr content, outward diffusion of Fe ions is hampered by the $FeCr_2O_4$ thus lowering in the oxidation rate is observed. Fe-base alloys containing 9-12% of Cr are capable of forming a continuous, protective chromia base scale in the case of oxidation under dry conditions. The chromium content of 9-12% is, however, insufficient to form a protective chromia base scale during oxidation in the presence of water vapour. After an initial protective stage of oxidation, formation of fast growing Fe-base oxides usually occurs. A permanent protective chromia base scale cannot be obtained unless the Cr concentration exceeds approximately 20wt.%. In the case of exposure to very corrosive atmospheres breakaway of the Cr-rich scale was reported to occur even for binary Fe-22% Cr alloys at 650°C [33]. The effect of chromium content on the oxide scale morphology of Fe-Cr alloys is schematically presented in Fig. 3.7. The actually occurring scale formation strongly depends on the temperature.

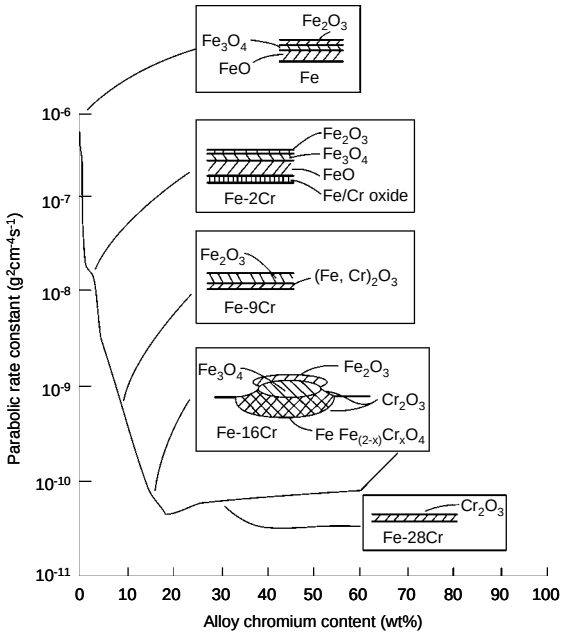

Figure 3.7: Effect of chromium on the oxidation resistance and oxide morphology of Fe-Cr alloys at 1000°C in oxygen [34]

Important to mention that steels designed for commercial applications commonly contain a number of minor alloying elements which may substantially affect the oxidation mechanisms during high temperature exposure.

3.6 Oxidation in water vapour

The kinetics and scale formation mechanisms during oxidation of Fe-Cr alloys in the presence of water vapour may considerably differ from those in oxygen or air. High-Cr steels frequently used as construction materials in heat exchanging components rely on the formation of a chromia surface layer for protection against rapid oxidation attack. However, as reported by many studies [35-37] faster degradation and breakaway of the protective oxide scale commonly occurs when the alloys are exposed to water vapour.

The detrimental effect of water vapour on the protective chromia base scale formation is an important factor for the application of, e.g., 9-12% Cr steels in conventional as well as newer type of power plants including those using oxy-fuel firing. It was suggested by Quadakkers *et al.* [38] that breakaway of the initially formed protective Cr-base oxide scale in steam was

accompanied by formation of rapidly growing Fe_3O_4 and an inner scale consisting of $Fe_3O_4 + (Fe,Cr)_3O_4$. Fast ionic transport across the oxide scale results in vacancy transport. These vacancies can locally condensate within the scale and/or the scale/alloy interface. Therefore, voids or gaps are frequently present within the outer oxide scale or near the interface between inner and outer oxide layers. Further growth of the scale depends to a large extent on transport processes within these voids or gaps by the so-called "H_2/H_2O-bridges" [39]. Because iron transport is significantly reduced due to the presence of voids, hematite is formed at the interface with the atmosphere (Fig. 3.8). Depending on the oxidation conditions (cyclic or isothermal exposure) healing processes within the scale may occur or partial spalling of the oxide layers. It was reported that the latter effect might be pronounced by buckle formation which in turn is most probably caused by compressive oxide growth stresses and/or thermal stresses [40, 41].

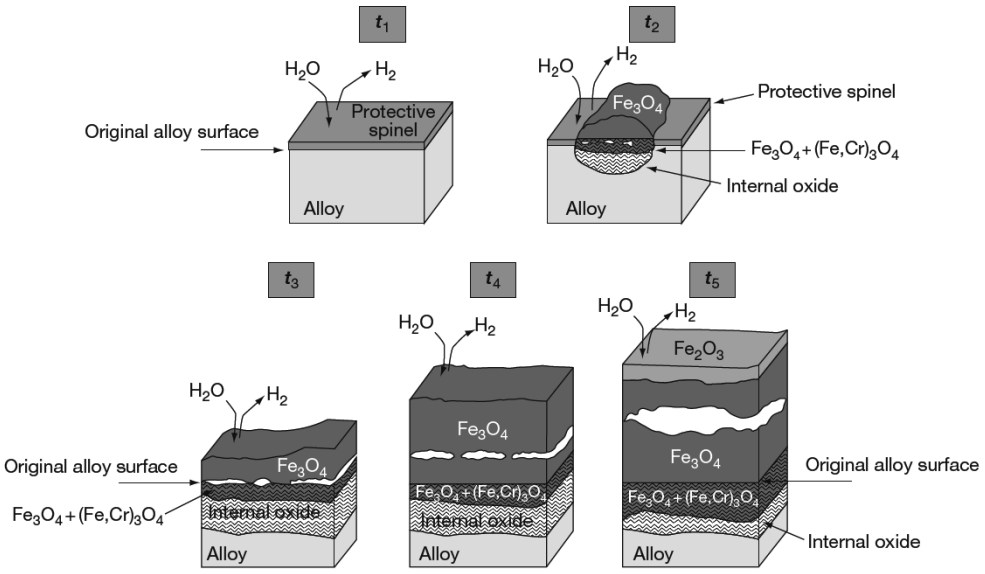

Figure 3.8: Proposed mechanism for the oxide scale formation on ferritic 10% Cr steel in Ar/H_2O mixtures. Times t_1, t_2, t_3, t_4, t_5 represent subsequent time steps during the oxidation process. Exact mechanisms and times depend on steel composition and exposure temperature. Reproduced from [42]

3.7 Evaporation of volatile Cr-species

A further factor which may contribute to deterioration of the protective chromia base scales on Fe-Cr base alloys is the formation of volatile species. In gases with substantial amounts of free oxygen, presence of water vapour results in the formation of gaseous $CrO_2(OH)_2$ with a higher vapor pressure than volatile CrO_3 which is the dominating volatile Cr species in dry air or dry

oxygen. In atmospheres in which both water vapour and free oxygen are present, the following reaction may substantially affect the overall oxidation kinetics [43]:

$$\frac{1}{2}Cr_2O_3^{(s)} + H_2O^{(g)} + \frac{3}{4}O_2^{(g)} = CrO_2(OH)_2^{(g)} \quad \text{(Eq. 3.15)}$$

The evaporation-induced accelerated loss of Cr promotes formation of less protective Fe-rich oxides. Not only martensitic 9-12% Cr but also high alloyed austenitic steels may be affected by the formation of volatile Cr-species in atmospheres containing H_2O and O_2 as a result of accelerated depletion of Cr.

The kinetics of evaporation from a pure chromia surface scale is frequently reported to be linear. During the oxidation process a competition between the parabolic Cr_2O_3 growth and the linear vaporization of $CrO_2(OH)_2$ is therefore observed. This type of reaction results in so-called para-linear kinetics [28]. The vaporization rate and thus the time to occurrence of breakaway oxidation strongly depend on gas velocity. If the flow rate is high, the total chromium loss can not be compensated by Cr diffusion from the alloy, resulting in a critical subsurface Cr depletion and finally breakaway oxidation during long-term exposures.

3.8 Carburization in CO_2-containing atmospheres

In oxy-fuel plants metallic heat exchanging components will be subjected to service environments containing high amounts of CO_2. The early investigations carried out show that Cr steels exposed to CO_2 atmosphere, similar to the findings observed during oxidation in water vapour, tend to form non-protective, Fe-base oxide scales [44-46]. It has also been described that, when these steels are oxidized in high CO_2-containing gas mixtures, carbide formation in the sub-scale region may occur if the steels form poorly protective, Fe-rich oxide scales. Some studies [47, 48] proposed that the carbide formation was in fact the trigger for the formation of the iron oxide base scales, because the carbides tie-up the free chromium in the steel matrix which would otherwise be available for forming protective, chromium-rich surface oxide scales. In studies on Fe-Cr and Ni-Cr alloys exposed in CO_2/CO atmospheres [49, 50] it was claimed that carburization did not occur if protective chromia base scales were formed, since these were considered to be impervious to carbon penetration. The occurrence of carburization is of major concern because it reduces the room temperature ductility [51-53].

Literature data indicate that carburization may occur even in the atmospheres with extremely low carbon potential, i.e., several orders of magnitude smaller than that required for chromium carbide formation. This seemingly contradiction was, however, explained by several authors [48, 54, 55] who suggested that under such conditions formation of Cr-carbides could occur in the alloy if carbon carrying species such CO_2 and/or CO could reach the metal surface by penetrating the oxide scale in molecular form.

For gases with high carbon activity (different from the conditions in the present study) formation of iron carbide (Fe_3C) is frequently reported as well as occurrence of so-called “metal dusting” phenomena which is the example of catastrophic degradation of metallic components [26, 56].

4. Experimental

4.1 Alloy selection

A wide range of high temperature resistant alloys is currently available on the market and has been used since several decades for power plant applications. The key components whose performance is critical for modern pulverized fuel power plants are high pressure steam piping, headers, re-heaters, super-heaters and water wall tubing. Depending on the economical requirements, operating temperatures and particular application, different types of alloys are used as construction materials.

The materials selected in this study are listed in Tab. 4.1. The detailed chemical compositions are given in Tab. 19.1 of the Appendix. For some experiments a number of binary Ni-Cr (Ni-10% Cr, Ni-20% Cr and Ni-25% Cr) as well as Fe-Cr (Fe-10% Cr) model alloys were additionally included.

Type of steel	Material name	Main alloying additions
Low alloyed	13CrMo4-4	1Cr-0.5Mo
9-12% Cr Ferritic/ martensitic	P92	9Cr-1W
	X20	11Cr-1Mo
	HCM12*	12Cr-1Mo-1W
	VM12 SHC	12Cr-2Co-2W
Austenitic	1.4910	16Cr-12Ni
	TP347H FG	18Cr-12Ni
	Super 304H	18Cr-9Ni
	DMV 310N	25Cr-20Ni
Ni-base	INCONEL 617	22Cr-55Ni-11Co

*duplex structure (tempered martensite and δ-ferrite)

Table 4.1: Metallic materials selected in this study. Main alloying additions given in wt.%

4.1.1 Ferritic/martensitic steels

Low alloyed creep resistant steels such as 13CrMo4-4 are widely used for piping and boiler tubes at service temperatures up to approximately 540°C. Those materials are characterized by good mechanical properties, good weldability and low manufacturing costs. High strength 9-12% Cr martensitic steels are widely used in thick section components for temperatures up to approximately 620°C, however, the recently developed experimental steels containing 11% Cr

such as SAVE12 and NF12 may be capable of long-term service even up to 650°C mainly due to higher concentrations of W and Co. These elements contribute to strengthening by producing fine and stable nitride precipitates which make the materials potentially suitable for operating at 650°C, however, they are still in a development stage [57-59]. The major advantage of 9-12% Cr steels compared to austenitic steels is their low thermal expansion coefficient (CTE) and high thermal conductivity. The 9-12% Cr martensitic steels are used for live steam and superheater pipes but, as reported in literature by many authors, those steels oxidize faster in steam environments than in air and the limited oxidation resistance seems to be the limiting factor for their application above approximately 600°C [60, 61] in environments containing water vapour.

4.1.2 Austenitic steels

For the applications with the temperatures above ~620°C austenitic steels are preferred because of their higher creep-rupture strength and oxidation resistance compared to ferritic/martensitic steels [59, 62]. The drawbacks of this grade of steels are lower thermal conductivity and significantly higher thermal expansion coefficient compared to the ferritic/martensitic steels. The greater CTE difference between the metal and the oxide provides the potential for increased cracking and spalling of the oxide scale [58]. Advanced austenitic steels for use as super- and re-heater tubing are available for service temperatures up to 650°C and possibly 700°C as reported in [59].

4.1.3 Ni-base alloys

For the highest application temperature around 700°C the use of Ni-base alloys will be necessary. These alloys possess substantially higher creep strength than martensitic and austenitic steels. The alloy chosen for the investigation in the present study (INCONEL 617) is commonly used as plate or sheet material in jet engines and industrial gas turbines. It is also a candidate construction material for high temperature gas-cooled reactors where the operating temperatures are envisaged to be as high as 850°C or even 950°C [63, 64].

Comparisons of the stress rupture properties of the alloys selected in this study are presented in Figs. 4.1-2.

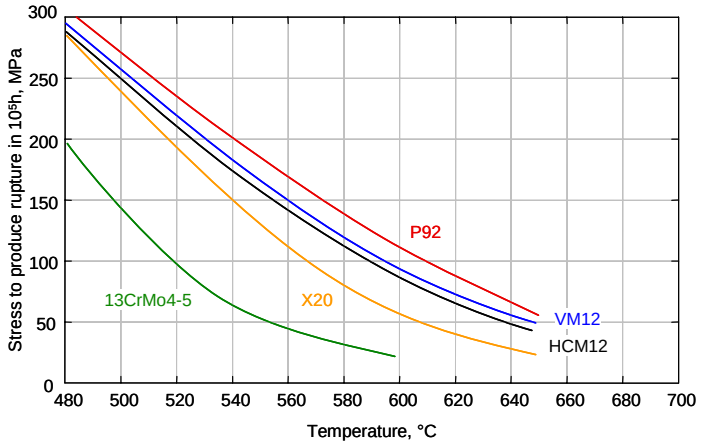

Figure 4.1: Stress rupture properties of ferritic/martensitic steels selected in this study. Source: Hitachi Power Europe GmbH

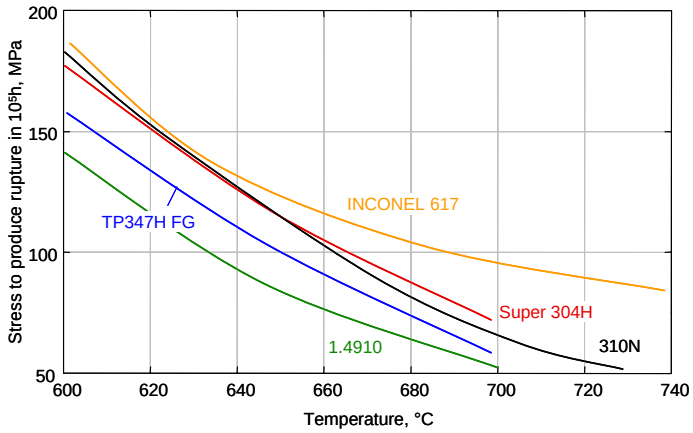

Figure 4.2: Stress rupture properties of austenitic steels and Ni-base alloy selected in this study. Source: Hitachi Power Europe GmbH

4.2 Specimen preparation

For most of the oxidation experiments, samples of 20x10x2mm^3 were cut from thick walled tubes and ground up to 1200 grit surface finish. Due to the requirements of the experimental set-up, in some of the specimens a 2mm diameter hole close to the short edge was drilled. Specimens which were envisaged to be analyzed by the very sensitive surface analysis techniques (SNMS) were polished up to 1µm using diamond paste prior to the oxidation test.

Additionally, for a number of experiments specimens were sandblasted prior to oxidation testing in order to investigate the effect of cold work on the oxidation behaviour. Each sample was cleaned using ethanol directly before oxidation testing.

4.3 Experimental set-up and oxidation testing

For all oxidation tests, horizontal furnaces with 3 heating element zones equipped with an alumina reaction chamber were used. For test gases containing H_2O one gas stream was mixed with water vapour by an evaporator. CO_2 gas was mixed with water vapour by injection of defined quantities of water already in the gas line and subsequently directed into the reaction chamber. As presented in Fig. 4.3 three identical furnaces were employed for the oxidation tests.

Figure 4.3: Horizontal experimental set-up for long- and short-term exposures in mixed gas environments

Some of the exposures in Ar/H_2O were performed in a vertically arranged furnace equipped with an alumina reaction tube. The Ar/H_2O atmosphere in this furnace was generated by bubbling argon at atmospheric pressure through a humidifier which was controlled at fixed temperature.

The long-term exposures were performed discontinuously. The maximum oxidation time was 1000h. Mass change measurements were carried out every 250h after cooling the specimens to room temperature in dry argon. After weight measurements the specimens were placed back into the alumina holder, then inserted in the reaction tube and heated in inert gas (Ar) up to the required temperature. When the test temperature was reached, the furnace was evacuated and switched to the test atmosphere. The heating rate was 10°C/min and the flow rate of the gas was 30 l/h for the horizontal set-up and 10 l/h in the case of the vertical furnace. The experimental approach provided for each specimen only the net mass gain, which meant that the obtained

weight changes did not include the oxygen uptake tied-up in oxide which might have spalled during oxidation, heating or cooling. To provide more insight into details of the oxidation mechanisms, a number of isothermal tests were performed with exposure times ranging from 5 to 500h in various atmospheres. Additionally, thermogravimetric (TGA) experiments were performed using a microbalance allowing a continuous recording of mass changes during the isothermal oxidation process. For technical reasons the maximum oxidation time in the latter experiments was limited to 72h during which the gas supply rate was 2 l/h.

4.4 Gas compositions

The oxidation tests were preformed in model gas mixtures containing high amounts of CO_2 and/or H_2O in the temperature range of 550-700°C up to exposure times of 1000h. In order to investigate the effect of variations in CO_2, H_2O, O_2 and SO_2 content on the oxidation process, the following gas mixtures were used (Tab. 4.2):

	Ar	**O_2**	**CO_2**	**H_2O**	**SO_2**
Ar/O_2	90	10	-	-	-
Ar/CO_2	50	-	50	-	-
$Ar/O_2/CO_2$	49	1	50	-	-
Ar/H_2O	50	-	-	50	-
$Ar/O_2/H_2O$	47	3	-	50	-
CO_2/H_2O	-	-	70	30	-
$Ar/O_2/CO_2/H_2O$	12	3	60	25	-
$Ar/CO_2/SO_2$	49.5	-	50	-	0.5
$Ar/O_2/CO_2/SO_2$	48.5	1	50	-	0.5

Table 4.2: Compositions (in vol.%) of used test gases

A few additional gas mixtures were used to study details of the oxidation process, such as the effect of CO_2 concentration and oxygen excess in Ar/CO_2. The compositions of these gases are given in Tab. 4.3.

	Ar	**O_2**	**CO_2**
Ar/CO_2	50	-	50
Ar/CO_2	90	-	10
$Ar/O_2/CO_2$	49	1	50
$Ar/O_2/CO_2$	47	3	50

Table 4.3: Compositions (in vol.%) of test gases used for fundamental studies

For experimental reasons, high CO_2- or H_2O-concentrations could not be employed in the TGA facility. Therefore, other gases were used for the TGA tests (Tab. 4.4). Additionally, a number of comparative tests were carried out in laboratory air. Equilibrium activities of the mean species in the CO_2- and/or H_2O-rich atmospheres from Tab. 4.2 as a function of temperature are presented in Figs. 4.4-5. Calculations were carried out using the FactSage software.

	Ar	**CO_2**	**H_2O**
Ar/CO_2	98	2	-
Ar/H_2O	98	-	2

Table 4.4: Compositions (in vol.%) of test gases used during thermogravimetric exposures

4.5 Characterization of oxidized specimens

The steel microstructure and the oxide scales formed on the specimen surfaces were examined using optical microscopy, Laser Raman Spectroscopy (LRS) and Scanning Electron Microscopy (SEM) combined with Energy-Dispersive X-ray (EDX) analysis. Selected specimens were examined by Transmission Electron Microscopy (TEM) using specimen preparation by the Focused Ion Beam (FIB) technique.

Secondary Neutrals Mass Spectrometry (SNMS) as well as Glow Discharge Optical Emission Spectrometry (GDOES) were employed for the analysis of a number of isothermally oxidized specimens. SNMS was additionally used for the analysis of oxide scales formed during exposures to gases containing labeled carbon or oxygen (^{13}C or ^{18}O) in CO_2 and H_2O containing gases. Procedures used for quantification of the SNMS and GDOES profiles are given elsewhere [65, 66].

For preparation of metallographic cross sections, the oxidized specimens were covered by a sputtered thin gold layer and then electroplated with Ni, mounted in an epoxy resin and subsequently treated using conventional grinding and fine polishing methods. The Ni-coating provided protection of the surface oxide layer during grinding and polishing and also ensured better optical contrast between oxide and mounting material. All specimens exposed to the CO_2-containing atmospheres were electrolytically etched using 25% NH_3 solution and subsequently analyzed by optical microscopy in order to evaluate possible presence of carburization zone.

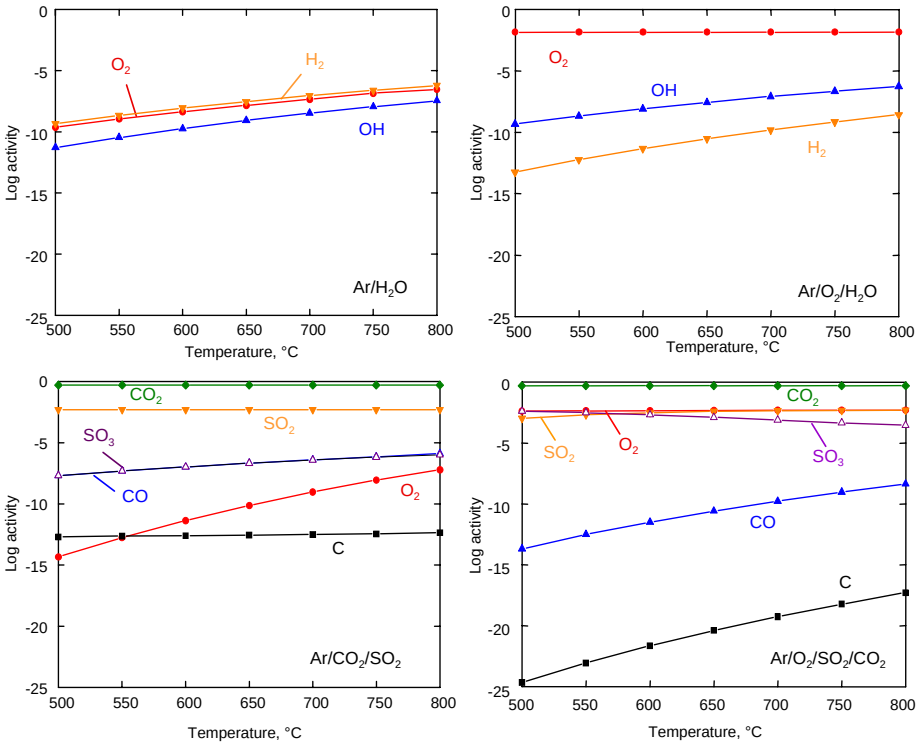

Figure 4.4: Equilibrium activities of main species in various test atmospheres as a function of temperature (calculated using FactSage software)

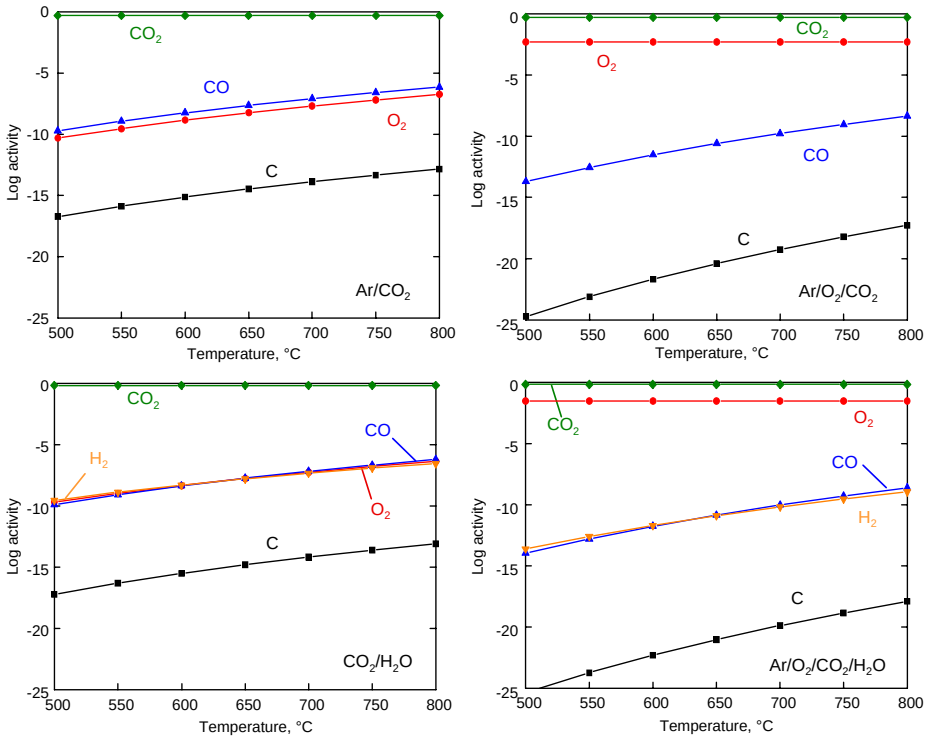

Figure 4.5: Equilibrium activities of main species in various test atmospheres as a function of temperature (calculated using FactSage software)

5. Oxidation behaviour of ferritic/martensitic steels

5.1 General remarks

The maximum exposure time for all selected materials in this study was 1000h. Samples were removed periodically (typically every 250h) from the furnace to take weight measurements and visual examination of the specimens surface. The experimental data points were subsequently recalculated in order to express the obtained weight gain or loss (in milligrams) per unit surface area (in square centimeters). By plotting the specimen weight changes as a function of time the oxidation behaviour of each material could be easily compared. This experimental procedure allowed to collect a maximum of five data points for each specimen during 1000h exposure.

Due to a large number of selected alloys tested in several different atmospheres in a wide range of temperatures it was decided to determine the k_p value of each experimental case and present it in a graphical form rather than plotting for all cases separated oxidation curves for each oxidized specimen. In this way the effect of gas composition and temperature on the oxidation behaviour of the tested steels can be easily compared. However, it must be mentioned that commercial alloys, when oxidized non-isothermally in a complex atmosphere, frequently exhibit deviations from an ideal parabolic rate law. Therefore, the given rate constants may not be in all cases very exact, however, they allow an easy comparison of the various materials and conditions.

For ferritic/martensitic steels the recorded weight changes of specimens were used to determine k_p for all atmospheres except for laboratory air oxidation where the parabolic rate constant was derived from the metallographic measurements of oxide scale thickness. The latter method was also used in the case of austenitic and Ni-base alloys oxidized in all gases, including exposures in laboratory air. Relationships among variously defined parabolic oxidation rate constants are explained in the literature [20]. The reason why two different methods were applied in this study is explained below.

The formation of an external Cr-rich oxide scale on 9-12% Cr steels provides a low oxidation rate as long as there is sufficient Cr flux from the bulk material towards the surface. Prolonged oxidation can deplete chromium beneath a critical level. The re-forming of the protective oxide scale is then no longer possible. Formation of cracks in the scale may then turn into a breakaway type oxidation, i.e., fast growing Fe-rich oxide phases form and grow on the metal surface.

The rate of the breakaway depends on many factors. In this study a frequently observed phenomenon was that Fe oxides tended to nucleate non-homogeneously on the metal surface to form locally separated oxide nodules. The growth rates of such nodules varied significantly from one alloy to another and were affected by temperature and gas composition. After prolonged exposure time further growth of the nodules may result in a covering of this oxide phase over the complete surface of the specimen. As presented in this chapter below, in many cases coexistence of a thin chromia scale and areas of much thicker Fe-base scales were found for 9-12% Cr steels.

A quite different situation was encountered when austenitic alloys were exposed to the oxidizing environments. At temperatures 550-600°C the formation of a protective Cr-rich oxide was typical, whereby no signs of the breakaway were found for most of the tested materials. Thus the recorded weight changes were frequently in the range of the detection limit of the analytical balance. At higher temperatures failure of the initially formed protective oxide scale occurred and spallation of the outer Fe-base oxide scale was frequently observed, especially for those alloys with lower Cr content. Negative weight changes were then recorded. In most cases, however, careful handling of the specimens during metallographic preparation revealed some remnants of an outer oxide scale thus the total oxide thickness could be measured.

In the following the k_p values of selected alloys will be presented as a function of reciprocal temperature for each atmosphere. In some selected cases oxidation curves will be shown to illustrate and discuss specific details of the oxidation behaviour.

Detailed analysis by optical microscopy was carried out for each oxidized specimen. In selected cases Scanning Electron Microscope (SEM) imaging as well as Transmission Electron Microscopy (TEM) was employed. A number of specimens were also analyzed by XRD, SNMS, LRS and GDOES. Due to the large amount of collected data it was decided to present only selected and most representative results.

The test temperatures used in this investigation were selected in such a way that they were representative for the actually envisaged service temperatures of the respective materials in real application [67-74]. In some cases the materials were exposed in a wider temperature range for obtaining data, for instance, estimating possible long-term behaviour at lower temperatures.

5.2 Oxidation in air

Air or oxygen exposure of construction materials at elevated temperatures is one of the most frequently used techniques by many researchers for the acquirement of fundamental data of the oxidation behaviour of materials. This method can provide information concerning the practical limits of operation conditions for steels and high temperature alloys in many practical applications. Therefore, the metallic materials selected in this study were first subjected to air oxidation to provide and to elucidate possible fundamental differences in oxidation behaviour compared to the oxy-fuel related test environments.

When the low alloyed steel 13CrMo4-4 was exposed to laboratory air at temperatures 550-650°C the formation of a multilayered Fe-base oxide scale was found to be formed on the metal surface (Fig. 5.1). The metallographic cross sections revealed a high hematite/magnetite ratio for the formed outer oxide scales. This is likely related to substantial stresses during cooling which favored the formation of in-scale cracks.

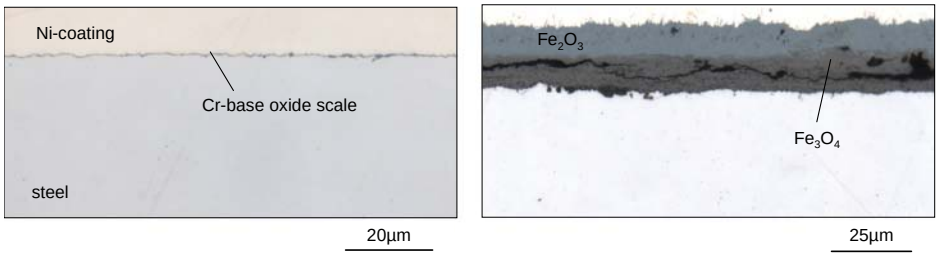

Figure 5.1: Metallographic cross sections of P92 (left) and 13CrMo4-4 (right) oxidized in laboratory air for 1000h at 550°C

Contrary to 13CrMo4-4 the martensitic 9-12% Cr steels exhibited very good oxidation resistance during air exposure at the mentioned temperatures. The general finding for those alloys was the formation of a thin and slowly growing Cr-based oxide scale on the metal surfaces (Fig. 5.1). No breakaway of the protective Cr-base oxide scale was observed at all test temperatures. The parabolic rate constants of the martensitic steels derived from oxide scale measurements are presented in Fig. 5.2.

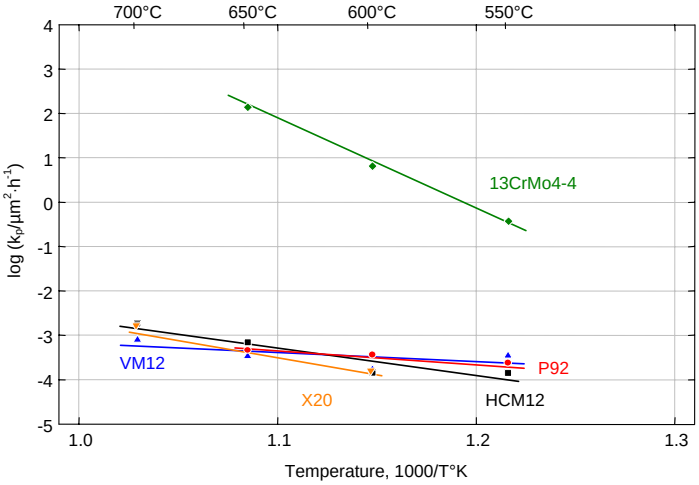

Figure 5.2: Parabolic rate constants as a function of reciprocal temperature of selected steels oxidized in laboratory air (k_p derived from scale thickness measurements)

5.3 Oxidation in Ar/H_2O

In contrast to the thin and highly protective oxide scales formed during air exposure of the 9-12% Cr steels, thick, multilayered Fe-base oxide scales were formed when oxidized in Ar/H_2O. This, however, was preceded by an initially formed thin and protective Cr-rich oxide. The time to breakaway differed from material to material. In the present investigation steels containing a higher Cr content locally maintained the protective scale even up to the maximum exposure time of 1000h.

It was observed that 13CrMo4-4 and other steels with clearly less than 12% Cr tend to form a non-protective iron base scale within less than 100 hours. This change from protective into non-protective oxide scale is a temperature dependent process. For most of the investigated alloys faster deterioration of the initially formed protective scale was observed with increasing temperature. The alloy oxidation behaviour expressed as their parabolic rate constants is presented in Fig. 5.3. The highest k_p values were found for the 1% Cr steel 13CrMo4-4, however, at 550°C the 9% Cr steel P92 and 11.5% Cr X20 showed very similar oxidation kinetics. Upon temperature increase the differences in oxidation rates for individual alloys became more apparent. At 600°C and above a clear tendency for a decreasing oxidation rate with increasing Cr content in the steel was observed.

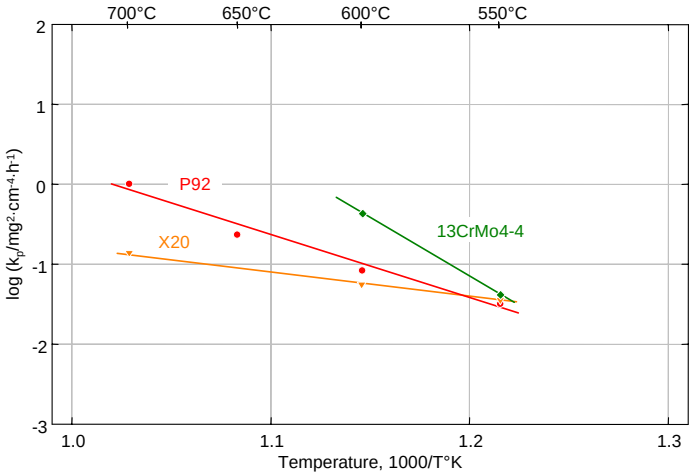

Figure 5.3: Parabolic rate constants as a function of reciprocal temperature of selected steels oxidized in Ar/H_2O (k_p derived from the weight change measurements)

The k_p of VM12 is not included in the graph presented in Fig. 5.3 due to great difficulties to fit the parabolic law to the obtained experimental points. This was explained by the high susceptibility of this alloy to nodule formation and, therefore, to formation of a non-homogeneous growth of the magnetite/hematite oxide phases on the metal surface when local breakaway of the initially formed protective Cr-rich scale occurred. This resulted in relatively smaller weight gains of VM12 specimens during oxidation in Ar/H_2O compared to the other investigated steels. Oxidation curves along with metallographic cross sections are, therefore, presented instead of evaluating the inaccurate parabolic rate constants (Fig. 5.4).

By comparing metallographic cross sections of the oxide scale with the high weight gains illustrated in Fig. 5.4a it can be seen that invariably higher mass gain was recorded after each measurement cycle, as a result of accelerated oxide growth in time. The reason of this very rapid oxidation could be that a thin and protective oxide was growing in the early stages of oxidation, while after cooling the specimen down to room temperature and heating it up again Fe-base oxides were nucleated on the metal surface possibly as a result of micro-crack formation. Those Fe-base nodules grew non-uniformly and after each cooling and heating cycle new nucleation sites were formed due to the damage of the original Cr-rich scale. The oxidation process can thus be presented as a stepwise process involving the growth of newly formed Fe-base oxide nodules after each time step.

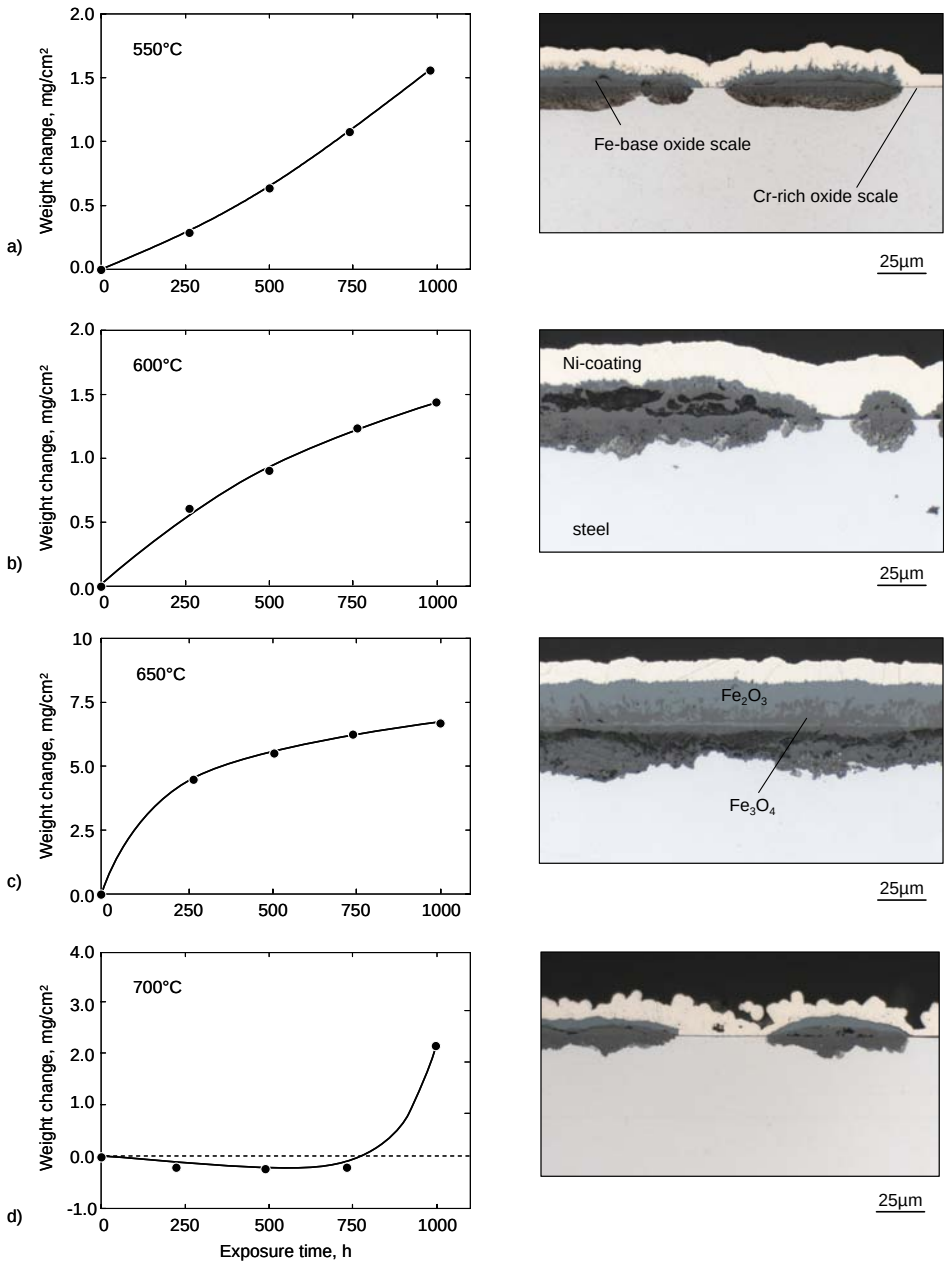

Figure 5.4: Weight changes as a function of time and corresponding cross sections of VM12 after 1000h exposure to Ar/H_2O at: 550°C (a); 600°C (b); 650°C (c) and 700°C (d)

A similar type of oxide scale was formed on VM12 at 600°C. However, the growth of Fe-base oxide nodules was faster and caused in larger areas of the specimen being covered by this oxide phase. At 650°C a continuous layer of magnetite, which was gradually transformed into hematite was present resulting in an oxidation curve following a nearly parabolic behaviour (Fig. 5.4c). The situation changed drastically when the steel was exposed at 700°C. The negative weight changes recorded up to 750h suggested a very minor loss of mass, however, no oxide scale spallation was observed. This could also be the sign of evaporation of volatile species from the surface, however, due to the low oxygen partial pressure in Ar/H_2O gas this was unlikely. A more probable explanation is that the very small weight changes were related to the accuracy of measurement. A rapid increase in mass gain occurred after the third weight measurement. Similar to the case discussed above this was related to breakdown of the protective chromia scale and subsequent rapid development of Fe-base oxide nodules (Fig. 5.4d). Because of the high temperature the protective Cr-base oxide scale could sustained up to the longer exposure times due to much faster Cr diffusion in the alloy. Thus, the scale failure and formation of breakaway type oxide was considerably retarded.

The scale structure observed for the other tested steels exhibited evenly distributed Fe-base, multilayered oxide scales which were already formed during short exposure time. After 250h of isothermal oxidation at 550°C P92 formed a typical two-layered scale consisting of magnetite and hematite in the outer part and an inner mixed oxide scale. A clearly visible internal oxidation consisting of Cr-rich oxide stringers embedded in the metal matrix had developed beneath the surface scale (Fig. 5.5).

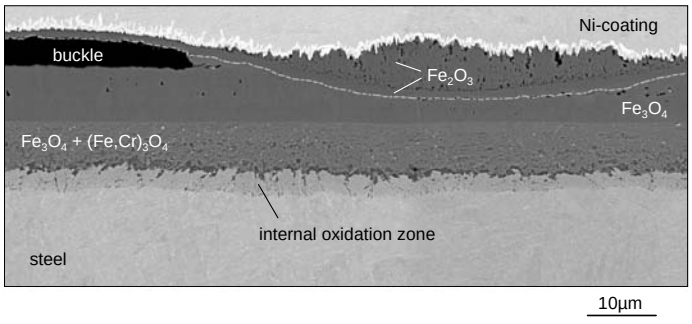

Figure 5.5: SEM image of cross section of P92 isothermally oxidized in Ar/H_2O for 250h at 550°C. The dashed line indicates the Fe_2O_3/Fe_3O_4 interface

One of the interesting features of the ferritic/martensitic steels oxidized in Ar/H_2O (and other H_2O-containing gases) was the local buckle formation in the outer part of the scale (Figs. 5.5-7). During the prolonged exposure this usually resulted in scale spallation upon repeated cooling cycles. This type of oxide scale spallation was observed especially at 600°C and above. Initially formed blisters lead to cracking of the outer scale accompanied by partial loss of the oxide scale. It seems that, independent of the Cr content in the steel, buckles may appear if a non-protective Fe-base oxide scale consisting of Fe_3O_4 and Fe_2O_3 is developed on the metal surface.

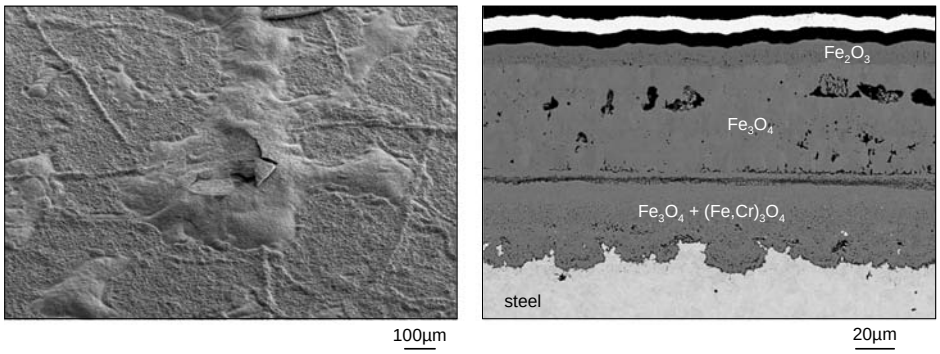

Figure 5.6: SEM images of the oxide surface (left) and cross section (right) of 13CrMo4-4 oxidized in Ar/H_2O for 1000h at 600°C

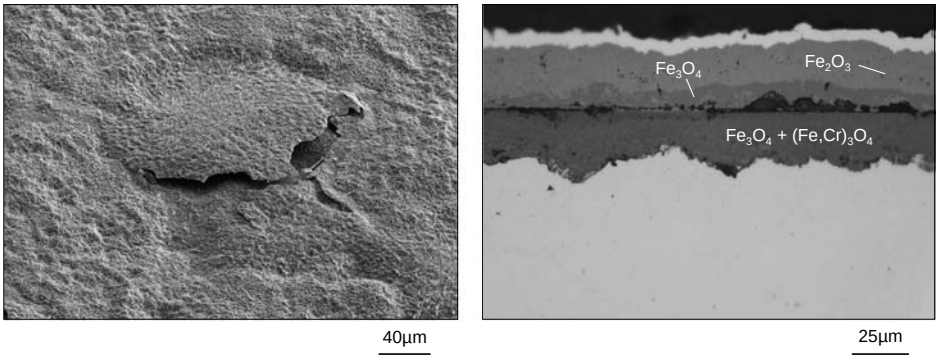

Figure 5.7: SEM image of the oxide surface (left) and metallographic cross section (right) of X20 oxidized in Ar/H_2O for 1000h at 600°C

5.4 Oxidation in Ar/CO_2

Parabolic rate constants for the studied ferritic/martensitic steels oxidized in Ar/CO_2 are presented in Fig. 5.8. It can be seen that in the temperature range of 550-650°C oxidation rates were observed very similar to those in the Ar/H_2O gas. At 700°C a significant decrease of oxidation rate was found for HCM12 and VM12. This is related to the capability of these materials to maintain the initially formed protective oxide scale and also to the formation of Cr-rich oxide bands within the inner oxide resulting in a decrease of in-scale Fe transport. This feature of 9-12% Cr steels was described in the literature as “bell shape” temperature dependence and will be further discussed in Chapter 9.

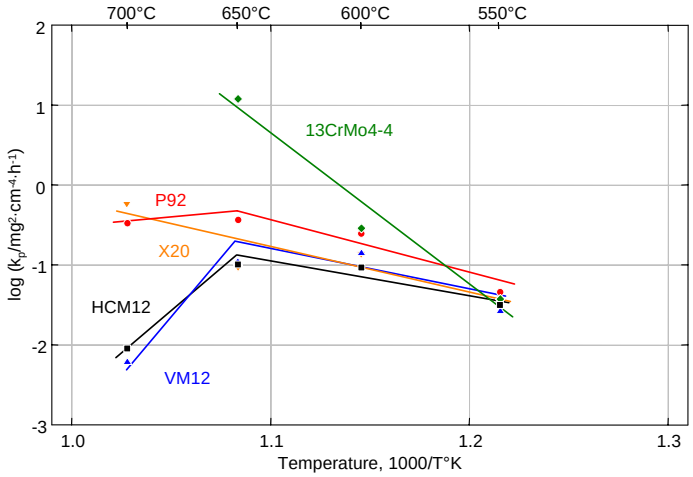

Figure 5.8: Parabolic rate constants as a function of reciprocal temperature of selected steels oxidized in Ar/CO_2 (k_p derived from the weight change measurements)

Figure 5.9 shows the surface morphology and metallographic cross section of the low alloyed steel 13CrMo4-4 after exposure to Ar/CO_2. Minor amounts of fine pores were distributed within the outer hematite layer while much larger voids were present in the magnetite layer. The pore formation is probably related to vacancy condensation during the oxidation process. It is expected that those voids may locally accumulate and cause delamination of the outer oxide scale after longer exposure time. However, as can be seen in the left picture in Fig. 5.9, the surface did not show any buckles or spallation from the metal substrate up to the exposure time of 1000h. This behaviour was found for all of the studied steels oxidized in Ar/CO_2. Cracks and extensive gaps were frequently formed during exposure in Ar/CO_2 for different steels, temperatures and exposure times, however, this never lead to the formation of buckles or blisters (Fig. 5.10).

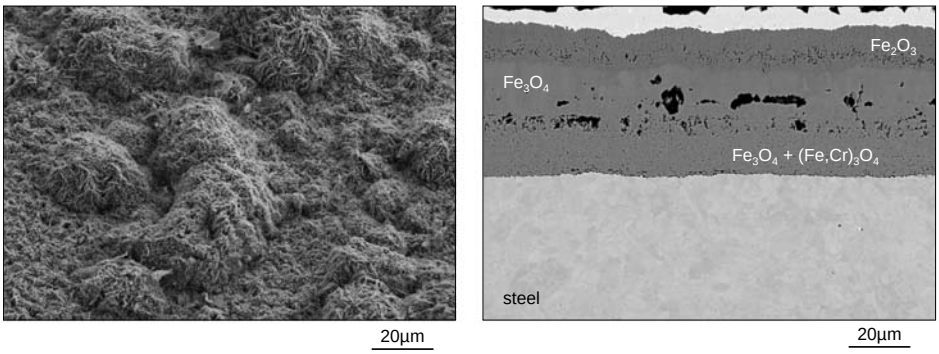

Figure 5.9: SEM images of the oxide surface (left) and cross section (right) of 13CrMo4-4 oxidized in Ar/CO_2 for 1000h at 550°C

In addition to the k_p values presented in Fig. 5.8, weight changes as a function of time of two selected steels during oxidation at 550°C are shown in Fig. 5.11. The higher weight gain observed for P92 was mainly the result of the lower Cr concentration in this steel compared to that of VM12. The time dependence of the oxide scale morphology of P92 is presented in Fig. 5.12. All specimens were oxidized isothermally except for the one which was exposed for 1000h. It can be seen that the oxide thickness increased gradually with increasing oxidation time which was consistent with the weight change data presented in Fig. 5.11.

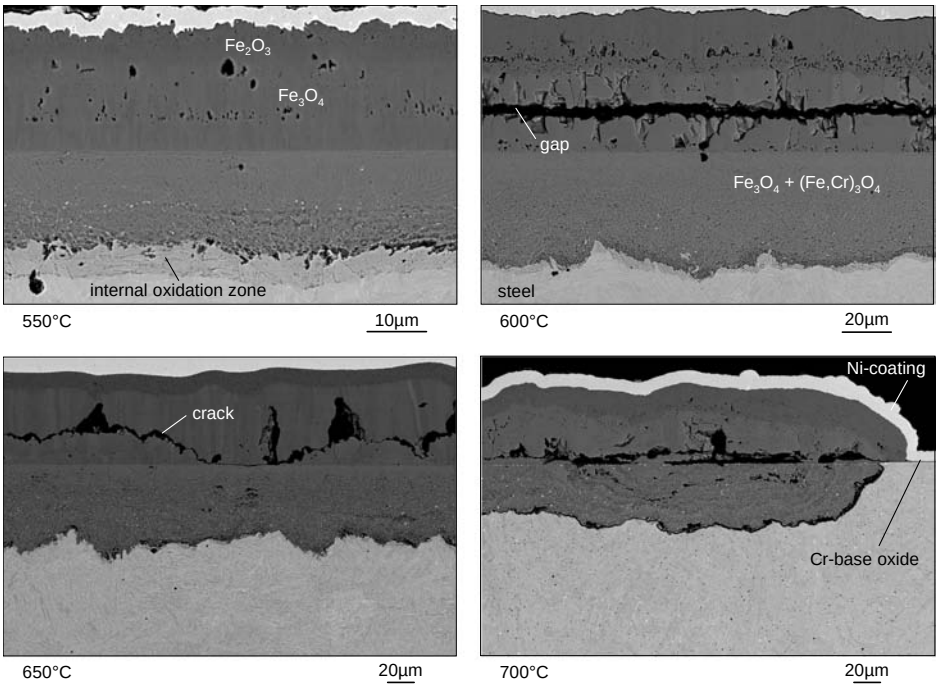

Figure 5.10: SEM images of the cross sections of P92 oxidized in Ar/CO_2 for 1000h at 550-700°C

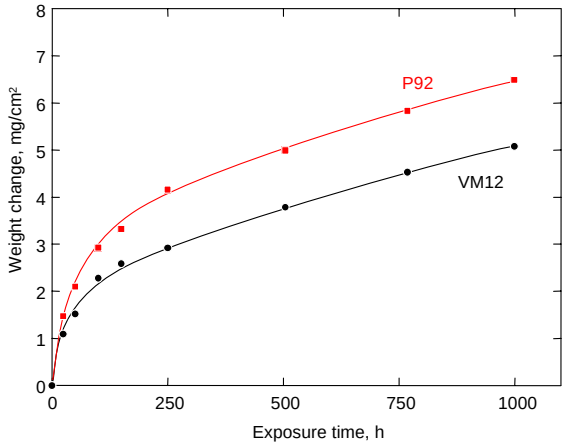

Figure 5.11: Weight changes of P92 (red) and VM12 (black) during oxidation in Ar/CO_2 at 550°C

Further analysis of the cross sections leads to the conclusion that the void formation began already within the first 24h of the exposure. A large extent of these macro-defects was subsequently annihilated by healing processes occurring due to the fast cationic transport in the scale. Additionally, CO_2 molecules were able to penetrate through the outer oxide layer as will be illustrated in Chapter 15. In these processes the voids could eventually completely vanish by a mechanism similar to that described for oxide scale formation in water vapour containing gases [42, 38]. After longer exposure times, the appearance of those voids might result in the formation of extensive gaps. This process seemed not to be substantially affected by temperature changes. Fig. 5.13 shows the metallographic cross section of P92 after isothermal oxidation for 250h in Ar/CO_2 at 550°C. The figure is combined with element depth profiles determined by GDOES analysis, represented in logarithmic scale as a function of sputtering time. In Ar/CO_2 a similar type of oxide sequence was formed as during the water vapour exposure. The scale consisted of Fe_3O_4 and Fe_2O_3 on the top. Beneath the original metal surface a mixed type of oxide is present.

Fig. 5.13 shows that Fe, Cr, Ni, Si, O and C were present in the external oxide layer as well as in the inner scale. Si and Cr showed here a slight enrichment compared to the bulk alloy. At 550°C an internal oxidation zone was found to be formed near the interface with the bulk alloy. This zone consisted of Cr-rich particles embedded in the metal matrix, similar to those found during Ar/H_2O exposure. At higher temperatures (>650°C) a tendency for vanishing of the internal oxidation zone was frequently observed, as further explained in Chapter 9.

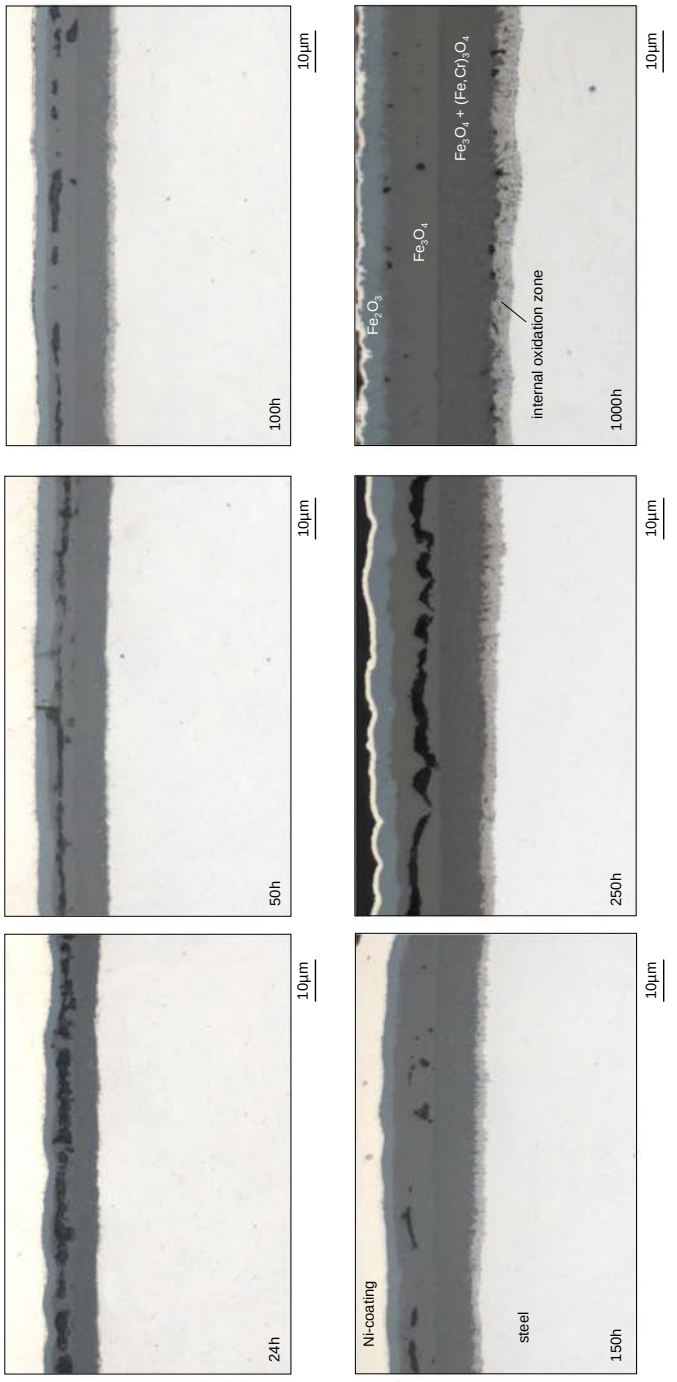

Figure 5.12: Metallographic cross sections of P92 oxidized in Ar/CO_2 for different exposure times at 550°C. Exposure times from 24h to 250h: isothermal oxidation; 1000h: discontinuous oxidation

Well noticeable nickel enrichment was found between the internal oxidation zone and the inner Fe-oxide layer (Fig. 5.13). This element is added to the 9-12% Cr steels to improve the toughness and also to reduce the tendency for undesirable δ-ferrite formation [75]. The effect of Ni, Si and Al on the oxidation behaviour will be further discussed in Chapter 13.

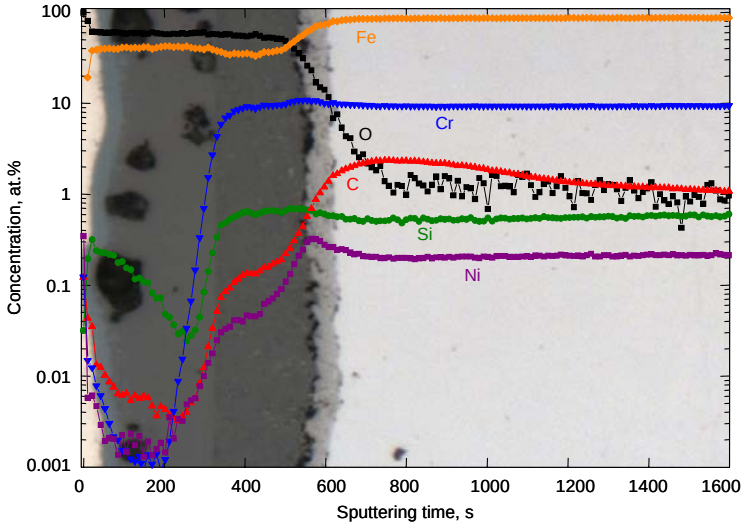

Figure 5.13: GDOES profile combined with metallographic cross section of P92 oxidized in Ar/CO_2 for 250h at 550°C

During the exposure of 9-12% Cr steels to Ar/CO_2 carburization of the bulk material was frequently found to occur immediately after the breakaway of the protective Cr-rich oxide scale. The carbon profile shown in the GDOES plot (Fig. 5.13) represented, therefore, the effect of inward diffusion of carbon containing species (CO_2 or CO) through the scale which subsequently form carbide precipitations whose concentration can vary considerably with exposure time and temperature. A detailed description of the carburization process will be given in Chapter 15.

With increasing oxidation temperature differences in scaling rate among individual alloys became more pronounced. The general tendency for the 9-12% Cr steels was that mass gains increased with increasing temperatures up to 650°C. Further temperature increase resulted in a decreased oxide thickness as well as a decreased mass gain. This behaviour is illustrated in Fig. 5.8 where for steels VM12 and HCM12 the lowest k_p was recorded at the highest test temperature. The cross sections of two selected steels exposed at 700°C to Ar/CO_2 are presented in Fig. 5.14.

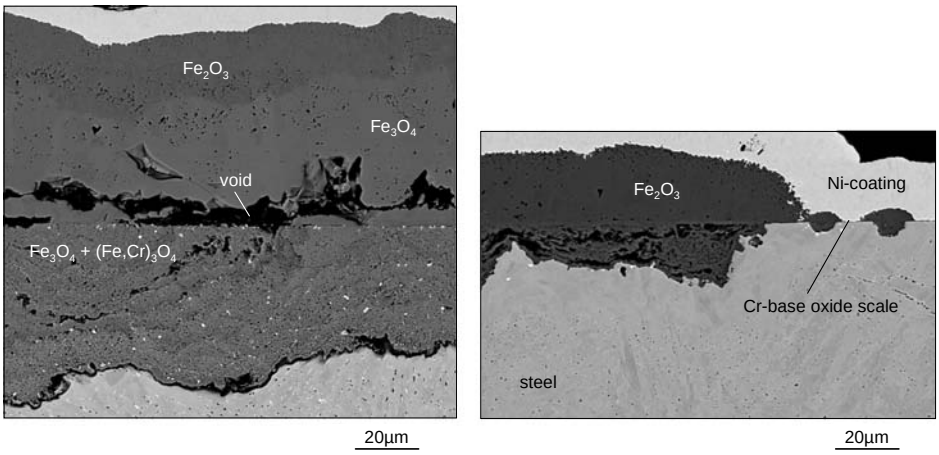

Figure 5.14: SEM images of the cross section of P92 (left) and VM12 (right) oxidized in Ar/CO_2 for 1000h at 700°C

The reason for the fact that some of the steels exhibited lower oxidation rates at 700°C than those, e.g., at 650°C is likely related to the enhanced diffusion of scale forming elements, primarily Cr, in the bulk steel. The higher mobility of chromium in the steel resulted in the formation of more protective Cr-rich $(Fe,Cr)_3O_4$. This oxide acted as diffusion barrier against outward migration of Fe cations. If a sufficiently high amount of Cr was present in the alloy the initially formed Cr-rich oxide scale could be maintained even after prolonged exposure times. Additionally, the outer Fe-base oxide scale consisted mainly of Fe_2O_3 in that case (Fig. 5.14). An explanation for the latter effect has been described for oxidation behaviour in water vapour rich gases [76].

A further series of exposures was carried out to investigate whether differences in CO_2 content might change the described oxidation behaviour of ferritic/martensitic steels in Ar/(50%)CO_2. For this purpose a number of steels was exposed in the gas mixture Ar/(10%)CO_2. The short-term isothermal test results showed that the decrease in CO_2 content did not substantially change the oxidation behaviour of the studied materials. The observed mass gains and oxide scale morphologies found for the low alloyed steel and the 9-12% Cr steels were similar to those observed in Ar/(50%)CO_2. As an example, cross sections of P92 exposed to the two test gases are presented in Fig. 5.15.

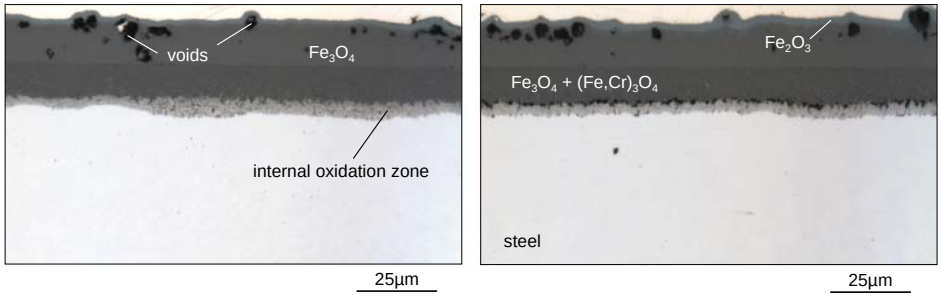

Figure 5.15: Metallographic cross sections of P92 isothermally oxidized in Ar/(10%)CO_2 (left) and Ar/(50%)CO_2 (right) for 250h at 550°C

5.5 Oxidation in CO_2/H_2O

The parabolic rate constants presented in Fig. 5.16 indicate that the oxidation rates of the low alloyed and martensitic steels exposed to CO_2/H_2O were slightly different from those observed during oxidation in Ar/CO_2. Comparing the k_p values obtained after exposure to the two CO_2-containing atmospheres it was apparent that at 550-600°C slightly lower oxidation rates were found in CO_2/H_2O whereas at higher temperatures the opposite effect was observed. This finding is consistent with the cross sections presented in Fig. 5.17 and Fig. 5.12.

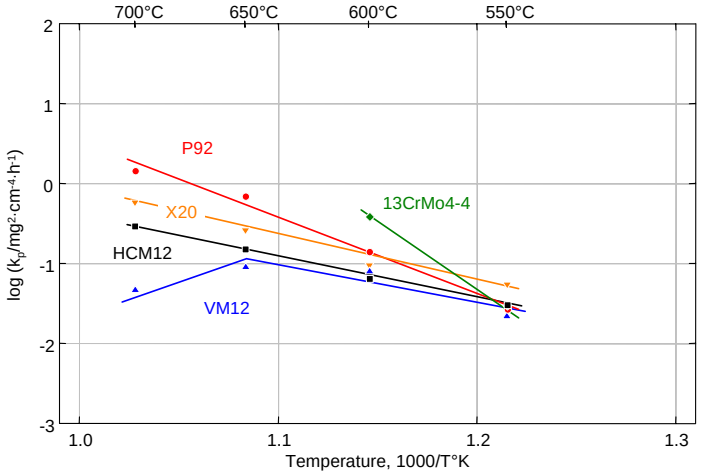

Figure 5.16: Parabolic rate constants as a function of reciprocal temperature of selected steels oxidized in CO_2/H_2O (k_p derived from the weight change measurements)

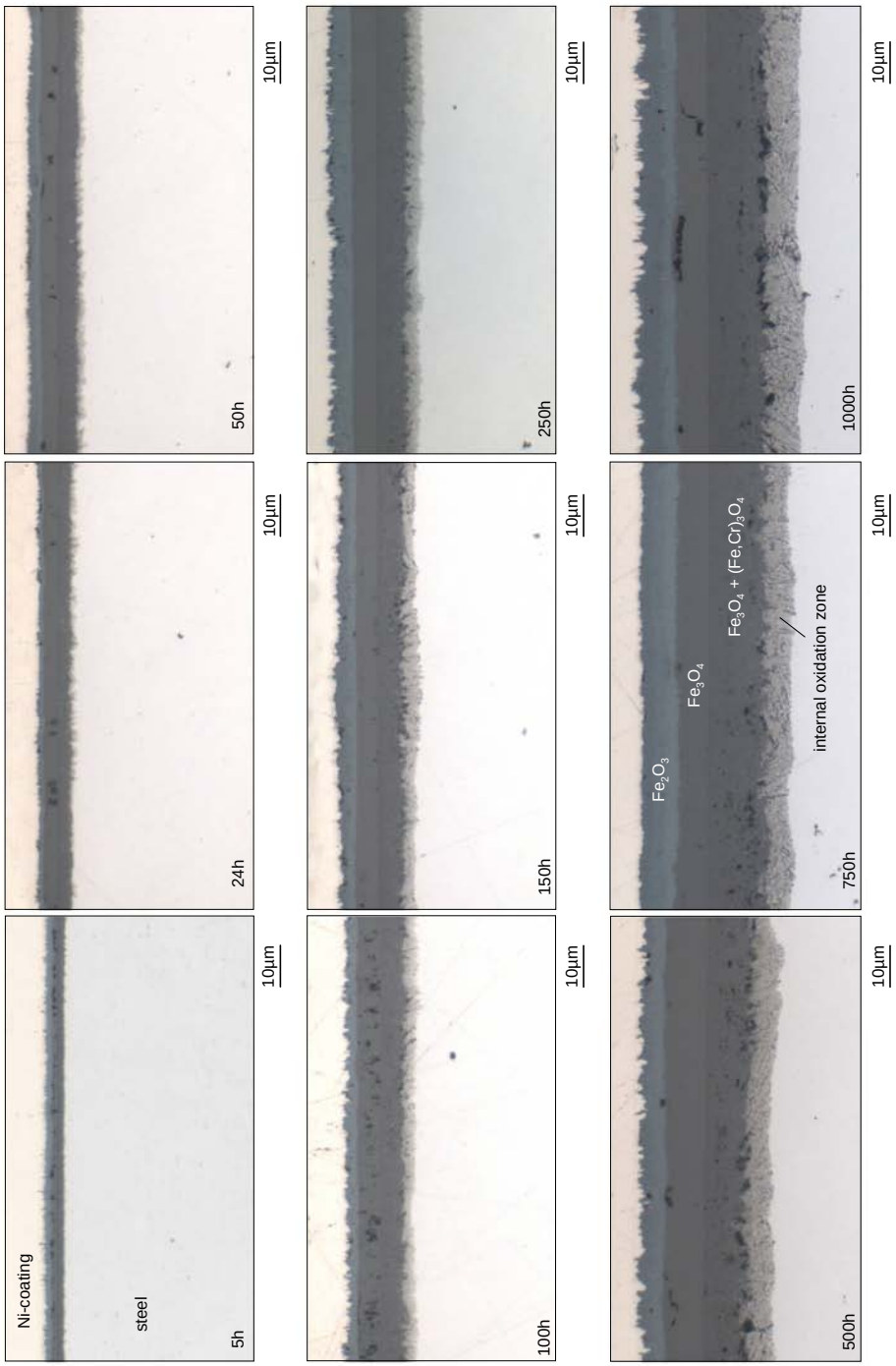

Figure 5.17: Metallographic cross sections of P92 oxidized in CO_2/H_2O for different exposure times at 550°C. Exposure times from 5h to 250h: isothermal oxidation; 500h-1000h: discontinuous oxidation

A noticeable difference was found in the oxidation behaviour between VM12 and the other martensitic 9-12% Cr steels. After 1000h exposure at 550°C VM12 was still able to maintain some areas on the metal surface covered by a thin and protective Cr-base oxide scale (Fig. 5.18). This was not observed for other alloys, even those with similar Cr content such as X20 and HCM12. The observed lower oxidation rate of VM12 resulted from the higher ability to maintain the protective oxide scale of this material is also presented in the cross sections in Fig. 5.19.

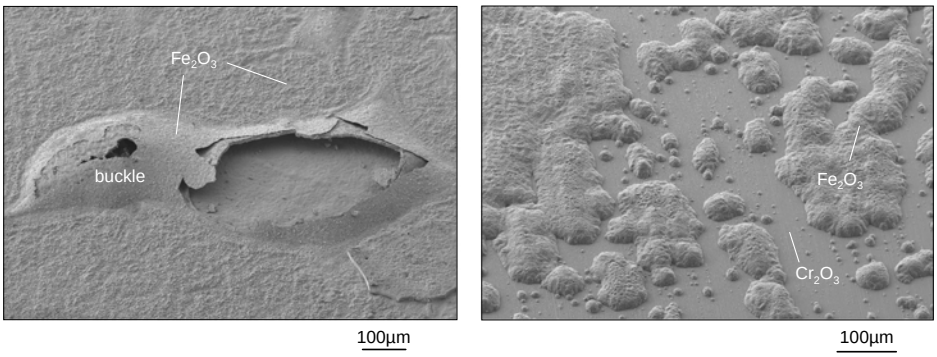

Figure 5.18: SEM images of the oxide surface formed on the P92 (left) and VM12 (right) after 1000h exposure to CO_2/H_2O at 550°C

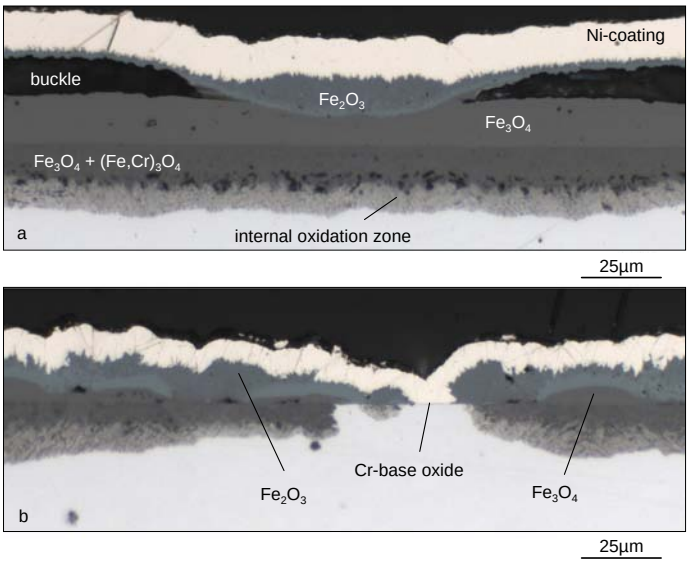

Figure 5.19: Metallographic cross sections of P92 (a) and VM12 (b) after 1000h oxidation in CO_2/H_2O at 550°C

In spite of this more protective behaviour of VM12, it should be mentioned that failure of the initial protection offered by a Cr-rich scale occurred within less than 100h of oxidation for all investigated martensitic 9-12% Cr steels. As in Ar/CO_2 the time to breakaway was found to be slightly shorter for alloys containing less chromium but apparently a Cr concentration even as high as 12wt.% was not sufficient to maintain the Cr-rich scale during long-term exposure. The composition of the outer Fe-base oxide scale was found to be similar to that growing during exposure to Ar/CO_2. The element distribution obtained by GDOES shown in Fig. 5.20 revealed an enrichment of some of the minor alloying elements, mainly silicon and nickel within the inner scale. A substantial enrichment of carbon in the metal matrix was also observed indicating susceptibility of this type of steels to carburization also in CO_2/H_2O. An internal oxidation zone was commonly observed beneath the Fe-rich oxide layer and was most pronounced at lower temperatures. Similar to the finding in Ar/CO_2 and Ar/H_2O, the internal oxidation zone had a strong tendency to vanish at higher temperatures. This can be seen in Fig. 5.21 where SEM cross sections of two steels exposed at temperatures between 600 and 700°C are presented.

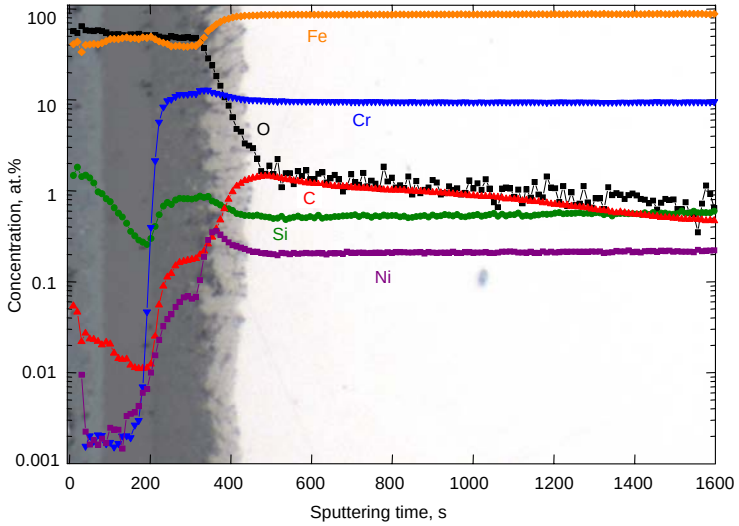

Figure 5.20: GDOES profile combined with metallographic cross section of P92 after oxidation in CO_2/H_2O for 150h at 550°C

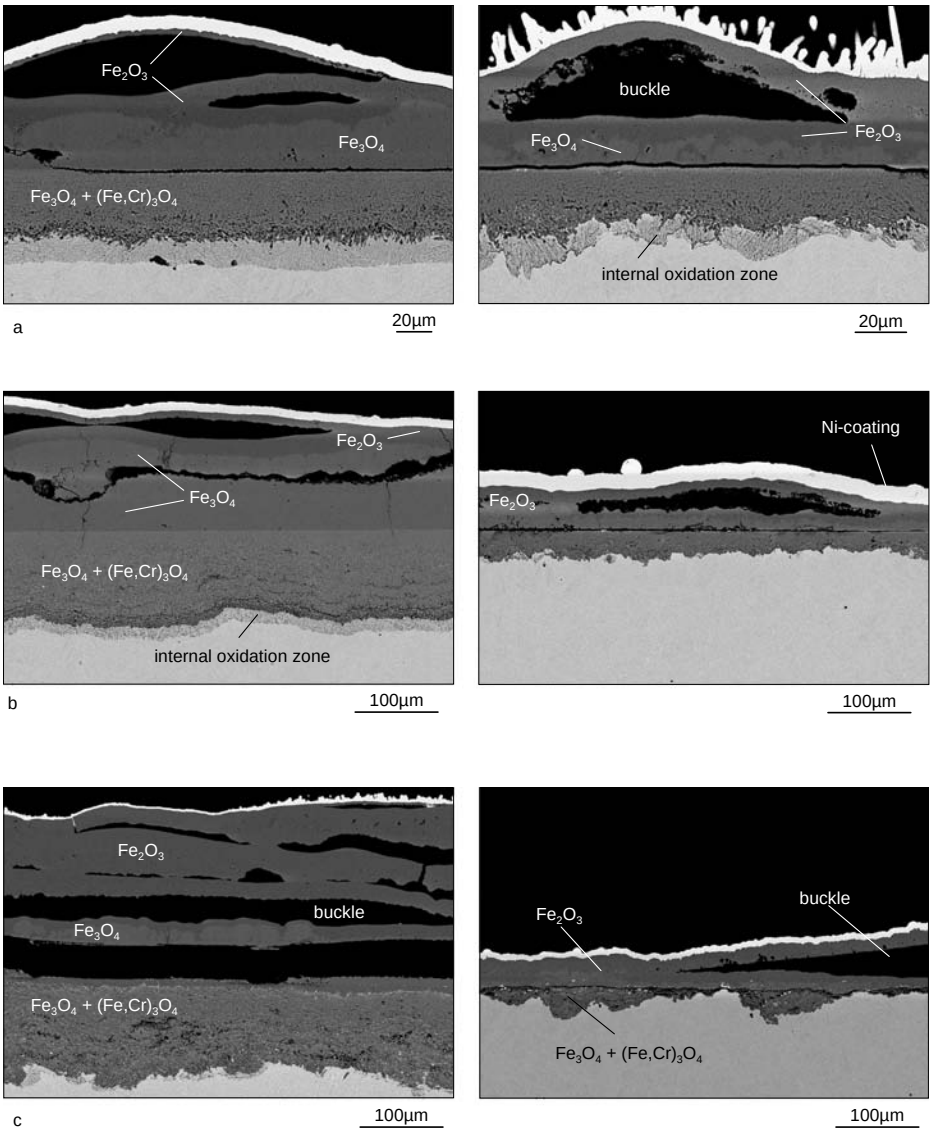

Figure 5.21: SEM images of the cross sections of P92 (left) and VM12 (right) oxidized in CO_2/H_2O for 1000h at: 600°C (a); 650°C (b) and 700°C (c)

On the basis of the cross sections from Fig. 5.21 a few general conclusions can be drawn. First of all, buckles tended to be formed within the outer scale, independent of the scale thickness and Cr content in the steel. The buckles were found at all temperatures, however, to a much larger extent at 650 and 700°C, especially for alloys with lower Cr content. Large buckles showed a tendency to "collapse" occasionally. Smaller buckles which were usually formed within thinner scales were relatively stable, even at 700°C. This was observed for, e.g., VM12. As already mentioned,

this steel showed a decrease in oxidation rate at this temperature. Different from the results obtained in Ar/CO_2 the oxide scale formed on the metal surface at 700°C was laterally homogeneous and consisted almost exclusively of Fe_2O_3 with only minor remnants of Fe_3O_4. The presence of an initially formed Cr-base oxide scale was not observed, while a strong enrichment of chromium was found within the inner layer formed at 650 and 700°C. The tendency for the development of Cr-rich bands in the inner scale increased with increasing Cr content in the steel (Fig. 5.22).

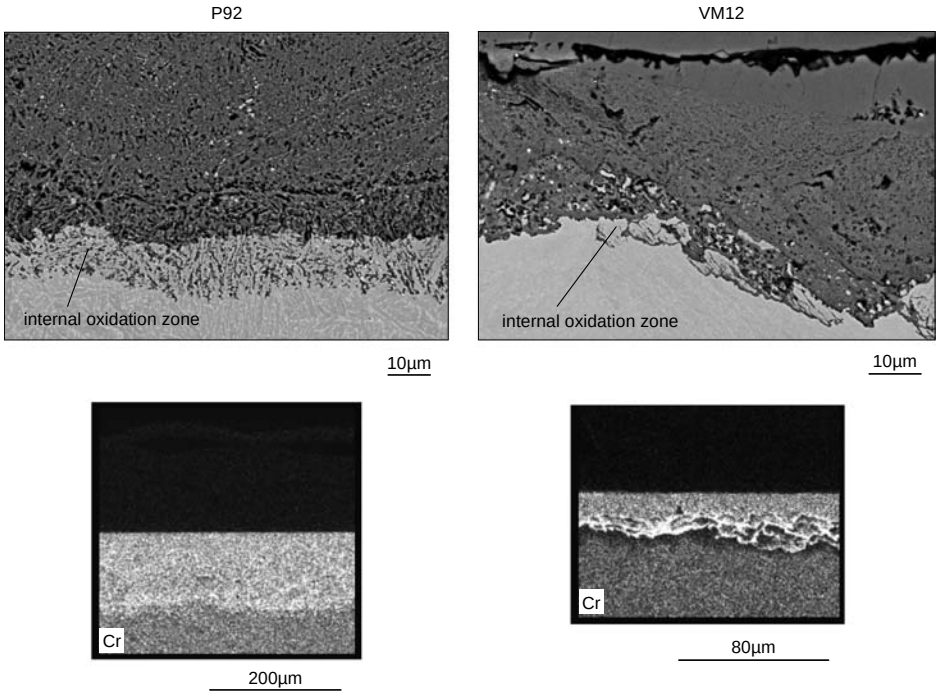

Figure 5.22: SEM images of the cross sections of the metal/oxide interface (upper images) and Cr distribution (lower images) in the inner oxide layer formed on P92 (left) and VM12 (right) during oxidation in CO_2/H_2O for 1000h at 650°C

5.6 Oxidation in $Ar/O_2/CO_2/H_2O$

The weight change curves of P92 and VM12 shown in Fig. 5.23 illustrate that the temperature dependence of the oxidation behaviour in $Ar/O_2/CO_2/H_2O$ differed from one alloy to another. The general finding was that for all 9-12% Cr steels the oxidation rate increased with increasing temperature, except for VM12.

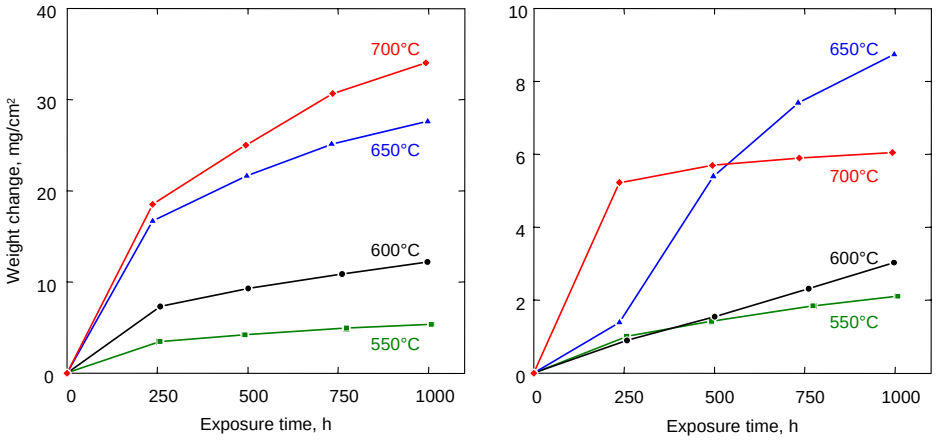

Figure 5.23: Weight change curves of P92 (left) and VM12 (right) during oxidation in $Ar/O_2/CO_2/H_2O$ at 550°C-700°C

Similar to the behaviour found in other test atmospheres, VM12 tended to exhibit lower oxidation rate at 700°C than that at 650°C. For this alloy no oxide spallation was observed, while some blisters were formed at 550-650°C. At 700°C the outer oxide scale consisted exclusively of a dense and pore-free hematite. The inner oxide scale consisted typically of Fe_3O_4 and $(Fe,Cr)_3O_4$ with substantial Cr enrichment (Fig. 5.24). The weight change curves of VM12 steel (Fig. 5.23) indicate a similar oxidation behaviour to that found in Ar/H_2O (section 5.3). In the early stages of oxidation a thin and protective Cr-base scale was formed. Upon prolonged exposure this protective scale was gradually consumed by faster growing Fe-rich oxide nodules. This conclusion is supported by the fact that after 1000h exposure at 550-600°C some areas of the specimen surface were still covered by the Cr-rich oxide scale. At higher temperatures, however, this was not observed.

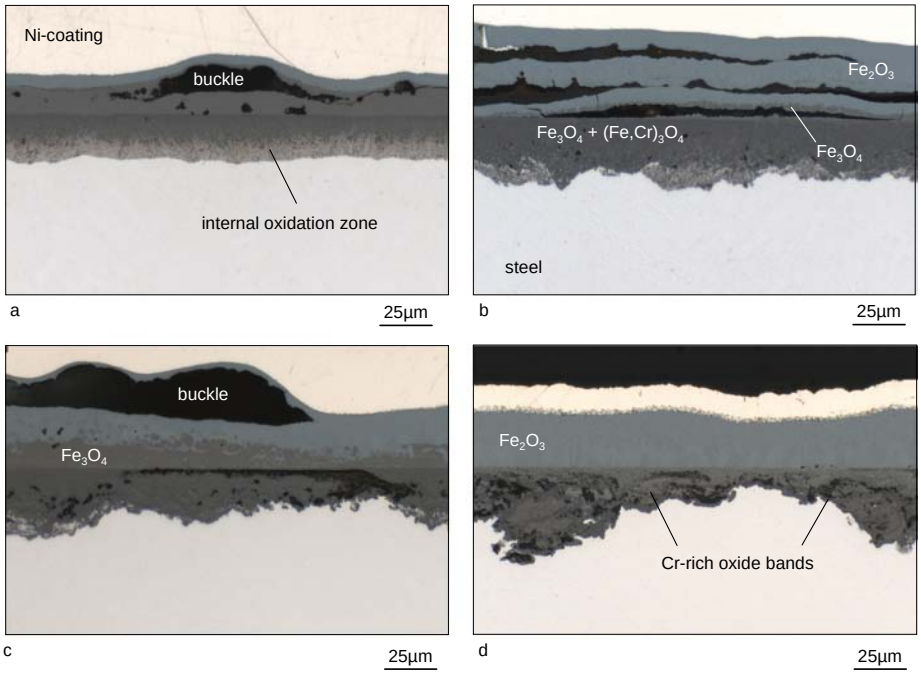

Figure 5.24: Metallographic cross sections of VM12 after 1000h oxidation in $Ar/O_2/CO_2/H_2O$ at: 550°C (a); 600°C (b); 650°C (c) and 700°C (d)

For the other ferritic/martensitic steels complete breakaway of the protective scale was also found after the total exposure time of 1000h. The cross sections presented in Fig. 5.25 show, as an example, the development of the oxide scale formed on P92. The composition of the oxide scale was very similar to that found after CO_2/H_2O exposure. At all temperatures a double layered outer scale consisting of hematite and magnetite was formed. The inner layer consisted of mixed oxide which was formed beneath the original metal surface. An internal oxidation zone was clearly visible after oxidation at 550-650°C. At 700°C, however, this zone was only partially formed because most of the Cr was incorporated into the inner oxide scale in the form of Cr-rich bands. Additionally, the outer scale showed a strong tendency to exhibit buckling. The scale morphology presented in Fig. 5.25 suggests that at 550-650°C these blisters were able to disappear by a “re-healing mechanism”. At 700°C the extent of buckling was very pronounced. For some alloys a multilayered blister structure was found additionally to exhibit a strong tendency to fracture of the outermost layers.

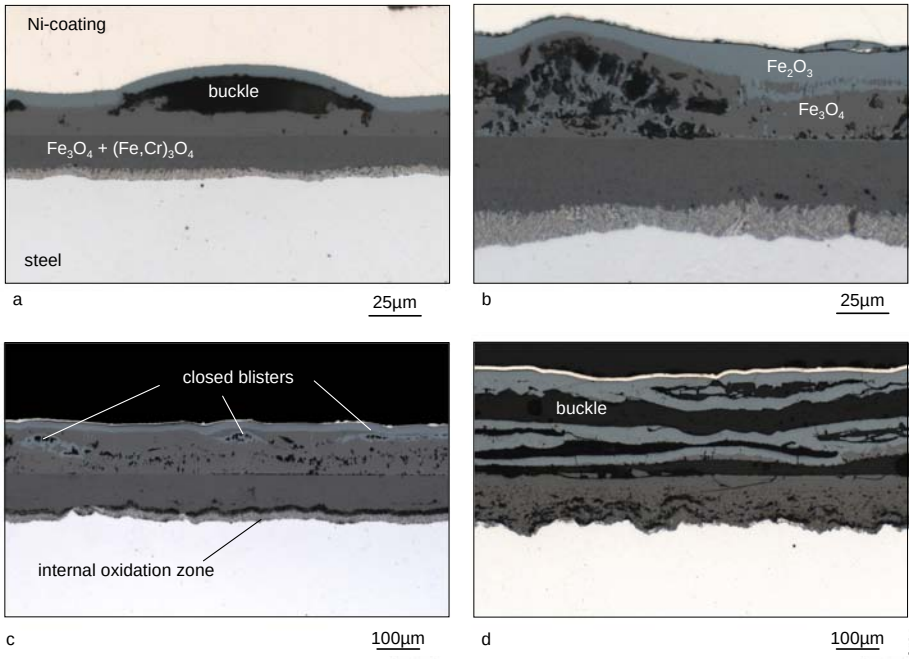

Figure 5.25: Metallographic cross sections of P92 after 1000h oxidation in $Ar/O_2/CO_2/H_2O$ at: 550°C (a); 600°C (b); 650°C (c) and 700°C (d)

Parabolic rate constants calculated from the weight change measurements are presented in Fig. 5.26. For most of the alloys exposed to $Ar/O_2/CO_2/H_2O$ a clear tendency was observed for a higher scaling rate with increased temperature. This was not the case for VM12, as already discussed above.

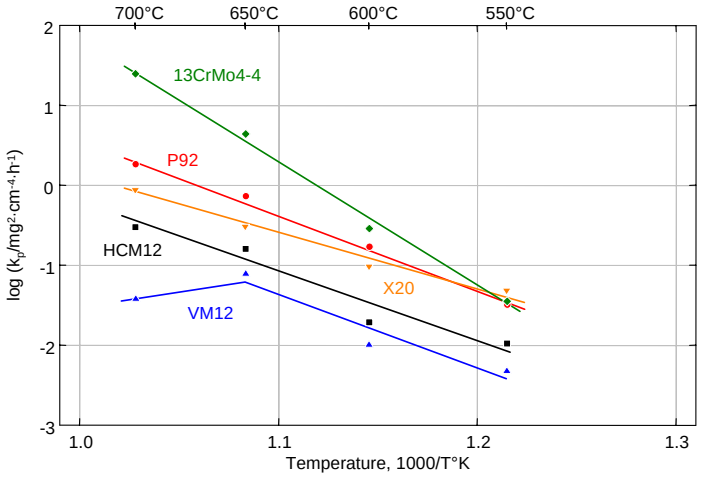

Figure 5.26: Parabolic rate constants as a function of reciprocal temperature of selected steels oxidized in $Ar/O_2/CO_2/H_2O$ (k_p derived from the weight change measurements)

6. Oxidation behaviour of austenitic steels

6.1 Oxidation in air

Exposure to laboratory air revealed excellent oxidation resistance for the tested austenitic steels at all test temperatures between 550 and 700°C. The smallest scaling rate was observed for alloy 310N containing approximately 25% Cr and for 1.4910 with approximately 16.5% Cr (Fig. 6.1). This illustrates that the air oxidation behaviour was not only governed by the Cr content but also by the minor alloying additions and/or steel microstructure.

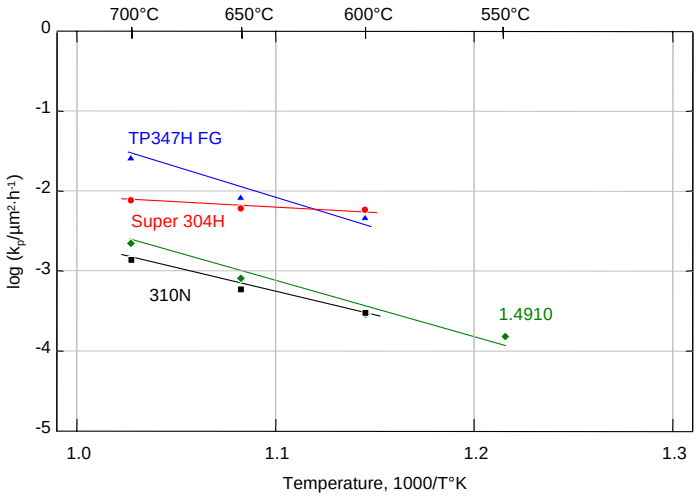

Figure 6.1: Parabolic rate constants as a function of reciprocal temperature of austenitic steels oxidized in laboratory air (k_p derived from scale thickness measurements)

The tendency for the formation of small oxide nodules randomly distributed on the metal surface appeared to be much more pronounced in the case of steels TP347H FG and Super 304H resulting in a higher overall weight gain for these steels. The measured average oxide thickness on these steels was thus higher than that on, e.g., 1.4910 (Fig. 6.2-3).

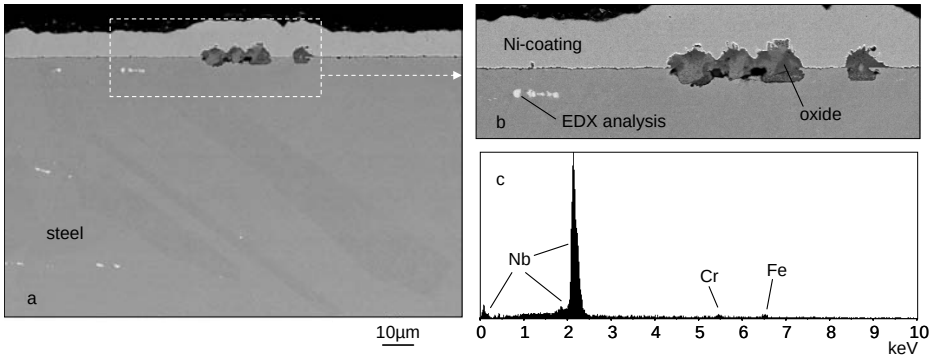

Figure 6.2: SEM images of the cross sections (a,b) and EDX point analysis (c) of TP 347H FG oxidized for 1000h in laboratory air at 650°C

The composition of these locally present oxide nodules growing on the metal surface was investigated by EDX analysis (Fig. 6.3). It was found that they contained high concentrations of niobium and chromium. No nickel enrichment was detected within the nodules which indicated that growth of this oxide phase likely occurred by the oxidation of locally present Nb-rich particles distributed within the bulk metal (Fig. 6.2). Steel TP347H FG as well as Super 304H contained 0.5wt% of Nb whereas 1.4910 did not contain any Nb addition.

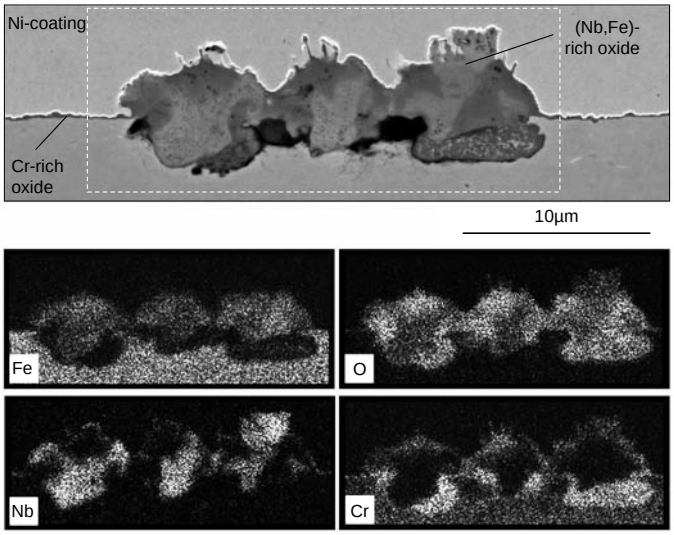

Figure 6.3: SEM cross section and corresponding X-ray mappings from the marked area of TP347H FG oxidized for 1000h in laboratory air at 650°C

6.2 Oxidation in Ar/H_2O

As steam oxidation data for the tested austenitic steels are widely available in literature [77-81], only results of one steel, 1.4910, are presented here as an example. The oxidation tests were carried out in the vertical test set-up described in Chapter 4. The measured scaling rate of 1.4910 at 600, 650 and 700°C presented in Fig. 6.4 was in good agreement with literature data [82].

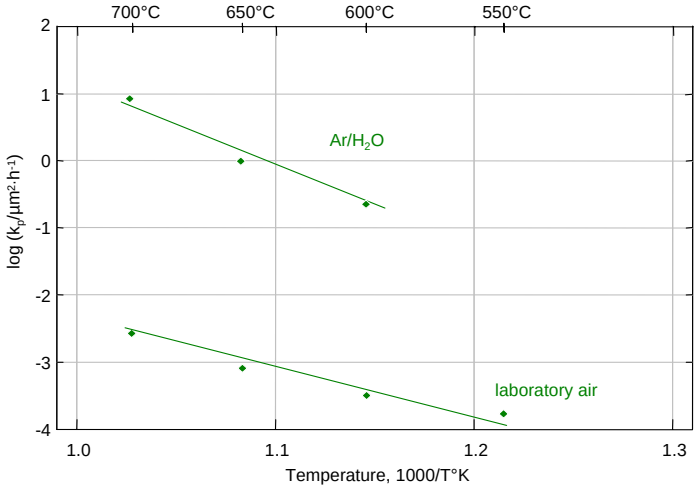

Figure 6.4: Parabolic rate constants as a function of reciprocal temperature for 1.4910 oxidized in Ar/H_2O compared with air oxidation data (see Fig. 6.1). k_p derived from total scale thickness measurements

The oxide scale observed after oxidation in Ar/H_2O typically consisted of an outer Fe_2O_3/Fe_3O_4 scale and inner oxide composed of $(Fe,Cr)_3O_4$ + Fe_3O_4. At temperatures up to 650°C the observed scale morphology exhibited discontinuous formation of Fe-base scale whereas some areas on the metal surface exhibited formation of a thin Cr-base oxide. At 700°C the scale structure was more uniform and deep internal oxidation attack beneath the metal surface was observed (Fig. 6.5). Substantial scale spallation occurred during the exposure at the highest test temperature.

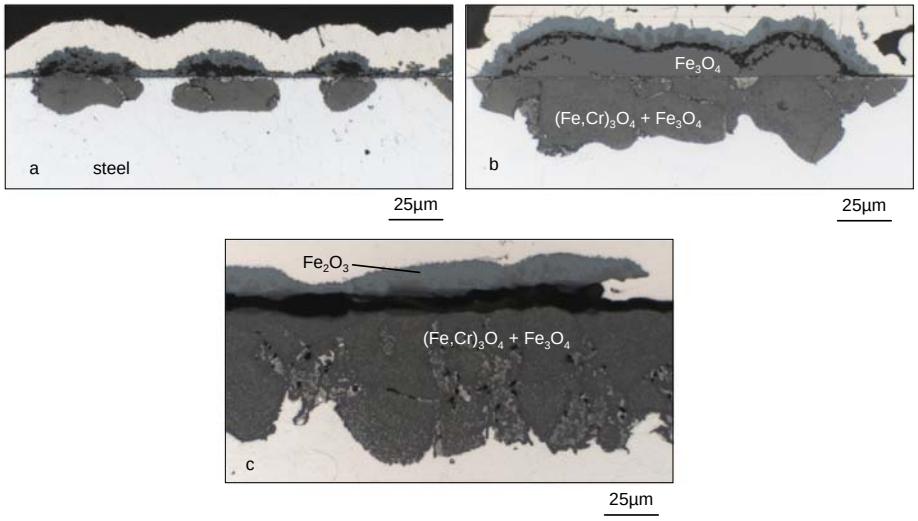

Figure 6.5: Cross sections of 1.4910 oxidized in Ar/H_2O for 1000h at 600 (a); 650°C (b) and 700°C (c)

6.3 Oxidation in Ar/CO_2

Good oxidation resistance of all tested austenitic alloys was observed during the exposure in Ar/CO_2 at 550°C. All alloys tended to form a protective Cr-rich oxide which remained at this temperature during 1000h exposition without any signs of breakaway. Locally, small oxide nodules rich in Nb and Cr were found in some cases, similar to those observed after air exposure (Fig. 6.6).

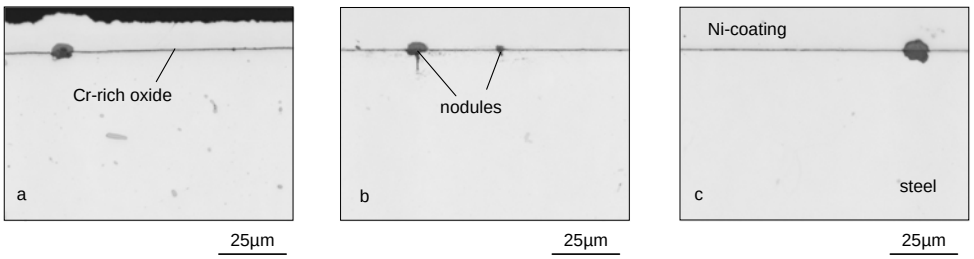

Figure 6.6: Metallographic cross sections of TP347H FG (a); Super 304H (b) and 310N (c) oxidized in Ar/CO_2 for 1000h at 550°C

This situation changed drastically upon temperature increase. At 600°C all austenitic steels, except for the one with the highest Cr content (310N), showed local formation of fast growing Fe-base oxide nodules. Some of the nodules exhibited a tendency to spallation from the metal surface, especially those formed on 1.4910 (Fig. 6.7).

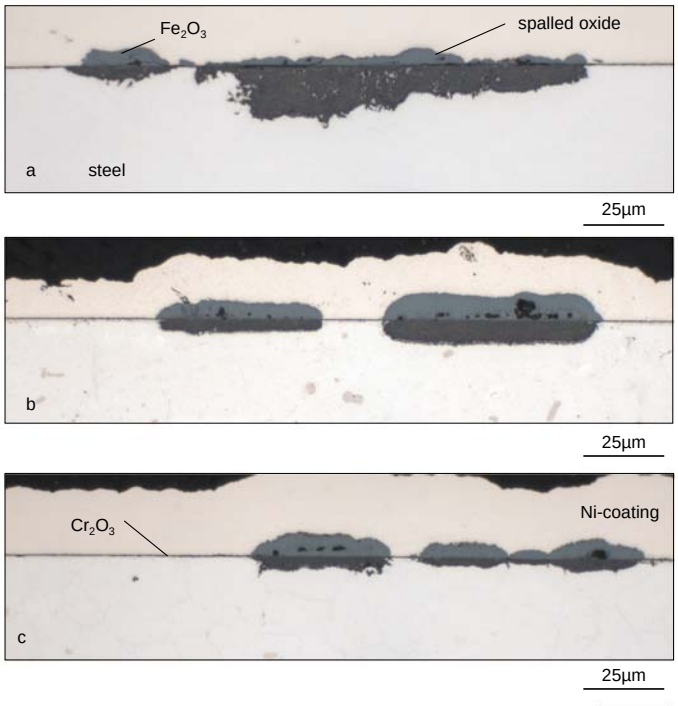

Figure 6.7: Metallographic cross sections of 1.4910 (a); TP 347H FG (b) and Super 304H (c) oxidized for 1000h in Ar/CO_2 at 600°C

The outer part of the nodules consisted of hematite whereas a thin layer of magnetite was growing close to the original steel surface. The inner part mainly consisted of $(Fe,Cr)_3O_4$ and Fe_3O_4. The formation of the nodules was most pronounced at the edges of the specimens.

As described in the literature the earlier occurrence of local breakaway at specimen edges is mainly related to two features:

- Compressive stresses generated in the oxide scale on the flat specimen surface turn into tensile stresses at specimen edges resulting in crack formation in the oxide allowing access of the gas to the Cr-depleted steel surface.
- On the flat surface the retaining of the protective Cr-rich scale is governed by the Cr-flux balance between the scale and the steel. At specimen edges a two-dimensional diffusion situation prevails with the result that the flux of Cr in the steel may be insufficient to sustain the amount of Cr consumed by the scale growth [83-85].

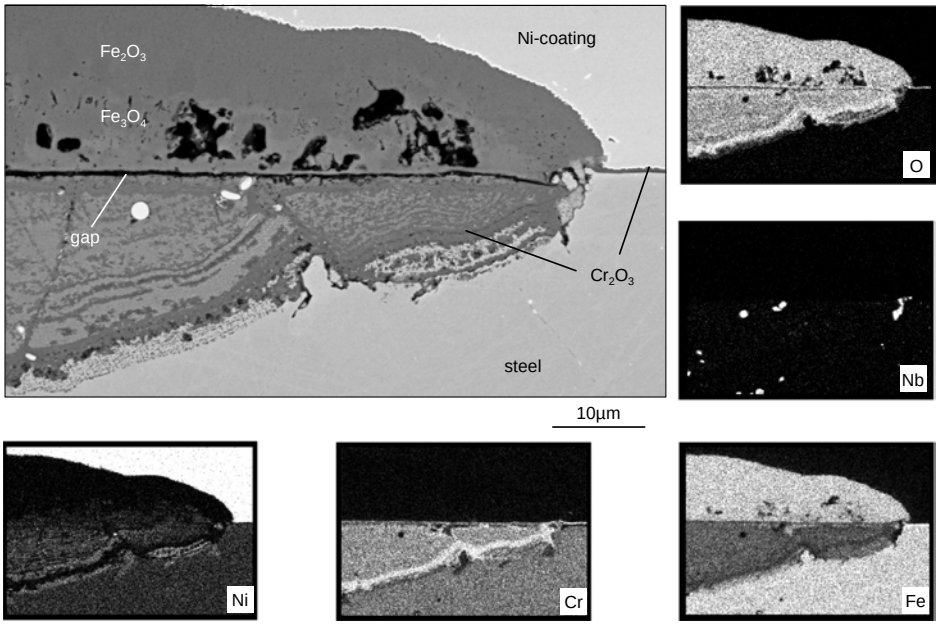

Figure 6.8: SEM images of the cross section of TP347H FG oxidized in Ar/CO_2 for 1000h at 650°C and corresponding X-ray mapping of elements

An increase of the oxidation temperature from 550°C to 650°C resulted in the formation of much larger areas with non-protective oxide nodules covering the metal surface. The development of thick and double-layered outer oxide scale as well as the formation of voids within the magnetite leads to local spallation of oxide during cooling to room temperature, mostly at the original metal surface. This was observed for 1.4910 and to a much lesser extent for TP347H FG. For the latter alloy and also for Super 304H the formation of large, isolated Fe-base oxide islands (Fig. 6.8) was more typical rather than the development of a continuous scale on the metal surface as observed for 1.4910. However, it must be mentioned that for all austenitic steels areas exhibiting the formation of protective Cr-base scale were still present after oxidation at 650°C. As a general rule it can be said that low Cr content in the material results in presence of a high ratio between non-protective and protective scale on the steel surface. Alloy 310N, with its high Cr content of approximately 25wt.%, showed excellent oxidation resistance by forming a thin Cr_2O_3 scale on the whole specimen surface at all test temperatures (Fig. 6.9).

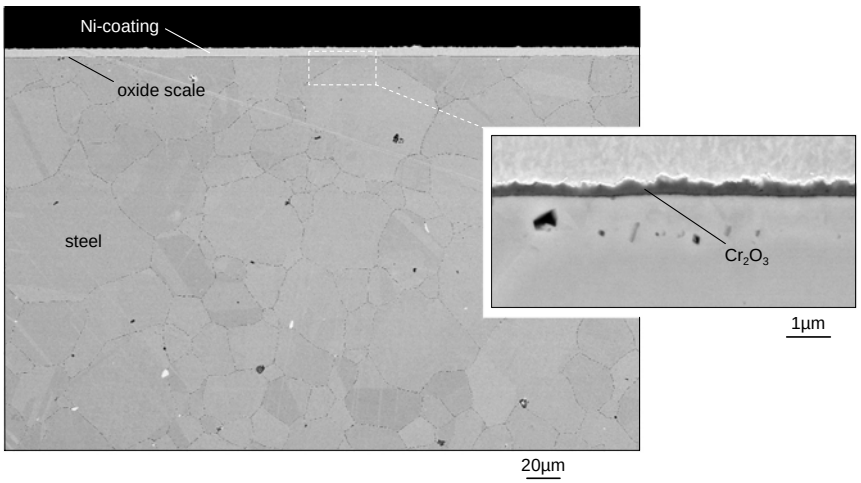

Figure 6.9: SEM images of the cross section of 310N oxidized for 1000h in Ar/CO_2 at 650°C

The parabolic rate constants of austenitic steels exposed at 600, 650 and 700°C to Ar/CO_2 are presented in Fig. 6.10. In the case of alloys with lower Cr content on which thick, Fe-base oxides were formed, the average scale thickness was calculated taking the inner and outer oxide into account. For alloy 310N only Cr-base scale was found after exposure at all temperatures. Therefore, high magnification SEM pictures were used to measure the chromia scale thickness (e.g., Fig. 6.9). For austenitic steels exposed at 550°C the SEM analysis was not performed, thus precise scale thickness measurements were not possible based only on metallographic cross sections. For austenitic steels oxidized at the lowest test temperature (i.e., 550°C), a parabolic rate constant is, therefore, not presented in Fig. 6.10.

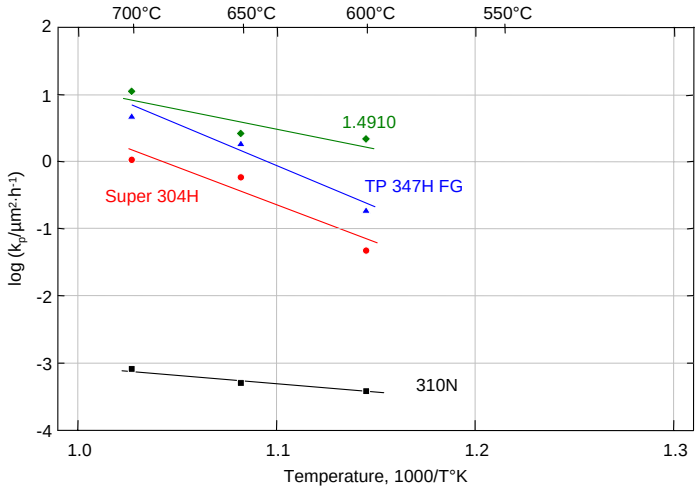

Figure 6.10: Parabolic rate constants as a function of reciprocal temperature of austenitic steels oxidized in Ar/CO_2 (k_p derived from scale thickness measurements)

The weight change curves presented in Fig. 6.11 compare the oxidation behaviour of the austenitic steels during exposure at 700°C. Alloy 310N showed a very small weigh gain (0.15 mg/cm^2 after 1000h), whereas substantial weight loss was recorded for the other materials due to the spallation of the outer oxide scale (Fig. 6.12). This effect was more pronounced for the steels with lower Cr content.

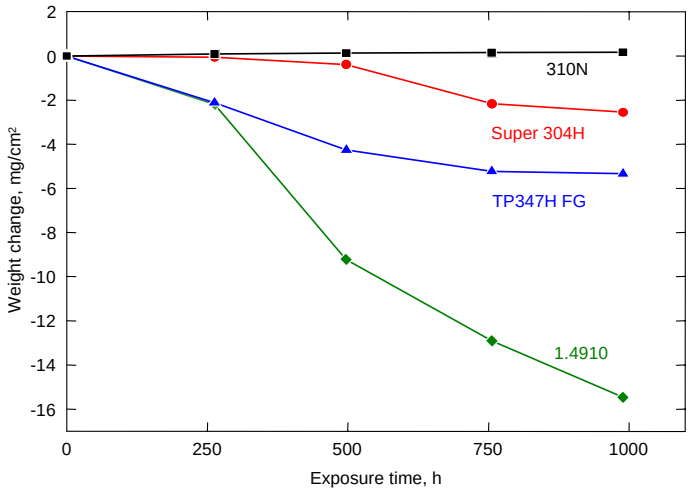

Figure 6.11: Weight changes of austenitic steels during oxidation in Ar/CO_2 at 700°C

At 700°C the austenitic steels except for 310N had marginal ability to develop a protective Cr-rich scale in Ar/CO_2. However, even after 1000h of exposure some areas were found on the Super 304H specimen which maintained a thin protective Cr_2O_3 layer. This alloy contains only around 0.5% more chromium than TP347H FG which was oxidized substantially faster at this temperature. It is believed that steel microstructure and/or the presence of minor alloying elements may be responsible for the better oxidation resistance of alloy Super 304H. For instance, the presence of 0.3% Cu in this material which was intentionally added to stabilize the austenite structure and also to increase the elevated temperature strength [86-89], resulted in a modification of the steel oxidation behaviour due to copper enrichment at the scale/substrate interface [90].

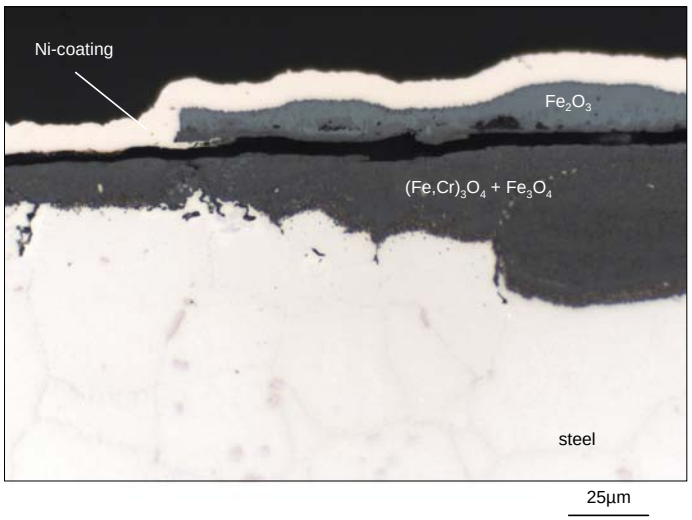

Figure 6.12: Metallographic cross section of TP347H FG after 1000h oxidation in Ar/CO_2 at 700°C

The discussed differences in spallation behaviour of the tested austenitic steels during exposure to Ar/CO_2 at temperatures between 550 and 700°C are summarized in Fig. 6.13.

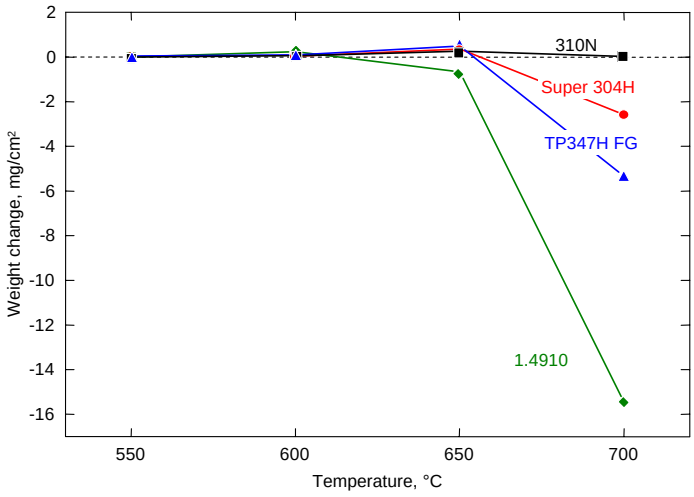

Figure 6.13: Weight changes of austenitic steels after 1000h oxidation in Ar/CO_2 at 550-700°C

6.4 Oxidation in CO_2/H_2O

The parabolic rate constants presented in Fig. 6.14 show that in CO_2/H_2O the oxidation of some austenitic steels was slightly higher than that during the exposure in Ar/H_2O or Ar/CO_2. This general rule was found for the steels containing lower Cr concentrations, i.e., 1.4910, TP347H FG and Super 304H. Steel 310N exhibited excellent oxidation resistance in Ar/CO_2 as well as CO_2/H_2O at temperatures up to 700°C.

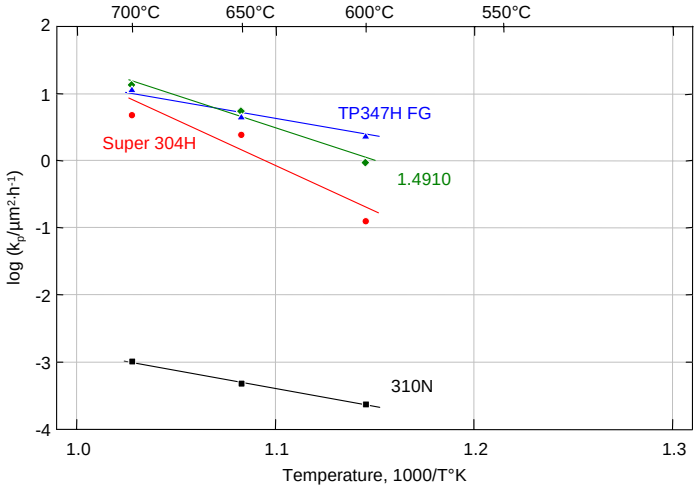

Figure 6.14: Parabolic rate constants as a function of reciprocal temperature of austenitic steels oxidized in CO_2/H_2O (k_p derived from scale thickness measurements)

The cross sections of austenitic steels exposed to CO_2/H_2O at 600°C (Fig. 6.15) showed local destruction of the initially formed Cr-base oxide scale. However, the extent of local breakaway was not the same for all tested materials. Small and separated Fe-base nodules were formed on Super 304H. Much larger nodules were characteristic for 1.4910, while large areas of the specimens were still covered by a thin chromia base scale. For TP347H FG progressive propagation of the Fe-oxide islands resulted in the formation of a near continuously growing layer of Fe_2O_3 covering almost the complete specimen surface. The formation of inner oxide was found in each case. For TP347H FG cracks developed at the interface between the inner and outer oxide scale eventually resulted in a partial exfoliation of the scale. The nodules formed on the other steels exhibited good adhesion and no spallation was observed up to the maximum exposure time of 1000h.

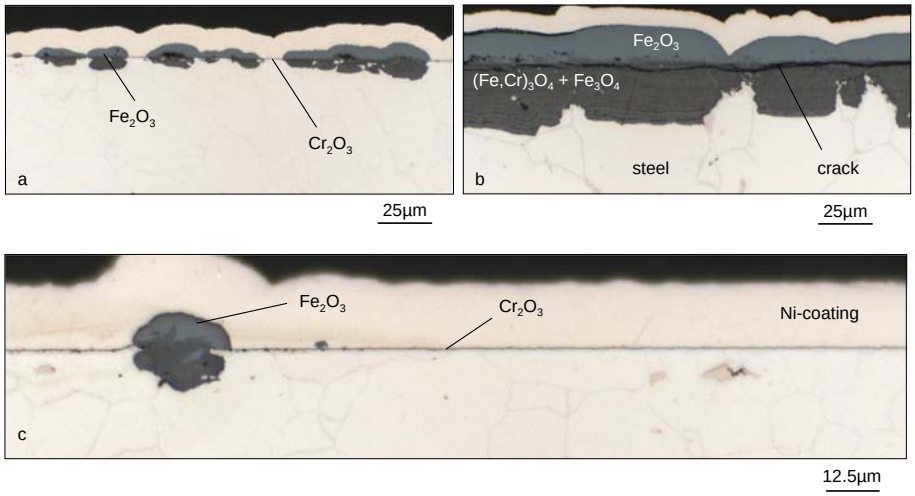

Figure 6.15: Metallographic cross sections of 1.4910 (a); TP347H FG (b) and Super 304H (c) after 1000h exposure to CO_2/H_2O at 600°C

Much thicker scales were formed on the austenitic alloys at 650°C. At this temperature the initially formed Cr_2O_3 scale was damaged quite fast by breakaway oxide. After the first 250h of exposure the scale spallation was observed for TP347H FG. After 500h all alloys, except for 310N, exhibited substantial loss in weight. The metallographic examination revealed the formation of a Fe_2O_3 layer growing in the outer scale with similar thickness for all of the steels with lower Cr content. The morphology of the inner oxide layers exhibited some differences among the tested steels. In the case of 1.4910 a uniform inner layer consisting of $(Fe,Cr)_3O_4$ and Fe_3O_4 was found and the oxide/steel interface was parallel to the initial metal surface. The same type of inner oxide was found on the other two steels. However, the oxide structure of these two steels indicated enhanced corrosion attack through the austenite grains. The depth of attack was similar for both steels along the grain boundaries. Additionally, the cross section of TP347H FG revealed cracks formation in the inner scale (Fig. 6.16b).

The austenitic steels with lower Cr content suffered rapid breakaway oxidation at 700°C, which resulted in the formation of non-protective scale and subsequent spallation during cooling cycles. The highest spallation rate was observed for TP347H FG, and then for 1.4910 and Super 304H, respectively (Fig. 6.17). The oxide scale composition was similar for all these steels. Additionally, it was found that at higher temperatures the inner oxide scales had a stronger tendency to form more protective Cr-rich oxide along the original alloy grain boundaries (Fig. 6.18). This is owing to the fact that alloy grain boundaries act as fast diffusion paths for

chromium. Therefore, the more protective oxide is preferentially formed at the intersections of the austenite grains.

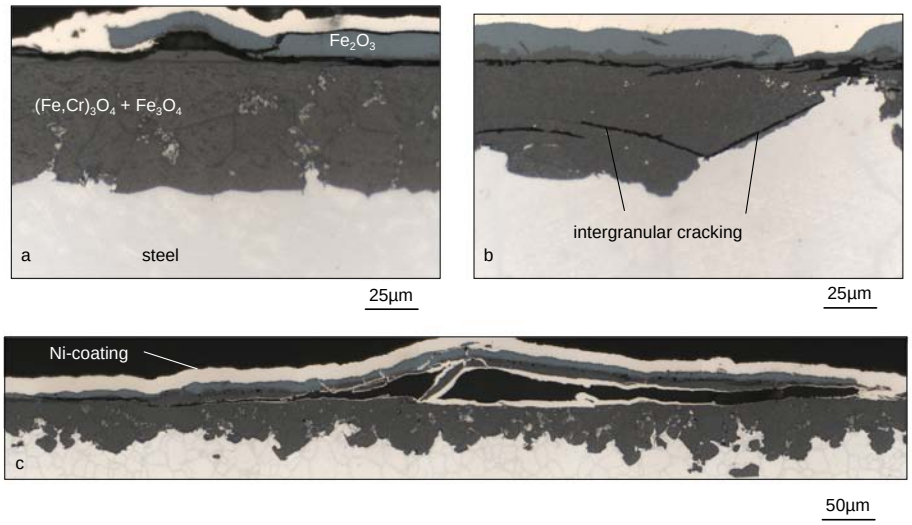

Figure 6.16: Metallographic cross sections of 1.4910 (a); TP347H FG (b) and Super 304H (c) after 1000h exposure to CO_2/H_2O at 650°C

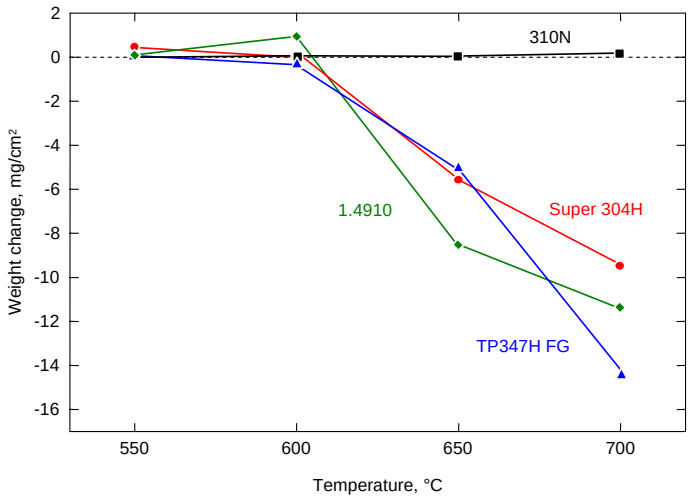

Figure 6.17: Weight changes of austenitic steels after 1000h exposure to CO_2/H_2O at 550-700°C

Contrary to the 16-18% Cr austenitic steels, 310N formed a protective Cr-rich surface scale exclusively at all testing temperatures resulting in very low oxidation rates. The etched cross sections of this steel presented in Fig. 6.19 showed Cr depletion beneath the surface oxide and

along the subsurface grain boundaries, resulting in dissolution of the Cr-rich carbide phases which were preferentially precipitated on the alloy grain boundaries.

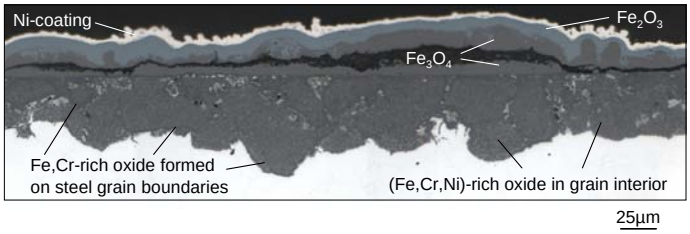

Figure 6.18: Metallographic cross section of 1.4910 after 1000h exposure to CO_2/H_2O at 700°C

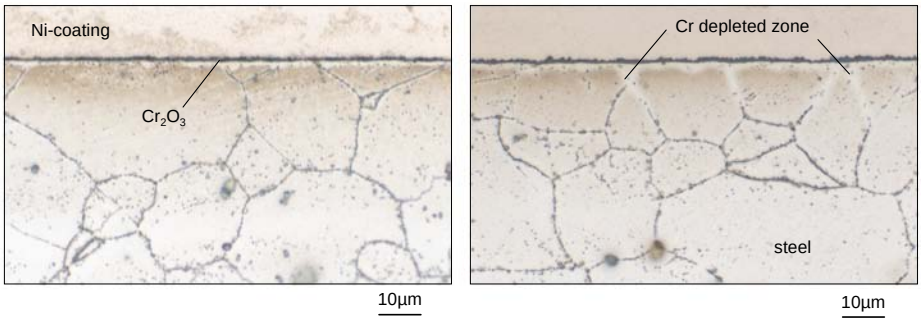

Figure 6.19: Metallographic cross sections of 310N after 1000h exposure to CO_2/H_2O at 650°C (left) and 700°C (right). Cross sections etched in NH_3 solution

6.5 Oxidation in $Ar/O_2/CO_2/H_2O$

In the case of the steels with lower Cr content the addition of oxygen to the CO_2/H_2O mixture did, up to the maximum exposure time of 1000h, not have a substantial effect on the scale growth rate and overall spallation kinetics. However, rapid deterioration of the initially formed Cr-base oxide scale was observed at temperatures between 600 and 700°C. The oxidation rates presented in Fig. 6.20 showed an increasing parabolic rate constant with increasing temperature. The cross sections presented in Fig. 6.21 showed irregular scale/alloy interfaces. The structure of the inner oxide layer was strongly affected by the alloy grain size and microstructure. For 1.4910 oxidized at 700°C, however, the oxidation front was flat, indicating that differences in oxidation rates between grains and grain boundaries were hardly present.

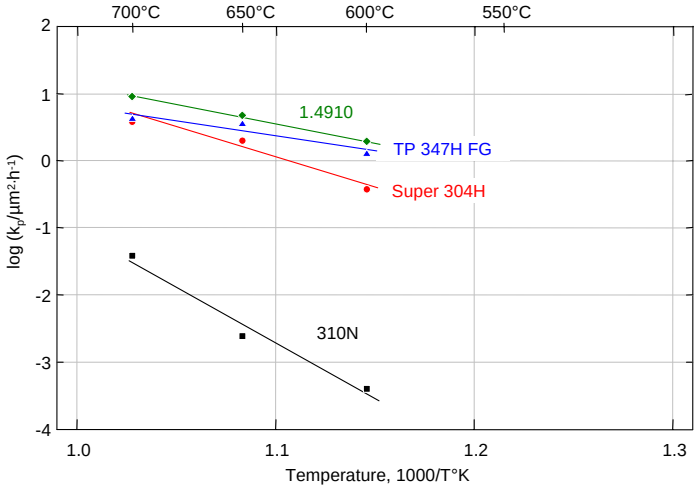

Figure 6.20: Parabolic rate constants as a function of reciprocal temperature of austenitic steels oxidized in $Ar/O_2/CO_2/H_2O$ (k_p derived from scale thickness measurements)

Additionally, the outer oxide scale was completely detached in the case of 1.4910 whereas the other materials retained at least partially the outer hematite layer. The thickness of the outer scale was similar for all materials suggesting that this oxide phase was periodically removed from the alloy surface by spallation and subsequent re-formation upon continued exposure. The repeating of this process resulted in a net mass loss for all the three steels with lower Cr content (Fig. 6.22).

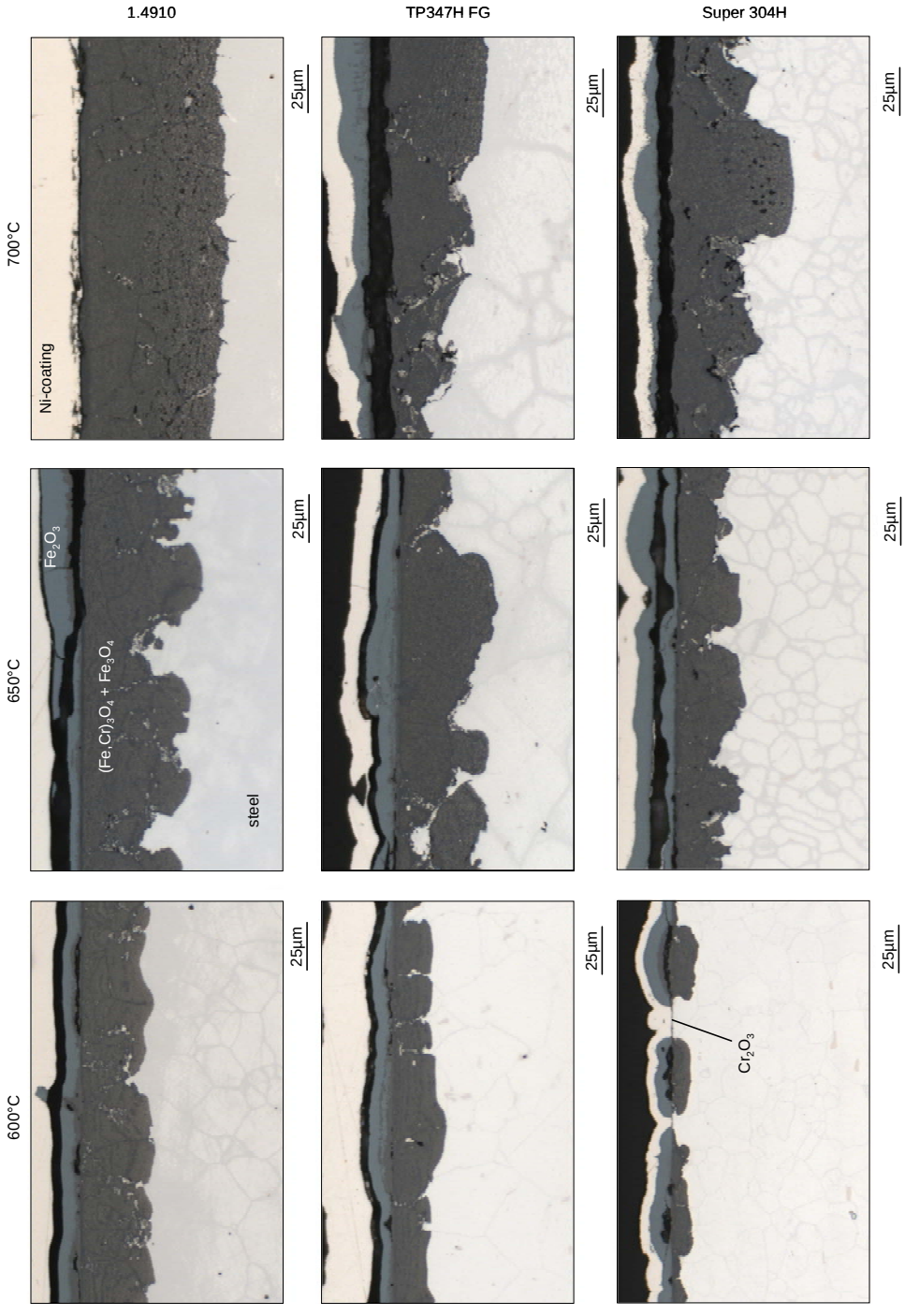

Figure 6.21: Metallographic cross sections of austenitic steels 1.4910 (upper figures), TP347H FG (middle figures), and Super 304H (lower figures) after 1000h exposure to $Ar/O_2/CO_2/H_2O$ at 600, 650 and 700°C

The oxidation behaviour of steel 310N was strongly affected by the addition of oxygen in the CO_2/H_2O atmosphere. A very small mass gain observed after exposure at 550 and 600°C indicated the formation of a protective and well adherent chromia surface scale. Upon exposure at 650 and 700°C clearly measurable weight gains were observed suggesting growth of less protective oxide phases on the metal surface (Fig. 6.23).

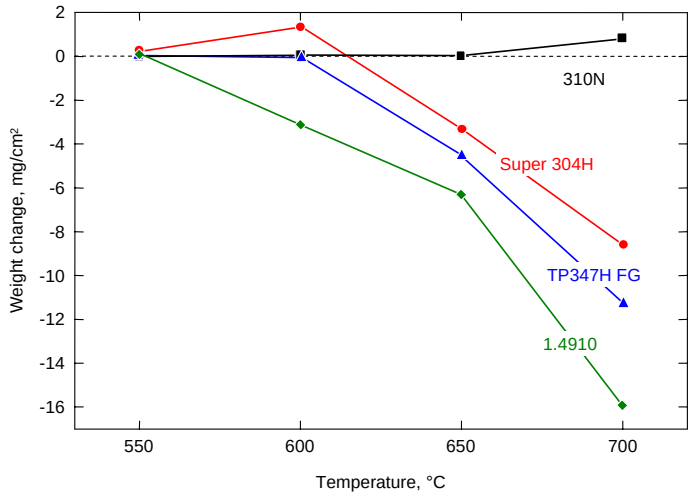

Figure 6.22: Weight changes of austenitic steels after 1000h exposure to $Ar/O_2/CO_2/H_2O$ at 550-700°C

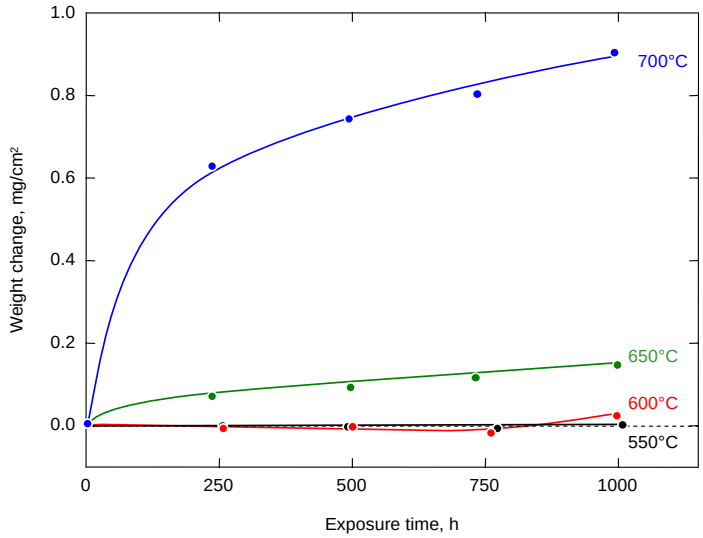

Figure 6.23: Oxidation behaviour of 310N during exposure to $Ar/O_2/CO_2/H_2O$ at 550-700°C

The metallographic cross sections of 310N (Fig. 6.24) as well as the EDX mappings (Fig. 6.25) revealed specimen areas with the formation of thin, protective chromium oxide and local oxide nodules mainly composed of hematite. At 650 and 700°C an oxide rich in iron and nickel was formed beneath the outer Fe_2O_3 layer. The part of the nodules formed beneath the original metal surface consisted of Cr-, Ni- and Fe-containing oxide. The concentration of iron in the inner scale was decreased with increased test temperature.

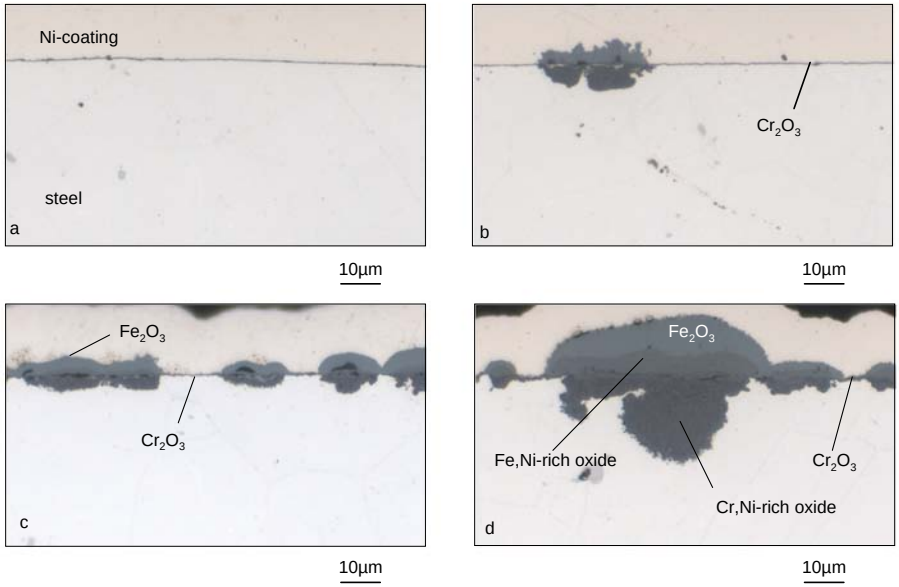

Figure 6.24: Metallographic cross sections of 310N oxidized in $Ar/O_2/CO_2/H_2O$ for 1000h at 550°C (a); 600°C(b); 650°C (c) and 700°C (d)

In section 6.3-4 it was shown that steel 310N exhibited excellent oxidation resistance in Ar/CO_2 and in CO_2/H_2O at all test temperatures. No deterioration of the Cr-base oxide scale was found during the exposure time up to 1000h. However, when oxygen was present in the atmosphere in combination with CO_2 and H_2O a local breakdown of the initially formed protective oxide scale was observed (Figs. 6.24-25). The main reason for the transition from a thin Cr-base protective oxide to a less protective Fe-rich oxide was due to the formation of volatile Cr species (see Chapter 11 for detailed explanation). In Ar/CO_2 and CO_2/H_2O the Cr supply in the bulk alloy towards the scale/steel interface was sufficiently fast to compensate the chromium loss related to the parabolic growth of the chromia surface scale. If an additional Cr loss prevailed as a result of formation of volatile Cr-oxyhydroxide in $Ar/O_2/CO_2/H_2O$, the Cr supply in the bulk alloy was apparently no longer sufficiently fast to sustain the growth of the Cr scale. This would result in the formation of Fe-rich oxide nodules.

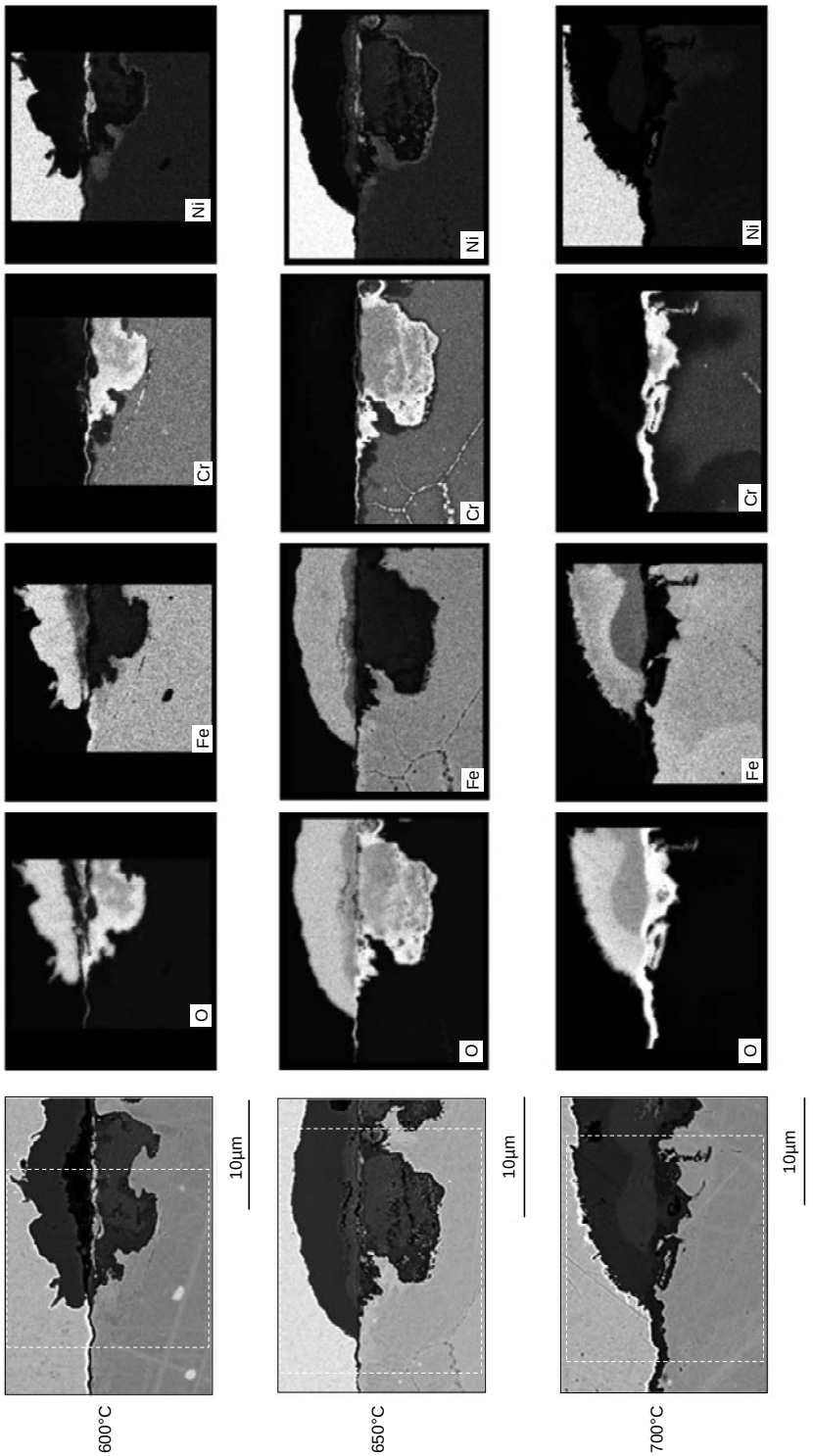

Figure 6.25: SEM cross sections and corresponding X-ray element mappings from the marked areas of 310N exposed to $Ar/O_2/CO_2/H_2O$ for 1000h at 600, 650 and 700°C

7. Oxidation behaviour of Ni-base alloys

In the present investigation INCONEL 617 was selected as a typical representative of Ni-base wrought alloys which are potentially suitable as construction materials for oxy-fuel plant components. Additionally, in some experiments model alloys with chromium contents of 10, 20 and 25wt.%, respectively, were used to investigate the influence of Cr concentration on the oxidation behaviour of Ni-base materials, thereby omitting possible effects of minor alloying additions.

At all test temperatures in the range from 550 to 700°C INCONEL 617 exhibited very good oxidation resistance in air, Ar/H_2O, Ar/CO_2, $Ar/O_2/CO_2$, CO_2/H_2O and $Ar/O_2/CO_2/H_2O$. The alloy always formed a thin protective Cr_2O_3 layer on the metal surface with minor amounts of internally oxidized Al precipitations.

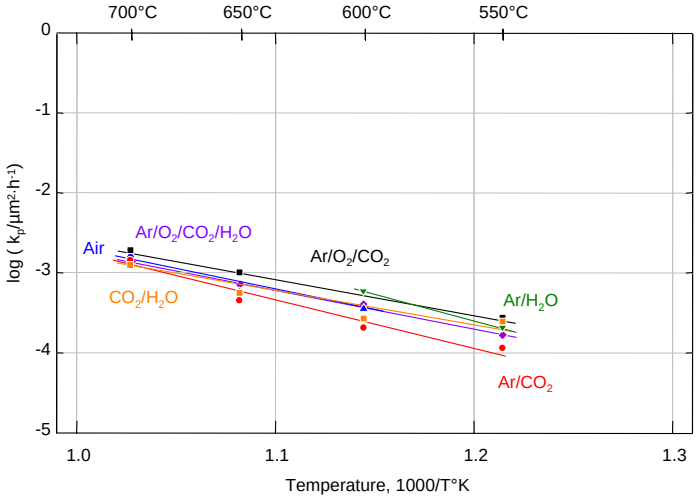

Figure 7.1: Parabolic rate constants as a function of reciprocal temperature of INCONEL 617 oxidized in different atmospheres (k_p derived from scale thickness measurements)

From the parabolic oxidation rate constants shown in Fig. 7.1 it is clear that thinner oxides were formed at lower temperatures. As seen in Fig. 7.2 large crystals of chromium oxide were locally formed on the metal surface thus affecting the measurement of the average scale thickness. It must be mentioned, however, that apart from such localized places on some specimen surfaces where larger crystals were encountered, the formed oxide scale did never exceed 1.5µm of thickness showing always good adhesion and protection.

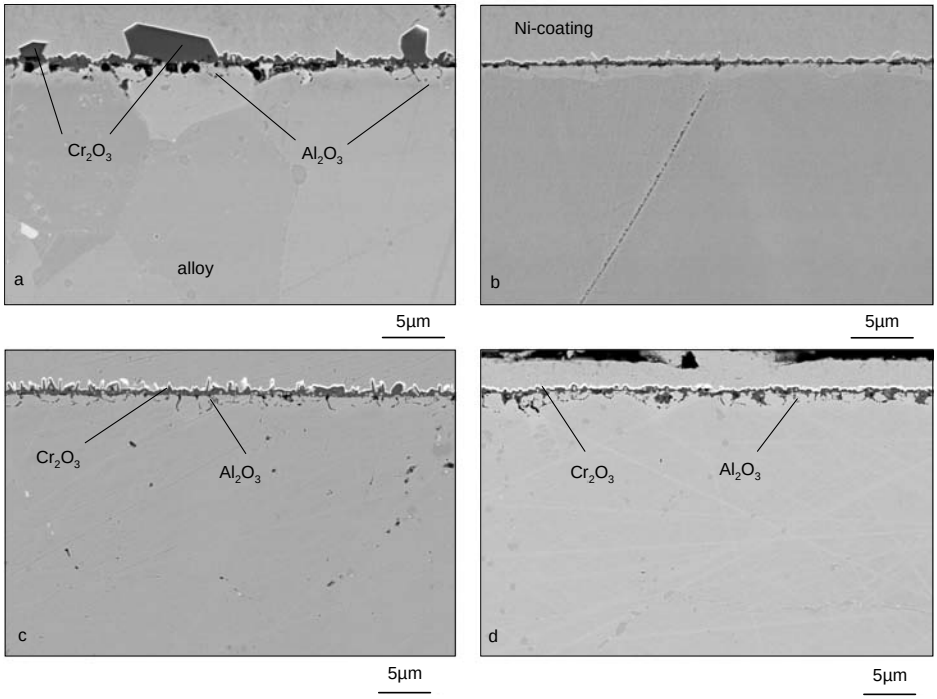

Figure 7.2: SEM images of the cross sections of INCONEL 617 after 1000h oxidation in laboratory air (a); Ar/CO_2 (b); CO_2/H_2O (c) and $Ar/O_2/CO_2/H_2O$ (d) at 700°C

Similar oxide thicknesses were found on specimens oxidized in $Ar/O_2/CO_2/H_2O$. Interestingly, the observed weight changes at and above 600°C showed negative values indicating loss of mass after prolonged oxidation (Fig. 7.3). It is assumed that this was a result of chromium loss due to volatilization mechanism, similar to that described for some of the austenitic alloys in the previous chapter. It is apparent from the oxidation curves of INCONEL 617 that higher exposure temperatures caused higher evaporation rates. It must be noted, therefore, that the k_p values in Fig. 7.1 do not express the real value of Cr consumption due to the oxidation. In the case of atmospheres in which both oxygen and water vapour were present, simultaneous growth (according to parabolic law) and thinning (linear) occurred due to evaporation. Thus, the presented parabolic rate constants express a more complex oxidation mechanism, which will further be discussed in Chapter 11.

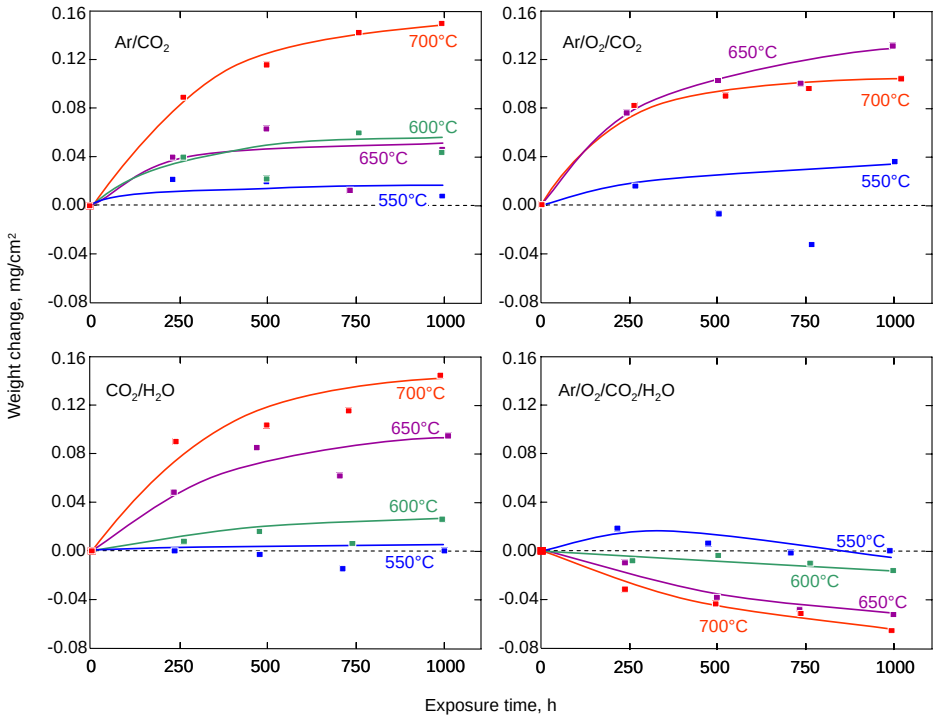

Figure 7.3: Weight changes of INCONEL 617 during exposure to different atmospheres and temperatures

By oxidizing a number of binary Ni-Cr model alloys with different Cr concentration the assumption that volatilization of gaseous Cr compounds occurs in O_2- and H_2O-rich atmospheres was confirmed. Additionally, this experiment showed that Cr loss from the metal surface was more pronounced for alloys with higher initial Cr concentration (Fig. 7.4). Moreover, comparison of the relative weight loss for INCONEL 617 containing 22% Cr with one of the model alloys with a similar Cr content (20 or 25% Cr) revealed that the microstructure and/or minor alloying elements could significantly affect the volatilization rate since after the same oxidation time and temperature the weight loss for the commercial material INCONEL 617 was approximately 3 times smaller than that for the model alloys.

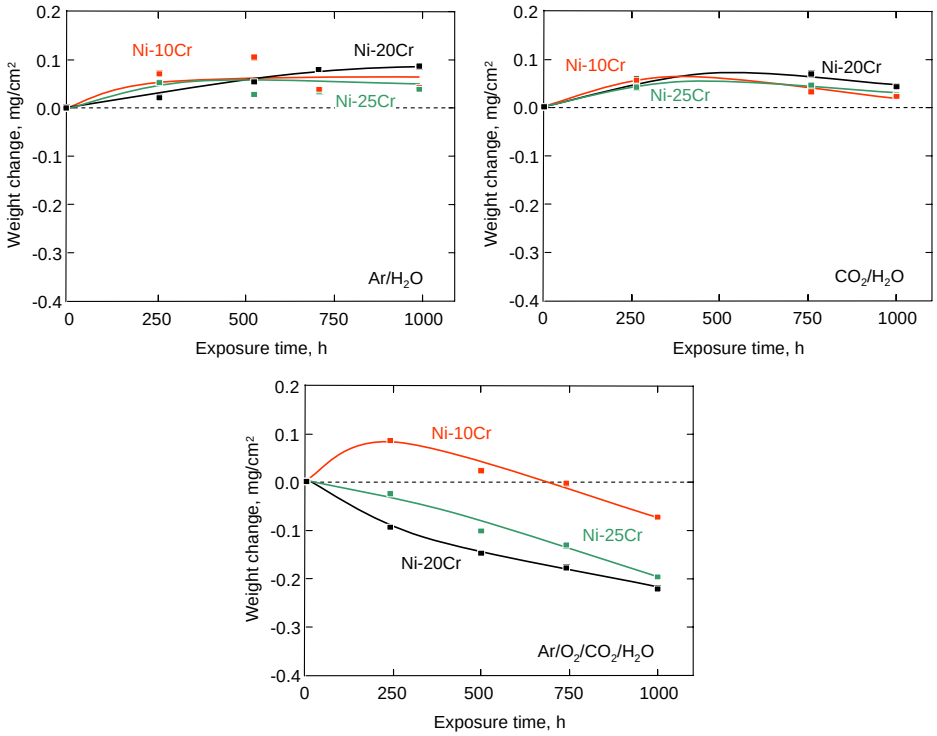

Figure 7.4: Weight changes of Ni-Cr model alloys during exposure to different atmospheres at 700°C

8. Oxide scale morphologies

8.1 Whisker formation

An interesting phenomenon observed during oxidation of ferritic/martensitic steels in this study was that the morphology of the outermost oxide layer formed on Fe-base oxide surface scales frequently exhibited significant differences. The top Fe_2O_3 layer formed on different alloys showed either a greyish or reddish appearance. More detailed investigations revealed that the growth of oxide whiskers, blades or platelets was observed on the reddish scale regions, whereas the hematite surface was flat on the grey-colored areas. These different types of hematite were frequently found to be formed on the same specimen and often in close vicinity to each other.

It is reported in the literature that whisker growth is a process which allows to relieve compressive growth stresses in the underlying oxide scale [91-94]. Several authors found that whisker formation was promoted by the presence of water vapour. This is explained by the fact that the dissociation of H_2O molecules is generally faster than that of O_2 molecules. It is suggested that whisker growth can be caused by the catalysis of H_2O reduction on the whisker surface [95]. A similar explanation was given by Zheng and Young [96] who claimed that tips of the growing whiskers could act as active sites for surface reactions in the case of H_2O as well as CO_2.

The extensive number of experiments carried out in the present investigation revealed that whiskers were formed on ferritic/martensitic steels exposed to dry as well as to water vapour containing atmospheres. The gas composition did not appear to have a significant influence on the formation of whiskers on the hematite layer. It was found that after short isothermal exposure (72h) of P92 to Ar/(2%)CO_2 the specimen surface was covered by a large number of small Fe-base oxide nodules growing next to the thin and protective Cr-rich oxide scale. These nodules (Fig. 8.1) were covered with a large number of thin and long whiskers growing perpendicular to the surface. The same was observed for VM12 in dry CO_2 gas containing additional oxygen. The locally present oxide nodules consisted of magnetite and outer hematite. Large amounts of thin and long oxide blades were found growing outwards from the Fe_2O_3 layer (Fig. 8.2). Apparently the high oxygen partial pressure did not change the tendency for the formation of this type of morphology on oxide scales. In the case of atmospheres containing water vapour

the formation of hematite platelets was observed among the long and curved whiskers (Fig. 8.3). In some cases the whiskers were as long as 100µm.

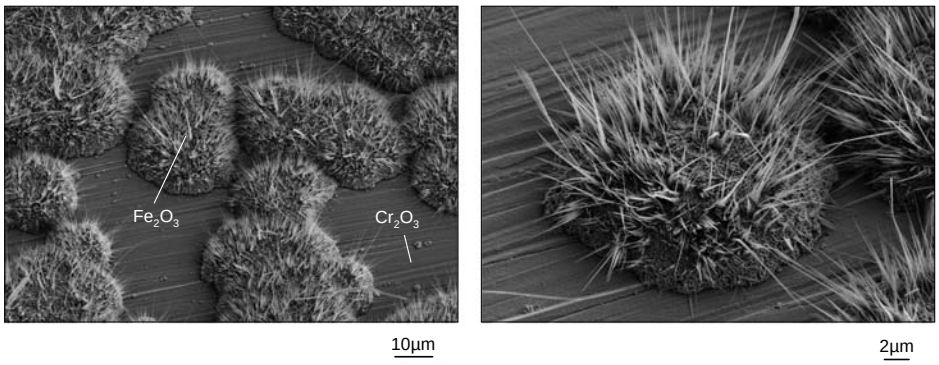

Figure 8.1: SEM images from the surface of P92 after 72h isothermal exposure to Ar/(2%)CO_2 at 550°C

Based on the above findings it is hard to determine how the oxide whisker growth was correlated with the presence of CO_2 or H_2O. Moreover, it seemed that the variation in oxygen partial pressure did not fundamentally affect the tendency of hematite to form whisker type morphology.

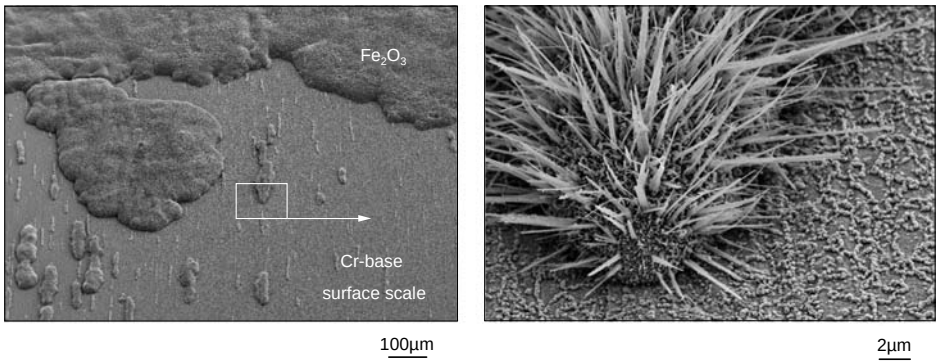

Figure 8.2: SEM images from the surface of VM12 after 1000h exposure to Ar/O_2/CO_2 at 650°C. Right picture shows details of Fe-base oxide nodule morphology

The experimental data revealed that formation of whiskers was strongly dependent on the transport properties in the oxide scale. As already discussed in Chapter 5, in the case of specimens exposed to H_2O-containing gases, buckling of the outer scale was frequently observed. It was additionally found that favourable conditions for whisker growth only prevailed in the case of the Fe_2O_3 layer showing good adherence to the rest of the scale. Any detachment or blistering resulted in the formation of flat and uniform greyish hematite (Fig. 8.4).

The necessary condition required to maintain the whisker type morphology was therefore found to be related to an uninterrupted outward flux of Fe cations to the oxide/gas interface.

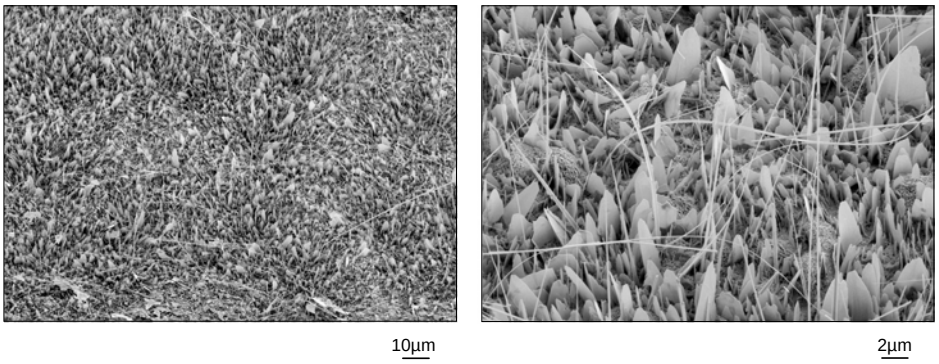

Figure 8.3: SEM images from the surface of VM12 after 500h isothermal exposure to CO_2/H_2O at 550°C

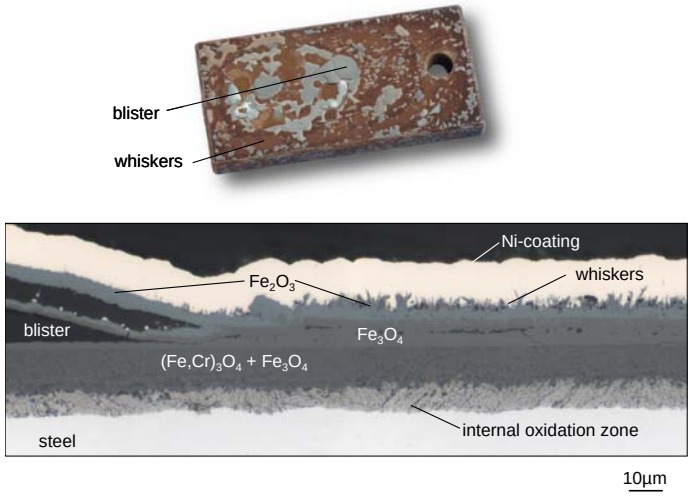

Figure 8.4: Macropicture of P92 specimen and corresponding cross section after 1000h exposure to Ar/H_2O at 550°C

Some other experimental evidences showed, however, that the observed differences in hematite colour were not necessarily related with formation of outward growing whiskers but with the internal structure of the Fe_2O_3 layer. When VM12 was exposed to Ar/CO_2 at 600°C, a flat and well adherent oxide scale was found which was composed of inner mixed oxide, a thin magnetite layer and a much thicker hematite layer which showed some morphological differences along the specimen surface (Fig. 8.5). The hematite formed near the front part of the specimen according to the gas flow, exhibited a substantial amount of voids located within the scale, whereas a compact hematite layer grew at the end of the specimen.

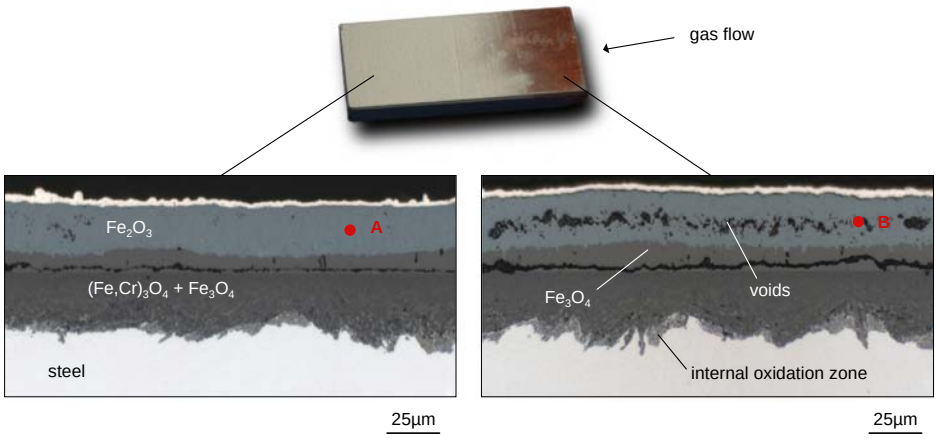

Figure 8.5: Macropicture and corresponding cross sections taken from the marked places of VM12 specimen after 500h exposure to Ar/CO_2 at 600°C. Red points show from where the FIB samples were taken (see Fig. 8.6)

FIB technique coupled with a TEM analysis was applied for obtaining more detailed information of the scales. It appeared that a slightly finer grain structure of the hematite layer was formed in the front part of the specimen than near the end part (Fig. 8.6). Additionally, the TEM investigation demonstrated a slightly different distribution of voids within the Fe_2O_3 scale. For the larger hematite grains a substantial numbers of small voids were located in the grain interior whereas in the case of the reddish coloured scale formed at the front part of the specimen, the voids were found mainly in the grain boundaries. It seemed that the relative amount of voids found in the TEM cross section taken from the greyish hematite (left images in Fig. 8.6) was higher than that found in the reddish hematite. Based on those observations the following mechanism can be proposed:

During the early stages of oxidation a thin layer of magnetite is formed on the metal surface. As oxidation continues, an outer layer of hematite starts to develop. It is believed that CO_2 from the gas predominantly reacts with the front of the specimen. The CO_2 molecule dissociates according to the reaction:

$$CO_2 = CO + \tfrac{1}{2}O_2 \qquad \text{(Eg. 8.1)}$$

During the reaction of CO_2 with the metal/oxide surface CO is produced. Therefore, a lower pO_2 is expected to prevail at the end of the exposed specimen. This is because the gas mixture

consists of CO_2 and CO at the specimen end rather than CO_2 which is the dominant gas species at the front specimen side. During the first hours of oxidation this could result in the formation of different oxide phases along the metal surface. However, after several hundred hours the equilibrium between the oxide and the gas is attained so hematite was present all around the metal surface and only small morphological differences in the oxide scale, such as enhanced void formation, suggest that the oxidation mechanism slightly varied in the different specimen places.

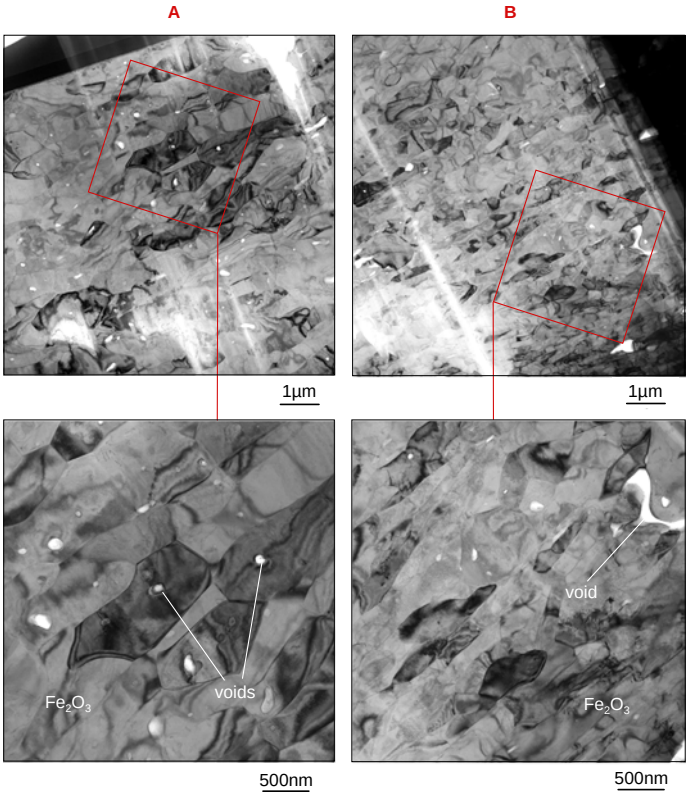

Figure 8.6: TEM images of outer Fe_2O_3 layer formed on VM12 during 500h isothermal oxidation in Ar/CO_2 at 600°C (A and B relate to the points in Fig. 8.5)

Finally, the observed structural differences within the hematite phase may result from the transformation of α-Fe_2O_3 into γ-Fe_2O_3. It is well-known that γ-Fe_2O_3 (maghemite) is thermodynamically metastable and transforms to the more stable α–phase upon heating. The crystallographic transition temperature at witch γ-Fe_2O_3 changes irreversibly to α-Fe_2O_3 was reported in literature in a wide range of temperatures ranging from 250°C [97] to 900°C [98]. The study carried out by Özdemir *et al.* [99] on synthetic maghemite using X-ray analysis revealed that acicular maghemite particles were stable at temperature 500°C and the transition

from γ to α took place at 510-660°C in air under atmospheric pressure after 30min of exposure. However, according to X-ray analysis, only approximately 50% of the primary γ-phase was transformed at the highest temperature.

Additionally, high pressure oxidation of X20 in CO_2 and H_2O gas mixtures performed by Hünert [100] revealed that maghemite was present within the α-Fe_2O_3 scale at 550°C after 1000h of exposure. The results obtained by Özdemir *et al*. and Hünert strongly indicate that coexistence of γ and α phase can occur in the temperature range used in the present study.

Some interesting results confirming the above considerations were found after the oxidation of a binary Fe-10Cr model alloy in Ar/H_2O. At 650°C formation of reddish hematite was found whereas the same material exposed at 700°C was covered almost entirely by grey Fe_2O_3 (Fig. 8.7). The X-ray analysis revealed that the outer oxide scales formed at both temperatures (650 and 700°C) consisted of α-Fe_2O_3 (Fig. 8.8). Comparing the results with those obtained by Özdemir *et al*. [99] it became clear that in fact reflections (400) and (513) corresponded to the γ-Fe_2O_3. The intensity of those peaks was very weak, however, indicated a minor contribution of γ-hematite in the formed oxide scale.

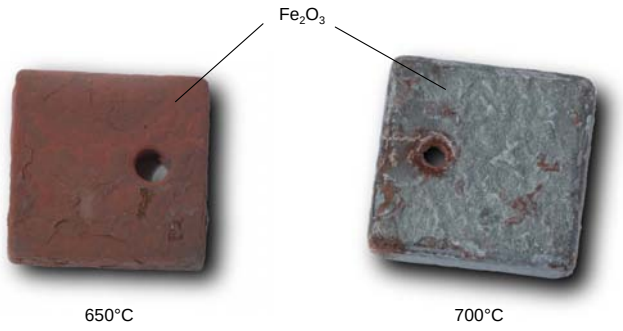

Figure 8.7: Macroscopic pictures of binary Fe-10Cr model alloy after 1000h oxidation in Ar/H_2O at 650°C (left) and 700°C (right)

An additional important finding was made during this experiment. The very high intensity of the (300) reflection for the specimen exposed at 650°C suggested a preferred crystal orientation in one crystallographic direction. Further metallographic investigation confirmed formation of whisker type morphology in the case of the reddish oxide scale, and a quite homogeneous scale structure for the material exposed at 700°C showing a greyish colour.

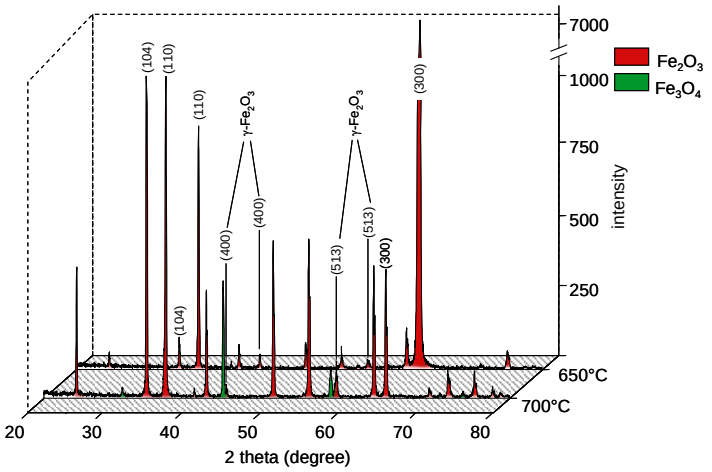

Figure 8.8: X-ray spectra of Fe-10Cr model alloy after 1000h oxidation in Ar/H_2O at 650°C and 700°C

It seems that the best explanation of whisker formation on Fe_2O_3 layers is, however, similar to that reported in literature for whisker growth on Cr_2O_3 scales [101, 102]. For this oxide the whisker growth was mainly attributed to the rapid transport of the metal through the oxide scale and results presented in Figs. 8.9-10 confirmed this assumption.

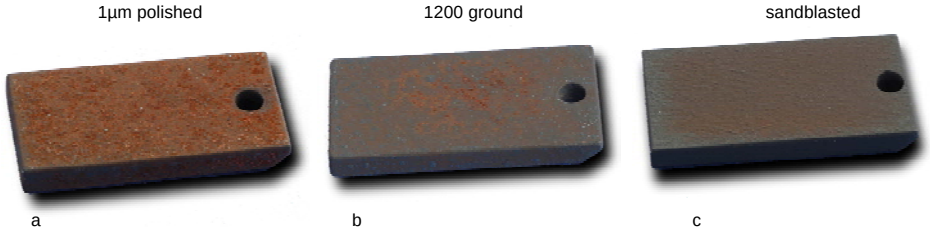

Figure 8.9: Macroscopic images of VM12 specimens exposed to Ar/O_2/CO_2/H_2O for 1000h at 650°C with different surface treatment prior to exposure: 1µm diamond paste polished (a); 1200 grid SiC abrasive paper ground (b) and sandblasted (c)

The diffusion rate of the scale forming elements can be changed to some extent by the surface treatment prior to exposure. By applying cold work to the metal surface it is expected to enhance the formation of more protective oxide scale during subsequent oxidation. On the other hand a polished metal surface should result in the formation of a less protective scale. SEM micrographs

and macroscopic specimen pictures (Figs. 8.9-10) clearly show that the sandblasted specimen exhibited a grey surface colour without whisker formation on the oxide scale, whereas a reddish colour of hematite and a large amount of whiskers were found on the specimen which had been polished prior to exposure. The ground specimen showed a mixed behaviour.

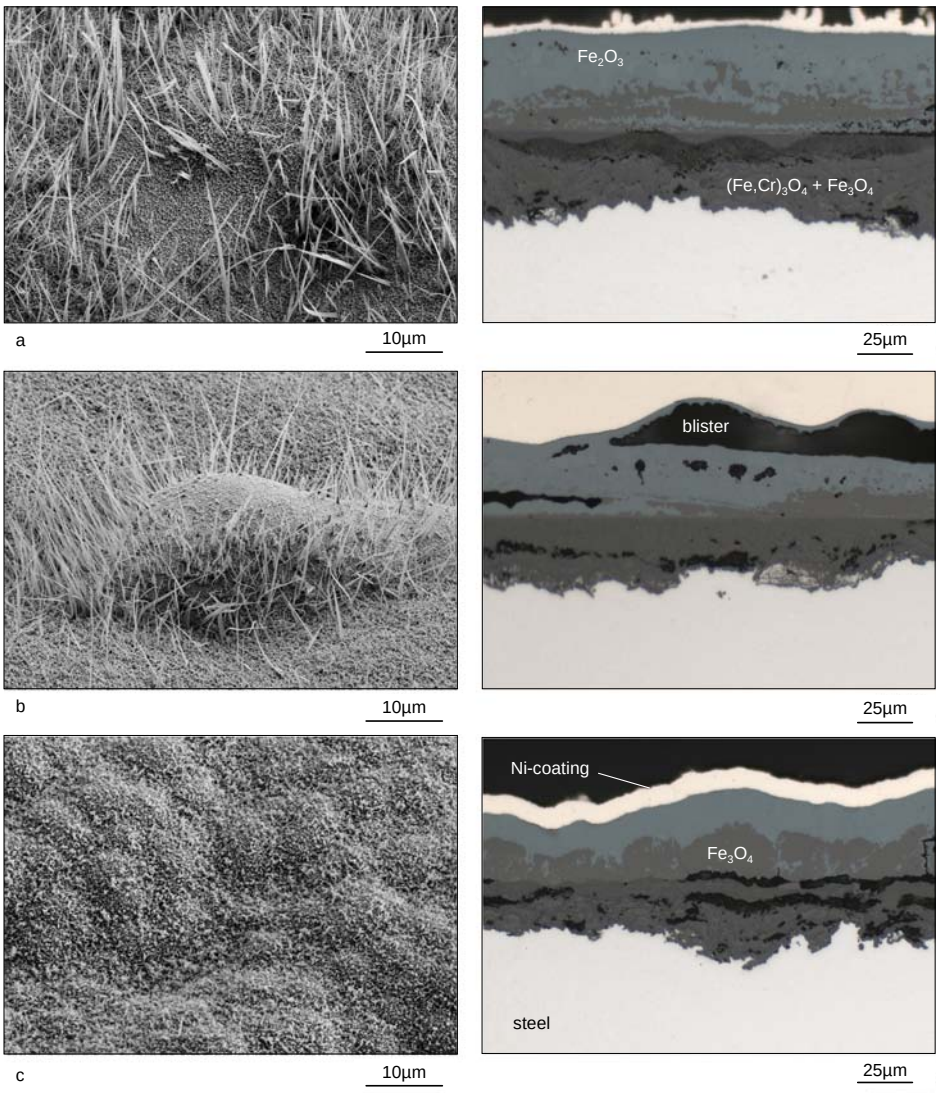

Figure 8.10: SEM images of the specimen surface (left) and metallographic cross sections (right) of VM12 with different surface treatments oxidized for 1000h in $Ar/O_2/CO_2/H_2O$ at 650°C: 1µm diamond paste polished (a); 1200 grid SiC abrasive paper ground (b) and sandblasted (c). Compare with macropictures in Fig. 8.9

8.2 Wustite formation

When pure iron oxidizes in air at high temperatures (>570°C), it grows a multi-layered scale consisting of FeO (wustite) as the phase growing next to the metal, then Fe_3O_4, and Fe_2O_3 at the interface with the oxidant (Fig. 8.11). The FeO phase can exist over a wide range of stoichiometry. It is reported that cation deficiency in this oxide can be as large as $Fe_{0.95}O$ to $Fe_{0.88}O$ at various temperatures between 800 and 1250°C. At constant pO_2 the deviation from stoichiometry in FeO decreases with increasing temperature [23]. This high cation-vacancy concentration allows extremely rapid transport of iron cations and electrons through this oxide phase and, therefore, the growth of this layer dominates the overall rate of oxidation. During oxidation below the FeO stability temperature (<570°C) only the formation of Fe_3O_4 and Fe_2O_3 is possible and thus the growth kinetics are generally much slower.

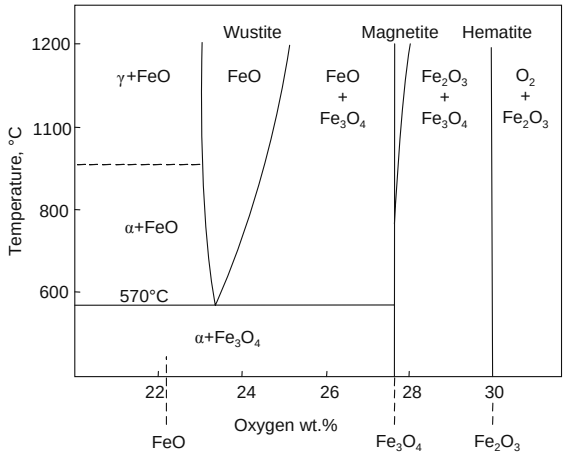

Figure 8.11: Part of iron-oxygen phase diagram. Reproduced from [26]

Alloying additions in Fe-base alloys may shift the wustite stability limit to lower or higher temperatures. As reported by Grobner *et al*. [103] additions like Cr, Mo and especially Ni have a strong tendency to increase the temperature above which FeO becomes stable, whereas Mn shows the opposite effect (Fig. 8.12). The observations made by Gulbransen *et al*. [104] indicate that the formation of FeO is possible at temperatures as low as 400°C in very thin oxide films. Similar observations were also made by Pinder *et al*. [105] who found the formation of FeO phase at 500°C within narrow cracks of the oxide scale. The extensive review by Viswanathan [58] shows that during steam oxidation the temperature of FeO occurrence strongly depends on

the alloy composition. The FeO was found to be formed on carbon steels at 570°C, whereas for a 1.25Cr0.5Mo steel it was found at 585°C and for a 2.25Cr1Mo steel at 615°C.

In this study the formation of FeO was observed at and above 650°C, however, not for all investigated steels. Depending on the test atmosphere at 650°C and higher 9-12% Cr steels had a strong tendency to form a protective Cr-base scale or at least incorporated substantial amounts of chromium into the inner oxide scale, thus reducing the overall oxide growth rate by impeding the ionic in-scale Fe transport. Results in the present study indicate that this hampered Fe diffusion was the main reason that the wustite phase was absent or at least undetectable in the growing oxide scales. Contrary to this, for alloys showing a higher scale growth rate, i.e., when iron transport was not hampered, FeO could be formed. This, of course, could be discussed further and an important question to be answered is whether the wustite formation was because of the high growth rate or the high growth rate was the result of wustite formation.

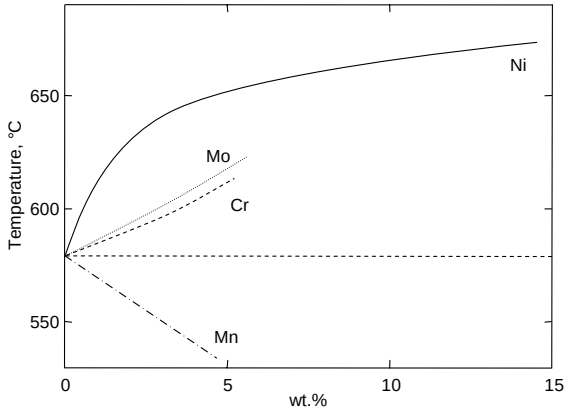

Figure 8.12: Effect of alloying elements on the temperature of wustite occurrence in the scale during oxidation in air. Reproduced from [103]

Figure 8.13 shows the SEM images of the cross section of the low alloyed steel 13CrMo4-4 after exposure to $Ar/O_2/CO_2/H_2O$ at 650°C. A multilayered oxide scale with a thickness of several hundreds of micrometers was formed consisting of a thin outer hematite layer and a much thicker magnetite beneath. FeO was found below the magnetite, however, not in the form of a single oxide layer like it is frequently observed in the case of pure Fe oxidation [23, 31, 32]. In the case of 13CrMo4-4 the wustite was speckled by magnetite spots. The structure of this two phase oxide layer is well visible in the high magnification image at the right side in Fig. 8.13. The chemical composition of the formed oxides was confirmed by energy dispersive X-ray analysis (Tab. 8.1) taken from points marked in Fig. 8.13.

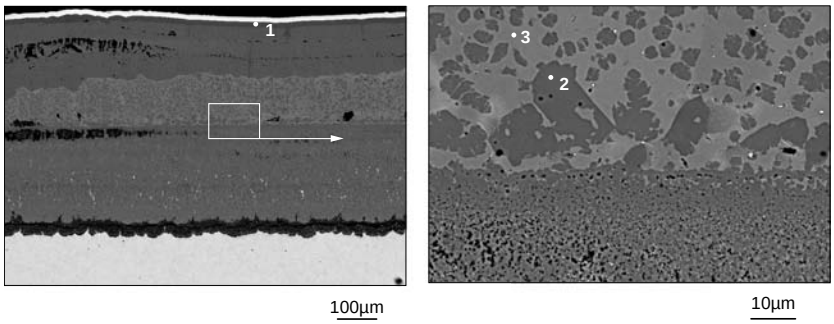

Figure 8.13: SEM images of the cross section of 13CrMo4-4 after 1000h exposure to $Ar/O_2/CO_2/H_2O$ at 650°C. Marked points indicate places of EDX analysis (see Tab. 8.1)

Such untypical structure can be explained by the topotactic transformation of the initially formed FeO into Fe_3O_4. In CO_2-rich gases this reaction can be expressed as follow:

$$3FeO + CO_2 = Fe_3O_4 + CO \qquad \text{(Eg. 8.2)}$$

A similar explanation was proposed by Valette *et al*. [106]. The authors investigated a ferritic low carbon steel as well as an austenitic steel with 36wt.% Ni under 10^5 Pa of CO_2 at temperatures between 840 and 1010°C. They found that FeO appeared only as an intermediate product of oxidation. After some time wustite was converted into magnetite which was explained by the drastic slowing down of iron diffusion from the bulk substrate towards the external interface.

	Element concentration in atomic %			
Point	**O**	**Mn**	**Fe**	**Oxide**
1	60.0	0.2	39.8	Fe_2O_3
2	57.5	0.3	42.2	Fe_3O_4
3	50.3	0.4	49.2	FeO

Table 8.1: Chemical composition of the oxide phases found in 13CrMo4-4 oxidized for 1000h in $Ar/O_2/CO_2/H_2O$ at 650°C (points 1-3 relate to Fig. 8.13)

During oxidation of the P92 batch with reduced Si concentration (exact chemical composition of this batch is given in Tab. 19.1) in Ar/CO_2 at 650°C some precipitations of FeO were found embedded in the magnetite layer close to the interface with the inner oxide (Fig. 8.14). Different from the previous example of the low alloyed steel no hematite was found at the interface with the atmosphere. This suggested that the oxide surface was not in equilibrium with the atmosphere. As will be explained in Chapter 13 lower concentrations of some of the alloying

elements (mainly Si) in this particular P92 batch resulted in rapid diffusion of Fe cations in the oxide scale.

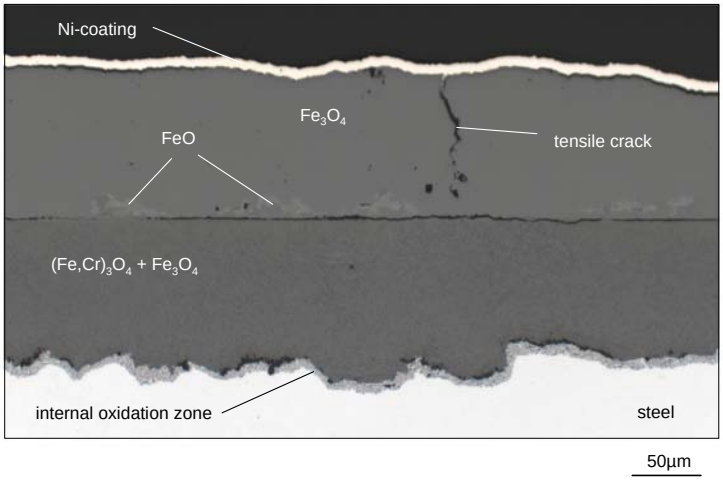

Figure 8.14: Metallographic cross section of P92-low Si after 1000h exposure to Ar/CO_2 at 650°C

For 9% Cr steels like P92 formation of protective Cr_2O_3 is usually not observed during prolonged exposure to CO_2-atmospheres at 650°C (see Chapter 5). At this temperature the Cr enrichment in the inner oxide scale could, however, substantially reduce the outward iron cation diffusion. This would result in reduced oxidation rates. When formation of more protective $(Fe,Cr)_3O_4$ in the inner oxide layer was not possible due to low Cr mobility in the alloy, a rapid transport of Fe cations in the scale was expected to occur. The overall oxidation rate could thus be as high as that observed for low alloyed steels. The mechanism of wustite phase formation in the case of the martensitic steel would be then similar to that proposed above.

The idea that wustite initially was formed near the metal surface and then transformed into magnetite was validated by additional experiments. A specimen of the low alloyed steel 13CrMo4-4 was isothermally exposed to Ar/CO_2 at 650°C for 250h. The surface of the formed oxide was then analyzed by X-ray diffraction. Then, part of the oxide scale was removed by progressive grinding with very fine SiC abrasive paper without using a lubricant. After every 30µm of oxide removal X-ray analyses were performed. The obtained results are presented in Fig. 8.15. The first peak of FeO was observed after removing approximately 120µm of oxide. Three peaks were found suggesting that wustite was present within the scale in a thickness of around 90µm. The last XRD measurement showed the presence of the peak coming from bulk iron. The Fe_3O_4 phase was found in each X-ray diffraction analysis. It should be mentioned here

that it is difficult to distinguish the reflections coming from Fe_3O_4 and those from $(Fe,Cr)_3O_4$ in X-ray spectrum. It should be therefore assumed that the inner oxide layer consisted of a mixture of Fe_3O_4 and $(Fe,Cr)_3O_4$.

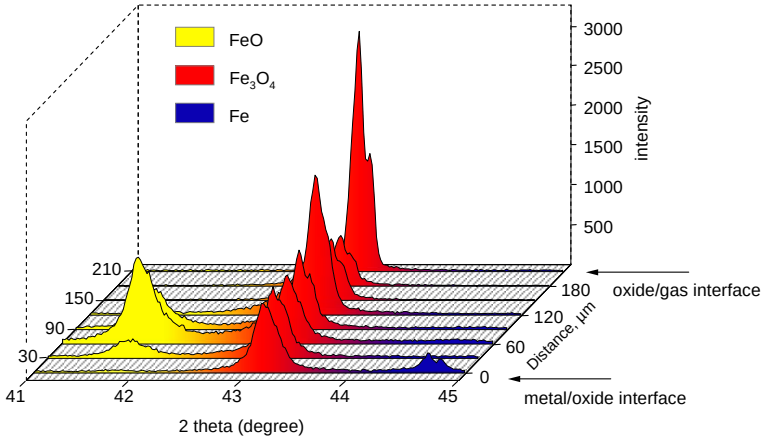

Figure 8.15: X-ray spectra taken from the oxide scale ground every 30µm (steel 13CrMo4-4) after 250h exposure to Ar/CO_2 at 650°C

The light microscopic observations of the 13CrMo4-4 cross section (from the non-ground specimen side) did not reveal any distinct wustite precipitates (Fig. 8.16). Apparently, this oxide was present in form of very small particles as remnants from the transformation to magnetite. This suggested that perhaps FeO could be formed at temperatures lower than 600°C and on other steels, although it was hard to detect by using standard analytical techniques. Additional experiments are necessary to confirm this hypothesis. In this study, however, FeO was never observed below 650°C. At 700°C only the binary Fe-10Cr model alloy exposed to the Ar/O_2/CO_2/H_2O exhibited a few areas near the original metal surface where wustite spots embedded in the magnetite layer were observed, similar to the finding presented in Fig. 8.14.

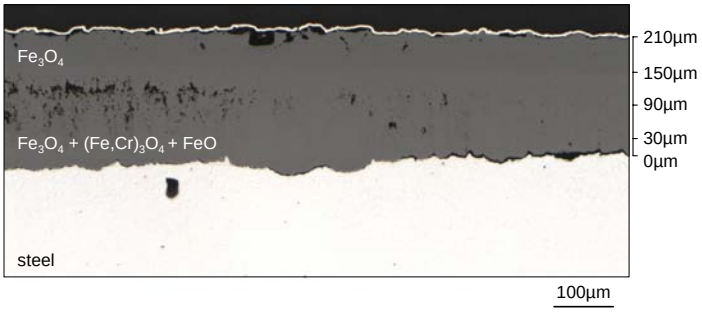

Figure 8.16: Metallographic cross section of 13CrMo4-4 after 250h exposure to Ar/CO_2 at 650°C (compare with Fig. 8.15)

9. Temperature dependence for oxidation of ferritic/martensitic steels

During the exposure of alloys to oxidizing environments it is commonly found that oxidation rates increase with increased temperature. However, in some cases, the oxidation rates may again decrease if a certain temperature is exceeded. In the literature this phenomenon was already discussed by several authors who termed this type of behaviour as “bell-shape” temperature dependence, anomalous temperature dependence or inversion effect [38, 107, 108]. For instance, for a number of martensitic steels the maximum oxidation rate in Ar/H_2O is, in some cases, not found at the highest test temperature, but frequently occurs at 650, 600 or even as low as 550°C [76, 109]. This finding is attributed to the formation of Fe-base oxide scales at lower temperatures and chromium rich oxides at higher temperatures. In the present study, some of the tested materials exhibited a similar feature when oxidized in atmospheres relevant to the oxy-fuel process, i.e., in high CO_2-containing gases.

Figure 9.1 presents the weight changes of two steels with different Cr content during exposure to Ar/CO_2 at temperatures from 550 to 700°C. The low alloyed steel 13CrMo4-4 clearly exhibited an increased scaling rate with increasing temperature, whereas the 12% Cr steel VM12 showed a much more complex temperature dependence of the oxidation rates. The highest mass gain occurred at 600°C; then it decreased upon temperature increase to 650°C and especially 700°C. The total weight gain after exposure at 700°C was even lower than that at 550°C. It is important to note that at 700°C the low weight gain of approximately 2 mg/cm^2 was already reached after 250h and for the remaining 750h of exposure the additional mass gain was less than 0.2 mg/cm^2.

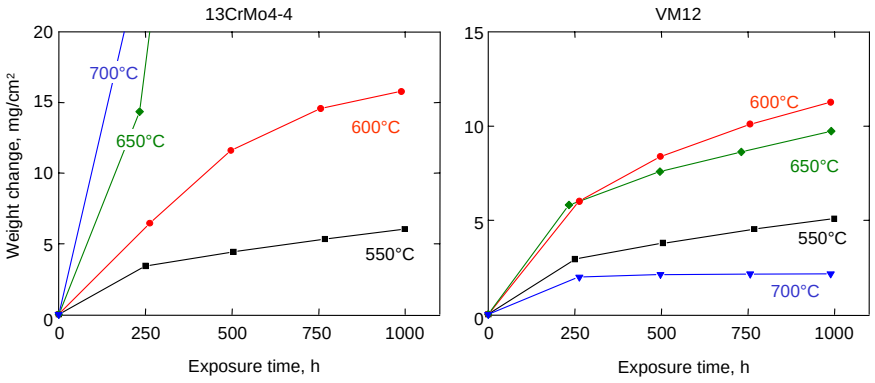

Figure 9.1: Weight change curves of 13CrMo4-4 (left) and VM12 (right) during exposure to Ar/CO_2 at 550-700°C

The cross section of VM12 oxidized for 1000h at 700°C revealed the formation of a very thin oxide scale on the metal surface with places where Fe-rich oxide nodules were found consisting mainly of an outer hematite layer and an inner mixed oxide (Fig. 9.2). These nodules apparently were formed in the early stages of oxidation since the weight of the specimen did not change after 250h (Fig. 9.1). It was estimated that 75% of the specimen surface exhibited formation of a thin and protective scale whereas the remaining 25% showed nodules of less protective Fe-base oxide.

When comparing the cross sections presented in Fig. 9.3 one may conclude that two steels with distinct differences of Cr content tended to form oxide scales with similar thickness and composition at 550°C in Ar/CO_2. The only major difference was that an internal oxidation zone was developed near the interface between oxide and metal in the case of 12% Cr steel (Fig. 9.4). Thus, despite the large difference in Cr content, very similar scaling rates were observed at 550°C (Fig. 9.1). However, upon temperature increase the beneficial effect of chromium on the oxidation resistance of VM12 became more apparent (Fig. 9.2). At all test temperatures chromium was present exclusively in the inner region of the Fe-rich oxide scales. For the 9-12% Cr steels the scale formation mechanism varied with increasing temperature. A strong Cr enrichment was found within the inner oxide scale at 650 and 700°C but not at lower temperatures.

At 550°C no clear Cr enrichment in the oxide scale was found for 9-12% Cr steels because chromium can be considered as virtually “immobile” at this temperature [42, 60]. Therefore, the observed oxidation kinetics do not differ significantly from those of steels containing less chromium. Cr is present in the steel matrix dissolved in the lattice and in the form of Cr-rich carbide precipitations in grain boundaries and along martensite laths, which means that during the oxidation process at lower temperatures these particles are incorporated into the inner oxide by the inwardly moving oxidation front [110]. The Cr-rich carbides are gradually transformed into Cr-rich oxides since the oxygen activity is considerably higher in the growing bulk oxide than near the oxide/metal interface. The distribution of the Cr-rich particles in the inner scale formed at 550°C can, therefore, be considered as a “finger print” of the steel microstructure, including primary carbide distribution in the underlying steel. This finding has already been described for scales formed during steam exposure [110, 111].

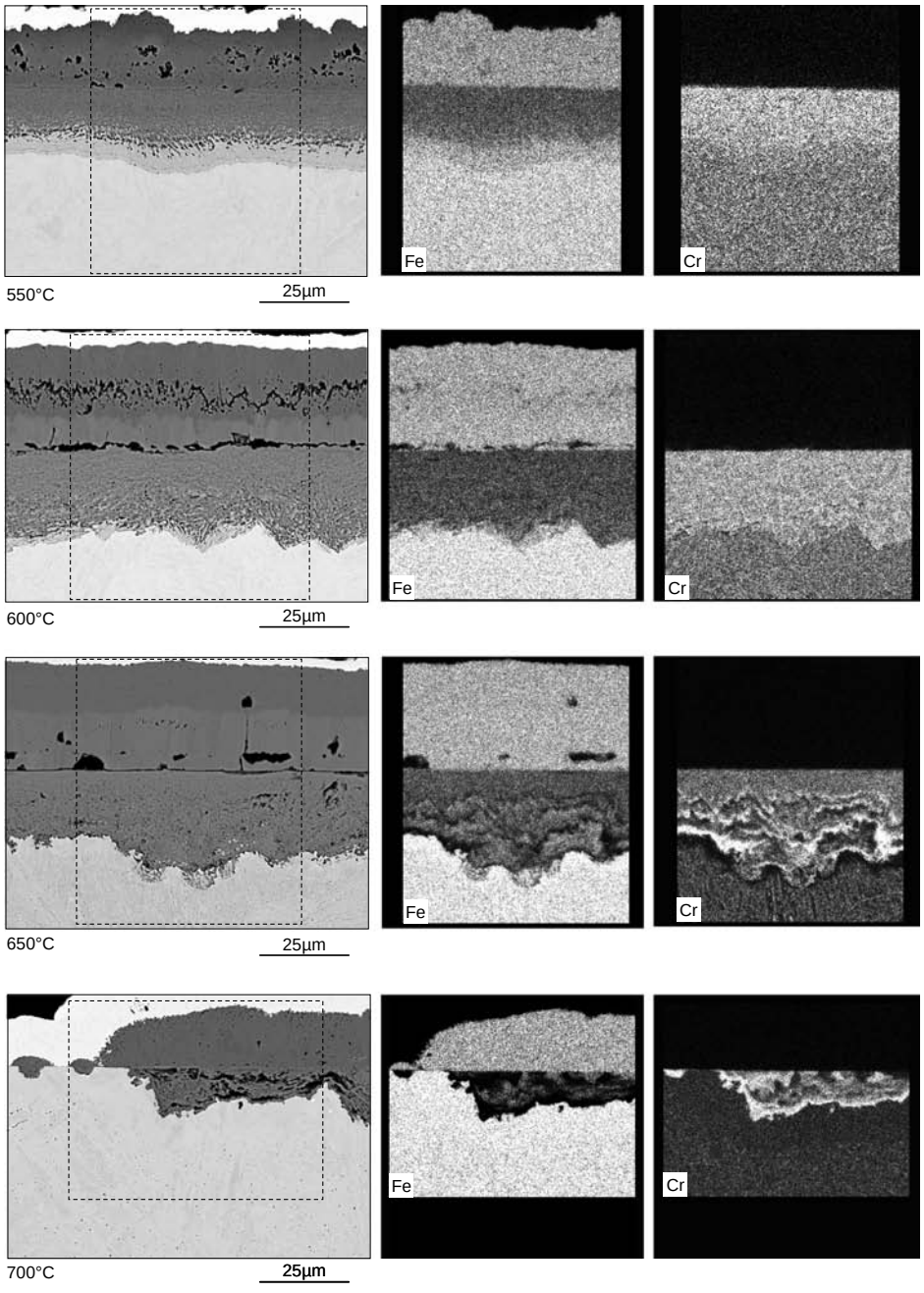

Figure 9.2: SEM images of the cross sections and corresponding X-ray element mappings from the marked areas of VM12 after 1000h oxidation in Ar/CO_2 at 500-700°C

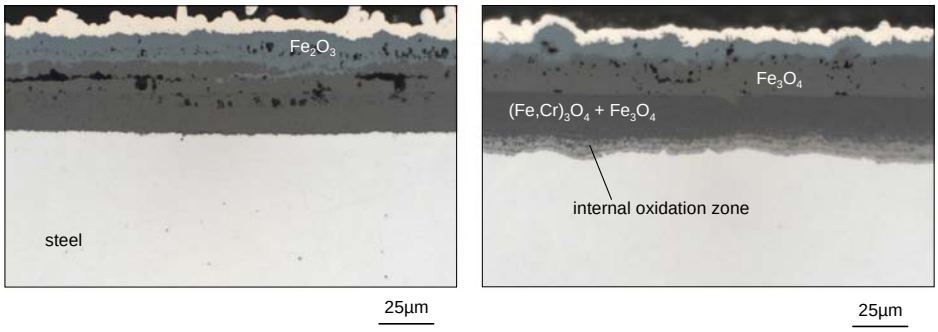

Figure 9.3: Metallographic cross sections of 13CrMo4-4 (left) and VM12 (right) after 1000h exposure to Ar/CO_2 at 550°C

The mechanism described above was confirmed by the TEM analysis. It was found that Cr-carbide precipitations tended to become oxidized and transformed into Cr-rich oxide in the inner scale as well as in the so-called internal oxidation zone near the scale/steel interface (Fig. 9.5). It was indicated that the carbide oxidation resulted in micro-voidage in the inner scale. At 600°C and 650°C the internal oxidation zone tended to vanish due to the increased chromium diffusivity in the steel and, as a consequence, stronger chromium enrichment in the inner scale was observed (Fig. 9.2). The Cr was then mainly present in the oxide scale in the form of chromium-rich bands, resulting in a hampering of oxide growth and thus a tendency for decreasing of oxidation rates.

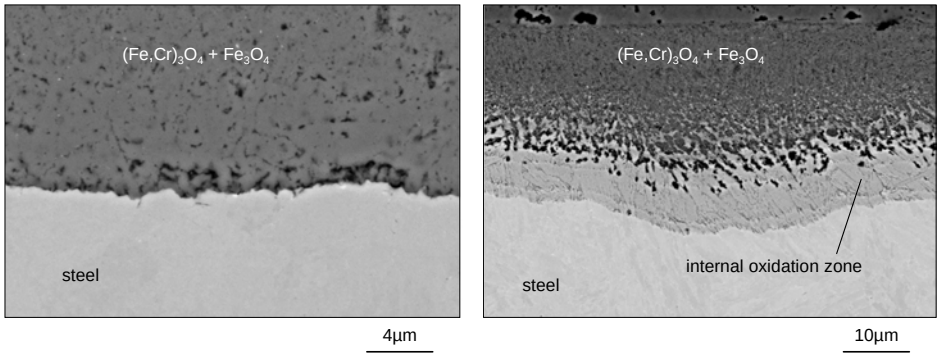

Figure 9.4: SEM images of the cross sections of 13CrMo4-4 (left) and VM12 (right) after 1000h exposure to Ar/CO_2 at 550°C showing details of the microstructure near the oxide/steel interface

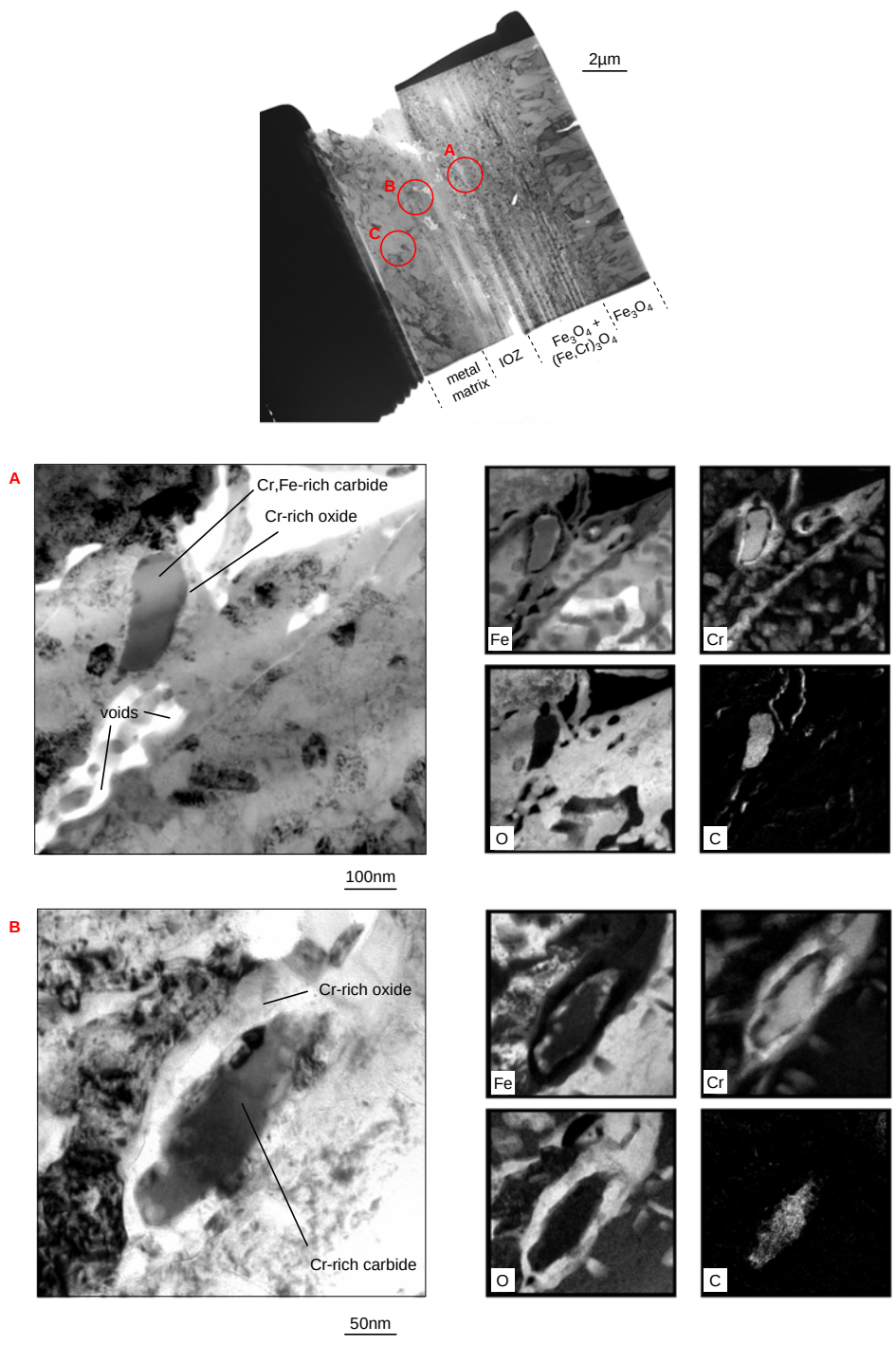

Figure 9.5: TEM lamella showing details of microstructure (upper figure) of P92 after 100h isothermal exposure to Ar/H_2O at 550°C and corresponding TEM cross sections (below) as well as X-ray mappings from the marked areas: A- inner oxide layer; B- IOZ (internal oxidation zone) and C- metal matrix (see Appendix for more TEM results from this specimen)

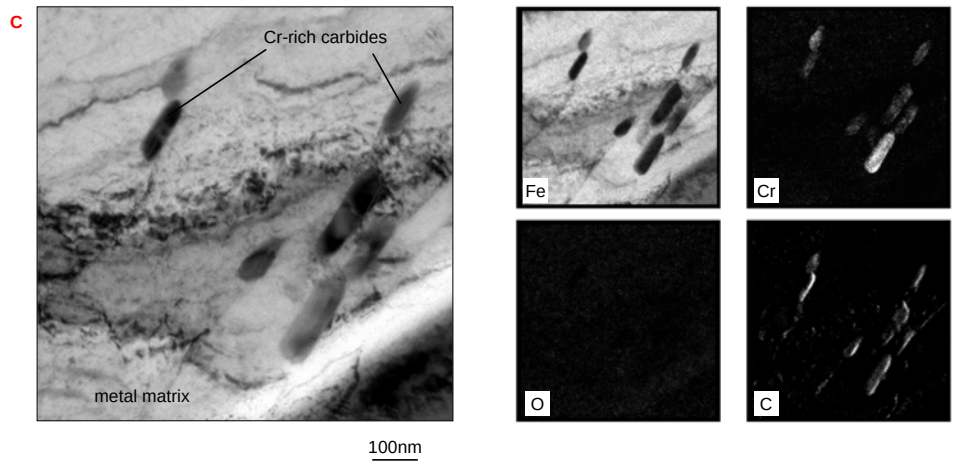

Figure 9.5: Continued

At 650 and especially 700°C strong chromium enrichment in the inner scale was found not only for VM12 but also for other 9-12% Cr martensitic steels being tested in this study. This can be illustrated using the results obtained for P92 (Fig. 9.6). For this steel additionally strong enrichment of silicon was detected in a narrow band near the scale/alloy interface, indicating that some of the minor alloying additions, besides chromium, would play an important role in the formation of the oxide scale during high temperature exposure. Further analysis of the elemental distribution (Fig. 9.6) leads to the question of which exact mechanism is responsible for the formation of such a stratified structure of the inner oxide layer. A study was done by Żurek [61] using steels of similar composition and temperatures as used in this study after exposure to Ar/H_2O. The author proposed that Cr-rich stringers in the inner oxide layer indicated more rapid Cr diffusion from the bulk alloy in the direction of the scale. The enhanced Cr diffusion allowed the formation of a Cr-rich $(Fe,Cr)_3O_4$ layer at the scale alloy interface. The preferential oxidation of Cr resulted in Cr depletion beneath the Cr-rich spinel layer in the alloy. After continued Cr depletion, the Cr-rich spinel could no longer remain stable. As a result, Fe-rich oxides were subsequently formed. Repetition of this process lead to layered microstructure in the inner part of the scale.

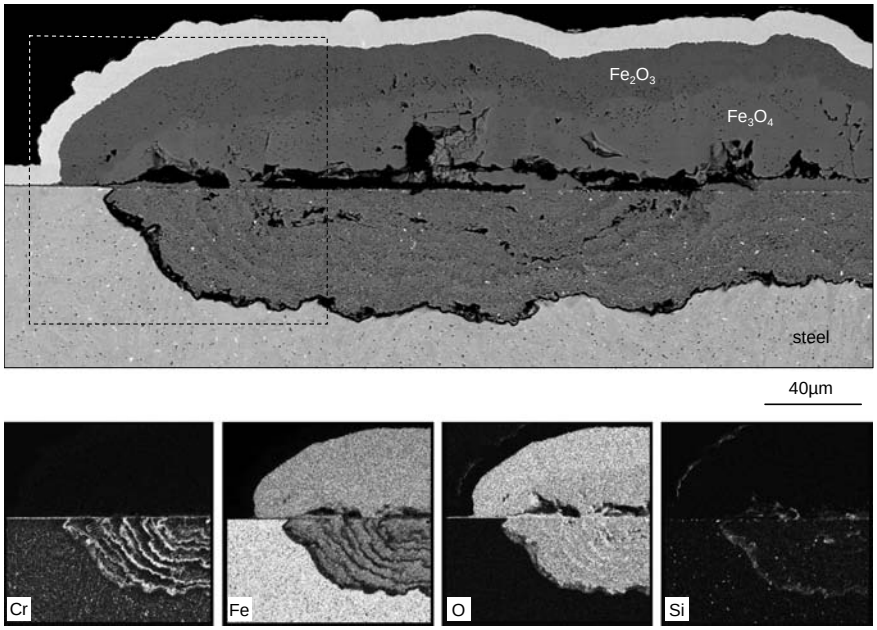

Figure 9.6: SEM images of the cross section (upper image) and corresponding X-ray element mappings from the marked area (lower images) of P92 after 1000h oxidation in Ar/CO_2 at 700°C

The formation of the observed Cr-rich bands might also be explained in the following way: If a sufficient amount of Cr and Si is present in the bulk material and sufficient mobility of these elements is attained, Cr/Si-rich bands are formed. Beneath this band, Cr and Si become depleted. Due to very low concentration, Si easily reaches the so-called “zero” level. In this condition chromium alone is not able to retain the protective oxide formation and as a consequence Fe-rich oxide is formed beneath the Cr/Si-rich oxide band. Beneath the newly formed oxide layer Fe becomes depleted allowing the local enrichment of Cr and Si. Formation of a new Cr/Si-rich band occurs. The process is repeated as long as the concentration of Cr and Si is sufficiently high. The results obtained in this study confirmed the above proposed mechanism that silicon significantly enhanced the formation of Cr-rich protective bands in the inner oxide layer. As will be further explained in Chapter 13 the steel P92 with much lower Si content did not possess the capability of forming protective Cr-rich bands as shown in Fig. 9.6

Incorporation of chromium into the inner oxide scale resulted in a decrease of the oxidation kinetics because outward Fe cation diffusion was significantly hampered. Furthermore, it was observed that at 650 and 700°C the initially formed thin Cr-base surface scale locally remained intact even after 1000h exposure. Therefore, some areas of the alloy surfaces exhibited

a protective Cr-base scale, whereas the others formed less protective Fe-base oxides (Fig. 9.6). As a consequence, lowering of the overall weight gain was observed for some of the 9-12% Cr steels at higher temperatures (Fig. 9.7).

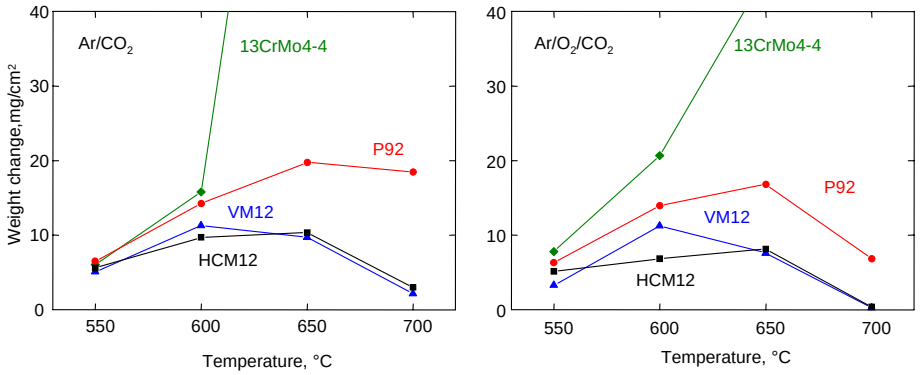

Figure 9.7: Temperature dependence for oxidation behaviour of selected steels after 1000h exposure to the dry CO_2-containig atmospheres at temperatures 550-700°C. Left figure: Ar/CO_2; right figure: Ar/O_2/CO_2

In the case of atmospheres containing both CO_2 and H_2O the tendency for decreasing scaling rate at higher temperatures was, however, only observed for one steel, i.e., VM12. Other 9-12% Cr steels showed a temperature dependence of the oxidation rates qualitatively similar to that of the low alloyed steel. For all these steels higher mass gains were found with increased temperature. Similar temperature dependence was found for HCM12 and P92, although the Cr content of the former (12% Cr) was close to that of VM12 (11.4% Cr). The total mass gain recorded for HCM12 was, however, significantly smaller than that of P92 (Fig. 9.8).

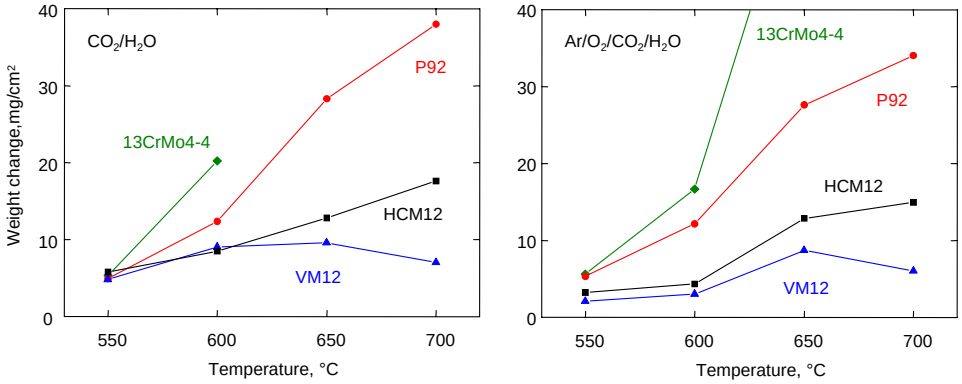

Figure 9.8: Temperature dependence for oxidation behaviour of selected steels after 1000h exposure to CO_2-and H_2O-containing atmospheres at temperatures 550-700°C. Left figure: CO_2/H_2O; right figure: Ar/O_2/CO_2/H_2O

10. Effect of oxygen addition

10.1 General remarks

In the following chapter the effect of oxygen additions on the oxidation behaviour in the CO_2- and CO_2/H_2O-containing gases will be presented. The effect of oxygen excess on the oxidation behaviour of construction materials is an important issue since excess of oxygen is expected in the real oxy-fuel gases.

Oxygen addition to Ar/CO_2 and CO_2/H_2O resulted in a significant increase of the oxygen partial pressure in these gas mixtures, while the carbon activity decreases considerably. In the temperature range used in this study (550-700°C) a_c in gases with added oxygen is at least 7 orders of magnitude lower than that calculated for gases containing CO_2 or CO_2/H_2O alone (see Fig. 4.5). This chapter will mainly focus on the effects of oxygen on oxide scale formation mechanisms on selected ferritic/martensitic and austenitic steels. Carburization phenomena occurring during oxidation in these atmospheres with oxygen addition will be discussed in Chapter 15.

10.2 Effect of oxygen addition to Ar/CO_2 on behaviour of ferritic/martensitic steels

For low alloy steel 13CrMo4-4 a slight increase was found in the scaling rate by a factor of about 1.3 after exposure to the atmosphere containing 1% oxygen at 600°C compared to that at 550°C. Thermodynamic calculations showed that the oxygen partial pressure in CO_2 and O_2/CO_2 is sufficiently high for the formation of both magnetite and hematite. This was confirmed by the metallographic analyses which revealed a similar morphology of the oxide scales in both gases. Porosity was found within the outer Fe_3O_4/Fe_2O_3 layers on specimens exposed to both gases. The only noticeable difference was that the oxide formed in $Ar/O_2/CO_2$ was slightly thicker than that formed in Ar/CO_2 which confirmed the gravimetric results shown in Fig. 10.1. Similar oxide morphology was observed at 600°C. No spallation was found during and after exposure to the mentioned gases at 550 and 600°C.

For the low alloy steel mass gain and oxide thickness increased when oxygen was added, while an opposite effect for the steels containing 9-12% Cr was observed. Apparently for this class of materials oxygen addition to Ar/CO_2 enhanced the formation of a protective Cr-rich oxide scale,

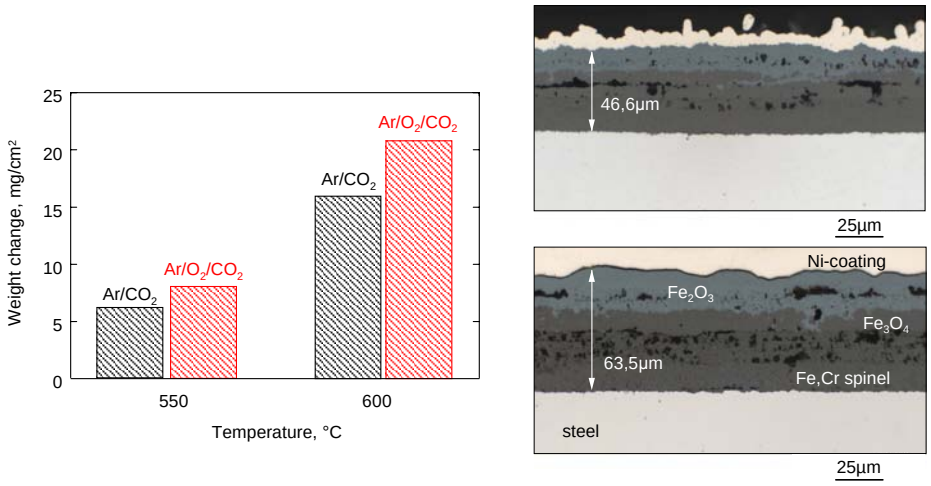

Figure 10.1: Weight changes of 13CrMo4-4 after 1000h exposure to Ar/CO_2 (black bars) and $Ar/O_2/CO_2$ (red bars) at 550 and 600°C and corresponding cross sections: Ar/CO_2 (upper figure) and $Ar/O_2/CO_2$ (lower figure) at 550°C

whereas in the case of steel 13CrMo4-4 insufficient concentration of protective scale forming elements, mainly Cr, was available to obtain a positive effect of oxygen addition. The gravimetric data of VM12 exposed to Ar/CO_2 with and without oxygen addition presented in Fig. 10.2 show that higher mass gain was observed for the specimen oxidized in Ar/CO_2 than for

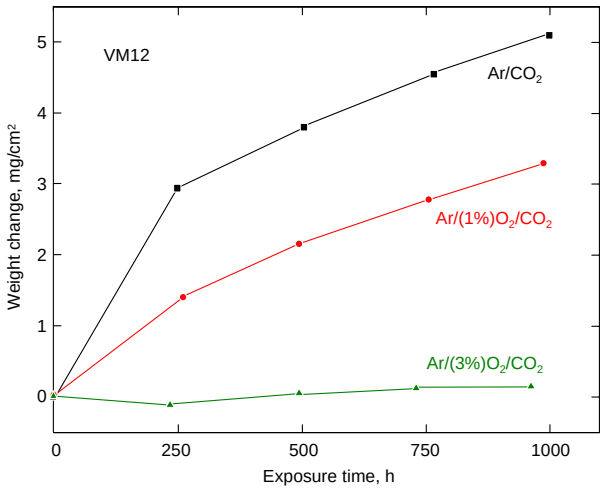

Figure 10.2: Effect of 1-3% of O_2 in Ar/CO_2 on the oxidation behaviour of VM12 during exposure at 550°C

that oxidized in $Ar/O_2/CO_2$. Increasing the oxygen concentration from 1 to 3% in the test gas resulted in lowering of the mass gain to a very low level characteristic for air oxidation (see Chapter 5). Metallographic cross sections revealed the reason why the observed kinetics differed so much if oxygen was added to the atmosphere. Fig. 10.3a shows the typical morphology of the non-protective, Fe-rich oxide scale formed during exposure to Ar/CO_2. It consisted of an inner spinel type oxide layer formed beneath the original metal surface, whereas Fe_3O_4 and an outer Fe_2O_3 layer were present above. After exposure to $Ar/O_2/CO_2$ the oxide morphology exhibited local formation of protective Cr-rich oxide. However, thick multilayered Fe oxides scale was also present covering most of the specimen surface (Fig. 10.3b). This situation changed dramatically when the concentration of oxygen increased from 1 to 3% resulting in overall coverage of Cr-rich oxide on the surface with only a few Fe-rich nodules (Fig. 10.3c).

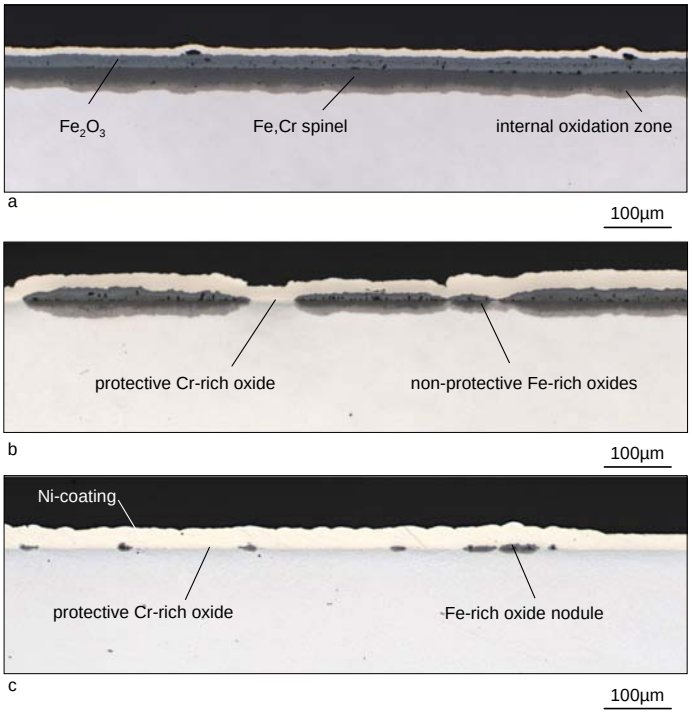

Figure 10.3: Metallographic cross sections of VM12 after 1000h exposure in Ar/CO_2 (a); $Ar/(1\%)O_2/CO_2$ (b) and $Ar/(3\%)O_2/CO_2$ (c) at 550°C

A direct reaction of the CO_2 molecule with the steel surface, preferentially chromium, can be assumed:

$$\tfrac{3}{2}CO_2 + 2Cr \rightarrow Cr_2O_3 + \tfrac{3}{2}[C] \qquad \text{(Eq. 10.1)}$$

Taking the CO_2 partial pressure of the test gas and assuming the Cr activity in the steel $\approx 10^{-1}$ a very high C activity is calculated. It is much higher than that required for Cr-carbide formation ($\approx 10^{-3}$).

$$6[C] + 23Cr \rightarrow Cr_{23}C_6 \qquad \text{(Eq. 10.2)}$$

Addition of free oxygen will result in a reaction of the carbide with O_2:

$$\tfrac{1}{2}Cr_{23}C_6 + 11\tfrac{5}{8}O_2 \rightarrow 5\tfrac{3}{4}Cr_2O_3 + 3CO_2 \qquad \text{(Eq. 10.3)}$$

Depending on the relative rates of reactions Eq. 10.1-3 carbide formation becomes significant or not. In the latter case, the steel will tend to form a Cr-base oxide scale similar to that formed in air or oxygen. In the other case, carbide formation will hamper Cr-transport to the surface resulting in the formation of Fe-rich oxides on an internally carburized alloy (see Chapter 15). It should be mentioned that reactions Eq. 10.1-3 could have CO formation as intermediate steps, as proposed by Meier *et al*. [33]. In this case it is expected that CO molecules will react with the O_2 in the gas phase forming CO_2 and thus keeping the carbon activity low which means that the formation of carbides would be significantly hampered.

It is obvious that the oxidation rate of metallic construction materials exposed at elevated temperatures strongly depends on their composition. In the case of ferritic/martensitic steels the Cr concentration is the most important factor which governs the formation of a protective surface scale. To illustrate the evolution of k_p value as a function of Cr content, a number of ferritic/martensitic steels were oxidized in CO_2 atmosphere containing 0, 1 or 3% of O_2. Fig. 10.4 shows the changes of k_p values under such conditions together with those obtained during air oxidation. The mechanism describing the change from protective properties of the oxide scale (low k_p) into non-protective behaviour (high k_p) was widely discussed in the literature by several authors [76, 111-113] and will be further explored in Chapter 12.

Therefore, only the effect of atmosphere variation at fixed temperature on the oxidation behaviour is discussed in this section.

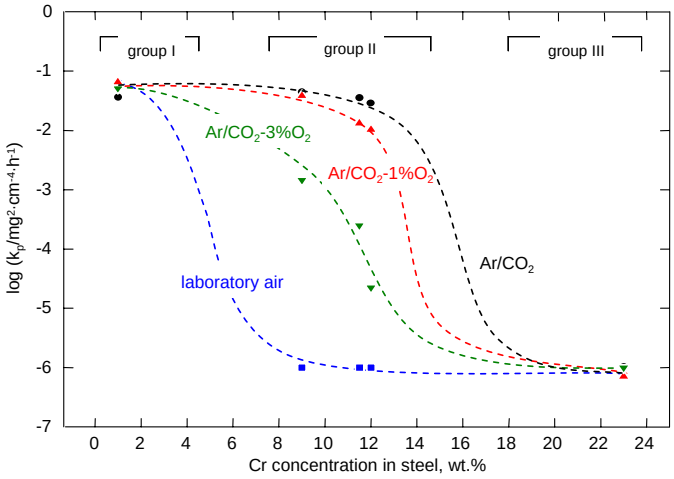

Figure 10.4: Oxidation rates of ferritic/martensitic steels as a function of Cr content in CO_2-containing atmospheres and in laboratory air at 550°C. Data points for 23% Cr steel relate to Crofer 22 APU (see Tab. 19.1). Experimental points are represented by symbols, whereas the dashed lines present the qualitative variation of k_p as a function of Cr content

Formation of multi-layered Fe-base oxide scales was observed when a low-Cr steel (group I in Fig. 10.4) was exposed to oxidizing gases at 550°C. It was found that the variation of oxygen addition to Ar/CO_2 did not play a significant role on the oxidation behaviour of this material. This situation would change significantly if the Cr concentration in the alloy was higher than a critical level above which Cr might be selectively oxidized. The selective oxidation of Cr in these steels (group II) was strongly affected by gas composition. The metallographic cross sections revealed coexistence of the protective and non-protective oxide scales on the same specimens when oxygen was intentionally added in the Ar/CO_2 (Fig. 10.3). Therefore, more protective oxide was formed on the metal surface with increased amount of oxygen in the atmosphere. This dependence was reflected in a decreasing k_p value with increasing oxygen content and was more pronounced for alloys with higher Cr content like VM12 and X20 than for P92. Assuming that in the early stages of oxidation the protective Cr-rich oxide scale was formed initially and Fe-base oxides were formed as a result of breakaway after prolonged exposure time, one might conclude that the addition of oxygen in Ar/CO_2 would retard the breakaway oxidation in this group of steels. In the case of the nominally 22% Cr ferritic steel Crofer 22 APU (group III) no effect of oxygen addition on the oxidation behaviour could be found since this material formed, in all tested atmospheres, very thin and well adherent chromia base oxide scale

without breakaway or spallation at temperatures in the range 550-700°C. A negative or positive effect of oxygen addition in Ar/CO_2 on oxidation behaviour could therefore not be derived.

The change from protective into non-protective oxide scale formation in the case of borderline alloys (group II in Fig. 10.4) depends on a number of factors. Even very small variation in alloy composition, microstructure, concentration of other scale forming elements (e.g., Mn, Si, Al) or impurities, may significantly change the oxidation resistance of the steel. As shown in Fig. 10.4 a small variation in gas composition could also change the protective oxide scale formation. However, if the Cr concentration in the steel exceeded a certain level, the susceptibility to gas variations did not occur at lower temperatures. This was observed for P92 at 550°C and 600°C, whereas a further increase of temperature promoted the formation of a more protective oxide. This means that the specimen surface after exposure to $Ar/O_2/CO_2$ at 650°C and 700°C exhibited a thin, locally retained Cr-base oxide scale (Figs. 10.5-6)

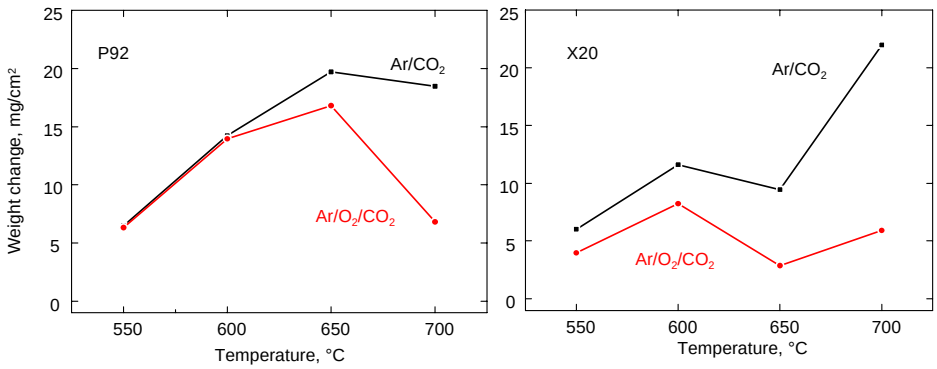

Figure 10.5: Temperature dependence on weight change for P92 (left) and X20 (right) after 1000h exposure to Ar/CO_2 (black) and $Ar/(1\%)O_2/CO_2$ (red)

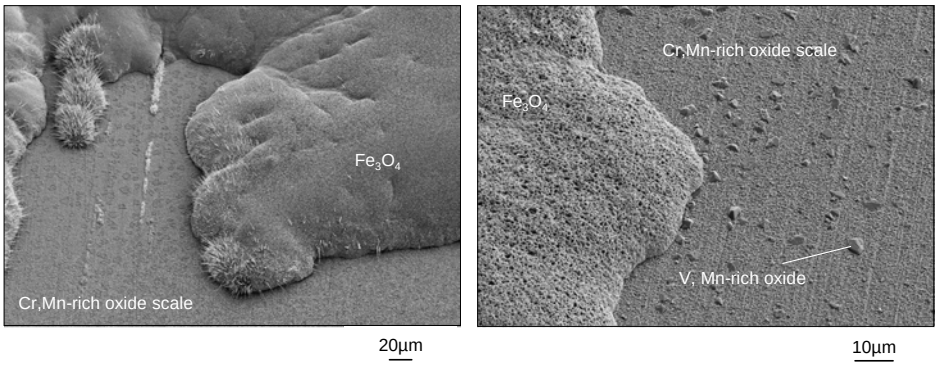

Figure 10.6: SEM images of the oxide surface on P92 (left) and X20 (right) after 1000h exposure to $Ar/O_2/CO_2$ at 650°C

To schematically illustrate how the oxidation rate of various steel types is changed in Ar/CO_2 with and without oxygen addition, k_p of three steels with different Cr concentrations was plotted as a function of reciprocal temperature in Fig. 10.7. It can be seen that k_p of 13CrMo4-4 was increased by oxygen addition. The opposite effect was found for the steel with 11% Cr (X20), while k_p of the 9% Cr steel (P92) hardly changed when the gas composition varied.

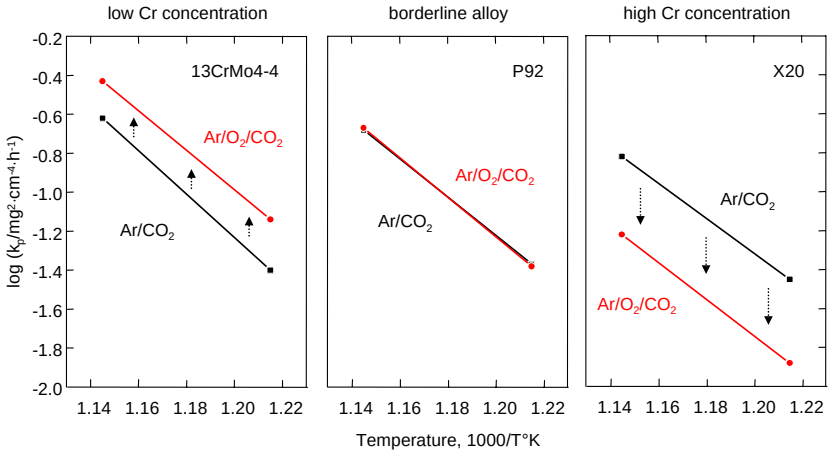

Figure 10.7: Change of k_p of different commercial steels during exposure to Ar/CO_2 (black) and $Ar/O_2/CO_2$ (red). 13CrMo4-4 (left), P92 (middle), X20 (right)

10.3 Effect of oxygen addition to Ar/CO_2 on behaviour of austenitic steels

Damage and subsequent spallation of the outer oxide scale is frequently encountered during oxidation of austenitic steels and is mainly caused by thermal stresses developed upon thermal cycling [34, 114]. In this study higher oxidation rates in CO_2- and/or H_2O-rich gases were observed for austenitic steels with lower Cr content. 1.4910 steel with its 16.5% Cr exhibited the lowest oxidation resistance and also the highest spallation rate when exposed to CO_2- and/or H_2O-rich gases. When comparing the oxidation behaviour of 1.4910 in Ar/CO_2 and $Ar/O_2/CO_2$ at 650°C it is clear that much more spallation occurred in $Ar/O_2/CO_2$ (Fig. 10.8). To measure the thickness of the spalled oxide was experimentally impossible. However, it can be assumed that the higher spallation in the atmosphere enriched with oxygen reflects the higher oxidation rates of this material similar as was observed for the low alloyed steel 13CrMo4-4.

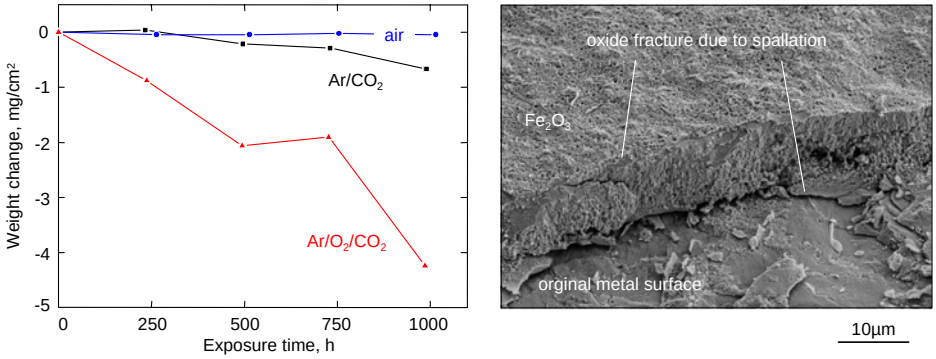

Figure 10.8: Weight changes of 1.4910 (left) during 1000h exposure to laboratory air, Ar/CO_2 and $Ar/O_2/CO_2$ at 650°C. SEM image (right) shows oxide scale morphology of 1.4910 after exposure to $Ar/O_2/CO_2$ at 650°C

At 700°C austenitic steels with lower Cr content (<18.5%) were prone to form a Fe-rich oxide scale which exhibited susceptibility to spallation in both atmospheres containing CO_2 (Fig. 10.9). Steel Super 304H, which can be considered as "borderline alloy" according to the nomenclature used in the previous section, exhibited better oxidation resistance in $Ar/O_2/CO_2$ than in Ar/CO_2 (Fig. 10.9). Apparently, for this steel additional oxygen had a positive effect on sustaining the protective properties of the initially formed scale.

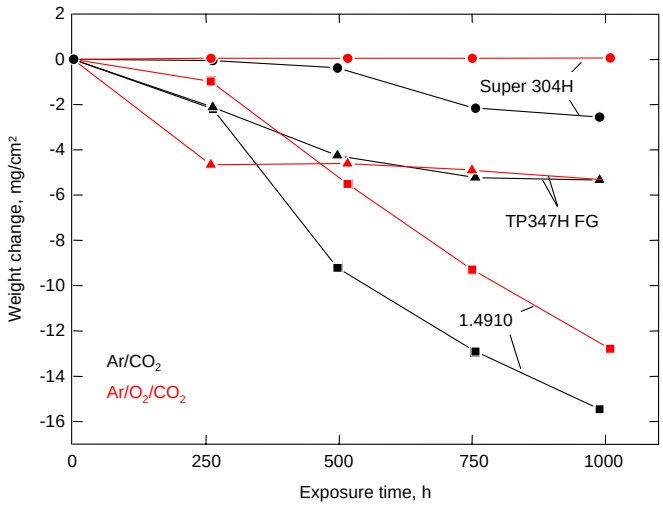

Figure 10.9: Oxidation behaviour of selected austenitic steels during 1000h exposure to Ar/CO_2 (black) and $Ar/O_2/CO_2$ (red) at 700°C

For 1.4910 a higher spallation rate occurred in $Ar/O_2/CO_2$ at 700°C than in Ar/CO_2. It should be mentioned that in laboratory testing the rates of oxide scale growth are generally quite

reproducible. However, spallation is a statistical process with the result that weight loss rates are subject to substantial scatter. Metallographic analysis revealed that the inner spinel type oxide was thicker when formed in $Ar/O_2/CO_2$ than in Ar/CO_2 (Fig. 10.10). The specimen weight change thus combines weight gain due to oxygen uptake by scale growth and weight loss owing to scale spallation. The differences in weight change observed for 1.4910 during exposure at 700°C can thus be considered as being only minor.

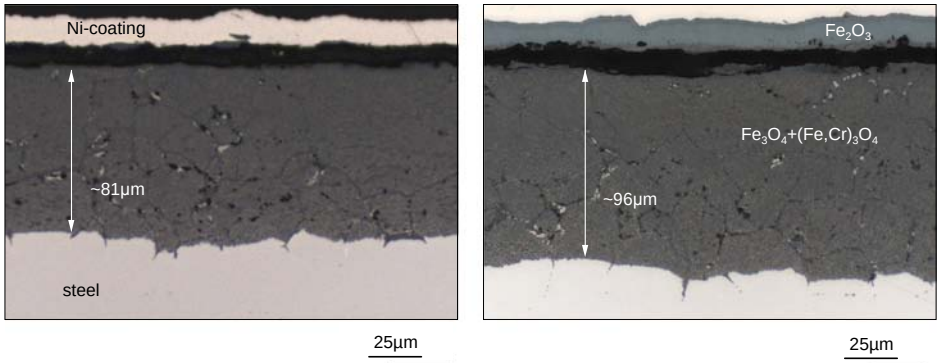

Figure 10.10: Metallographic cross sections of 1.4910 after 1000h exposure to Ar/CO_2 (left) and $Ar/O_2/CO_2$ (right) at 700°C

Austenitic steels containing more than 18.5% chromium exhibited better oxidation resistance in the gas with higher pO_2. The positive effect of oxygen on oxidation resistance of Super 304H was already demonstrated in Fig. 10.9 where an extremely small weight change was recorded after exposure to $Ar/O_2/CO_2$ but not to Ar/CO_2. The metallographic cross sections of this steel presented in Fig. 10.11 show the formation of a thin and protective Cr-base oxide scale in the case of the Ar/CO_2 and an Fe-base oxide scale with some evidences of spallation after exposure to $Ar/O_2/CO_2$ gas. Steel 310N (>24% Cr) revealed extremely low oxidation rates at all test temperatures in Ar/CO_2 as well as in $Ar/O_2/CO_2$.

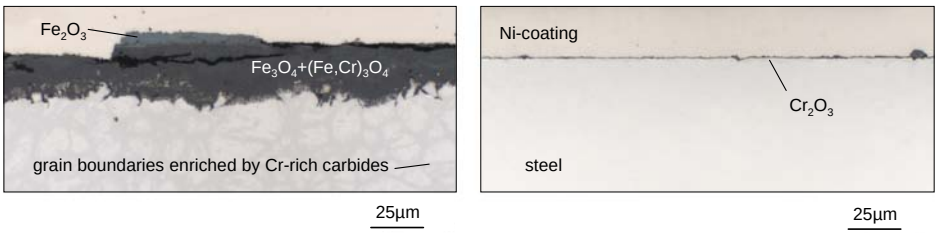

Figure 10.11: Metallographic cross sections of Super 304H after 1000h exposure to Ar/CO_2 (left) and $Ar/O_2/CO_2$ (right) at 700°C

Similar to Fig. 10.4 for ferritic/martensitic steels, the evolution of k_p as a function of Cr content in austenitic steels exposed to Ar/CO_2 with and without 1% O_2 at 650°C are plotted in Fig. 10.12. Additionally the k_p values obtained during air oxidation are presented.

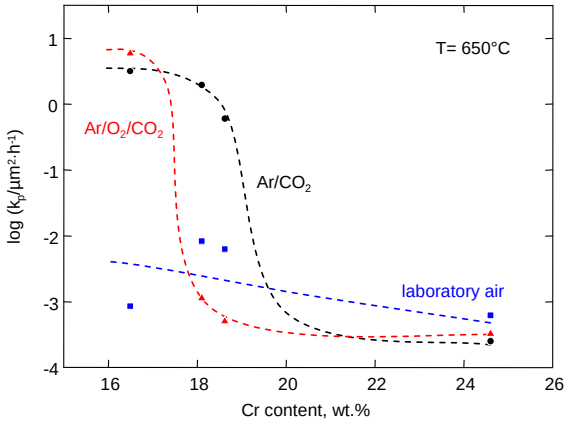

Figure 10.12: Oxidation rates of commercial austenitic steels as function of Cr content in the CO_2-containing atmospheres and laboratory air at 650°C. Experimental points are represented by symbols, whereas dashed lines qualitatively indicate the k_p dependence of Cr content (k_p determined from oxide scale thickness)

10.4 Effect of oxygen addition to CO_2/H_2O on the behaviour of ferritic/martensitic steels

As shown earlier, the scale morphology and oxidation kinetics of 13CrMo4-4 did not vary considerably in Ar/CO_2 and $Ar/O_2/CO_2$, while only a slight increase of the scaling rate was found in the case of the atmosphere with oxygen addition. A similar effect was observed when 3% oxygen was added to CO_2/H_2O (Fig. 10.13). Outward diffusion of Fe cations through the oxide was the rate-determining step in the case of the low alloyed steels and was apparently hardly affected by the oxygen addition.

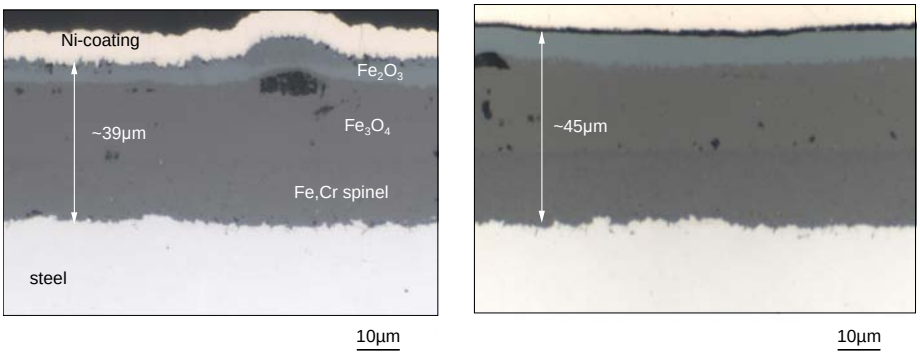

Figure 10.13: Metallographic cross sections of 13CrMo4-4 after 1000h exposure to CO_2/H_2O (left) and $Ar/O_2/CO_2/H_2O$ (right) at 550°C

The oxidation rate of the 9% Cr steel P92 in $Ar/O_2/CO_2/H_2O$ was similar to that observed in CO_2/H_2O. The weight changes and oxide scale morphologies did not vary significantly when oxygen was present in the atmosphere (Fig. 10.14). At 700°C minor exfoliation of the outer hematite layer was observed for P92. The metallographic cross sections (Fig. 10.15) revealed very similar oxide morphologies for specimens exposed to CO_2/H_2O and $Ar/O_2/CO_2/H_2O$ at 550°C. The inner layer consisted of $(Fe,Cr)_3O_4$ and was covered by outer magnetite and hematite layers. At this temperature an internal oxidation zone was formed which was typical for this class of materials after exposure to the CO_2- and/or /H_2O-rich atmospheres (see Chapter 5).

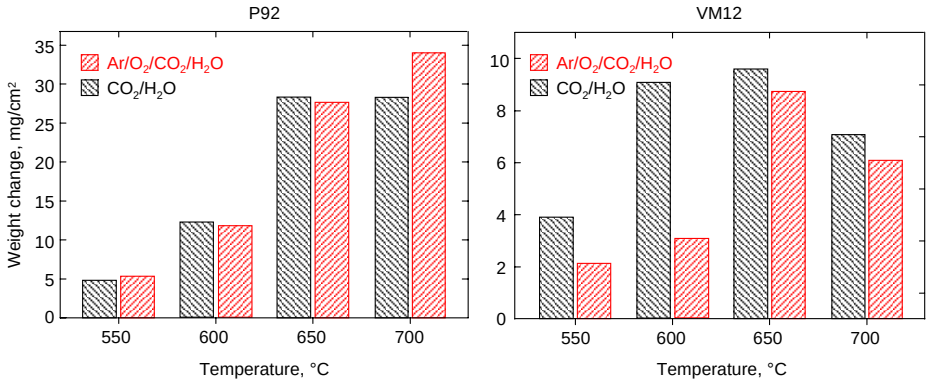

Figure 10.14: Weight change data of P92 (left) and VM12 (right) during 1000h exposure to CO_2/H_2O and $Ar/O_2/CO_2/H_2O$ at 550-700°C. The weight change data for P92 at 700°C are affected by minor spallation

A substantial porosity was found in the case of the P92 specimen near the interface between the internal oxidation zone and the inner oxide layer after exposure to CO_2/H_2O but not to $Ar/O_2/CO_2/H_2O$ (Fig. 10.15). This phenomenon was also observed on the other studied alloys, i.e., X20, HCM12 and VM12, however, for those alloys with higher Cr content this effect was less pronounced. Till now, no clear explanation for this effect can be provided.

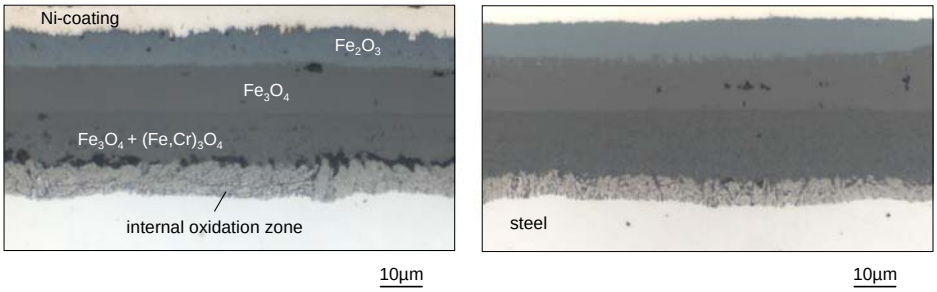

Figure 10.15: Metallographic cross sections of P92 after 1000h exposure to CO_2/H_2O (left) and $Ar/O_2/CO_2/H_2O$ (right) at 550°C

The right part of Fig. 10.14 shows weight changes of VM12 oxidized in CO_2/H_2O with and without oxygen for 1000h. Important to note that the weight gain at 700°C was smaller than that at 650°C which is explained by the enhanced incorporation of Cr into the inner layer of the oxide scale. This effect was frequently observed for 9-12% Cr steels at temperatures around 650°C. However, as discussed in detail in Chapter 9, it should be mentioned that only the steels with more than 10% Cr exhibited this so-called "bell shape" temperature dependence in H_2O-containing gases, whereas in dry gases it could be observed for all 9-12% Cr steels examined in this study (compared with Fig. 10.5).

After analyzing the results obtained for VM12 the general conclusion can be drawn that an oxygen addition had a beneficial effect and causes a decrease in oxidation rate. This was characteristic for all tested temperatures, however, a much more distinct improvement was observed for 550 and 600°C. Hardly any effect of oxygen was observed for P92 and other martensitic steels.

As mentioned in Section 10.2, 9-12% Cr steels belong to the so-called "group II alloys" when describing the capability of forming protective Cr-rich oxide scales. A common feature of these steels is that small variations of composition, microstructure or even surface preparation may significantly change their oxidation behaviour. Among the studied martensitic steels, VM12 exhibited the best oxidation resistance followed by HCM12 and X20, while P92 was considered as the martensitic steel with the worst oxidation resistance.

As discussed in Chapter 5, all studied 9-12% Cr steels formed a thin Cr-rich oxide layer during the early stages of oxidation in CO_2- and/or H_2O-rich gases which was gradually "consumed" by the fast growing Fe-base oxides during prolonged exposure. This was common for all tested steels but the time required for the scale transformation from protective into non-protective at a given temperature was different for each material. In this context VM12 exhibited the longest time to sustain the protective properties of the initially formed oxide scale, although the Cr content in the steel was not the highest among the 9-12% Cr steels studied here. This could be due to its microstructure or the presence of other minor alloying elements such as, e.g., Co which was found only in VM12 with relatively high amount (1.5wt.%). Previous studies showed that Co had positive effect on the oxidation behaviour, especially at higher temperatures [109, 126].

At 650°C VM12 exhibited significant differences in the oxidation kinetics in the gases with and without oxygen addition. The total mass gain after 1000h exposure was similar for specimens oxidized either in CO_2/H_2O or in $Ar/O_2/CO_2/H_2O$ (9.59mg/cm^2 and 8.73 mg/cm^2, respectively). However, as shown in Fig. 10.16, VM12 exhibited approximately parabolic oxidation in the CO_2/H_2O gas, whereas a much lower mass gain was observed in the early stages of oxidation (250h) in the gas with oxygen addition. This is characteristic for an initially formed protective Cr-rich scale. After 250h the oxidation curve shows a rapid increase of the weight which was attributed to the formation of Fe-base oxides. The typical sequence of iron base oxides covering the complete metal surface was found after 1000h. However, in the early stages of oxidation the oxygen in the wet atmosphere apparently hampered the occurrence of the breakaway oxidation process.

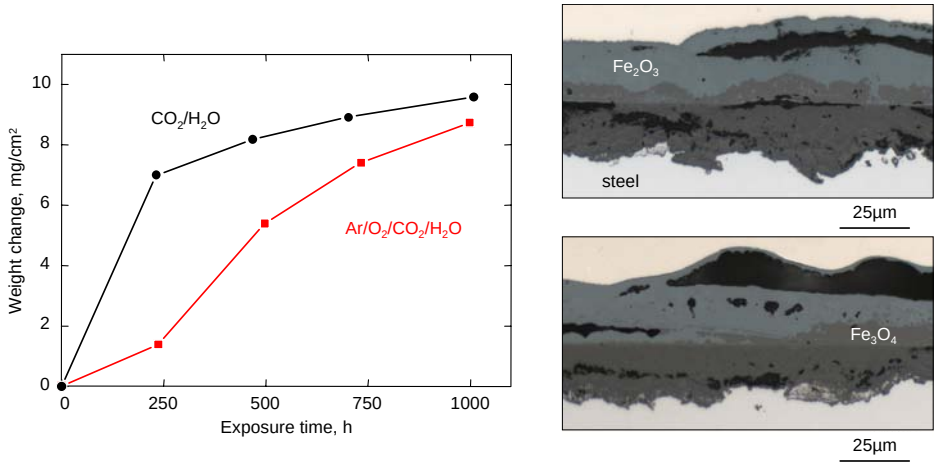

Figure 10.16: Weight changes of VM12 during 1000h exposure to CO_2/H_2O (black) and $Ar/O_2/CO_2/H_2O$ (red) at 650°C. Corresponding cross sections on right side after 1000h exposure at 650°C: CO_2/H_2O (top) and $Ar/O_2/CO_2/H_2O$ (bottom)

10.5 Effect of oxygen addition to CO_2/H_2O on behaviour of austenitic steels

The delay of the breakaway oxidation by addition of oxygen to the environment containing H_2O and CO_2 found for the 12% Cr martensitic steel was not observed for austenitic steels. In contrast, breakaway oxidation was accelerated by oxygen addition to CO_2/H_2O. To explain the obtained results only a brief discussion of possible factors causing failure of protective oxide will be presented here, since more details will be given in Chapter 11.

Low mass gains and corresponding thin and protective Cr-rich oxides were observed for all the austenitic steels tested at 550°C in CO_2/H_2O and $Ar/O_2/CO_2/H_2O$ similar to those obtained during air exposure. However, at higher temperature differences in oxidation behaviour were found for specimens oxidized in CO_2/H_2O and in $Ar/O_2/CO_2/H_2O$. In the latter case, steels with lower Cr content (<24wt.%) tended to form Fe-rich oxides. This was, for instance, observed for 1.4910 at 600°C (Fig. 10.17). During the exposure in CO_2/H_2O a small weight gain was found during the first 750h; and then a larger increase of the weight gain took place. It was found that tiny Fe-rich oxide nodules started to grow on the initially formed Cr-base oxide scale. This was not the case in the atmosphere containing 3% oxygen, where a much higher oxidation rate occurred accompanied by strong spallation of the outer Fe oxide layer even within the first 250h (Fig. 10.17). It can be concluded that in both atmospheres occurrence of breakaway is a matter of time, however, this would be much shorter if oxygen together with water vapour is present in the environment.

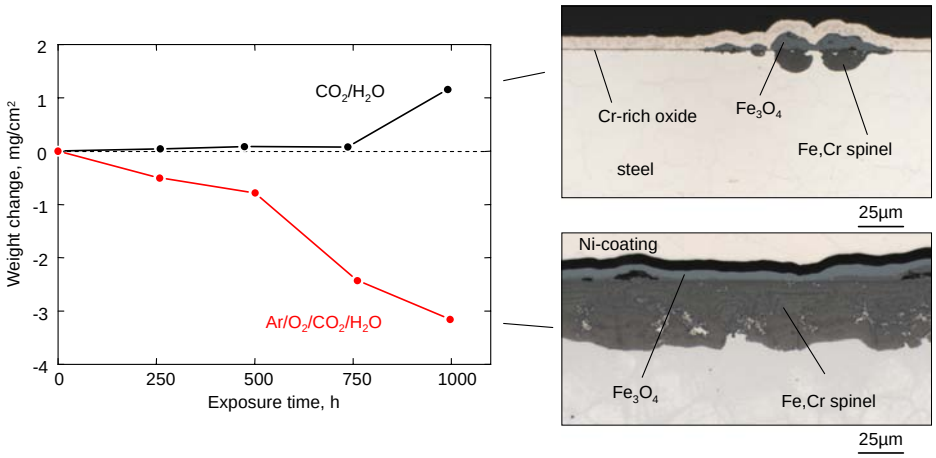

Figure 10.17: Weight change of 1.4910 during 1000h exposure to CO_2/H_2O (black) and $Ar/O_2/CO_2/H_2O$ (red) at 600°C. Corresponding cross sections on right side after 1000h exposure: CO_2/H_2O (top) and $Ar/O_2/CO_2/H_2O$ (bottom)

A similar effect was observed for Super 304H. A very low scaling rate occurred at 550°C in both gases, which tended to accelerate at 600°C in the $Ar/O_2/CO_2/H_2O$ atmosphere but not in CO_2/H_2O where only formation of protective Cr-base oxide scale was found (Fig. 10.18). Further increase in temperature resulted in a higher oxidation rate and enhanced deterioration of the oxide scale with a strong tendency of spallation, independent of the gas composition.

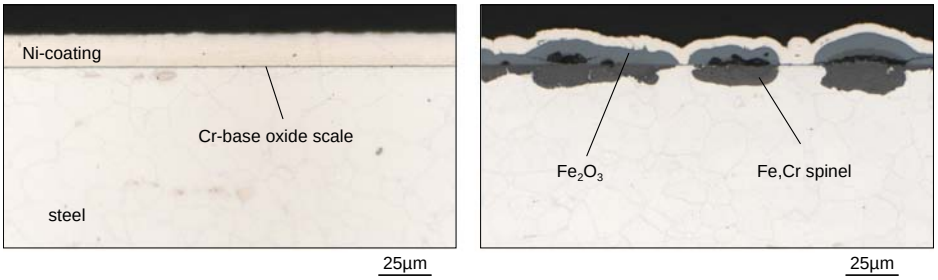

Figure 10.18: Metallographic cross sections of Super 304H after 1000h exposure to CO_2/H_2O (left) and $Ar/O_2/CO_2/H_2O$ (right) at 600°C

The general conclusion is that hardly any effect of oxygen was observed for austenitic steels with low and intermediate Cr content at 650 and 700°C (Fig. 10.19). A quite different situation was observed for 310N when exposed to CO_2/H_2O and $Ar/O_2/CO_2/H_2O$. This steel exhibited significant increase in mass when exposed to the latter atmosphere (Fig. 10.19).

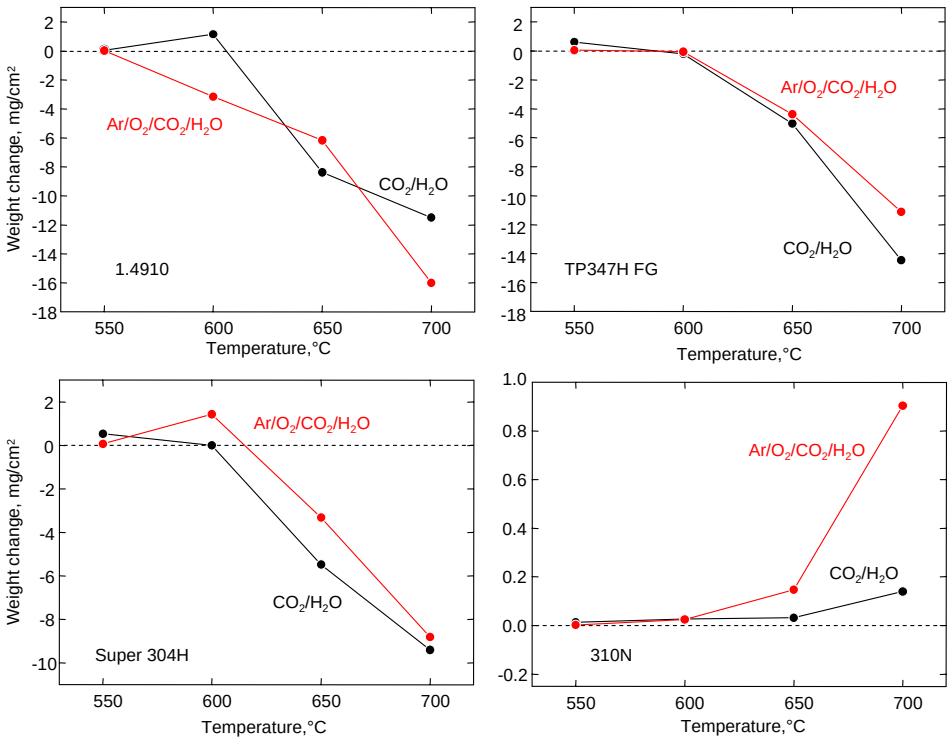

Figure 10.19: Temperature dependence on weight change for austenitic steels after 1000h exposure to CO_2/H_2O (black) and $Ar/O_2/CO_2/H_2O$ (red)

As presented in Fig. 10.20 this increase in weight was related to the formation of Fe-base oxide nodules growing on the metal surface, similar to the observation made for Super 304H (Fig. 10.18). In CO_2/H_2O steel 310N formed exclusively a thin and well adhering Cr-base scale. However, when additional oxygen was present in CO_2/H_2O, breakaway of protective oxide scale occurred at and above 650°C. The deterioration of initially formed Cr-base oxide scale on 310N was most likely related to the Cr-oxyhydroxide evaporation. This phenomenon was recognized as the major reason of the observed change from protective into non-protective oxidation behaviour and further will be explained in Chapter 11.

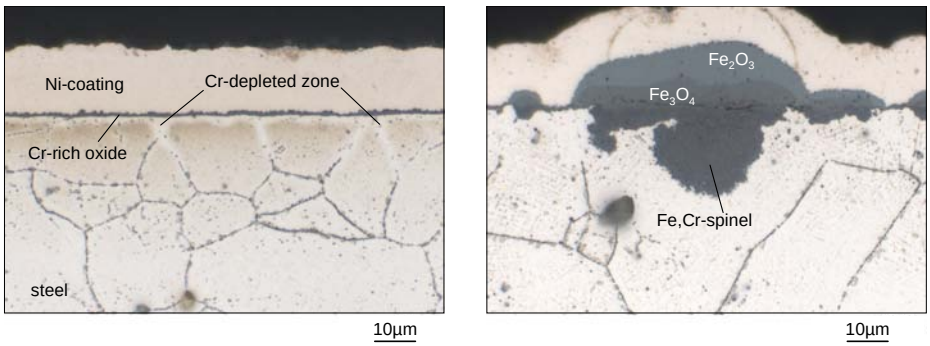

Figure 10.20: Metallographic cross sections of 310N after 1000h exposure to CO_2/H_2O (left) and $Ar/O_2/CO_2/H_2O$ (right) at 700°C. Additional etching was applied to reveal the Cr depletion beneath the oxide scale

10.6 Summary of the results concerning oxygen addition

After comparison of the results obtained during oxidation of the martensitic and austenitic steels in atmospheres with and without oxygen addition the following conclusions can be established:

- 9-12% Cr martensitic steels exposed to CO_2 and/or H_2O form barely protective Fe-base oxide scale at all test temperatures. Due to faster chromium diffusion at 650°C and especially 700°C the 9-12% Cr martensitic steels tend to form Fe,Cr-rich spinel in the inner oxide scale. At 650°C and 700°C martensitic steels exhibit local formation of protective Cr-base oxide scale in dry CO_2. This, however, is not observed in Ar/H_2O and CO_2/H_2O.

- For these steels oxygen addition to Ar/CO_2 improves selective oxidation of chromium, thus protective oxide scale formation is observed in $Ar/(1\%)O_2/CO_2$ and especially in

Ar/(3%)O_2/CO_2. The positive effect of oxygen addition to CO_2/H_2O on the oxidation behaviour of the martensitic steels is marginal, most likely due to much faster H_2O molecule adsorption on the metal surface.

- CO_2 and H_2O give similar results with respect to the oxidation behaviour of the austenitic steels. At and below 600°C these steels tend to form protective Cr-base oxide scales. At higher temperatures, however, formation of Fe-base oxide is found. This behaviour is typical for austenitic steels with less than 24% Cr.

- Addition of oxygen to dry CO_2 resulted in deterioration of the oxidation resistance for austenitic steels with lower Cr content at 650°C. At higher temperature an improvement of oxidation resistance due to extra oxygen is observed only for steel Super 304H (18.6wt.% Cr). Steel 310N exhibits exclusive formation of a thin chromia base scale in both atmospheres and at all test temperatures.

- When 3% oxygen is introduced to CO_2/H_2O much faster deterioration of the protective Cr-base oxide scale is observed for all austenitic steels. The detrimental effect of oxygen in water vapour containing atmospheres on the oxidation behaviour of steel 310N is most likely attributed to the formation of volatile Cr-oxyhydroxide.

- The adverse effect of volatile species formation on protective chromia base scale formation is less pronounced than the effect of H_2O and/or CO_2 observed for austenitic steels with lower Cr content, i.e., the negative effect of oxygen addition to H_2O-containing gases becomes only apparent when the mechanism responsible for Cr-base scale degradation in oxygen-free H_2O-rich atmospheres is not “active”.

11. Evaporation of volatile species

11.1 High chromium austenitic steel

During exposure of alloy 310N to various atmospheres containing CO_2 and/or H_2O very small weight gains were observed at all test temperatures from 550 to 700°C which was related to the formation of a thin and well-adhering Cr-base oxide scale (Fig. 11.1). In the atmosphere in which oxygen and water vapour were present simultaneously, a significant increase in the oxidation rate of 310N was observed at and above 650°C. The cross sections revealed that the enhanced oxidation in $Ar/O_2/CO_2/H_2O$ was due to local formation of Fe-rich oxide on the metal surfaces whereas in CO_2/H_2O and the other test gases exclusive formation of a protective Cr-base oxide scale was noticed (Fig. 11.2).

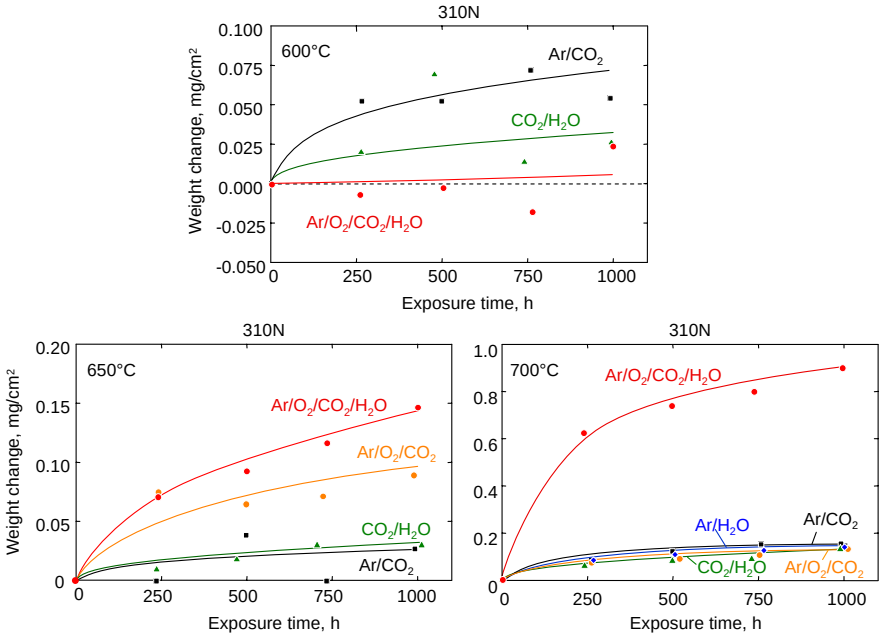

Figure 11.1: Weight changes of 310N during exposure to different atmospheres at temperatures between 600 and 700°C

Further analysis of the oxide scale morphology on 310N revealed that the locally enhanced oxidation mainly occurred on the surface between the alloy grain boundaries (Fig. 11.3). A similar finding was reported by Asteman *et al.* [115, 116] who studied alloy 310 in H_2O/O_2 at 600°C. The authors suggested that this preferential formation of hematite islands was mainly attributed to the poor supply of chromium from the bulk alloy inside the alloy grains.

Since the Cr diffusion rate along the grain boundaries is much faster than that in the crystal lattice, the oxide formed on the parts of the surface corresponding to the interior of the alloy grains tended to be more susceptible to breakdown of the initially present chromia scale. Asteman *et al*. draw this conclusion from the results obtained after short (168h) isothermal oxidation. In the longer term exposures in the present studies similar observations were made at 600 and 650°C. At 700°C, however, the degradation of the thin Cr-base scale was much more severe and no preferential formation of breakaway oxide on the metal grain surfaces was observed. The single and separated Fe-oxide islands formed at 600 and 650°C exhibited fast lateral growth at 700°C and had a strong tendency to merge, thus finally covered the metal surface independent of the grain and grain boundary areas of the specimen surface.

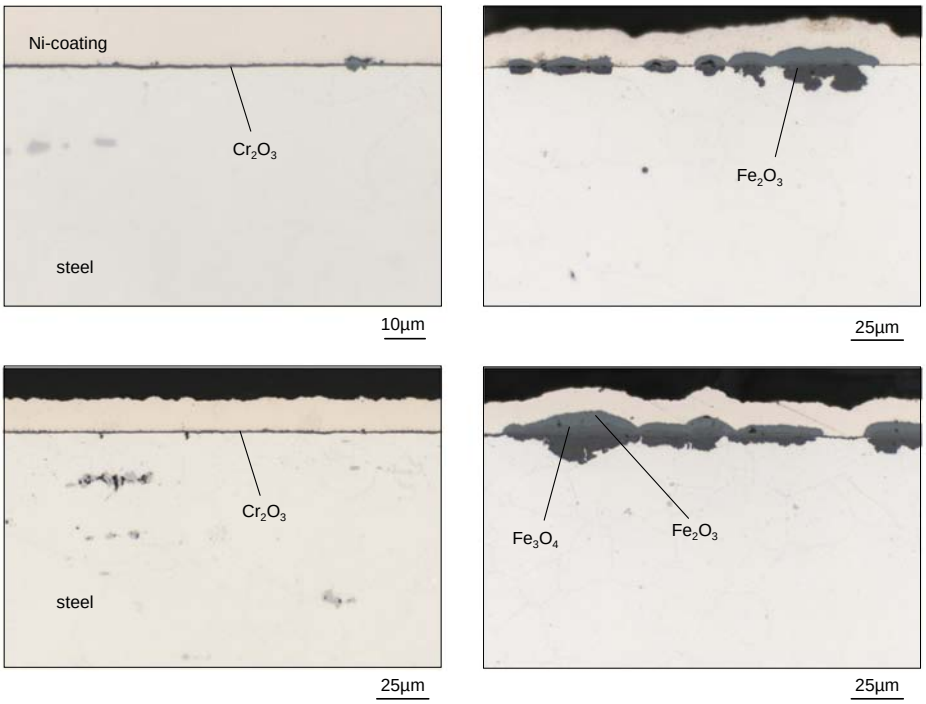

Figure 11.2: Metallographic cross sections of 310N after 1000h exposure to CO_2/H_2O (left) and to $Ar/O_2/CO_2/H_2O$ (right) at 650°C (upper pictures) and 700°C (lower pictures)

Using the typical electrolytic etching of specimen cross sections in NH_3 solution, carbide precipitates could be easily observed. When the parameters of the etching process were modified, i.e., if the electrolytic bath time was slightly prolonged, it turned out that this technique could also accurately reveal the formation of a chromium depleted zone near the

steel/oxide interface (Fig. 11.3). This zone was commonly observed to form at higher temperatures in the case of chromia formers because chromium as an alloying element was progressively consumed from the bulk steel due to its selective oxidation. The extent of depletion of an element being selectively oxidized depends on a number of factors such as initial concentration of the oxidized element, the scale growth rate and the alloy interdiffusion coefficient. If Cr is depleted beneath the concentration required to provide a sufficient Cr flux in the direction of the alloy/oxide interface in order to maintain the stability of the chromia layer, breakaway can subsequently occur [20].

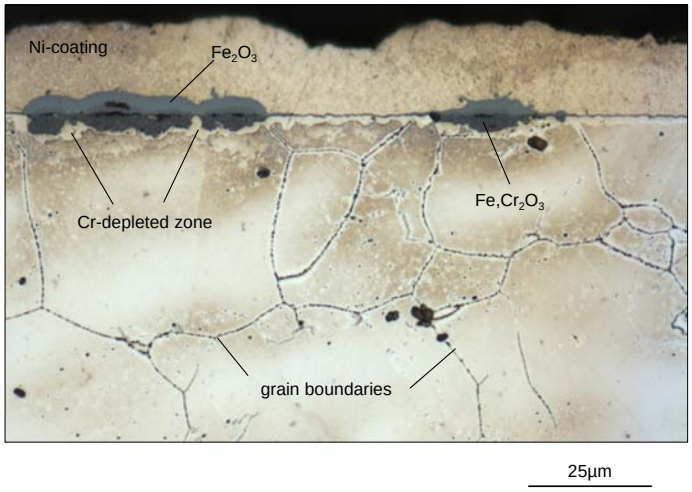

Figure 11.3: Metallographic cross section of 310N after 1000h exposure to Ar/O_2/CO_2/H_2O at 650°C (etched in ammonia solution)

During oxidation in the other four environments shown in Fig. 11.1, steel 310N formed a well protective thin layer of chromium oxide without any indication for the formation of Fe-rich oxide nodules. The growth of the thin chromia layer can, within the accuracy of measurement, be described by a near parabolic time dependence of the scale thickness.

Breakdown of an initially protective Cr-rich oxide layer discussed in the previous chapter was also found to occur for the martensitic and the low-Cr austenitic steels in gases containing H_2O and/or CO_2. In all these cases the addition of oxygen had either hardly any or a positive effect on sustaining the protective chromia base scale. In the examples shown in Fig. 10.20 for the high Cr steel 310N, however, oxygen addition to CO_2/H_2O had an adverse effect on the protective scale formation whereas it had no detectable effect when added to Ar/CO_2. These results, in combination with a number of recent publications, strongly indicate that the breakdown of the

protective Cr-rich oxide scale was related to the formation of volatile Cr-oxyhydroxide due to the reaction:

$$\tfrac{1}{2}Cr_2O_3^{(s)} + H_2O^{(g)} + \tfrac{3}{4}O_2^{(g)} = CrO_2(OH)_2^{(g)} \qquad \text{(Eq. 11.1)}$$

It is apparent from this equation that:

$$pCrO_2(OH)_2^{(g)} = K \cdot p(H_2O) \cdot p(O_2)^{3/4} \qquad \text{(Eq. 11.2)}$$

in which K is the equilibrium constant for reaction Eq. 11.1.

During oxidation of a steel such as 310N a protective Cr-rich $(Cr,Fe)_2O_3$ forms on the metal surface rather than pure Cr_2O_3. Therefore the above reaction may be more precisely expressed as [117]:

$$\tfrac{1}{2}(Fe_{1-x}Cr_x)_2O_3^{(s)} + xH_2O^{(g)} + \tfrac{3}{4}xO_2^{(g)} = xCrO_2(OH)_2^{(g)} + \tfrac{1}{2}(1-x)Fe_2O_3^{(s)} \qquad \text{(Eq. 11.3)}$$

From the diagram presented in Fig. 11.4 it is apparent that among various volatile Cr-rich species forming in oxygen containing wet atmospheres, the $CrO_2(OH)_2$ possesses the highest equilibrium partial pressure in the temperature range used in the present study and was the main volatile compound formed during oxidation of chromia formers in atmospheres rich in O_2 and H_2O. Additionally the diagram indicates that the equilibrium partial pressure of the $CrO_2(OH)_2$ shows a very weak temperature dependence, i.e., the partial pressure does not change drastically upon temperature change. At temperatures between 550°C and 700°C the values of the equilibrium partial pressure ranged only from approximately 1.5×10^{-8} to 1.0×10^{-7} bar.

Equation 11.2 reveals that the partial pressure of the Cr-oxyhydroxide is proportional to $p(O_2)^{3/4}$ and pH_2O. Comparing a typical flue gas in a coal-fired power plant using conventional combustion and that from the oxy-fuel process (Tab. 1.1), the tendency for the formation of volatile Cr-oxyhydroxide is much more pronounced in the latter atmosphere. Assuming a similar oxygen partial pressure in both service environments, the evaporation loss of Cr species is expected to be 3 to 4 times larger in the oxy-fuel environment than that in the conventional flue gas.

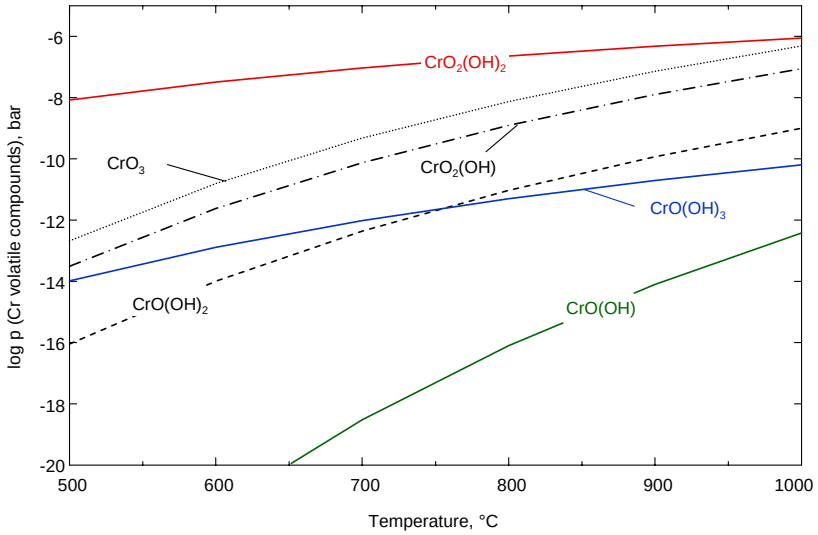

Figure 11.4: Equilibrium partial pressure of various volatile Cr species as a function of temperature. Calculated with FactSage software

As the partial pressure of the Cr-oxyhydroxide increases with increasing oxygen partial pressure, a constant evaporation rate of volatile compounds will occur from the oxide surface. The growth of oxide scale governed by solid state diffusion in combination with the formation of volatile species at the oxide/gas interface can be expressed by para-linear kinetics [118]:

$$\frac{dx}{dt} = \frac{k_p}{x} - k_l \qquad \text{(Eq. 11.4)}$$

where x is the oxide thickness, t the exposure time, k_p the parabolic rate constant in terms of oxide thickness and k_l the rate of volatilization.

Equation 11.4 shows that the oxide scale thickness after a given time is smaller than that in the case of absence of volatilization. The oxide initially thickens up to a given value after which a time independent oxide thickness prevails. In terms of weight change measurements, a weight increase is initially found which gradually changes into a weight loss during prolonged exposure. The time at which the change from weight gain to weight loss occurs, depends on the ratio k_p / k_l [119]. The kinetics given by Eq. 11.4 have clearly been found, e.g., during oxidation of pure Cr [29]. In the case of steel 310N the kinetics are different because the Cr loss by volatile species results in enhanced scale growth due to Fe-rich oxide formation.

A more detailed analysis of Fig. 11.4 leads to the conclusion that evaporation from chromia scales could also occur in dry gases with a high oxygen partial pressure. Formation of Cr(VI)oxide follows then according to the reaction:

$$Cr_2O_3^{(s)} + \tfrac{3}{2}O_2^{(g)} = 2CrO_3^{(g)} \qquad \text{(Eq. 11.5)}$$

The partial pressure of this specie is, however, in $Ar/O_2/CO_2/H_2O$ much smaller than that of $CrO_2(OH)_2$ (Fig. 11.4) and therefore is not considered in this investigation as the one responsible for degradation of chromia rich surfaces formed on steel 310N. Nevertheless, as shown in Chapter 6, austenitic steels containing less chromium tended to form non-protective Fe-base surface scale during oxidation in dry Ar/CO_2. It is thus reasonable to ask the question whether evaporation of initially formed protective Cr-rich scale in gases containing no H_2O can affect the observed breakaway at 650 and 700°C in this atmosphere.

When comparing the oxidation behaviour of low-Cr austenitic steels (e.g., 1.4910) in laboratory air and Ar/CO_2 it can be concluded that breakdown of the protective scale was observed only in the latter gas. The reaction from Eq. 11.5 is promoted in high oxygen pressure atmospheres because:

$$pCrO_3 = K^{3/4} \cdot p(O_2)^{3/4} \qquad \text{(Eq. 11.6)}$$

in which K is the equilibrium constant for reaction 11.5.

The oxygen partial pressure in laboratory air is much higher than that in Ar/CO_2 (or e.g., Ar/H_2O or CO_2/H_2O) which is approximately $2 \cdot 10^{-8}$ atm at 700°C. The formation of gaseous CrO_3 in laboratory air apparently did not occur or was at least not sufficiently large to trigger breakaway of the protective oxide scale. It is therefore obvious that in an environment with very low pO_2 like Ar/CO_2 or Ar/H_2O this volatile species cannot be considered as a main reason for the observed chromia scale breakdown at elevated temperatures.

11.2 Martensitic 9-12% Cr steels

Figures 11.5-6 provides an example showing that in an atmosphere containing both oxygen and water vapour enhanced formation of less protective iron-base oxide scale on 12% Cr ferritic steel may occur compared to an atmosphere in which only water vapour is present. The steel VM12 showed the formation of a thin and protective oxide scale after 250h of isothermal exposure to Ar/H_2O with only small fractions of Fe-base oxide nodules growing on the surface.

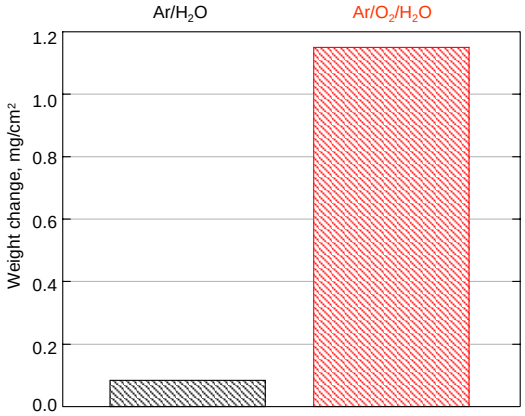

Figure 11.5: Weight changes of VM12 after 250h isothermal exposure at 550°C to Ar/H_2O and $Ar/O_2/H_2O$

The same alloy exposed to the gas in which intentionally 3% oxygen was added showed a much faster degradation of the protective Cr-base scale. This can be observed in the cross sections in Fig. 11.6 where additionally macroscopic pictures of the oxidized specimens are presented. The gravimetric results from Fig. 11.5 confirm the metallographic observations that a substantially higher oxidation rate occurred in the case of the $Ar/O_2/H_2O$ atmosphere than in Ar/H_2O.

It is a well known fact that water vapour can trigger breakaway of 9-12% Cr steels [38, 42]. This was already discussed in Chapter 5 where ferritic/martensitic alloys exposed to Ar/H_2O showed, unlike under air exposure, the formation of a non-protective oxide scale at all test temperatures. Based on the results from Fig. 11.5-6 the degradation process of the initially formed Cr-rich scale seemed here to be accelerated when additional oxygen was introduced to the Ar/H_2O. The results presented in this section suggest that formation of volatile Cr-compounds (mainly $CrO_2(OH)_2$) may be in some cases (low temperature and short exposure times) relevant when discussing the possible mechanisms of the deterioration of oxidation resistance of martensitic steels in H_2O- and O_2-containing atmospheres.

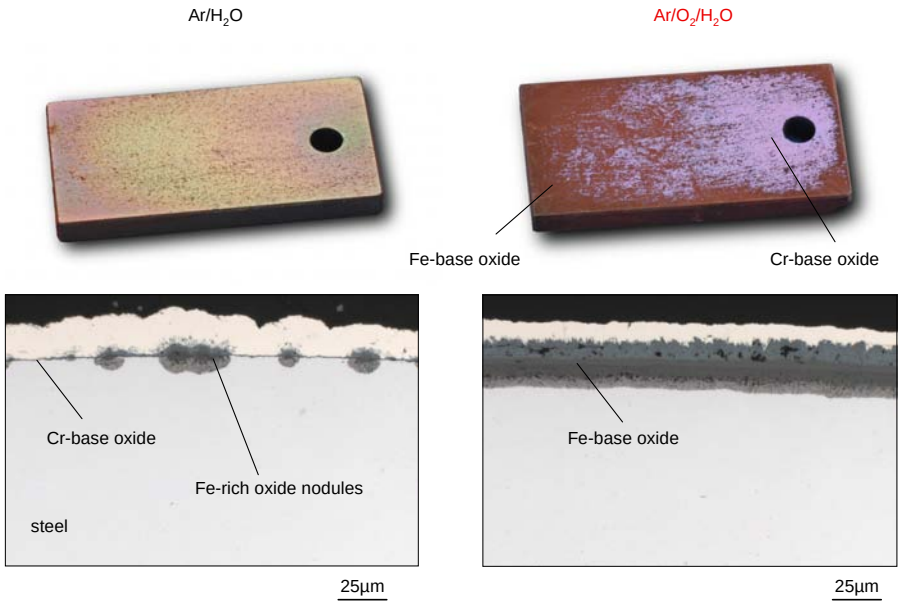

Figure 11.6: Macroscopic specimen images and corresponding cross sections of VM12 after 250h isothermal exposure at 550°C to Ar/H_2O (left) and Ar/O_2/H_2O (right)

11.3 Ni-base alloys

The gravimetric results obtained during oxidation of INCONEL 617 to the various test gases are presented in Fig. 11.7. In all gases, except for Ar/O_2/CO_2/H_2O, very small weight gains occurred and no significant differences between the scale formation in the various atmospheres were found. However, in the Ar/O_2/CO_2/H_2O test atmosphere the material showed a clear weight loss.

Different from austenitic 310N, INCONEL 617 during the exposure to the Ar/O_2/CO_2/H_2O atmosphere up to the maximum time of 1000h did not lead to a change from chromia formation into, e.g., Ni-rich oxide scale growth. The scales formed in this gas still consisted of virtually pure chromia although the scale was thinner than that formed in CO_2/H_2O (Fig. 11.8). This effect, which was measured at 700°C as well as at 650°C (Fig. 11.9), is clearly correlated to the formation of volatile Cr-oxyhydroxide (Eq. 11.1).

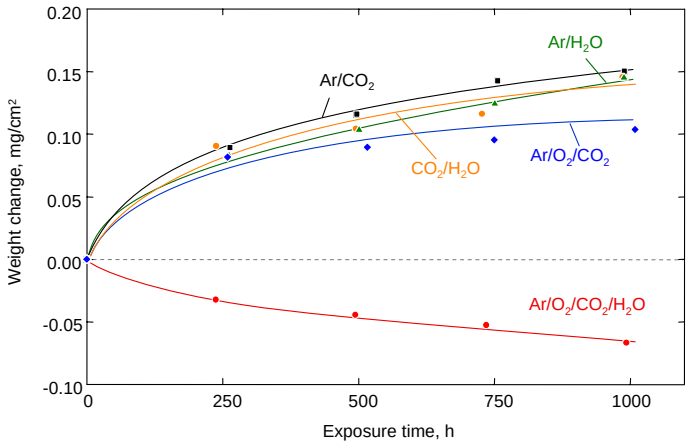

Figure 11.7: Weight changes of INCONEL 617 during 1000h exposure to different atmospheres at 700°C

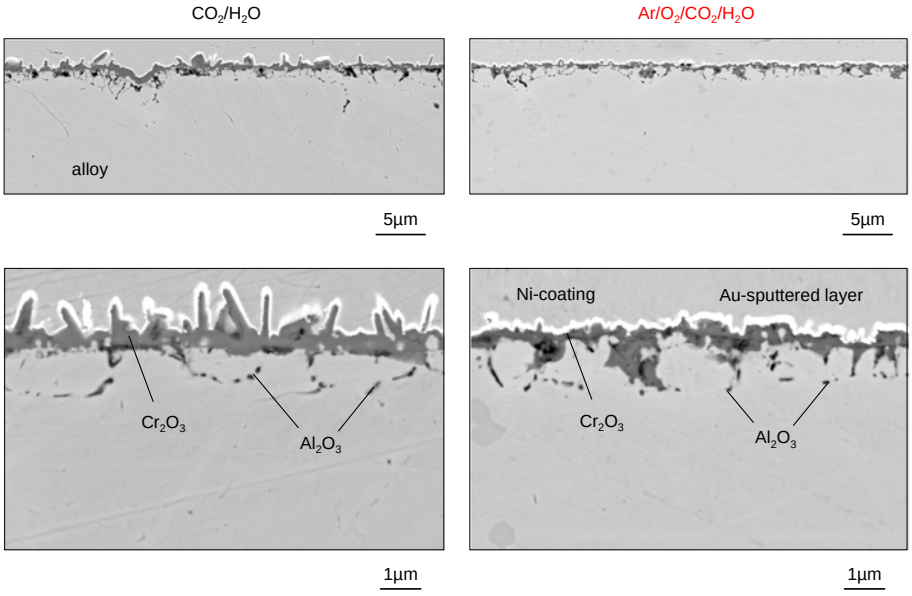

Figure 11.8: SEM images of the cross sections of the oxide scales formed on INCONEL 617 after 1000h exposure to CO_2/H_2O (left) and $Ar/O_2/CO_2/H_2O$ (right) at 700°C (lower figures show higher magnification of the upper figures)

A number of papers are available in which attempts were made to calculate the amount of chromium loss by volatile oxyhydroxide formation [43, 120, 121]. A major problem in these evaluations is the relatively large scatter in vapour pressure data for the Cr-oxyhydroxide [122, 123]. Based on the weight change measurements from Fig. 11.9 the evaporation rate in the

$Ar/O_2/CO_2/H_2O$ atmosphere was roughly 10^{-4} mg·cm^{-2}·h^{-1} at 700°C. This is of the same order of magnitude as the data obtained by Trebbels [124] who measured the Cr evaporation by transpiration experiments for Crofer 22 APU at 800-900°C in humidified air.

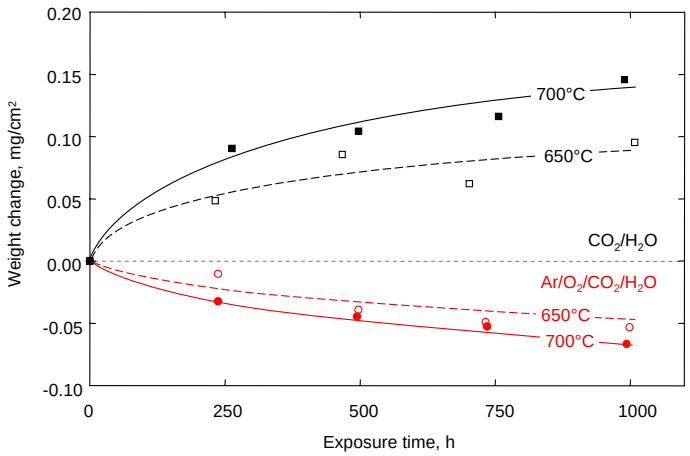

Figure 11.9: Weight changes of INCONEL 617 during 1000h exposure to CO_2/H_2O (black) and $Ar/O_2/CO_2/H_2O$ (red) at 650°C and 700°C

An interesting question to be answered is, whether the chromium loss by volatilization will in fact obey a linear time dependence even in the case of very long operation times prevailing in practical applications. The discussion described above assumes equilibrium between the chromia scale and the oxygen/water vapour containing gas mixture. As long as the gas is in direct contact with pure chromia, a linear time dependence of chromium loss by volatile oxyhydroxide formation is expected. However, if the enhanced Cr loss by the formation of volatile species results in the formation of an outer iron rich oxide (like for the austenitic steel 310N), the atmosphere will no longer be in direct contact with the chromia scale. Therefore, a reduced rate of formation of volatile chromium species with increasing exposure time is expected [119].

The evaporation from chromia surface scales was during the present investigation not only found for 310N and INCONEL 617 but also for binary Ni-Cr model alloys (Fig. 7.4). The effect was already found after quite short exposure times. The results obtained after isothermal exposure at 550°C in Ar/H_2O and $Ar/O_2/H_2O$ clearly show that a Ni-25Cr binary model alloy exhibited a weight loss when exposed to the latter gas, whereas a weight gain was observed in Ar/H_2O (Fig. 11.10).

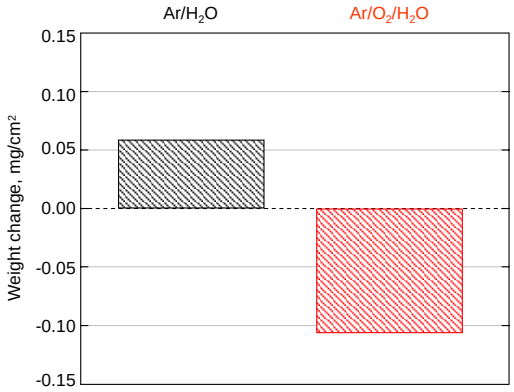

Figure 11.10: Weight changes of binary Ni-25Cr model alloy after 250h isothermal exposure at 550°C to Ar/H_2O and $Ar/O_2/H_2O$

11.4 General conclusions

Comparing the results obtained after oxidation of different materials in H_2O- and/or O_2-containing gases the simple question might be asked whether oxygen in oxidizing environments containing water vapour has a beneficial or a detrimental effect. As shown in Fig. 10.14, 3% oxygen in CO_2/H_2O could substantially decrease the oxidation rate at lower temperatures in the case of VM12. Other results clearly indicate that oxygen had a negative effect on the oxidation resistance, e.g., for austenitic steels (Fig. 10.17-18). It is well known that O_2 promotes the formation of protective scales and also can suppress to some extent the adsorption of H_2O molecules on the metal surface, thus reduce the hydrogen dissolution in the metal matrix. On the other hand the formation of volatile Cr-compounds in presence of H_2O and O_2 could significantly hamper the formation of protective Cr-base oxide scales.

An observation of great importance was made by Ehlers *et al*. [111] that in such situations the ratio between oxygen and water vapour was crucial. The authors oxidized P91 steel at 650°C in several atmospheres with different H_2O and O_2 content. The general conclusion was that the ratio between water vapour and oxygen was the crucial factor for occurrence of breakaway oxidation. They provided a simple equation for a critical condition for breakaway:

$$\frac{pH_2O}{pO_2} \geq 1 \qquad \text{(Eq. 11.7)}$$

from which it appears that in atmospheres where a higher pO_2 prevails over pH_2O the formation of a protective oxide scale can be obtained. In this study, however, this ratio was much larger than unity, therefore protective chromia scale formation was generally not observed in $Ar/O_2/CO_2/H_2O$ or CO_2/H_2O.

Additionally, it was shown that in water vapour containing gases extra oxygen might be detrimental because of the formation of volatile Cr species since this might lead to the formation of non-protective oxide. Anyway, based on the data obtained by Ehlers *et al*. [111] it is assumed that the formation of protective scale could be attained in atmospheres with much higher pO_2 compared to pH_2O. In that case, the protective behaviour is not affected by the absolute value of pO_2 and pH_2O. This is contrary for the conditions of the formation of volatile Cr-species which is affected by the absolute value of pO_2 and pH_2O (Eq. 11.2). Formation of volatile species did not play a substantial role in the studies of Ehlers *et al*. because they used low pO_2 and pH_2O gases. This is schematically presented in Fig. 11.11.

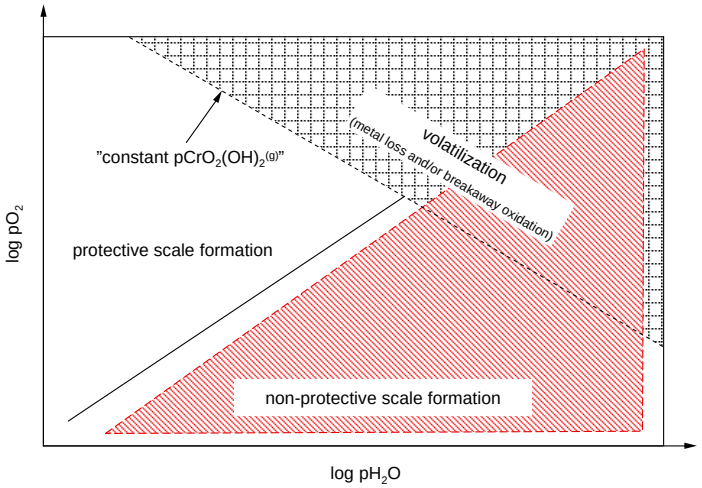

Figure 11.11: Schematic chart showing different types of oxidation behaviour for Fe-Cr alloys exposed to H_2O/O_2-containing atmospheres

12. Protective and non-protective scale formation of martensitic steels

12.1 Suppression of the protective scale in CO_2- and/or H_2O-rich atmospheres

Apart from 13CrMo4-4, all materials studied in the present investigation contain substantial amount of Cr, i.e., 9-12wt.% for the martensitic steels, 18-25wt.% for the austenites and 22wt.% for the Ni-base INCONEL 617. The high Cr content offers the possibility to form a protective Cr-rich surface oxide scale during high temperature exposure. During air exposure chromia base scale was generally formed, even in the case of the martensitic steels with the relatively low Cr content of 9-12% (Chapter 5).

It is well-known that the formation of the protective oxide scale is strongly affected by the service environment to which the metallic material is exposed. In the current investigation it was already presented that in CO_2- and/or H_2O-rich gases the martensitic steels tended to exhibit an initial stage of oxidation in which a thin Cr-rich oxide scale was formed. After longer exposure time breakaway of this protective layer lead to the formation of rapidly growing, less protective Fe-base oxide scales. A qualitatively similar behaviour, although less pronounced, was also found for the low-Cr austenites. In this chapter, the possible reasons for the transformation from protective into non-protective behaviour during exposure to CO_2- and/or H_2O-rich gases will be explored.

Several mechanisms have been proposed to explain the suppression of the formation of protective Cr-rich surface scales in H_2O-rich gases, such as dissociation processes due to H_2/H_2O bridges in voids at the scale/alloy interface and/or within the scale [39], incorporation of hydrogen in the scale in the form of H^+ and/or OH^- [125], formation of volatile Fe-hydroxides [126] or volatile Cr-oxyhydroxides [120, 127], enhanced surface reaction kinetics, preferential adsorption at inner scale surfaces [111] and enhanced growth stresses leading to scale cracking [128]. These mechanisms are not applicable for explaining all results obtained under the current experimental conditions. For instance, mechanisms involving the evaporation of chromium rich species are only significant for atmospheres with a high equilibrium oxygen partial pressure [129]. Therefore, they are applied to explain only the oxidation behaviour when $Ar/O_2/H_2O$ or $Ar/O_2/CO_2/H_2O$ is used. In the present study, when Ar/CO_2, Ar/H_2O or CO_2/H_2O was used, it was thus not considered as the mechanism involving the evaporation of Cr-rich species.

Based on the morphologies and compositions of the scales formed in the low pO_2 gases Ar/CO_2 and Ar/H_2O it is not unreasonable to assume that the mechanism responsible for the suppression of the protective chromia scale formation in those atmospheres might be similar. In both gas types the martensitic steels tended to form, during exposure at 550°C, an internal oxidation zone beneath a two-phase layer consisting of magnetite and Fe,Cr spinel. Above the original metal surface a magnetite layer was present and in the outer scale hematite could be seen. Although the scales formed in Ar/CO_2 and Ar/H_2O consisted of the same types of oxides, the scales differed with respect to morphology (buckling in H_2O-rich gases) and relative amounts of the various oxide phases (Chapter 5).

When looking for a mechanism for the suppression of protective chromia-base scale formation, e.g., on the martensitic steel in both gas types it seems that from the mechanisms proposed above to explain the enhanced oxidation in water vapour rich gases, only one is able to simultaneously explain the results observed in Ar/CO_2 as well as in Ar/H_2O. This is the mechanism proposed by Rahmel and Tobolski [39], in which it is assumed that voids formed at the scale/metal interface and within the scale due to vacancy condensation are “bridged” by mixtures of H_2-H_2O or CO-CO_2. During exposure to dry gas or air the oxygen partial pressure in a void near the metal/scale interface will be extremely low, i.e., near the dissociation pressure of the Cr-rich oxide. Using the Langmuir equation [130] it can be shown that the rate of oxygen transfer to the inner surface of the void is extremely small and thus sufficient time is available for Cr to diffuse from the bulk steel towards the void/steel interface. In this way void healing occurs due to reformation of a Cr-rich oxide. However, in Ar/CO_2 and Ar/H_2O, oxygen transfer in the void is orders of magnitude higher than that in dry gas because it occurs via H_2O- and/or CO_2-molecules. As a result, rapidly growing Fe-rich oxides can form and void healing by formation of a Cr-rich scale is suppressed in these types of gases.

Additionally, there are two mechanisms associated with internal precipitation of Cr-compounds which can impede the development of continuous external scales in H_2O- and CO_2-rich gases. Essuman *et al*. [113, 131] proposed a mechanism which may explain the suppression of protective chromium rich oxide formation on steels in water vapour rich environments. The authors found that Fe-Cr alloys with intermediate chromium contents of 10% to 20% (in wt.%) formed Fe-rich oxide scales in Ar/H_2O at 900 and 1050°C. It was proposed that hydrogen dissolved in the alloy which then promoted the internal oxidation of the protective scale forming

element chromium. This effect was explained considering the H-O-H_2O equilibrium at the metal surface, such that when the hydrogen concentration was reduced by rapid inward diffusion, an increased concentration of dissolved oxygen would be established, i.e., a higher inward flux of oxygen which would be responsible for the larger tendency for chromium to become oxidized internally. The scale forming element chromium was thus tied-up in the internal oxide precipitates and the chromium flux toward the surface was reduced. The formation of Fe-rich surface oxide scales was then just the result of the oxidation of the Cr-depleted steel matrix. The experimental data obtained in the present study revealed indications for the mechanism proposed by Essuman *et al.* In Fig. 12.1 the cross sections of P92 clearly show the width of the internal oxidation zone being wider in the CO_2/H_2O atmosphere than in Ar/CO_2. This could be explained by the enhanced oxygen solubility/diffusion in the alloy due to hydrogen uptake.

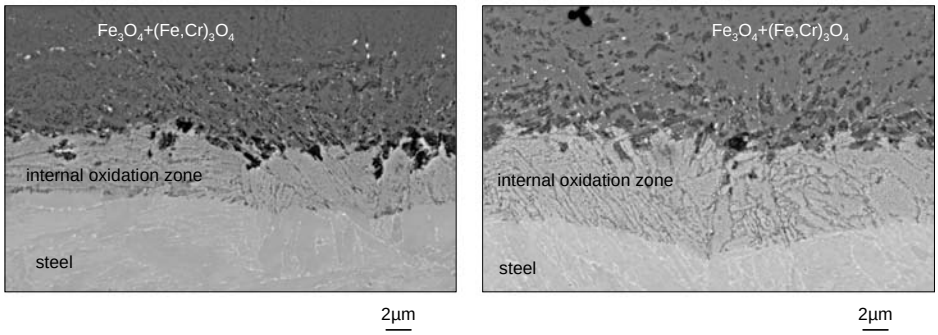

Figure 12.1: SEM images of the cross sections showing internal oxidation zone formed in P92 during 1000h exposure to Ar/CO_2 (left) and CO_2/H_2O (right) at 550°C

A second mechanism which also impeded the formation of a protective external Cr-rich oxide scale by reducing the flux of chromium toward the surface is active in the Ar/CO_2 atmosphere, as proposed in [47, 48]. The results in the present study showed that carburization of the martensitic steel occurred in the CO_2-containing gases under all studied conditions. Carbide formation would decrease the chromium activity in the steel matrix and thus decrease the driving force for chromium diffusion toward the surface. This would have the consequence that protective chromia scale formation is hampered resulting in growth of Fe-rich oxide scales as it was actually seen after exposure in Ar/CO_2. The internal carbides are eventually converted to internal oxides as the local oxygen potential increases, after longer exposure times.

From classical oxidation theory it is known that the first criterion which must be fulfilled to form an external Cr_2O_3 scale is [20]:

$$N_{Cr} > \left[\frac{\pi g^*}{3} N_O^{(s)} \frac{D_O V_m}{\tilde{D}_{Fe-Cr} V_{Cr_2O_3}} \right]^{\frac{1}{2}} \qquad \text{(Eq. 12.1)}$$

where $N_O^{(s)}$ is the oxygen solubility in the alloy, D_O the diffusivity of oxygen in the alloy, $\tilde{D}_{Fe-Cr}$ the alloy inter-diffusion coefficient and V_m and $V_{Cr_2O_3}$ are the molar volumes of the alloy and oxide, respectively. The factor g^* is generally approximated as about 0.3 [132]. Based on the considerations in the previous paragraph, incorporation of hydrogen and carbon into the steel has qualitatively a very similar effect on the overall oxidation process, namely increasing the value of N_{Cr} in Eq. 12.1, i.e., the critical mole fraction of Cr for obtaining external scale formation. The underlying mechanisms are, however, different. The dissolution of hydrogen affects $N_O^{(s)}$ and D_O in Eq. 12.1, thus increasing the flux of oxygen into the steel with the result that internal oxidation is promoted [131]. The formation of carbides affects the transport of chromium from the bulk steel towards the surface. This has qualitatively the same effect as a decrease in $\tilde{D}_{Fe-Cr}$ in Eq. 12.1. The incorporation of chromium into the inner part of the scale occurs, to a large extent, by oxidation of the carbides. The dissimilarity in the underlying mechanisms for the formation of the Fe-rich oxide scales in Ar/H_2O and Ar/CO_2 is the reason for the observed differences in the width of the internal oxidation zone found after exposure to the various test gases (Fig. 12.1).

The interaction between CO_2 and H_2O molecules in the atmosphere and subsequently their effect on the oxidation process is hard to determine since the oxidation rates and oxide scales produced during exposure to Ar/H_2O, Ar/CO_2 and CO_2/H_2O show large similarities. Hydrogen and carbon dissolution in the steel, as a result of the reaction with H_2O or CO_2, respectively, have completely different effects regarding the compound formation in the steel. Nevertheless, the result in respect to their effect on protective scale formation is similar, i.e., delayed transport of chromium towards the surface.

Considering the mentioned scale formation mechanisms, the molecular transport of H_2O and CO_2 through the oxide scale is a major requirement for the formation of the barely protective Fe-

rich oxide scales. Based on the results from this study there is some evidence that H_2O plays a more detrimental role for the suppression of protective chromia formation on ferritic/martensitic steels than CO_2. The results presented in Fig. 12.2 show thermogravimetric curves obtained during exposure to Ar/(2%)H_2O and Ar/(2%)CO_2. Initially both specimens followed the parabolic rate law, however, after around 10 hours of oxidation the kinetics changed into near-linear and the specimen exposed to the water vapour gas exhibited a much faster weight gain than that in Ar/CO_2.

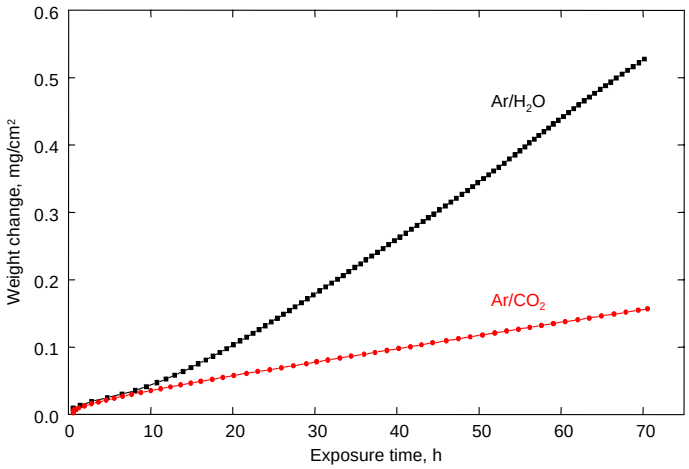

Figure 12.2: Thermogravimetric curves of P92 during isothermal oxidation in Ar/(2%)CO_2 and Ar/(2%)H_2O at 550°C

12.2 Competition of reactions

When exposed at temperatures around 550°C to air or Ar/O_2 the martensitic 9-12% Cr steels tended to form very thin chromia base oxide scales (section 5.2). This is not the case when they were exposed to Ar/CO_2 or Ar/H_2O where more rapidly growing Fe-base oxide scales were formed (section 5.3-4).

The question then arises: which type of oxide scales were formed in Ar/O_2/CO_2 and Ar/O_2/H_2O. The results in section 10.2 revealed that the addition of only a minor amount of oxygen to Ar/CO_2 tended to suppress the Fe-base oxide formation. This was not the case when a similar amount of oxygen was added to Ar/H_2O where much faster deterioration of the protective oxide scale was observed (section 11.2). Whether the negative effect of CO_2 and H_2O on protective scale formation would be suppressed by a certain oxygen addition will be governed

by the rates of reaction of oxygen molecules on external and especially internal surfaces. Especially for the transfer of carbon (in the case of CO_2 exposure) or hydrogen (in the case of H_2O exposure) into the metal, the selective reaction rates of the gas molecules at the metal surface would be relevant. This, however, is extremely difficult to estimate experimentally as exposure to CO_2 and/or H_2O would immediately lead to the formation of a surface scale. The growth of the typical Fe-base oxide scales as shown in the previous chapters would be initially controlled by the kinetics of the surface reaction. Additionally, a contribution of molecular transport is shown to prevail. In the case of a dense, very slowly growing chromia scale, e.g., formed on the nickel base INCONEL 617 (Chapter 7), the scale growth rate will be governed by diffusion in the scale. In this case the scale thickness up to the value at which surface reactions are rate controlling is much thinner than in the case of the rapidly growing Fe-base oxides. For getting more insight in the relative rates of reaction in the case of surface reaction controlled kinetics, a number of tracer studies were carried out using the low alloy steel 13CrMo4-4 because it obviously formed virtually only Fe-oxides.

Figure 12.3 shows that the oxygen transfer via H_2O molecules is more pronounced than that for CO_2. This is in total agreement with the data obtained by Zheng and Young [96]. The authors showed that in terms of competitive adsorption of the various gas species on oxide surfaces and grain boundaries preferential adsorption of H_2O became favoured rather than CO_2. The important consequence of this finding might be that carburization rates were smaller in the case of the CO_2-rich atmospheres with H_2O addition. This will be more extensively discussed in Chapter 15.

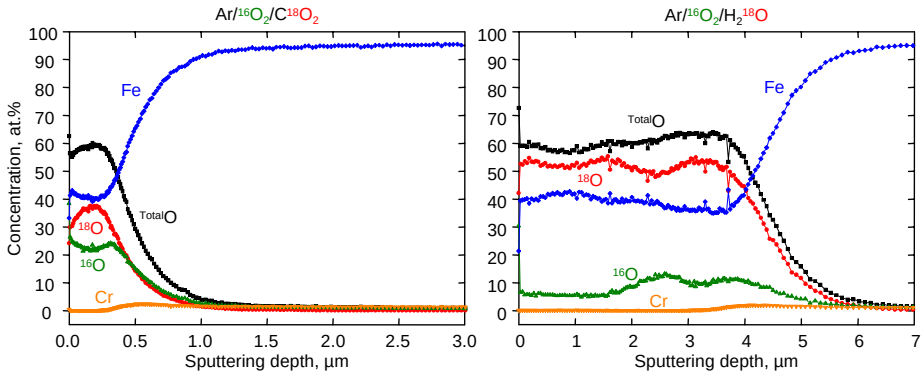

Figure 12.3: SNMS concentration profiles of 13CrMo4-4 after 2h exposure to Ar/(1%)$^{16}O_2$/(1%)$C^{18}O_2$ (left) and Ar/(1%)$^{16}O_2$/(2%)$H_2{}^{18}O$ (right) at 550°C

The results presented above (Fig. 12.3) also indicate that oxygen derived from H_2O and CO_2 was, at the given exposure time, the major component of the oxide formed on the metal surface. The same effect was also observed for P92 (Fig. 12.4) whereas the differences in ^{18}O and ^{16}O concentrations were less pronounced for the Ni-base alloy (Fig. 12.5). Those findings partially answer the question about kinetics reactions during exposure to $Ar/O_2/CO_2/H_2O$. Since the oxidation rate, scale composition and morphology in this gas mixture is very similar to that found in CO_2/H_2O it can be concluded that increased oxygen partial pressure did not change significantly the overall surface reactions as long as kinetics of surface reactions were rate determining.

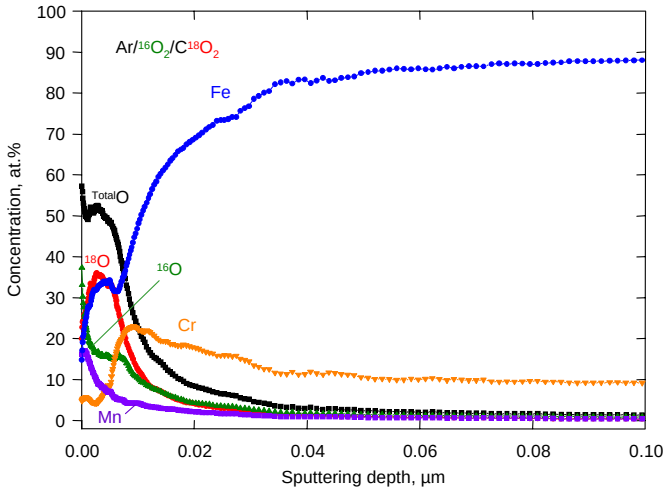

Figure 12.4: SNMS concentration profile of P92 after 7h exposure to Ar/(1%)$^{16}O_2$/(1%)C$^{18}O_2$ at 650°C

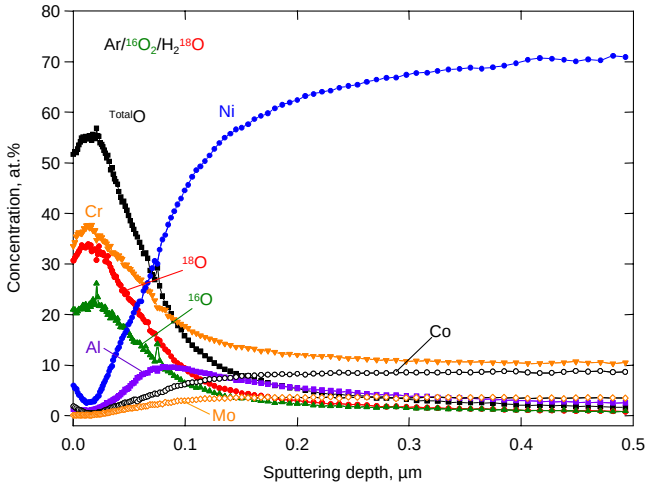

Figure 12.5: SNMS profile of INCONEL 617 after 7h exposure to Ar/(1%)$^{16}O_2$/(2%)$H_2{}^{18}O$ at 900°C

13. Effect of minor alloying elements

13.1 General remarks

The oxidation behaviour of the materials discussed in this study was mainly governed by the steel Cr content. However, it is well-known that for commercial alloys, minor alloying elements may significantly affect the oxidation behaviour in various oxidizing atmospheres [109, 133, 134]. The presence of common alloying elements may be due to manufacturing reasons or intentional addition to adjust the alloy mechanical properties [19, 135].

The necessity for further investigation of minor alloying elements on the oxidation behaviour arose in this study when two batches of the same alloy exhibited large differences in oxidation resistance during exposure to the same conditions. This difference between the batches was observed independent of the used atmospheres or temperatures (Fig. 13.1). Interestingly, the chemical analysis indicated that the Cr content was slightly higher for the batch which exhibited lower oxidation resistance.

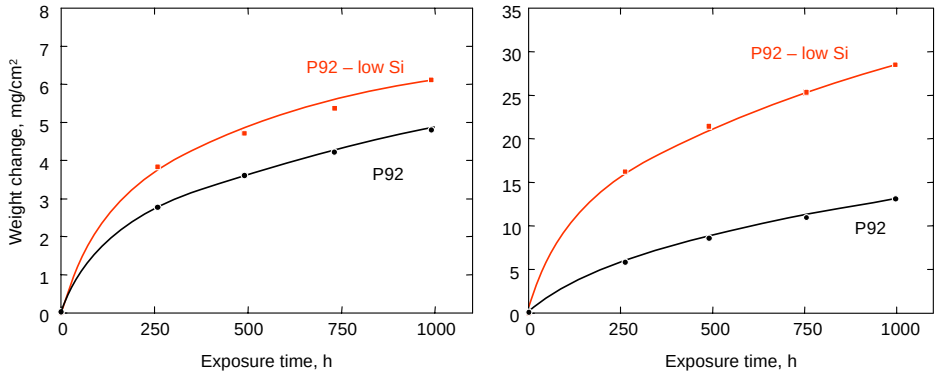

Figure 13.1: Weight changes of P92 with different Si content during 1000h exposure to CO_2/H_2O at 550°C (left) and to Ar/CO_2 at 650°C (right)

Metallographic observations showed a similar microstructure of the two batches in the as-received condition (Fig. 13.2). A more detailed investigation revealed, however, a much finer structure of the martensite laths in the case of the batch showing the higher oxidation rates (Fig. 13.3). For this grade of steel a finer microstructure is usually claimed to provide better oxidation resistance than coarse grained materials.

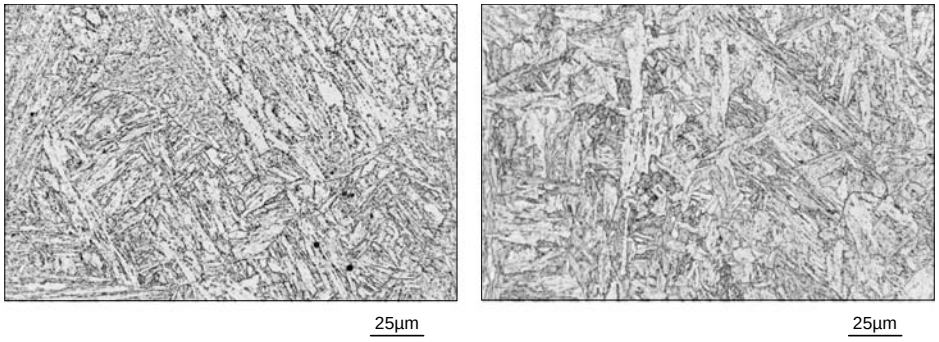

Figure 13.2: As-received microstructures of P92 (left) and P92-low Si (right). Etching agent: H_2O/Cr(VI)-oxide/NaOH

The experimental findings mentioned above pointed to the idea that variations in concentrations of minor alloying elements might explain the observed differences in oxidation behaviour of the two steel batches.

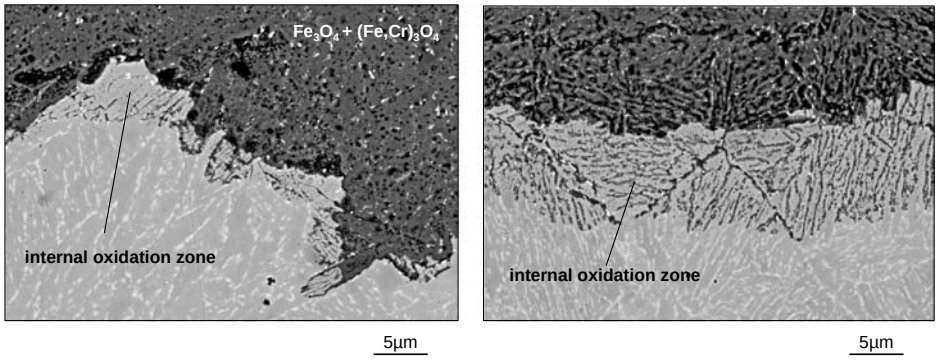

Figure 13.3: Microstructural details of martensite laths and internal oxidation zones formed on P92 (left) and P92-low Si (right) after 1000h exposure in Ar/CO_2 at 650°C

The main differences in the composition of the investigated P92 batches are given in Tab. 13.1. It can be seen that the concentrations of Si, Al and Ni vary from one batch to the other. These three elements were therefore selected for further detailed investigation.

	Cr	Ni	Mo	C	Al	Si	Mn	Fe
P92	8.90	0.23	0.38	0.093	0.028	0.30	0.43	Bal.
P92-low Si	8.96	0.06	0.47	0.106	0.007	0.04	0.45	Bal.

Table 13.1: Concentrations of main scale forming elements (wt.%) of the two investigated batches of steel P92 (full chemical composition is given in Tab. 19.1)

13.2 Effect of silicon

The most likely explanation for the different scaling rates of the two P92 batches was the difference in silicon content. Several researchers investigated the influence of this element on the oxidation behaviour of a number of conventional alloys during high temperature exposure. Improved oxidation resistance by Si was frequently attributed to the formation of a silica sub-layer beneath the chromia scale [31, 136].

However, a beneficial effect of Si was also found when it was added in steels with low Cr content such as 1.5wt.% Cr-Mo steels [25]. For different types of Fe-Cr alloys a beneficial effect of silicon was found during exposure to various environments, for instance water vapour [137], carbon dioxide [138] and other atmospheres [139-141]. Higher Si addition (up to 4wt.%) to binary Fe-Cr alloys resulted in formation of an iron-silicate layer during exposure at temperatures between 750-1050°C [142]. However, a high Si content adversely affects material toughness [75] and therefore the Si content in advanced 9-12% Cr martensitic steels usually does not exceed 0.5wt.%.

From the cross sections in Fig. 13.4 it is apparent that the scale on the low-Si batch after exposure to Ar/CO_2 was thicker than that on the standard P92. The oxide surface was apparently not in equilibrium with the atmosphere because the outer oxide layer consisted exclusively of Fe_3O_4. This was caused by the rapid transport of iron cations towards the oxide surface. For the P92 specimen with normal Si content the formation of Fe_2O_3 was clearly distinguished on the top of the scale although not in the form of a continuous layer. The appearance of the hematite phase seemed to be correlated with the presence of voids which slowed down the in-scale mass transport.

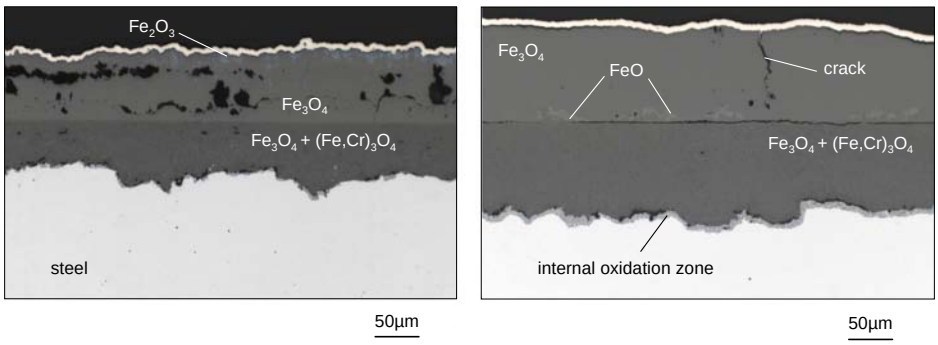

Figure 13.4: Metallographic cross sections of P92 (left) and P92-low Si (right) after 1000h exposure to Ar/CO_2 at 650°C

The EDX element mappings presented in Figs. 13.5-6 indicate a quite different morphology of the inner oxide layers formed beneath the initial metal surface of the two steel batches. The chromium distribution in the inner oxide was homogenous for the specimen with lower Si content whereas a substantial enrichment of this element was observed in the case of the steel with normal Si level. At and above 650°C a more pronounced formation of Cr-rich bands within the inner oxide layer was observed for all 9-12% Cr alloys independent of the used test atmosphere, but not for P92-low Si.

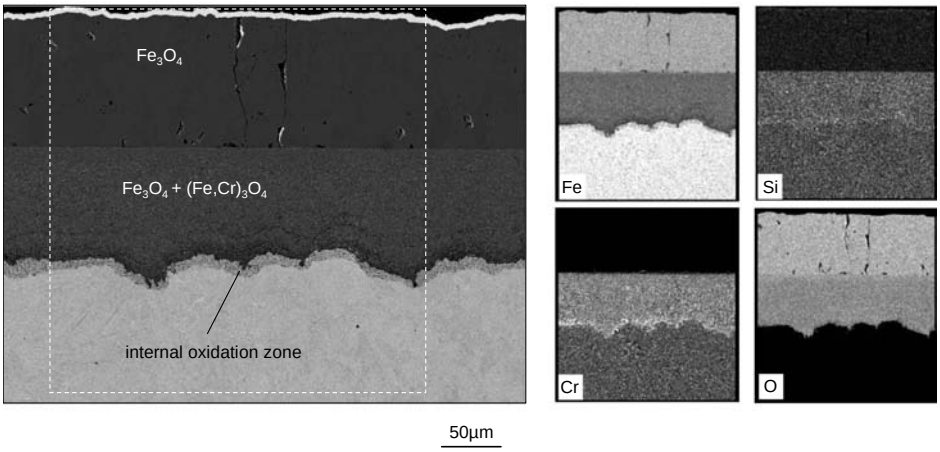

Figure 13.5: SEM image of the cross section of P92-low Si after 1000h oxidation in Ar/CO_2 at 650°C and corresponding X-ray element mappings from the marked area

It is important to note that for the other martensitic steels selected in this study the silicon content was typically one order of magnitude higher than that in the investigated P92 batch marked as "low Si". This supported the idea that silicon in fact was the element responsible for the differences in oxidation rates between the two P92 batches. For P92 silicon enrichment was found by EDX elements distribution in the inner scale. However, this was far less pronounced than that for chromium since silicon was present in the bulk alloy in a concentration of only 0.3wt.%. The Si distribution presented in Fig. 13.6 reveals that some Si-rich precipitates were present as distinct particles in the inner oxide which was not the case for the low silicon P92 batch (Fig. 13.5).

Another interesting finding was that a wide internal oxidation zone was found to be present near the metal/oxide interface for the low Si batch of P92 after exposure at 650°C to Ar/CO_2 (Figs. 13.4-5). For martensitic 9-12% Cr steels the internal oxidation zone, if present, consisted mainly of Cr_2O_3 particles embedded in the metal matrix. Generally, for 9-12% Cr steels the

internal oxidation zone was formed at lower temperatures (~550°C) but had a strong tendency to vanish at and above 650°C (Chapter 9). This was related to the enhanced Cr mobility at higher temperatures, during which the formation of Cr-rich bands in the inner oxide scale was promoted. The structure of the inner oxide layer typically exhibited Cr-rich oxide bands embedded in $(Fe,Cr)_3O_4$ (Fig. 13.6). As a consequence, some of the alloys, including the standard P92, showed decreased oxidation rates if the temperature was raised above ~650°C. This behaviour was discussed in Chapter 9.

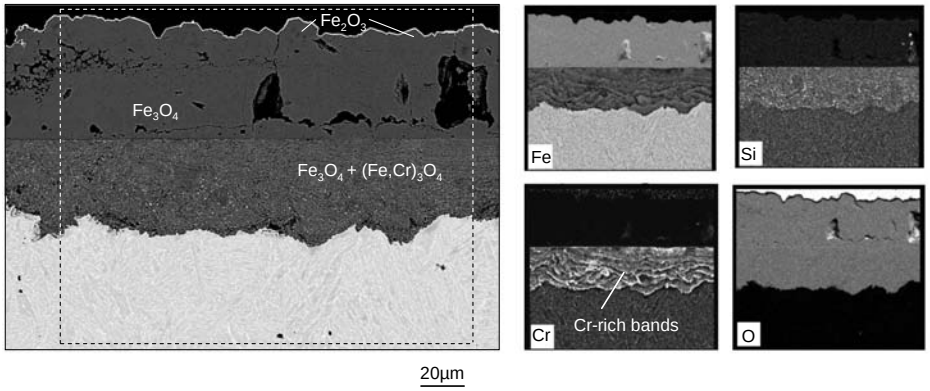

Figure 13.6: SEM image of the cross section of P92 after 1000h oxidation in Ar/CO_2 at 650°C and corresponding X-ray element mappings from the marked area

After 1000h exposure to $Ar/O_2/CO_2/H_2O$ formation of an internal oxidation zone in the low-Si P92 batch was observed even at 700°C. The gravimetric data obtained during exposure to this atmosphere showed almost twice the mass gain for the lower Si content steel as for the steel with the normal Si level. At 600°C the difference in oxidation rate between the two batches was much smaller but still significant (Fig. 13.7).

Ishitsuka *et al*. [143] carried out steam exposures of several martensitic steels with various Si contents. The chemical compositions of the steels selected by the authors were very similar to those of the P92 batches described in this section. They studied the effect of Si on the steam oxidation behaviour at temperatures between 500 and 700°C. The results obtained by Ishitsuka *et al*. are compared with those from the present study in Fig. 13.8. Very similar results were found in both studies at 550°C. At 600 and 700°C higher oxidation rates were observed for the P92 batches in this study than for the steels investigated by Ishitsuka *et al*. The substantial differences in mass gain found in both studies might be related to the fact that carburization was

commonly observed during exposure of P92 to the CO_2-containing gases used in the present study, which affected the weight changes.

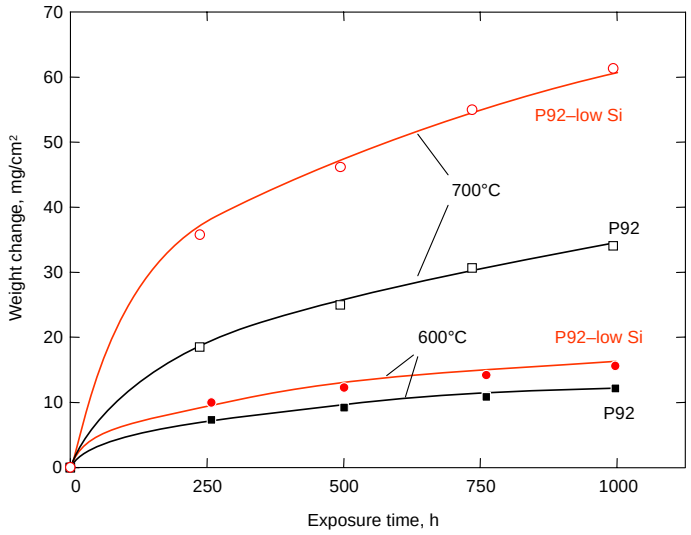

Figure 13.7: Weight changes of P92 (black) and P92-low Si (red) during 1000h exposure to $Ar/O_2/CO_2/H_2O$ at 600°C and 700°C

In summary, it can be said that the amount of silicon added to the P92 alloy is in any case insufficient to form a dense layer of silica under the present experimental conditions. However, Si clearly has a beneficial effect on the oxidation rate. This finding was confirmed for instance by Murata *et al*. [144] and Ennis *et al*. [145]. Evans *et al*. [146] showed a beneficial effect of Si addition on the growth of the surface chromia layer on austenitic steels exposed to a CO_2-base atmosphere at 850°C. The authors found that addition of 0.92wt.% of Si was the optimum level for decreasing the oxidation rate whereas alloys with more or less than 0.92wt.% exhibited higher values of k_p. The alloys used by the authors were chromia formers, so they cannot be directly compared with those used in the present study. However, the general tendency of a decreasing scaling rate due to small Si additions agreed with the results obtained in the present research.

It seems that independent of the type of the formed oxide scale, silicon may improve the oxidation resistance by forming a thin silica sub-layer as presented by Evans *et al*. [146] or by amorphous SiO_2 and Fe_2SiO_4 formation in the inner oxide scale as suggested by Ishitsuka *et al*. [143]. The latter promotes the incorporation of Cr into the inner oxide and therefore slows down the Fe cation diffusion as observed in the present investigation.

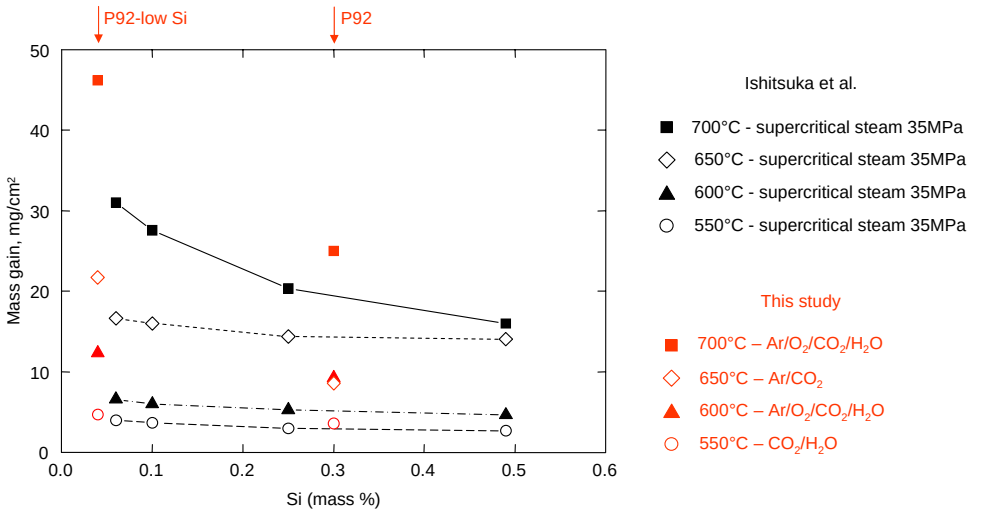

Figure 13.8: Relationship between silicon content and mass gain of P92 after 500 h oxidation at 550-700°C. Black symbols represent data obtained by Ishitsuka *et al.* [143] in supercritical steam. Red symbols represent data from this study

13.3 Effect of nickel

Addition of nickel in the range of less than 0.5% to high temperature alloys may improve to some extent the strength and resistance to nitridation and carburization. A minor positive effect is sometimes observed with respect to improvement of resistance to oxidation [147]. In ferritic/martensitic steels the nickel content usually does not exceed a few tenths of a weight percent. Therefore, it is unlikely that decreasing the concentration of this element from 0.23 to 0.06wt.% as in the two P92 batches studied here (Tab. 13.1) could significantly change the oxidation behaviour.

During GDOES measurements noticeable nickel enrichment was frequently observed for many 9-12% Cr steels exposed to different CO_2-containing atmospheres (Fig. 13.10). Such a Ni enrichment did not occur in the cases where a protective Cr-base scale was formed on the metal surface during, e.g., air or Ar/O_2 exposure (Fig. 13.10). In the latter situation SNMS was employed instead of the GDOES technique, mainly due to the better depth resolution of the SNMS. This was required in order to measure the concentration of elements within the oxide scale with a thickness of at least 50 times smaller than that formed in Ar/CO_2.

Considering the mechanisms of oxidation one should bare in mind that the Ni-enrichment near the scale/steel interface is not necessarily related to a diffusion of nickel from the bulk alloy in the direction of that interface. If a protective chromia scale is formed during, e.g., air exposure, Cr depletion will occur in a narrow sub-surface zone. Consequently, the concentration of alloying elements not participating in the oxidation process will increase as the compensation effect. The Ni enrichment will in that case be quite small because of the low Cr content in the steel. In the case of the non-protective scale formation, mainly the base element Fe will be oxidized. Non-oxidized elements such as Ni will thus become apparently enriched during long term exposure beneath the inwardly moving oxidation front.

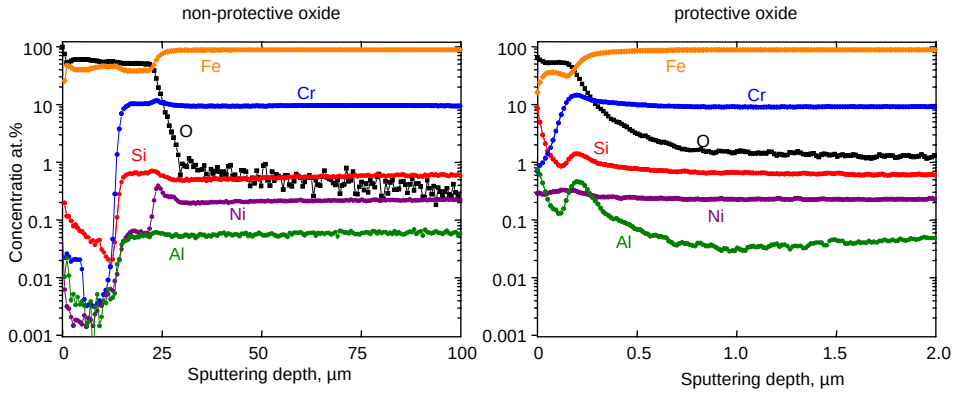

Figure 13.10: GDOES profile of P92 exposed isothermally for 100h to Ar/CO_2 at 550°C (left) and SNMS profile of P92 exposed isothermally for 100h to Ar/CO_2 preceded by 100h oxidation in Ar/O_2 at 550°C in order to obtain a protective Cr-base scale (right). Note the difference in the X-axis range

13.4 Effect of aluminium

Hardly any aluminium enrichment was observed within the oxide scale formed on the 9-12% Cr martensitic steels exposed to CO_2-containing atmospheres, including the two batches of P92 described in this chapter. However, after short isothermal exposure at temperatures between 600 and 700°C in laboratory air, a significant difference in Al distribution near the scale/steel interface was observed for the investigated P92 batches. For instance, at 650°C the SNMS depth profile revealed that after 24h exposure aluminium tended to diffuse rapidly from the bulk steel towards the surface and subsequently enrichment of this element was observed within the inner Cr-base oxide scale. This was found for the steel containing 0.028wt.% Al but not for that with 0.007wt.% Al (Fig. 13.11). In the same figure the differences of the silicon concentrations are also apparent. In the left picture in Fig. 13.11 the well distinguished peaks of Al and Si coincide

with the Cr peak. This might indicate a contribution of Al and Si during formation of the inner Cr-base oxide scale which seemed to be more protective in this case compared to that of the steel in which Al and Si peaks were hardly present. This may be concluded by comparison of the oxide scale thicknesses. During oxidation in the atmospheres other than laboratory air or Ar/O_2 no clear evidence of Al incorporation in the scale was found. GDOES depth profiles of different alloys isothermally oxidized in Ar/CO_2 and CO_2/H_2O for different times ranging from 24 to 250h revealed that after breakdown of the initial Cr-base oxide scale no significant Al enrichment in the scale was found (Fig. 13.10). Al was present in the inner scale in a concentration similar to that in the bulk alloy. This indicates that the internally oxidized Al became gradually incorporated in the inner scale due to the inwardly moving oxidation front whereby hardly any real enrichment occurred. The included Al oxide particles would act as a diffusion barrier for Fe-cations, however, due to the very small Al content the effect on oxidation rate would be marginal.

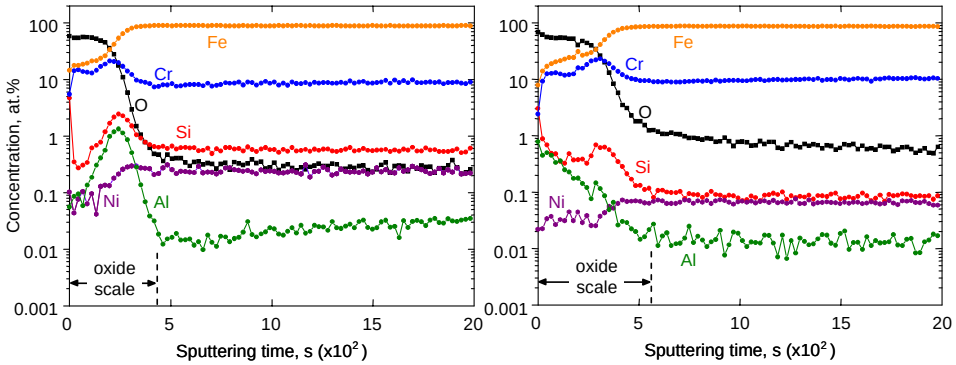

Figure 13.11: SNMS concentration profiles of P92 (left) and P92-low Si (right) exposed isothermally for 24h to laboratory air at 650°C

Guan and co-workers [148] found a positive synergistic effect of Al and Si during oxidation of Fe-Al-Si alloys in dry oxygen at 800-900°C. They explained the beneficial effect of silicon and aluminum additions on the oxidation properties by interactions resulting in an increased Al activity and outward diffusion of Al to the oxide/alloy interface. However, these studies were related to alloys with quite high Al and Si content so that it is difficult to say whether the finding can be transferred to the experimental conditions in the present study.

14. Improvement of oxidation resistance by surface modification

14.1 General remarks

Improvement of oxidation resistance of metallic components exposed at elevated temperatures can be achieved by surface modifications. Any low-temperature mechanical treatment of the surface, such as machining, grinding, blast cleaning, shotpeening, and so on, deforms the subsurface metal, introducing a large numbers of dislocations. As the alloy is heated, the deformed material recrystallizes, forming a generally finer grain and subgrain structure than the non-deformed alloy [26]. This in turn can significantly enhance the diffusivity of protective scale forming elements (mainly chromium in the case of the alloys used in the present study) from the bulk to the surface of the metal. Moreover, a large concentration of dislocations near the sample surfaces introduced by cold work provides an effective mechanism for vacancy annihilation, thus reduces the tendency of scale-alloy separation during oxidation [90].

A number of specimens with the typical dimensions used in this study (20x10x2mm) was prepared for testing the effect of cold work on selected martensitic and austenitic steels in dry (Ar/CO_2) and wet (CO_2/H_2O, $Ar/O_2/CO_2/H_2O$) atmospheres at various temperatures. Each specimen was ground up to 1200 grit surface finish using SiC paper and subsequently sandblasted at 6 bars for 30 seconds by high purity fine corundum shot with particle size of 125 µm. The extent of the cold worked zone created by this procedure was approximately 12-15µm wide as shown for of the austenitic steel TP347H FG (Fig. 14.1). For the rest of the investigated alloys, the width of the deformed zone was assumed to be in the same range. For comparison, some of the commercially available techniques which use different types and size of shot particle materials, blasting pressure and operating time can affect the alloy microstructure up to 50 µm in depth under the metal surface [149].

14.2 Oxidation in dry atmosphere (Ar/CO_2)

The effect of cold work on the oxidation resistance in Ar/CO_2 at 700°C is presented in Fig. 14.2. In the case of the two austenitic steels 1.4910 and TP347H FG and the martensitic steel VM12 a small weight gain was observed for sandblasted specimens which was attributed to the formation

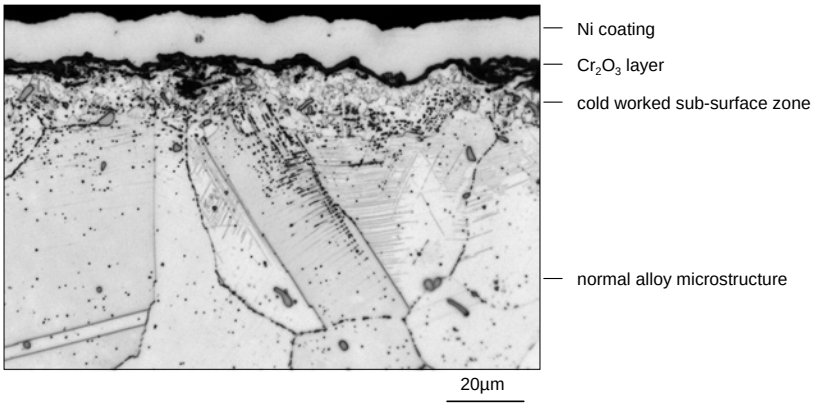

Figure 14.1: Metallographic cross section of TP347H FG after 1000h exposure to Ar/CO_2 at 700°C (etched in V2 agent) showing microstructural changes in sub-surface zone due to cold work as a result of sandblasting prior to exposure

of thin oxide layer that was well adherent to the metal substrate and consisted mainly of Cr_2O_3 partially covered by an Fe_2O_3 layer. At 700°C the non-treated austenitic steel with lower Cr content formed unsatisfactorily protective breakaway type oxide scale in Ar/CO_2 (Fig. 14.3). This type of scale had a strong tendency for spallation of the outer Fe_3O_4/Fe_2O_3 layers during thermal cycling as illustrated in Chapter 6. At 700°C this behaviour was already observed after the first 250h of oxidation. Further loss of oxide was found to occur during continued oxidation. However, when cold work was applied prior to the exposure, no spallation was observed and only a protective Cr-rich oxide scale was developed (Fig. 14.3). The reason of this dramatic change in oxidation behaviour from non-protective into protective behaviour is mainly attributed to the high dislocation density and subgrain boundaries in the subsurface zone, resulting in an increased effective value of Cr diffusion providing sufficient supply of this element to form the protective chromia base scale.

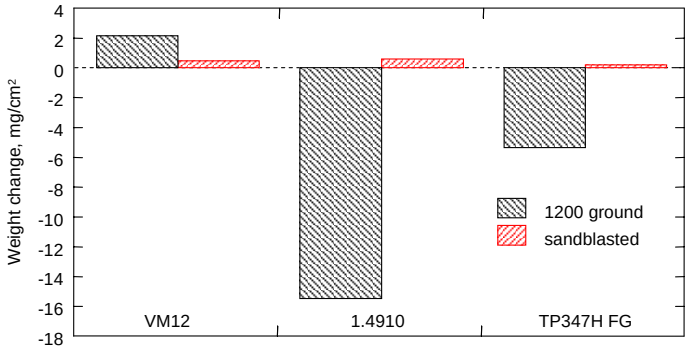

Figure 14.2: Weight changes of selected steels with and without sandblasting applied prior to 1000h exposure to Ar/CO_2 at 700°C

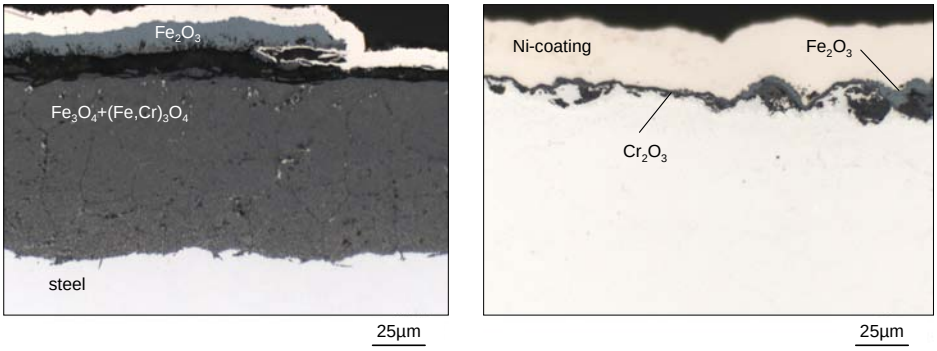

Figure 14.3: Metallographic cross sections of 1.4910 without (left) and with (right) sandblasting applied prior to 1000h exposure to Ar/CO_2 at 700°C

The Nb-stabilized austenitic steel TP347H FG was developed by Mitsubishi and Sumitomo. The previous version of this steel designed for tubes to be used under ultra supercritical steam conditions was coarse grained. The oxidation resistance of this steel at 650 and 700°C was significantly improved by grain refinement [150]. In the present study, it was shown that in Ar/CO_2 this alloy exhibited only moderate oxidation resistance (Fig. 6.11-12). However, the combination of fine grain size and cold work resulted in the formation of a protective Cr-rich oxide scale (Fig. 14.1). Some authors suggested that for Super 304H and TP347H FG shot peening combined with grain refinement could improve the oxidation resistance at temperatures above 700°C (in H_2O-rich atmosphere) up to the level which is typically encountered for steels containing 25% Cr [151, 152].

Due to the relatively high diffusivity of chromium in ferritic and martensitic materials, it is expected that they might be less susceptible to obtain improved oxidation resistance by cold work than austenitic steels. Therefore, additional surface treatment such as cold work is expected to have a less pronounced effect on the improvement of oxidation resistance. However, as presented in Fig. 14.4, surface modification could significantly decrease the scaling rate of VM12. The observed oxide scale on sandblasted VM12 was much thinner than that on non-treated material. It consisted of a chromia layer which was only partially covered by thin Fe_2O_3.

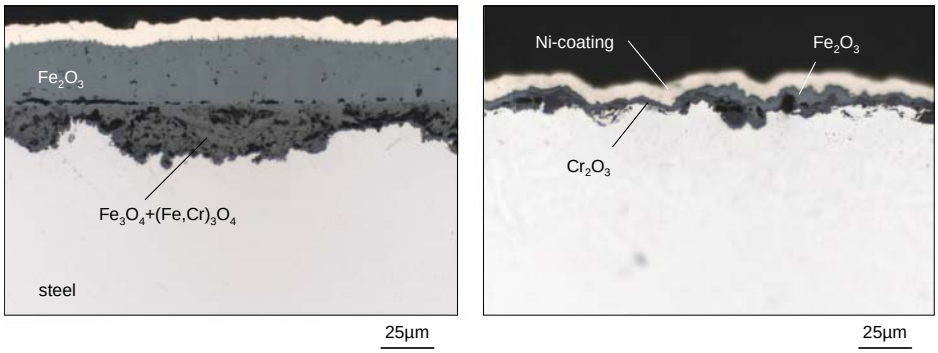

Figure 14.4: Metallographic cross section of VM12 without (left) and with (right) sandblasting applied prior to 1000h exposure to Ar/CO_2 at 700°C

14.3 Oxidation in H_2O-containing atmospheres (CO_2/H_2O, $Ar/O_2/CO_2/H_2O$)

The effect of surface modification on the oxidation behaviour in CO_2/H_2O was investigated at lower temperature, i.e., 550°C. Only 9-12% Cr martensitic steels were selected for this investigation since austenitic steels showed at 550°C low oxidation rates and the formation of non-protective Fe-base oxide scales was not observed.

The cross section of one of the selected steels presented in Fig. 14.5 clearly shows that hardly any positive effect of sandblasting could be observed in this case. Apparently at low temperature the improvement of Cr diffusivity in the steel toward the metal surface could not be achieved by cold work to form more protective oxide scale. Similar results were obtained for P92 and VM12.

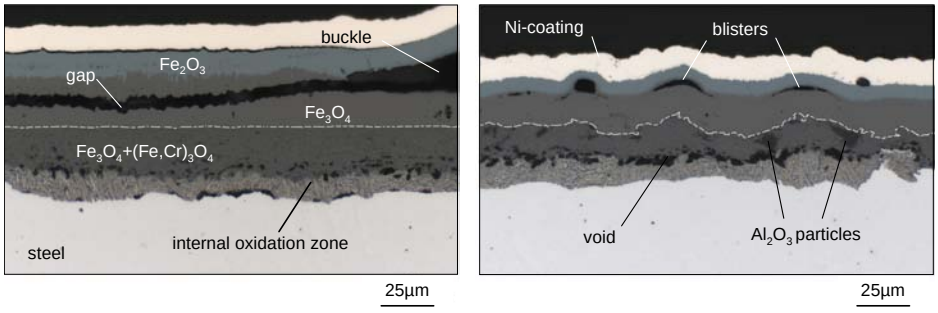

Figure 14.5: Cross sections of ground (left) and sandblasted (right) X20 specimens after 1000h exposure to CO_2/H_2O at 550°C. Dashed lines indicate the original metal surface

A much wider temperature range was used in the case of martensitic steels oxidized in $Ar/O_2/CO_2/H_2O$. From the oxide scale morphology of VM12 specimens exposed at 600°C

presented in Fig. 14.6 it is evident that surface cold work had no effect on the Fe-base non-protective oxide growth. Apart from the minor differences of the scale morphology, the thickness of the scale was similar in both cases. Therefore, it was obvious that the scale growth rate was comparable at 600°C for ground and sandblasted VM12.

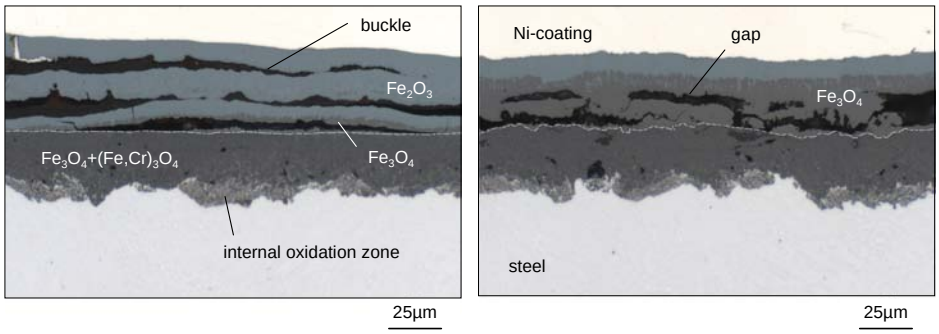

Figure 14.6: Metallographic cross sections of ground (left) and sandblasted (right) VM12 specimens after 1000h exposure to $Ar/O_2/CO_2/H_2O$ at 600°C. Dashed lines indicate the original metal surface

However, when comparing the macroscopic images of the VM12 specimens oxidized in $Ar/O_2/CO_2/H_2O$ at 600°C it becomes clear that the thin and protective Cr-base scale was formed on VM12 without sandblasting treatment (Fig. 14.7).

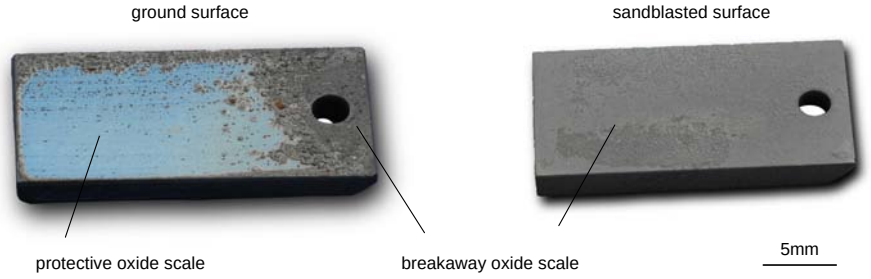

Figure 14.7: Macroscopic pictures of ground (left) and sandblasted (right) VM12 specimens after 1000h exposure to $Ar/O_2/CO_2/H_2O$ at 600°C

The above finding shows that at 600°C in $Ar/O_2/CO_2/H_2O$ sandblasting might have a detrimental effect on the oxidation resistance for some alloys (in this case VM12). This can be explained on the basis of the already discussed situation for “borderline alloys” when oxidized in atmospheres with different oxygen contents (Chapter 10). It was shown that small variations in gas composition could change the oxidation behaviour from protective into non-protective. The 9-12% Cr martensitic steels were susceptible to such changes and apparently surface

treatment could also adversely affect the oxidation behaviour. In this particular case it is believed that the detrimental effect of sandblasting (Fig. 14.7) was mainly related to the changes of the surface roughness on a "micro-level". When the metal surface is flat the chromium diffusion from the bulk alloy toward the surface is fast enough to form a protective oxide scale. This can be changed by surface modification (e.g., sandblasting), i.e., when the metal surface is rough it promotes formation of less protective oxide due to insufficient Cr transport from bulk metal. However, upon temperature increase this effect was not observed. Faster chromium diffusion at 650 and especially 700°C seemed to compensate the negative effect of surface roughness and decreases in weight gain were recorded for VM12 (Fig. 14.8).

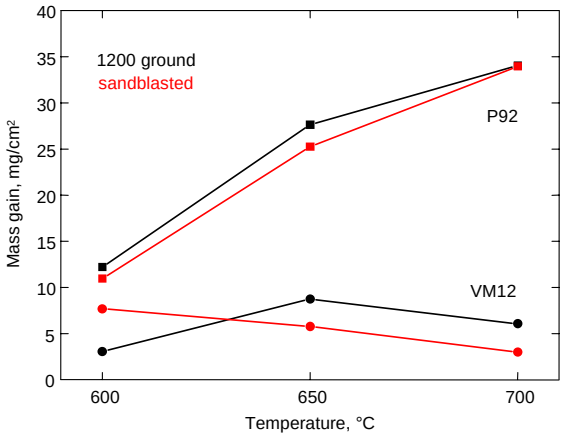

Figure 14.8: Mass gains of P92 and VM12 with and without sandblasting applied prior to 1000h exposure to $Ar/O_2/CO_2/H_2O$ at 600, 650 and 700°C

VM12 exposed at 650 and 700°C exhibited the formation of Fe-base oxide scale both for ground and sandblasted specimens. The outer part of the oxide scales consisted mainly of well adherent and non-porous Fe_2O_3, especially at 700°C (Fig. 14.9). Such oxide can be considered as at least partially protective, preventing buckling and scale delamination. High concentration of chromium in the inner oxide resulted in the formation of a more or less continuous Cr_2O_3 layer at the metal/oxide interface. The outward Fe cation migration was thus significantly reduced and as a consequence only hematite was present in the outer scale. For P92 only a minor effect of cold work by sandblasting was observed at 600-650°C whereas at 700°C no effect was observed, and both specimens exhibited the formation of an Fe-base oxide scale with a strong tendency to buckling (Fig. 14.10).

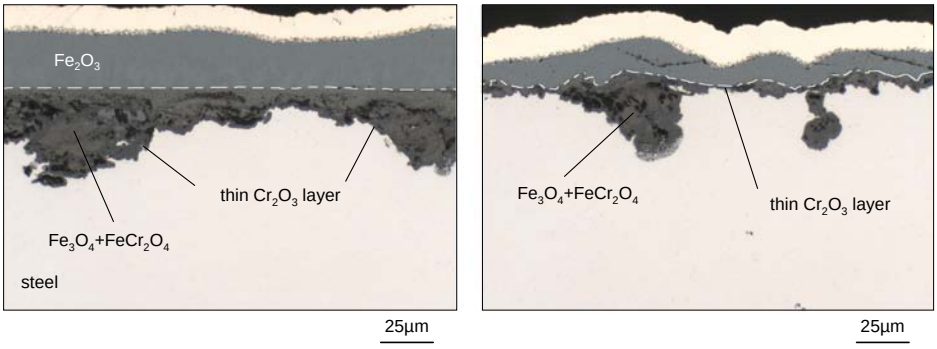

Figure 14.9: Metallographic cross sections of ground (left) and sandblasted (right) VM12 specimens after 1000h exposure to Ar/O_2/CO_2/H_2O at 700°C. Dashed lines indicate the original metal surface

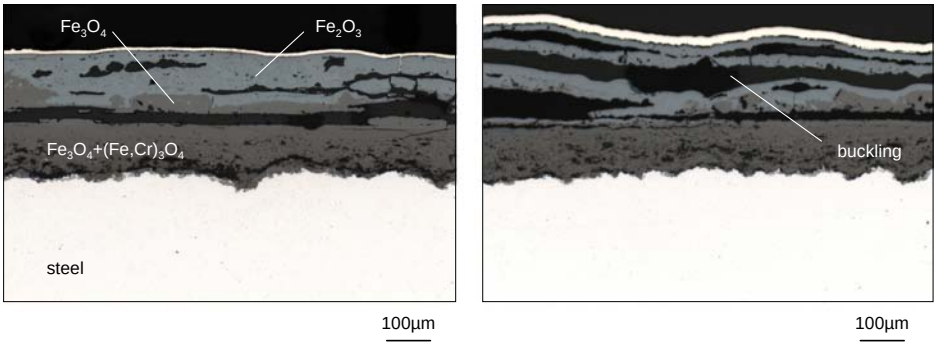

Figure 14.10: Metallographic cross sections of ground (left) and sandblasted (right) P92 specimens after 1000h exposure to Ar/O_2/CO_2/H_2O at 700°C

For austenitic steels accelerated breakaway oxidation was observed when oxygen was added to CO_2/H_2O (Chapter 6). This finding was assumed to be related to the formation of volatile Cr-species (Chapter 11) resulting in faster degradation of the protective Cr-rich oxide scale. Therefore, it was important to investigate whether sandblasting could affect the oxidation behaviour of austenitic steels with lower Cr content in this gas in a similar manner as found during exposure to Ar/CO_2.

Figure 14.11 shows that chromium base scale formation occurred on the sandblasted specimen at 650°C. At 700°C some areas of the sandblasted metal surface exhibited the formation of a Fe-base oxide scale, however, after 1000h exposure some parts of the specimen were still covered by a Cr-rich scale (Fig. 14.12). The weight changes of 1.4910 presented in Fig. 14.12 suggest that the breakaway oxidation process at 700°C was preceded by initial formation of a protective Cr-rich scale.

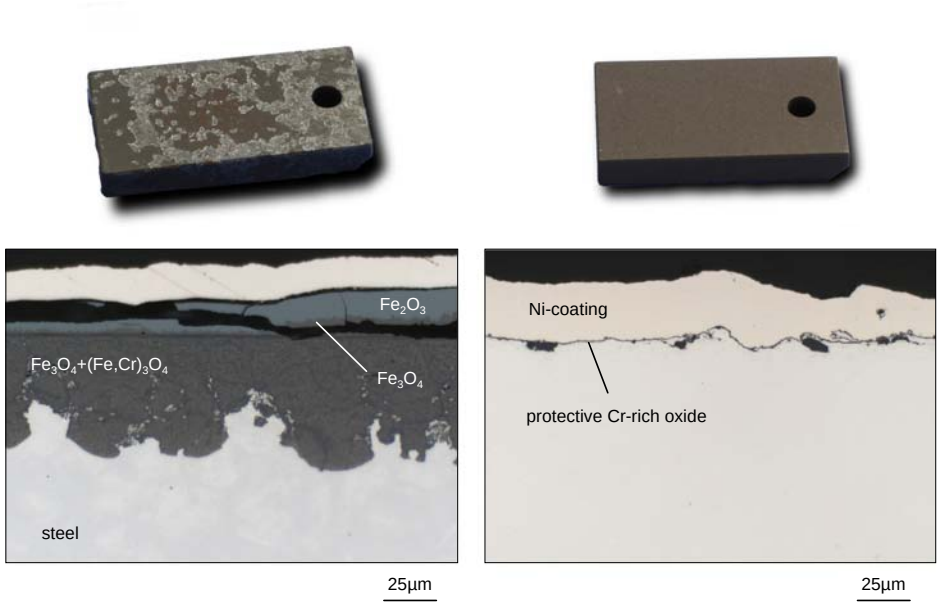

Figure 14.11: Macro images and cross sections of ground (left) and sandblasted (right) 1.4910 specimens after 1000h exposure to $Ar/O_2/CO_2/H_2O$ at 650°C

Upon continuing oxidation a gradual deterioration of this scale occurred. Rapid acceleration of scale growth was observed after approximately 500h oxidation. This is most probably associated with scale damage due to formation of volatile Cr-species. The surface scale degradation of ground 1.4910 exposed at 700°C was much more severe (compare with Fig. 6.21).

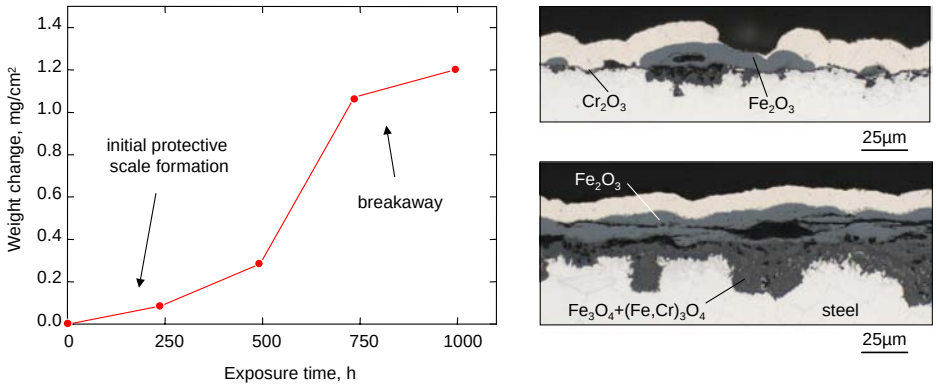

Figure 14.12: Weight change of sandblasted 1.4910 during 1000h exposure to $Ar/O_2/CO_2/H_2O$ at 700°C (left) and corresponding cross sections from the same specimen after 1000h exposure (right)

The temperature dependence of weight changes of 1.4910 with and without sandblasting prior to the exposure is presented in Fig. 14.13. At 600-650°C oxide spallation was noticeable for 1.4910, however, not for specimens which were sandblasted prior to the exposure. In those cases only protective Cr-base scales were developed. At 700°C substantial spallation was observed for ground 1.4910. The sandblasted specimen showed the formation of Fe-base oxide scale, however, after 1000h exposure some areas still exhibited the presence of a thin chromia base scale (Fig. 14.12). The findings above illustrate that significant improvement of the oxidation resistance was obtained for 1.4910 by sandblasting.

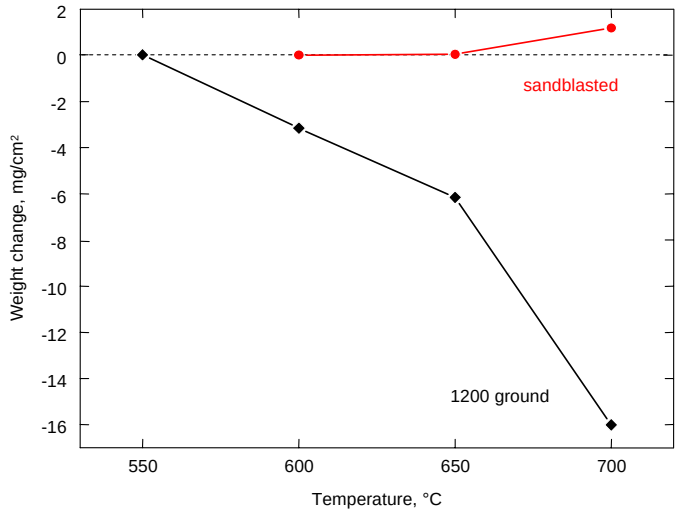

Figure 14.13: Weight changes of 1.4910 with and without sandblasting applied prior to 1000h exposure to $Ar/O_2/CO_2/H_2O$ at 550-700°C

15. Carburization in CO_2-containing gases

15.1 General remarks

As demonstrated in previous chapters the morphology of the Fe-base scale formed on the martensitic steels was very similar when they were exposed to CO_2- and/or H_2O-containing gases. Fe-rich oxide scales developed on the metal surface after an incubation period during which a chromia base scale was formed.

A number of studies have shown that when exposed to CO_2-rich gases, metallic construction materials may exhibit internal carburization apart from oxide scale formation [54, 153, 154]. Carburization is a commonly observed process in CH_4- and/or CO/H_2-rich gases and is of concern because it may substantially affect the mechanical properties of the materials, especially their ductility [52, 53]. In CH_4- and/or CO/H_2-rich environments the C-activity may, depending on temperature, be typically in the range of 10^{-4} to 1. However, in a number of studies it was reported that carburization might also occur in CO_2-rich gases in spite of the fact that in such environments the carbon activity was quite small, typically 10^{-16} - 10^{-25}, depending on temperature and exact gas composition. In the present study, the possible occurrence of carbon uptake in the various types of the tested materials is discussed.

15.2 Behaviour of low alloy steel 13CrMo4-4

None of the etched metallographic cross sections of 13CrMo4-4 exposed to the CO_2-containing atmospheres revealed the formation of carbides beneath the oxide scale. Apparently, the very low Cr concentration in 13CrMo4-4 could not provide sufficient driving force for substantial carbon uptake into the bulk material. For steels with low Cr concentration, ingress of carbon into the metal may result in the formation of iron carbide, i.e., cementite (Fe_3C). However, according to thermodynamic calculations the formation of Fe_3C at temperatures below 763°C is possible only if $a_c>1$ [56]. This value is far higher than the carbon activity prevailing in CO_2-rich atmospheres used in this study. Therefore, the formation of cementite would not be expected.

Nevertheless, the recent investigations carried out by Hünert *et al.* [155, 156] clearly showed that cementite was formed in the oxide scale and near the scale/metal interface in 13CrMo4-4 when exposed to atmospheres consisting of CO_2 and H_2O at ambient pressure and at

temperatures above 600°C. The authors also observed that some Fe-carbide precipitations were formed in the case of $O_2/CO_2/H_2O$ gas at 550°C at a total gas pressure of about 8MPa. Those findings indicated that Fe_3C might be formed at relatively low temperatures in low alloyed steels exposed to CO_2-rich gases with low carbon activity.

In the present study, indication for minor carbon enrichment was observed after exposure to $Ar/O_2/CO_2$ (Fig. 15.1). Experiments performed with 13CrMo4-4 in an atmosphere containing labeled carbon ^{13}C indicated that in the case of this steel apparently no driving force exists for carbon transfer from the oxidizing atmosphere into the metal. The SNMS profile presented in Fig. 15.1 shows a slight carbon enrichment near the scale/metal interface, however, the ^{13}C concentration is very low and exhibits a flat profile. A possible explanation for the slight enrichment of ^{12}C might simply be related to the inwardly moving steel/oxide interface during the ongoing oxidation process. It has been frequently shown, that this may result in carbon being "pushed back" in the bulk material resulting in so-called "self-carburization".

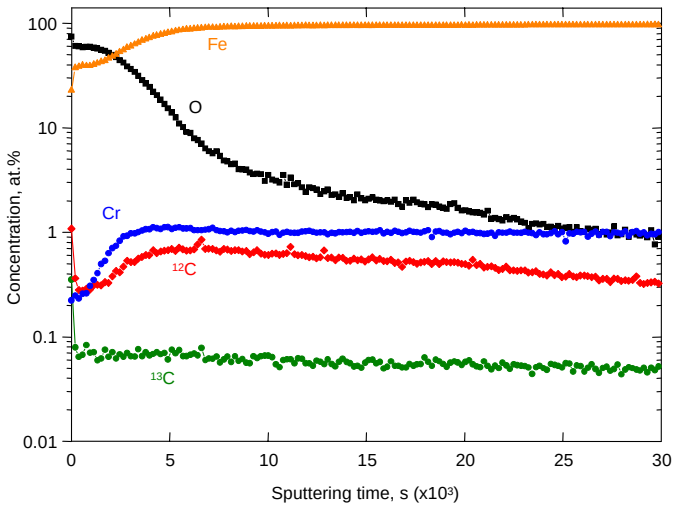

Figure 15.1: SNMS profile of main scale forming elements of 13CrMo4-4 exposed to $Ar/(1\%)O_2/(1\%)^{13}CO_2$ for 7h at 550°C

Only the microstructure of the bulk steel was revealed by etching and apparently no carburization zone was formed beneath the Fe-base oxide scale in 13CrMo4-4 (Fig. 15.2).

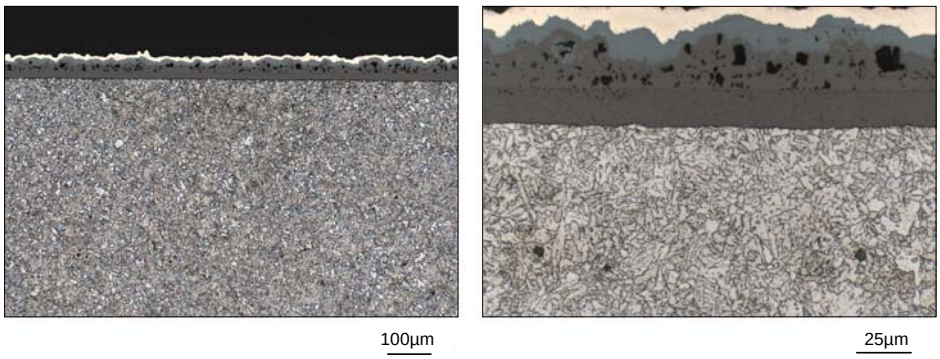

Figure 15.2: Etched cross sections of 13CrMo4-4 after oxidation in Ar/CO_2 for 1000h at 550°C

15.3 Carburization of martensitic 9-12% Cr steels

In the present study carburization of 9-12% Cr steels was observed when exposed to Ar/CO_2, $Ar/O_2/CO_2$, CO_2/H_2O and $Ar/O_2/CO_2/H_2O$. The carburization zone which was rich in Cr-base carbides only developed beneath the Fe-base oxide scales and was not clearly observed under the Cr-rich oxide scale (Fig. 15.3). It is probably because the gas tight chromia scale prevented CO_2 from penetration into the steel.

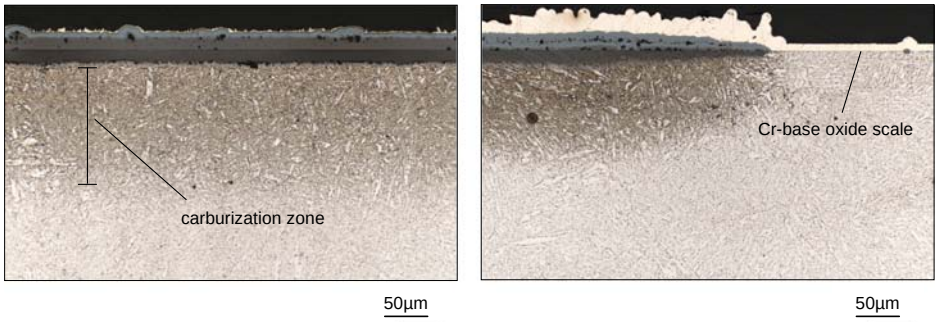

Figure 15.3: Etched metallographic cross sections of P92 (left) and VM12 (right) oxidized in Ar/CO_2 for 1000h at 550°C

This was further confirmed by a number of experiments involving pre-oxidation of VM12 in Ar/O_2 and subsequently in Ar/CO_2. During 100h oxidation in Ar/O_2 a thin and protective Cr-base oxide scale was developed on the metal surface. After this first stage of exposure the atmosphere was switched to Ar/CO_2 without cooling the specimen down. The exposure to Ar/CO_2 lasted for another 100h before the specimens were characterized by X-ray diffraction and SNMS analyses. The obtained results revealed the formation of a thin and protective chromia layer covered by Fe_2O_3 for the specimen exposed to Ar/O_2 as well as that oxidized in Ar/O_2+Ar/CO_2 (Fig. 15.4). The carbon concentration profiles obtained by SNMS analysis clearly indicated that some carbon

enrichment was present in the inner part of the oxide scale but not in the bulk material even for the specimen exposed to Ar/CO_2 gas after the pre-oxidation in Ar/O_2, indicating that Cr-base oxide scale provided effective protection of the alloy against carbon penetration.

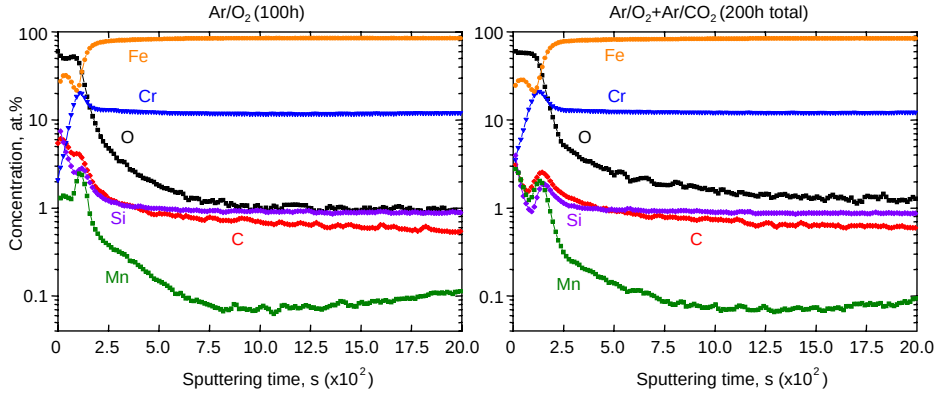

Figure 15.4: SNMS profiles of VM12 isothermally oxidized in Ar/O_2 at 550°C for 100h (left) followed by a further 100h in Ar/CO_2 at 550°C (right). The change of the gas from Ar/O_2 to Ar/CO_2 was carried out isothermally

In contrast, when the breakdown of the initially formed Cr-base oxide scale occurred, carbon could be transferred from the oxidizing atmosphere into the steel through the less protective Fe-base oxide resulting in the formation of a clearly visible carburization zone. The formation of Cr-rich carbides could be easily revealed by etching of the metallographic cross section in NH_3 solution (Fig. 15.3). From the GDOES profiles showed in Fig. 15.5 it is obvious that a substantial enrichment of carbon occurred beneath the Fe-base oxide scale for P92 and VM12 after 150h isothermal exposure to Ar/CO_2 at 550°C. The graphs in Fig. 15.5 also reveal that the carbon uptake for VM12 was more significant than for P92.

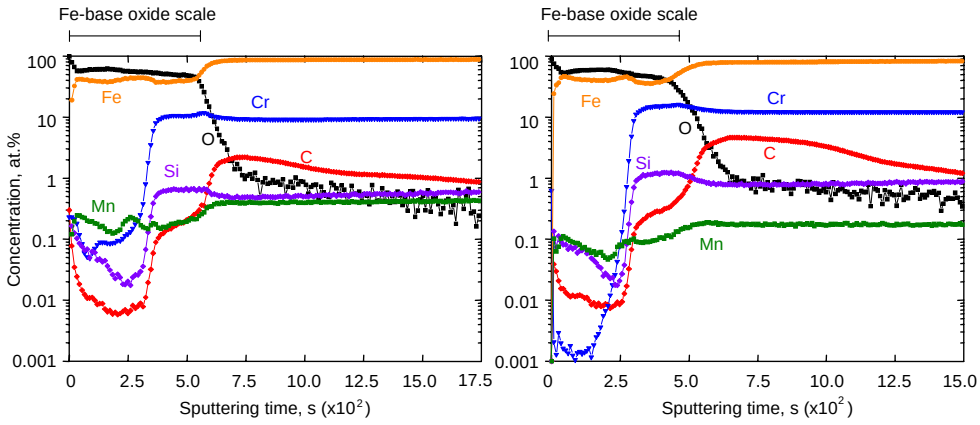

Figure 15.5: GDOES profiles of P92 (left) and VM12 (right) exposed to Ar/CO_2 for 150h at 550°C

15.4 Mechanisms of carburization

According to the stability diagram for the Cr-C-O_2 system (Fig. 15.6), it seems impossible that carburization occurred in Ar/CO_2 (and other CO_2-containing gases), since the equilibrium carbon activity in the test atmospheres was several orders of magnitude lower than that required for chromium carbide formation. Therefore, there was no apparent driving force for carbon diffusion through the scale from the gas/oxide to the metal/oxide interface. However, it was shown by several authors [48, 54, 55] that under such conditions carburization beneath the oxide scale could occur in the alloy if one assumes that carbon-carrying species could reach the metal surface by penetrating the oxide scale in molecular form.

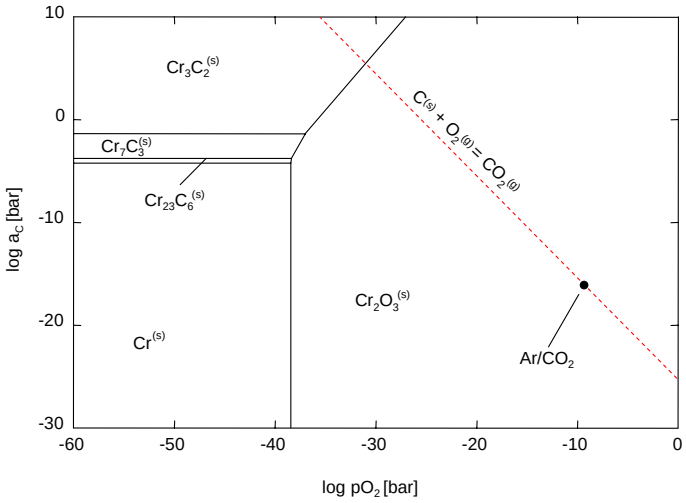

Figure 15.6: Cr-C-O_2 stability diagram at 550°C. Red dashed line shows the CO_2 isobar

To calculate the equilibrium values of pO_2 in Ar/CO_2, the following equilibria should be considered:

$$2CO_2 = 2CO + O_2 \qquad \text{(Eq. 15.1)}$$

$$2CO = CO_2 + C \qquad \text{(Eq. 15.2)}$$

In CO_2 a relation exists between carbon activity and oxygen partial pressure. In the simplest form, this relation can be considered as the sum of the above two reactions:

$$CO_2^{(g)} = C^{(s)} + O_2^{(g)} \qquad \text{(Eq. 15.3)}$$

The equilibrium constant of the Eq. 15.3 is defined by:

$$K = \frac{aC^{(s)} \cdot pO_2{}^{(g)}}{pCO_2{}^{(g)}} \qquad \text{(Eq. 15.4)}$$

Equation 15.3 reveals that the carbon activity is inversely proportional to the oxygen partial pressure. As the pO_2 at the scale/metal interface is close to the dissociation pressure of Cr_2O_3 (or Fe-oxide), the carbon activity, due to the presence of CO_2 at this interface, may reach a value much higher than that needed to form Cr-rich carbides (Fig. 15.6). The extent of carburization is thus expected to be mainly governed by the gas permeability of the oxide scale rather than by the exact equilibrium carbon activity of the gas [157]. In fact, the occurrence of internal carburization confirms the proposal [47, 48, 158] that in oxide scales showing morphologies and compositions as, e.g., in Fig. 15.3, gas molecules of CO_2 can penetrate the external oxide scale. Molecular transport occurred in oxides grown on the ferritic steel P91 when exposed in water vapor rich gases [111]. This molecular transport in the scales formed in Ar/H_2O or Ar/CO_2 promotes the mechanisms explaining the suppression of external chromia formation in this type of environment by enhanced internal oxidation of chromium and/or by internal carbide precipitations [159]. In Fig. 15.7 the changes in activities of selected species are presented in the CO_2/H_2O gas assuming local thermodynamic equilibrium during the above discussed molecular transport through the Fe-base oxide scale. It can be seen that from the scale/gas to the scale/steel interface the C activity as well as the concentration of CO and H_2 increases.

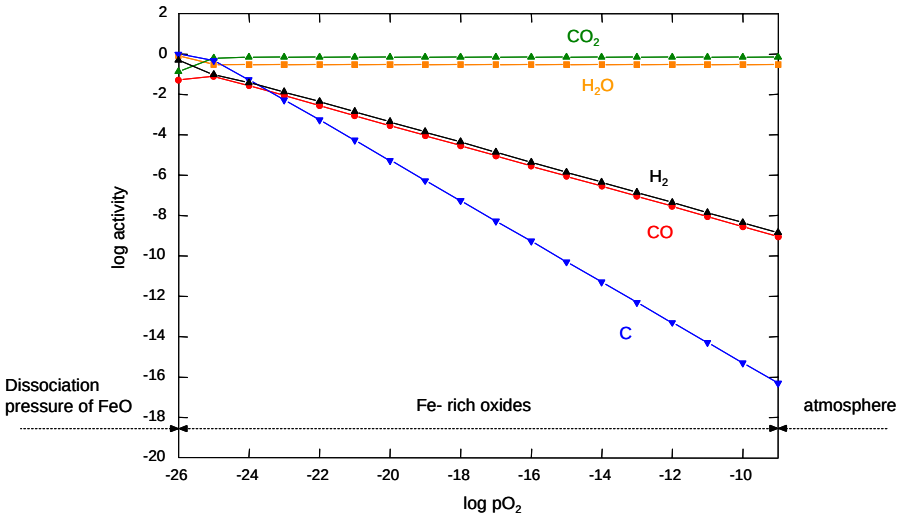

Figure 15.7: Change in activities during molecular transport of CO_2/H_2O gas mixture through the Fe-base oxide scale at 550°C assuming local thermodynamic equilibrium (calculated with FactSage)

15.5 Kinetics of carburization

A number of short-term exposures to different CO_2-containing gases revealed that carburization of the 9-12% Cr steels was a time-dependent process. As shown in Fig. 15.8 the carbon content in VM12 and P92 increased with increasing exposure time after oxidation in Ar/CO_2 and CO_2/H_2O.

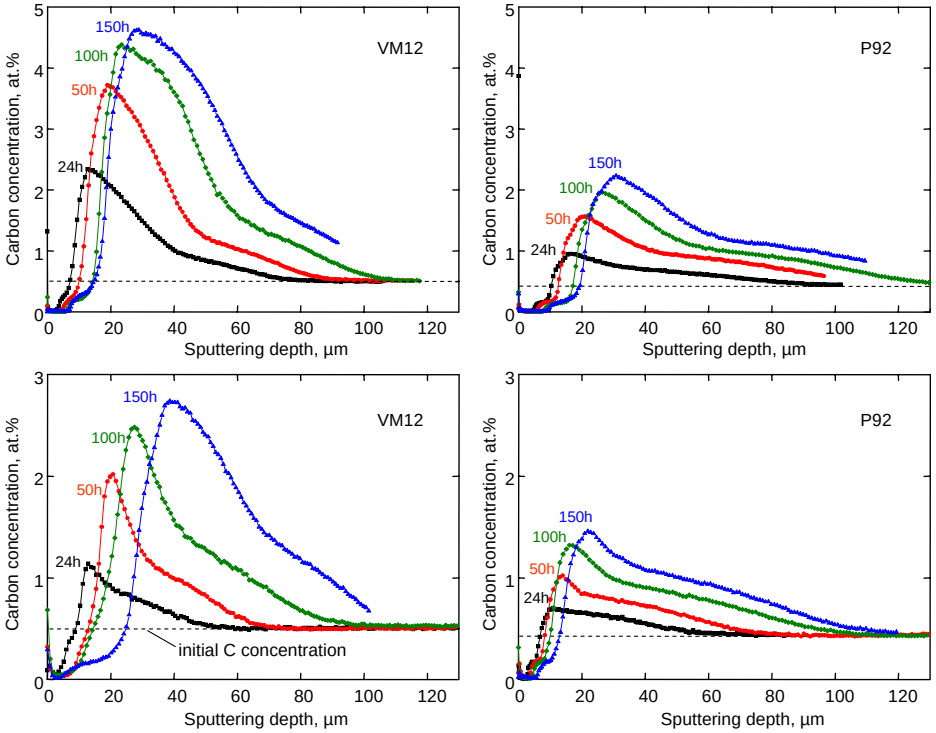

Figure 15.8: GDOES profiles of carbon uptake for VM12 (left) and P92 (right) isothermally exposed to Ar/CO_2 (upper figures) and CO_2/H_2O (lower figures) for 24h, 50h, 100h and 150h at 550°C

Fig. 15.8 also indicates that the total carbon uptake was higher for VM12 than for P92. This could be because the oxide scale formed on P92 could provide better protection against the penetration of CO_2 molecules into the steel from the atmosphere. This explanation, however, is hard to be applied in reality since the scaling rates of P92 were higher compared to VM12 as discussed previously in Chapter 5. Another explanation might be that VM12 with higher Cr content had simply higher capability to form Cr-rich carbides.

However, the depth of the formed carbide, i.e., carburization zone was largest in the P92 which had the lowest Cr content (~9% Cr) among the 9-12% Cr steels studied (Fig. 15.9). In contrast,

HCM12 containing 12% Cr showed a considerably smaller carburization depth. This finding can be easily explained if one assumes that carburization is in fact a form of internal corrosion and its kinetics can be therefore described using Wagner's theory. The equation describing the rate at which the carbide precipitation zone widens (assuming that only Cr-carbides are formed) and can be expressed as [26]:

$$(x^{(i)})^2 = k_p^{(i)} \cdot t \qquad \text{(Eq. 15.5)}$$

$$\text{with } k_p^{(i)} = \frac{\varepsilon N_C^{(s)} D_C}{\nu N_{Cr}^{(o)}} \qquad \text{(Eq. 15.6)}$$

where $N_{Cr}^{(o)}$ is the initial Cr concentration in the alloy, ν is a stoichiometric coefficient of the formed carbides, $N_C^{(s)} D_C$ is the carbon permeability and ε represents a diffusional blocking parameter.

From the equations 15.5-6 it is clear that the carburization depth is proportional to $t^{1/2}$ and inversely proportional to the concentration of the reactive solute metal (here Cr), thus the interpretation of results presented in Fig 15.9 does not give rise to any difficulties.

The carburization kinetics of Cr steels and Ni-base alloys depends on numerous factors. If an alloy is exposed to a gas with high carbon activity and this activity establishes rapidly at the metal surface in absence of a surface oxide scale, the kinetics of carburization can be described by Eqs. 15.5-6. The equations show that the depth of carburization is inversely proportional to the Cr content in the alloy. It is also proportional to $t^{1/2}$ because it is governed by C diffusion in the alloy. The total amount of carbon taken up, however, increases with Cr content. This has been frequently confirmed experimentally and also illustrated by finite difference modeling [160, 161]. Important is that under these experimental conditions, the surface carbon content is temperature independent for a given alloy.

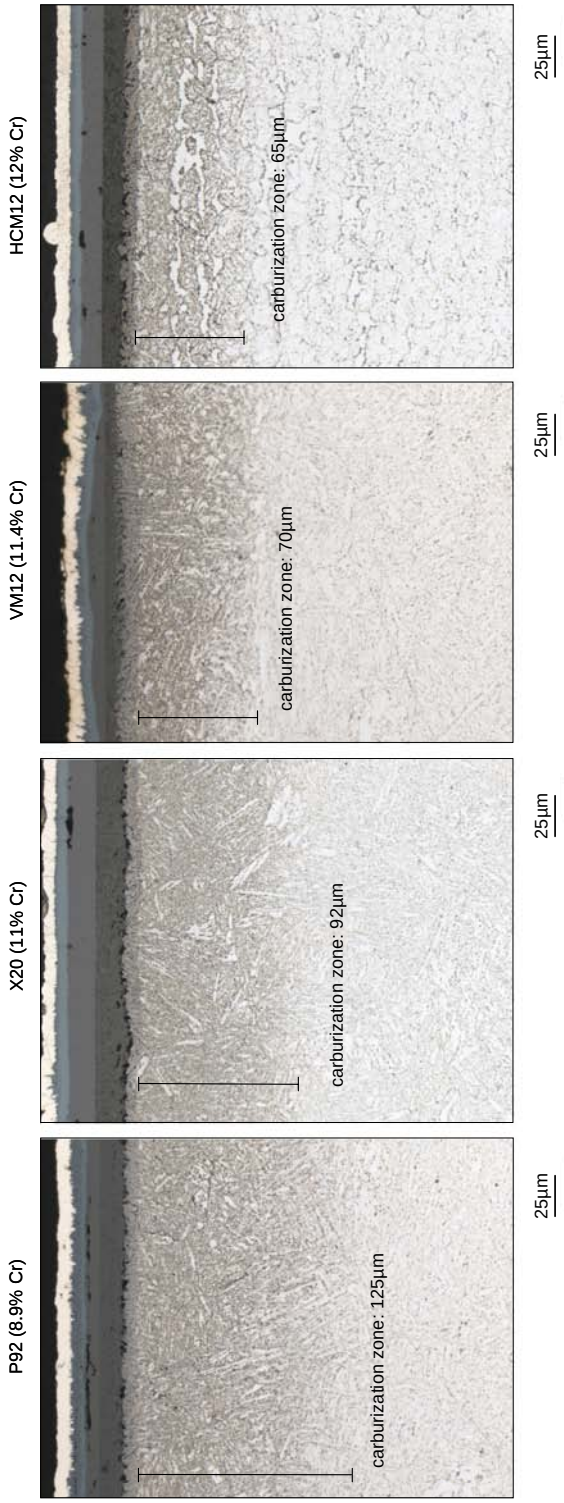

Figure 15.9: Etched metallographic cross sections of 9-12% Cr steels after 1000h exposure to CO_2/H_2O at 550°C

The latter appears not to be the case under the prevailing experimental conditions where the carbon content near the scale/alloy interface, after exposure to, e.g., Ar/CO_2, increases with time (Fig. 15.8). This finding might be related to two factors:

- the rate of carbon uptake is likely governed by the kinetics of C transfer (via CO_2 molecules) through the oxide layer;
- the metal/oxide interface moves inwardly with increasing exposure time.

Figure 15.10 shows that the measured total amount of C uptake tends to exhibit a linear time dependence. This would indicate that the reaction occurring in the scale or at the scale/alloy interface is rate determining for carbon uptake. One might consider the reactions in the scale to occur in the following steps:

$$CO_2 + 2Me \rightarrow 2MeO + [C] \qquad \text{(Eq. 15.7)}$$

$$6[C] + 23Me \rightarrow Me_{23}C_6 \qquad \text{(Eq. 15.8)}$$

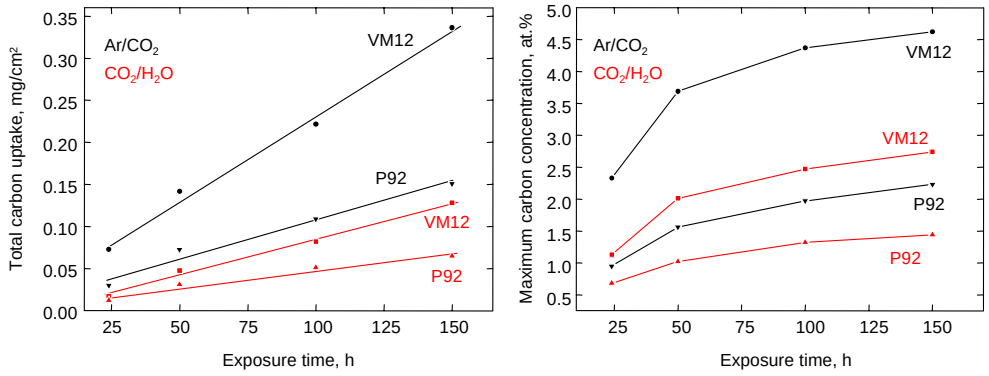

Figure 15.10: Carburization kinetics of P92 and VM12 isothermally oxidized in Ar/CO_2 and CO_2/H_2O (left) and the maximum carbon concentration as a function of time for the same specimens (right) at 550°C

As described by Grabke [55], the carburization is assumed to occur via the transport of CO_2 molecules through the oxide scale. The reaction between CO_2 molecules and Cr from the steel can be summarized as:

$$6CO_2 + 23Cr \rightarrow Cr_{23}C_6 + 6O_2 \qquad \text{(Eq. 15.9)}$$

While the released carbon is consumed by carbide formation, the oxygen is subsequently "tied-up" as oxide. The atomic ratio of C "tied-up" as carbide and O in the form of oxide will thus be $^{6}/_{12} = {}^{1}/_{2}$. So, the C/O weight ratio would be $^{12}/_{32}$. If the carbon uptake for VM12 after 150h, according to the GDOES profiles equals 0.33 mg/cm^2 (Fig. 15.10), the oxygen uptake as a result of scale formation according to reaction Eq. 15.9 would be:

$$0.33 \times \frac{32}{12}\ [mg \cdot cm^{-2}] \approx 0.33 \times \frac{32}{12} \times 8\ [\mu m] = 7.04 \mu m$$

The measured value of the oxide scale thickness in the cross section of VM12 oxidized in Ar/CO_2 for 150h was about 20µm. Therefore, approximately 35% of the scale was formed by the reaction from Eq. 15.8.

It is concluded that internal carburization of Fe-Cr alloys is controlled by lattice diffusion of carbon through the depleted metal matrix as well as by the permeability of the metal matrix. A large amount of data available in literature suggested that carburization of Fe-Cr as well as Ni-Cr alloys follows parabolic behaviour [26, 52, 162]. This finding has also been confirmed in the present study, however, only in respect of the carburization depth which was measured after electrolytic etching. As will be shown later, the electrolytic technique is a very convenient method for visualization of carbides in specimen cross sections but has relatively low accuracy, especially in the case of specimens exposed to higher temperatures. The advantage of GDOES analysis is that not only the carburization depth but also the total amount of carbon can be obtained as illustrated in Fig. 15.8.

The calculations of the total carbon uptake based on the GDOES results revealed that the carburization kinetics cannot be described by a parabolic rate law. The results presented in Fig. 15.10 clearly indicate that the carbon uptake of P92 and VM12 after isothermal exposure to Ar/CO_2 and CO_2/H_2O shows a linear tendency. The total carbon uptake observed for VM12 was higher than that of P92. The non-parabolic nature of the carburization process can be explained if the following mechanism of carbon uptake is considered:

In the first stages of reaction CO_2 molecules react with the bare metal surface. It has been frequently shown that during this transient stage oxides and carbides may form simultaneously. After a surface scale has formed, molecular transport of carbon from the atmosphere through the

oxide layer occurs resulting in the formation of Cr-rich carbides in the alloy matrix. Chromium carbide formation removes Cr from the steel matrix thus reducing the availability of Cr to become incorporated into the surface oxide scale. At lower temperatures (e.g., 550°C) carbon diffusion is much faster than that of chromium and thus formation of carbide precipitations prevails over the selective oxidation of chromium on the metal surface. As a consequence of the retarded chromium diffusion, the formation of less protective Fe-base oxide occurs on the metal surface.

The internal oxidation zone is partly resulted from the oxidation of Cr-rich carbide particles. This process does not lead to complete removal of the surface-near carbides as illustrated by the fact that remnants of carbides were still present in the inner part of the surface oxide scale (Fig. 15.11). The internal oxidation zone and the inner Fe_3O_4 + $(Fe,Cr)_3O_4$ mixed oxide layer thus "consume" most of the carbides by transformation into Cr-rich oxide as soon as the pO_2 is sufficiently high:

$$Cr_{23}C_6 + 17\tfrac{1}{4}O_2 = 11\tfrac{1}{2}Cr_2O_3 + 6C \qquad \text{(Eq. 15.10)}$$

in the internal oxidation zone and:

$$Cr_{23}C_6 + 20\tfrac{1}{4}O_2 = 11\tfrac{1}{2}Cr_2O_3 + 6CO \qquad \text{(Eq. 15.11)}$$

in the inner oxide layer.

The carbon formed by reaction Eq. 15.10 will obviously diffuse into the bulk steel. As a consequence of reaction Eq. 15.11 carbon bearing gas species are formed (most probably CO) which will likely react with the metal surface resulting in carbon uptake into the alloy. It is thus likely that carbon from the initially formed carburization zone is progressively pushed away in direction of the bulk steel thus contributing to formation of new Cr-rich carbides. The schematic drawing of the proposed mechanism is outlined in Fig. 15.12.

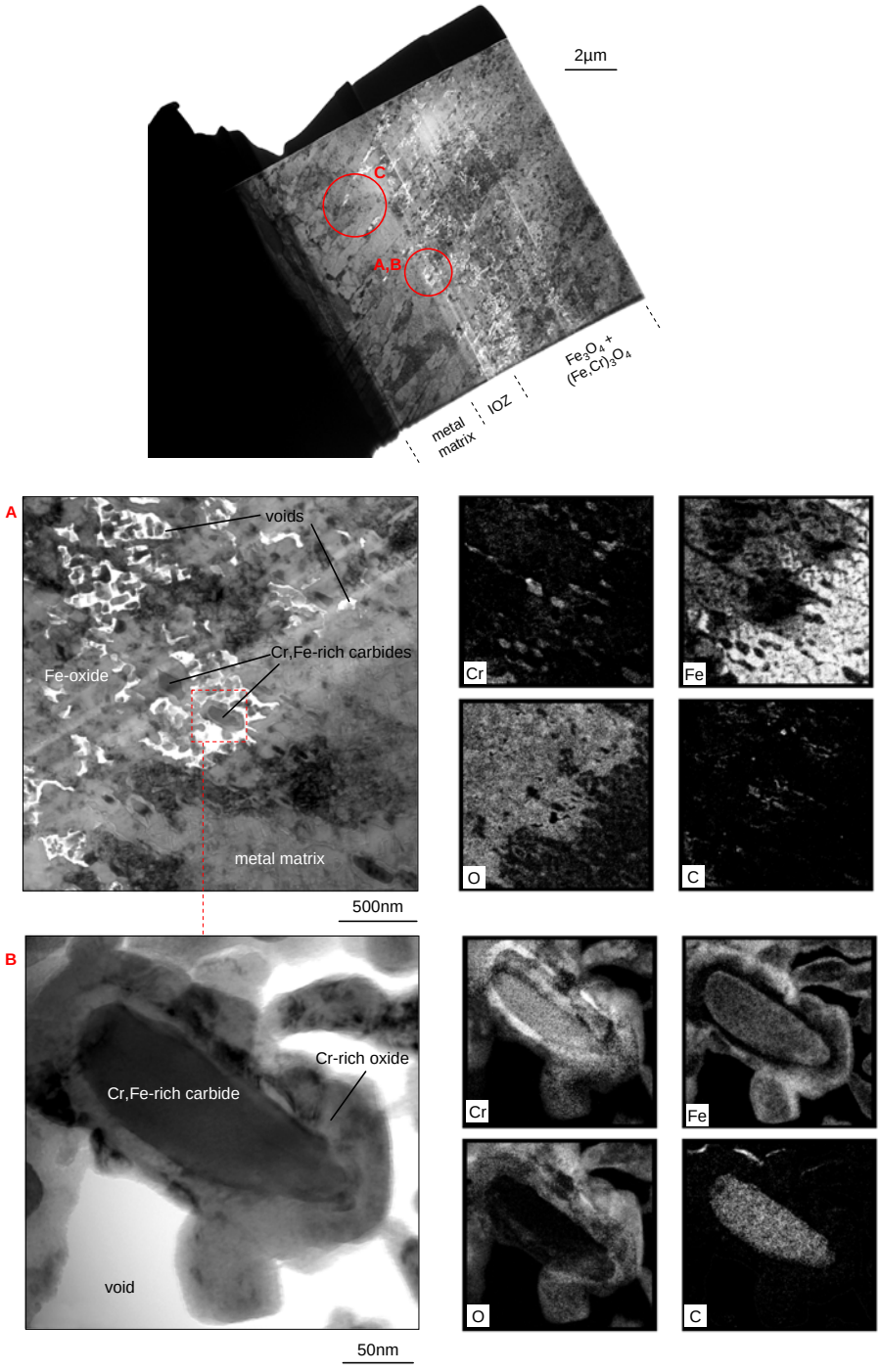

Figure 15.11: TEM lamella showing details of microstructure (upper figure) from the inner oxide scale formed on P92 after 100h isothermal exposure to CO_2/H_2O at 550°C and corresponding TEM cross sections (below) as well as X-ray mappings from the marked areas: A, B – interface between non-oxidized metal and IOZ (internal oxidation zone); C- internal oxidation zone (Figure B shows higher magnification from the part of the Figure A). See also Appendix for more TEM results

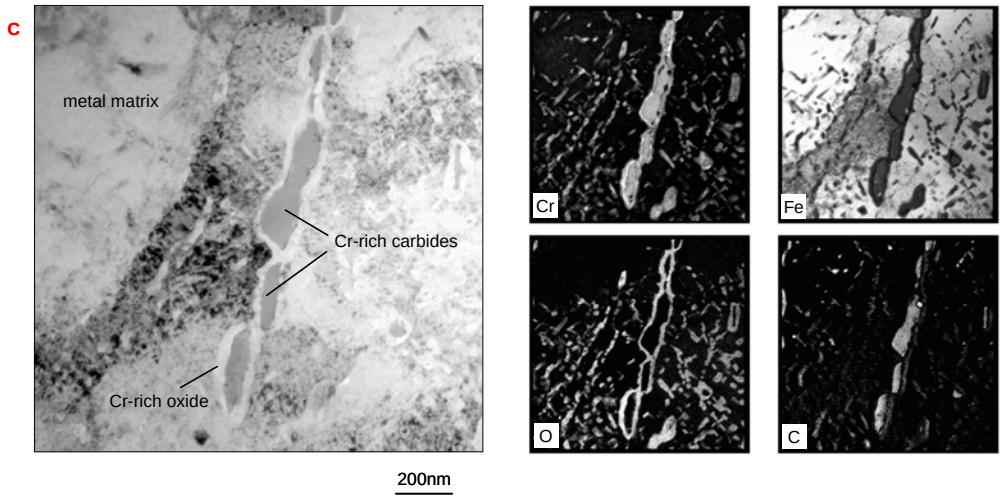

Figure 15.11: Continued

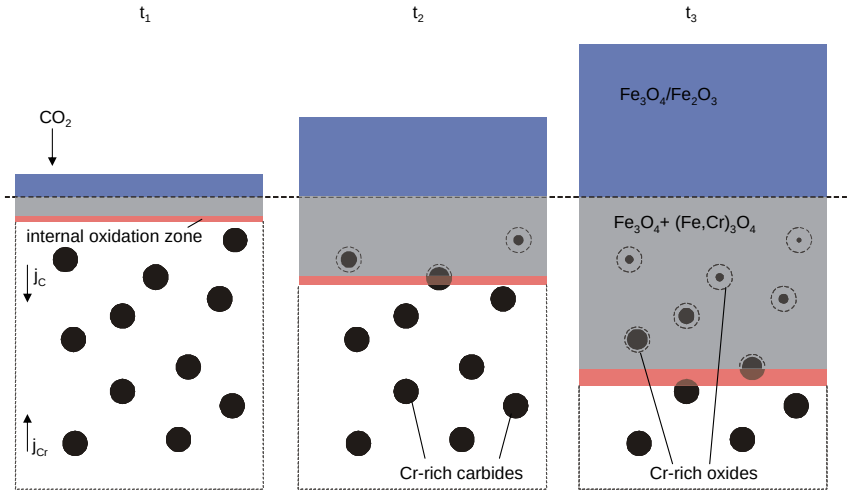

Figure 15.12: Mechanism of carburization of 9-12% Cr steels in CO_2-containing atmospheres:

t_1: Molecular transport of carbon through the oxide and formation of (mainly) Fe-rich oxides and Cr-rich carbides

t_2: Internal oxidation zone and inner oxide layer „consumes" part of the carbides which are oxidized to Cr-rich oxide

t_3: Carbides formed in the early stages are gradually transformed into oxide in the surface scale

The TEM results in Fig. 15.11 confirm that Cr-rich carbides undergo a transformation into oxides within the inner oxide layer. Moreover, large amounts of voids were found in the vicinity of the embedded carbide precipitations which were gradually being oxidized. This strongly indicates that some of the gaseous compounds were indeed formed during the carbide-oxide transformation process.

An important finding in the current investigation is that the presence of water vapour in atmospheres containing CO_2 significantly reduced the rate of carburization of 9-12% Cr steels (Fig. 15.8). This finding was generally observed at all test temperatures. A typical example of this finding is presented in Fig. 15.13 where etched cross sections of HCM12 after 600°C exposure in dry and wet CO_2 show a much wider carburization zone in the dry atmosphere. The quantitative data obtained by GDOES measurements of several specimens isothermally exposed to Ar/CO_2 and CO_2/H_2O for short times are presented in Fig. 15.10. The effect of water vapour on the carburization process can be explained if one assumes that carbon transfer from the atmosphere into the metal depends on the gas permeability of the surface oxide scales and on the competitive adsorption of the various gas molecules on the reaction surfaces, i.e., mainly the scale/steel interface. Anghel *et al*. [163] showed that the tendency for adsorption on oxidized chromium exhibits the following ranking:

$$H_2O^{(g)} > CO^{(g)} > H_2{}^{(g)} > N_2{}^{(g)}$$

In mixed gases the presence of water vapour results in blocking of the adsorption sites for the other gas species. Zheng and Young [96] found subscale nitride formation for pure Cr in N_2-CO-CO_2 but not in N_2-H_2-H_2O and explained the results in terms of a competitive adsorption of the various gas species. Apparently the tendency of adsorption of $H_2O^{(g)}$ is larger than that of $N_2{}^{(g)}$ and especially $CO^{(g)}$. Based on the present results it seems likely, that $H_2O^{(g)}$ adsorption is also faster than that of $CO_2{}^{(g)}$. Preferential adsorption of water vapour on oxide surfaces in mixed gas environments was also reported by Grabke [164].

The temperature dependence of carburization depth of P92 and VM12 is presented in Fig. 15.14. For P92 increasing temperature resulted in the formation of a wider carburization zone, while for VM12 decrease of the carburization depth was observed when exposure was conducted at temperatures at and above 650°C.

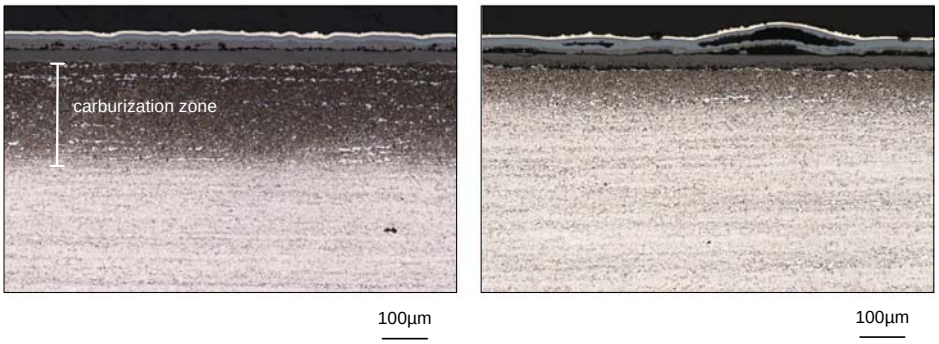

Figure 15.13: Etched cross sections of HCM12 after 1000h exposure in Ar/CO_2 (left) and CO_2/H_2O (right) at 600°C

The difference is attributed to the varied Cr content in the two steels. As discussed in Chapter 9, at higher temperatures larger amounts of Cr were incorporated into the oxide scale of VM12 than in the case of P92, thus promoting the protective properties of the scale and consequently decreasing permeability of CO_2 in the scale.

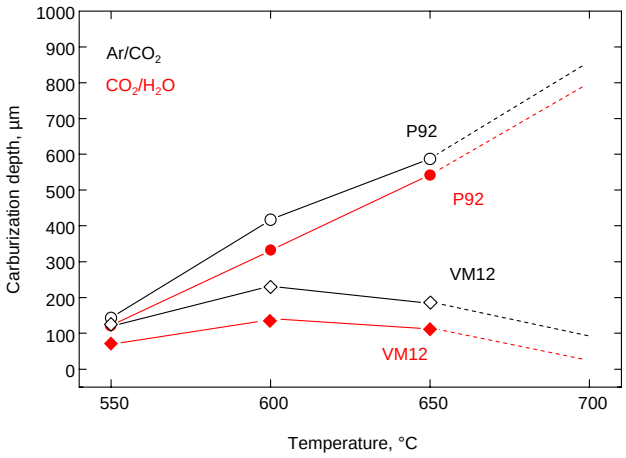

Figure 15.14: Temperature dependence of carburization depth (measured from metallographic cross sections) for P92 and VM12 after 1000h oxidation in Ar/CO_2 (black) and CO_2/H_2O (red)

The dashed lines in Fig. 15.14 show the decreasing tendency of the carburization depth for VM12 and increasing in the case of P92. It has to be mentioned that at 700°C the carburization zone formed on 9-12% Cr martensitic steels was clearly visible but no precise measurements of its depth could be done since the boundary between carburization zone and the steel matrix was hardly distinguished (Fig. 15.15). At this temperature the depth of the carburization zone seemed to be the highest, however, the density of carbide precipitations was relatively low compared

with that at lower temperatures. Thus, at the highest test temperature the values from Fig. 15.14 do not represent the exact carburization depth. They just give an indication about the depth of the metallographically clearly visible zone of enhanced carbide formation.

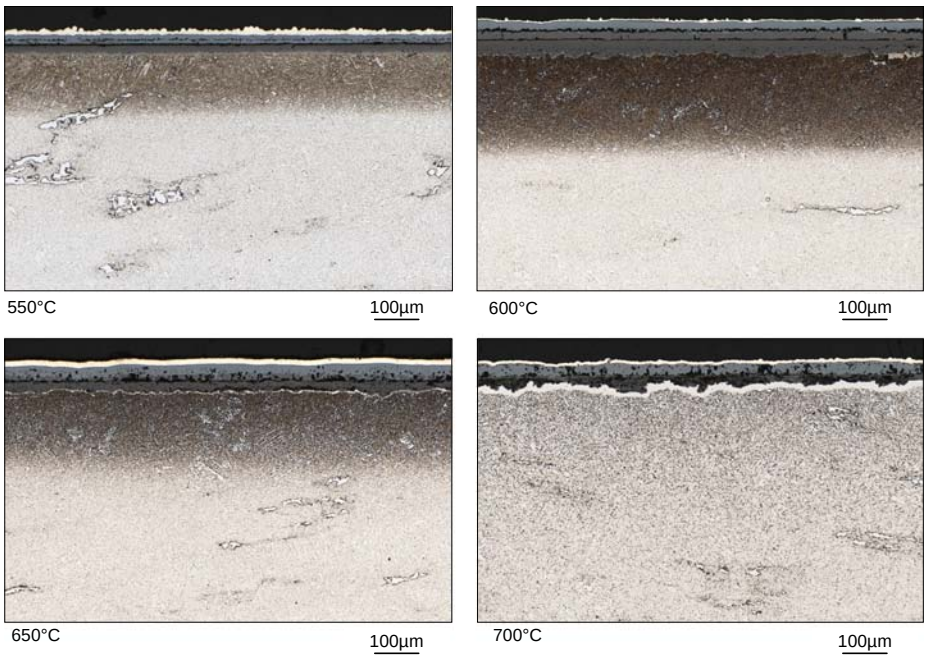

Figure 15.15: Metallographic etched cross sections of VM12 after 1000h exposure to Ar/CO_2 at 550-700°C

At 650°C and 700°C the relative amount of Cr in the oxide scale increases which is clearly verified by the fact that a carbide-free zone is visible at the scale/steel interface. The occurrence of this carbide-free zone was caused by the chromium depletion in the alloy resulting from enhanced incorporation of this element into the oxide scale. As shown in Chapter 9 this was also accompanied by vanishing of the internal oxidation zone. The enhanced Cr incorporation resulted in more protective properties of the scale, i.e., the scale exhibited a lower growth rate and became less permeable for CO_2 molecules.

As indicated in the ternary Fe-Cr-C phase diagram (Fig. 15.16) different types of Cr-base carbides can be formed when martensitic 9-12% Cr steels are exposed to CO_2-containing atmosphere. If the carbon uptake during the carburization process at 550°C is less than approximately 1.4at.% for P92 and 2.0at.% for VM12, respectively, formation of $(Fe,Cr)_{23}C_6$ is expected to occur exclusively. This would be, for instance, the case for P92 exposed to Ar/CO_2 for 24h. However, the phase diagram clearly indicates that when VM12 is exposed to the same

conditions, $(Fe,Cr)_7C_3$ becomes the stable carbide because the total carbon uptake was found to be significantly higher than that of P92. Depending on the local carbon concentration in the steel the formation of either $(Fe,Cr)_{23}C_6$ or $(Fe,Cr)_7C_3$ would therefore be expected (Fig. 15.17).

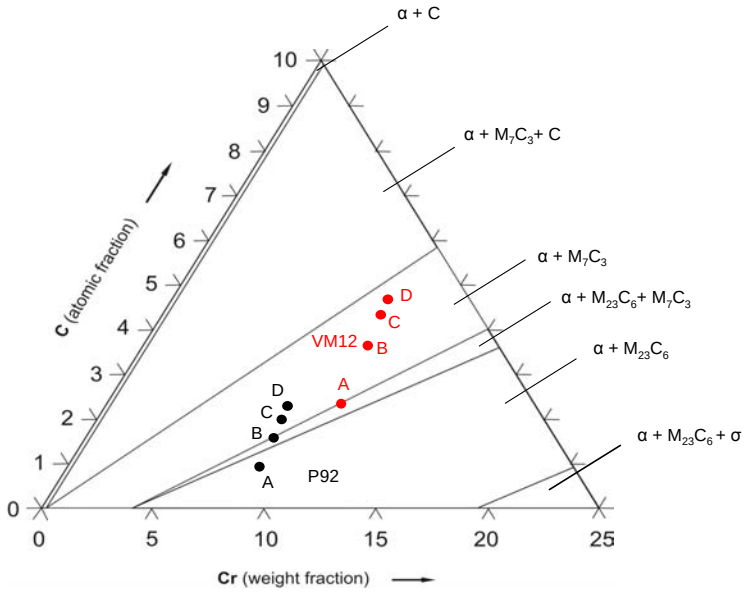

Figure 15.16: Ternary Fe-Cr-C phase diagram at 550°C calculated using Thermocalc software. The black and red points represent the maximum carbon uptake measured by GDOES for P92 and VM12 respectively (see Fig. 5.10) after isothermal exposure to Ar/CO_2 for: A-24h; B-50h; C-100h and D-150h

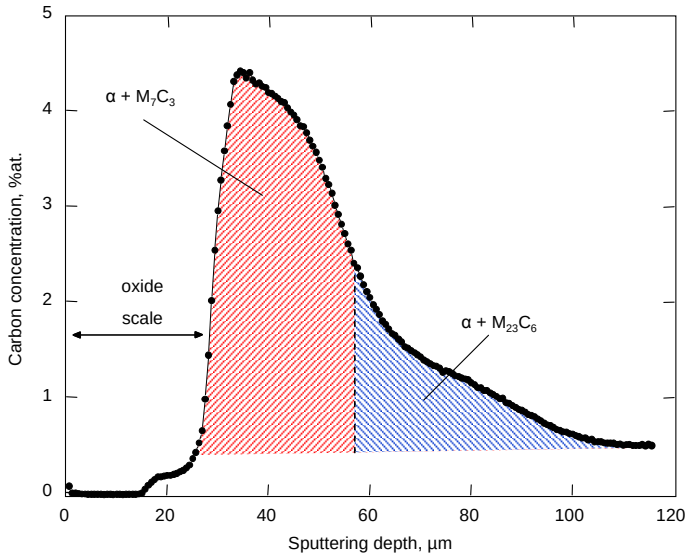

Figure 15.17: Carbon profile in VM12 measured by GDOES after 100h isothermal exposure to Ar/CO_2 at 550°C

Similar observations were recently made by Rouillard *et al*. [153] based on results from steel T91 oxidized in dry CO_2 at 550°C. The authors measured the carbon concentration near the metal/spinel oxide boundary by GDOES and showed that after 322 and 1000h the carbon uptake was 2.5at.% and 2.7at.% respectively. They subsequently concluded that after 322 h there was still a small fraction of chromium carburized in $M_{23}C_6$ carbides. Additionally they proposed that carbides formed preferentially at prior austenite grain boundaries and subgrain boundaries where carbon diffused fast and where the interfacial energy of carbide formation was lower.

15.6 Effect of oxygen on carburization behaviour

No quantitative GDOES data are provided in this study of the carburization behaviour in CO_2-rich atmospheres with oxygen addition. However, a large number of microscopic observations suggested that addition of 3% oxygen in the Ar/CO_2 or CO_2/H_2O atmosphere has no clear effect on carburization or, at least, it could not be observed from metallographic cross sections (Figs. 15.18-19). The general finding is that the rate of carburization is strongly affected by the protective properties of the oxide scale, i.e., smaller carbon uptake would be expected if a more protective oxide scale is formed. It was already presented in Chapter 10 that addition of small amounts of oxygen into Ar/CO_2 had a beneficial effect on the formation of a Cr-base scale at 550°C. Obviously, in such cases carburization would be significantly hampered. However, when no protective Cr-rich scale developed on the metal surface, no significant effect of oxygen in dry or wet gas on carburization behaviour was observed.

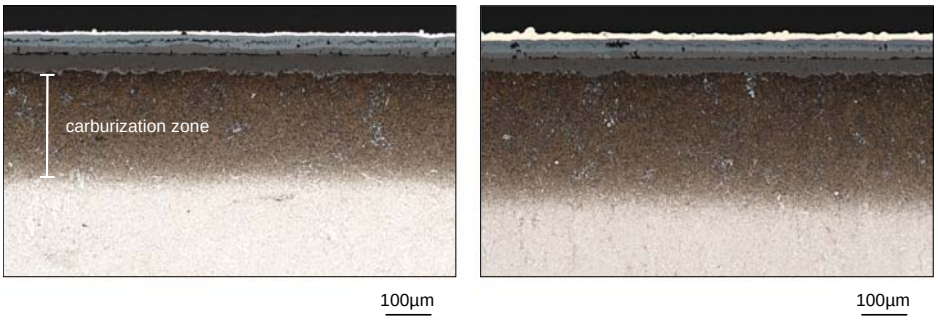

Figure 15.18: Etched cross sections of VM12 after 1000h exposure to Ar/CO_2 (left) and $Ar/O_2/CO_2$ (right) at 600°C

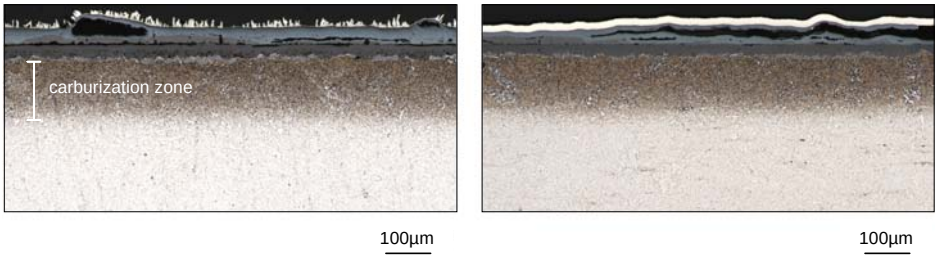

Figure 15.19: Etched cross sections of VM12 after 1000h exposure to CO_2/H_2O (left) and $Ar/O_2/CO_2/H_2O$ (right) at 600°C

15.7 Carburization of austenitic steels

When considering possible carburization of austenitic steels in CO_2-rich gases it has to be born in mind that $M_{23}C_6$ precipitates are already present in the alloy in the as-received condition, especially at grain boundaries. This is illustrated in Fig. 15.20. During air exposure, the depletion of chromium as a result of the formation of a Cr-rich oxide scale resulted in the formation of a zone in which the carbides were dissolved. Similar to the findings for the 9-12% Cr steels, formation of a protective chromia base scale on the metal surface in CO_2-rich gas protects the austenitic steels against carburization attack.

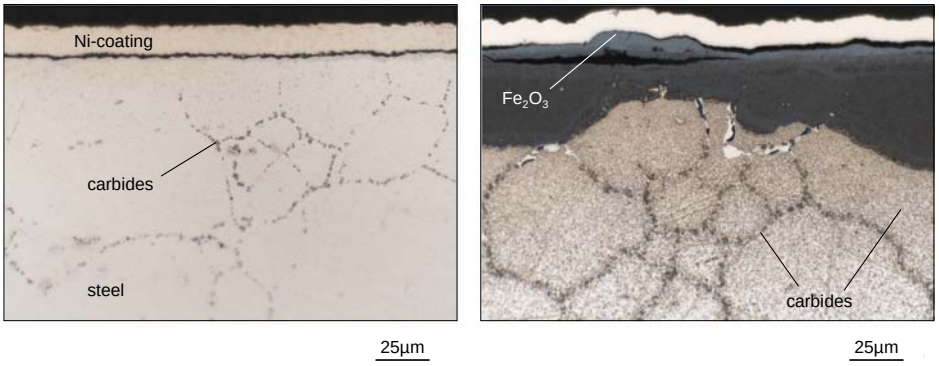

Figure 15.20: Etched metallographic cross sections of TP347H FG after 1000h exposure to laboratory air (left) and to Ar/CO_2 (right) at 700°C

However, minor carburization was frequently observed to occur in some cases, especially after prolonged exposure times (Fig. 15.21). When the initial protective chromia base scale formed in CO_2-rich gases undergoes failure, Fe-base oxide scales would develop on the metal surface. This subsequently resulted in the formation of a carburization zone beneath the oxide scale (Fig. 15.20) in a similar way as described for the martensitic steels. The carburization

preferentially occurred along the steel grain boundaries where $M_{23}C_6$ type carbides were formed. However, upon prolonged exposure the grain interior could also undergo carburization where presumably M_7C_3 carbides precipitated.

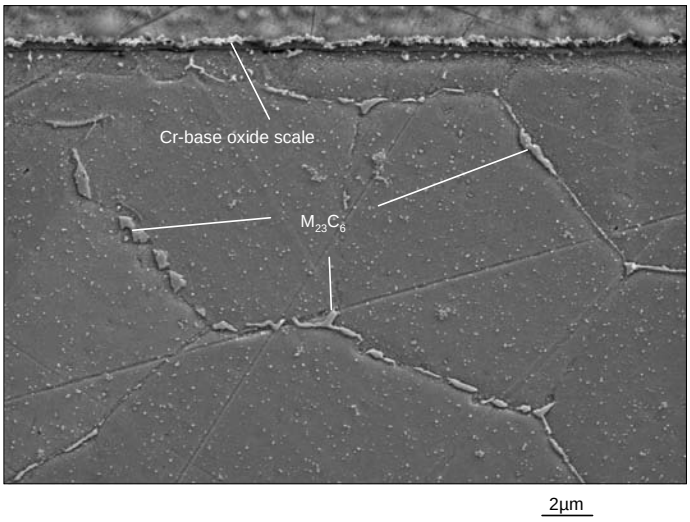

Figure 15.21: SEM image of the cross section of 1.4910 after 1000h exposure to Ar/CO_2 at 650°C

Due to technical reasons, GDOES measurements on austenitic steels are unreliable because the materials usually show extensive outer oxide scale spallation. Therefore, a number of hardness measurements were carried out in order to investigate the extent of carburization in the case of austenitic steels. The obtained results clearly indicate that carbon ingress into the bulk metal resulted in significant increase of the material hardness (Fig. 15.22) which reached the highest values just beneath the inner oxide layer. The carburization zone was approximately 100µm deep in the discussed example from Fig. 15.22 as clearly revealed by the etching process. However, it is believed that the carbon uptake along the grain boundaries extended to a much larger depth than within the grains. The quantitative evaluation of the carburization rate is therefore more problematic than for the 9-12% Cr steels. The effect of water vapour in CO_2-containing atmospheres on carburization behaviour seemed to be qualitatively similar to that observed for the martensitic steels, i.e., presence of H_2O reduced the carbon ingress from the atmosphere (Fig. 15.23). The comparison of cross sections in Fig. 15.23 provides some evidence that not only the carburization depth was smaller after exposure in wet gas but apparently also the amount of precipitated carbides within the austenite grains was lower. These findings are in good agreement with the previous observations about the positive effect of water vapour on decreasing the carburization rate during exposure of the martensitic steels to CO_2-rich atmospheres.

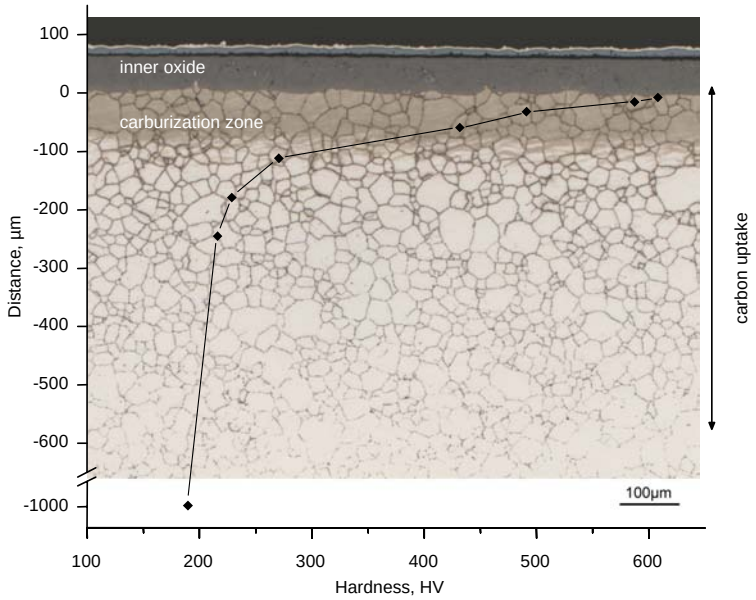

Figure 15.22: Hardness measurement on metallographic cross section of 1.4910 after 1000h exposure to $Ar/O_2/CO_2$ at 650°C

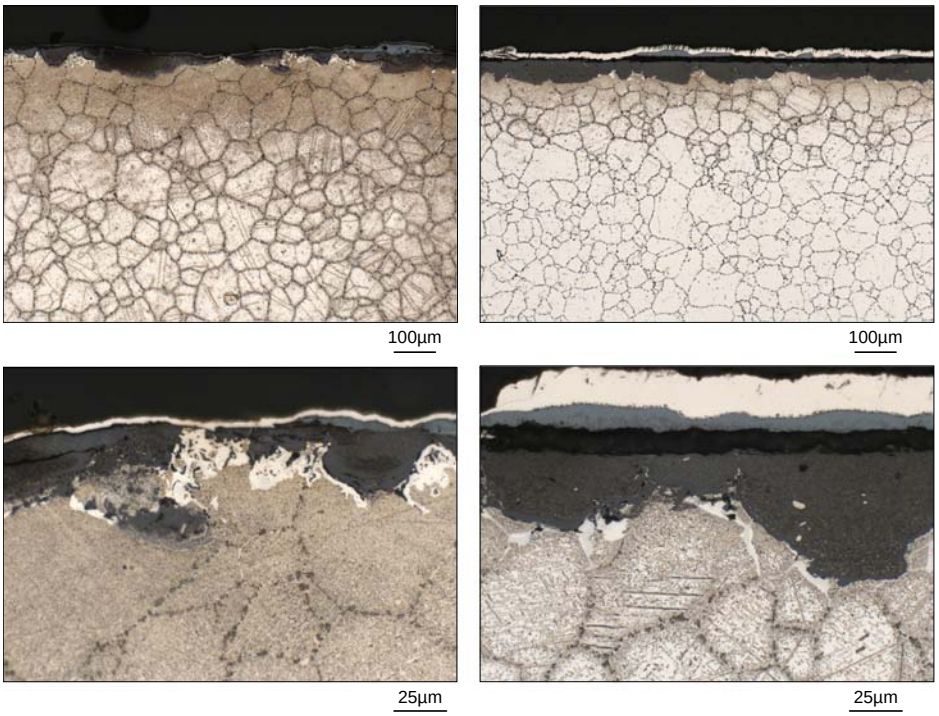

Figure 15.23: Etched cross sections of TP347H FG after 1000h exposure to $Ar/O_2/CO_2$ (left) and $Ar/O_2/CO_2/H_2O$ (right) at 700°C (bottom pictures show higher magnifications of the surface-near regions)

16. Effect of SO_2 on oxidation and carburization behaviour of martensitic steels

As the oxy-fuel flue gases contain considerably higher amounts of SO_2 than those of conventional air firing, it is important to investigate the effect of high amounts of sulfur dioxide on the oxidation behaviour of candidate materials for the heat exchanging components. In this chapter the effect of SO_2 on the oxidation behaviour is briefly described thereby placing the main emphasis on the effect of SO_2 addition on the carburization behaviour in CO_2-rich atmospheres. Fig. 16.1 presents the GDOES profiles of the major scale forming elements of VM12 after isothermal exposure to Ar/CO_2 and $Ar/CO_2/SO_2$ at 550°C. It can be seen that in the latter case the extent of carburization is significantly smaller than after exposure to Ar/CO_2.

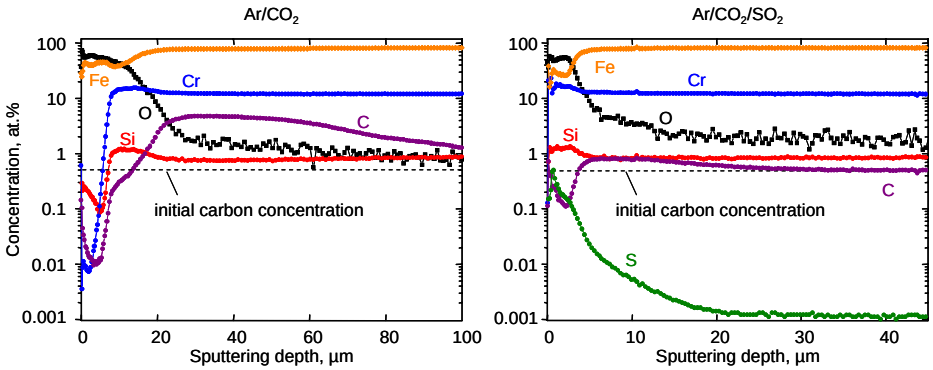

Figure 16.1: GDOES profiles of VM12 after 250h isothermal exposure to Ar/CO_2 (left) and $Ar/CO_2/SO_2$ (right) at 550°C

This was additionally confirmed by metallographic cross sections (Fig. 16.2) in which a well distinguished carburization zone was found after electrolytic etching of VM12 exposed to Ar/CO_2 but hardly any carburization zone was formed in the case of $Ar/CO_2/SO_2$.

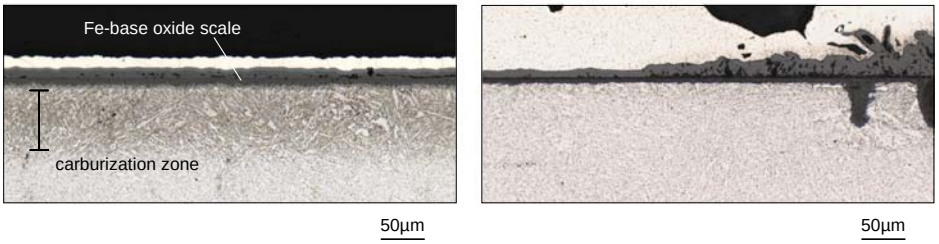

Figure 16.2: Metallographic etched cross sections of VM12 after 250h isothermal oxidation in Ar/CO_2 (left) and $Ar/CO_2/SO_2$ (right) at 550°C

Using the concentration profiles of carbon, it is possible to quantify the total carbon uptake in a similar way as it was done and presented in Chapter 15. The calculations revealed that after 250h isothermal exposure at 550°C to Ar/CO_2 the carbon uptake for VM12 was 0.41 mg/cm^2, whereas in the atmosphere containing additionally 0.5vol.% of SO_2 the carbon uptake was only 0.005 mg/cm^2. The obtained results thus show that the carbon uptake was reduced by approximately a factor of 82 due to the addition of only a small amount of SO_2 to Ar/CO_2. As shown in Fig. 15.8 and 15.10 in Chapter 15, the carbon uptake for VM12 was only decreased by a factor of 2.7 to 4.2 (depending on the exposure time) due to the water vapour addition in CO_2. The same calculations for P92 revealed that after 250h exposure at 550°C carbon uptake was reduced by a factor of 18 if 0.5vol.% of SO_2 was introduced to Ar/CO_2, while the carbon uptake in CO_2/H_2O comparing with Ar/CO_2 was only reduced by a factor between 2.1-2.4 (depending on the exposure time). The comparison of carbon profiles obtained after exposure to atmospheres discussed in this chapter for VM12 and P92 are given in Fig. 16.3.

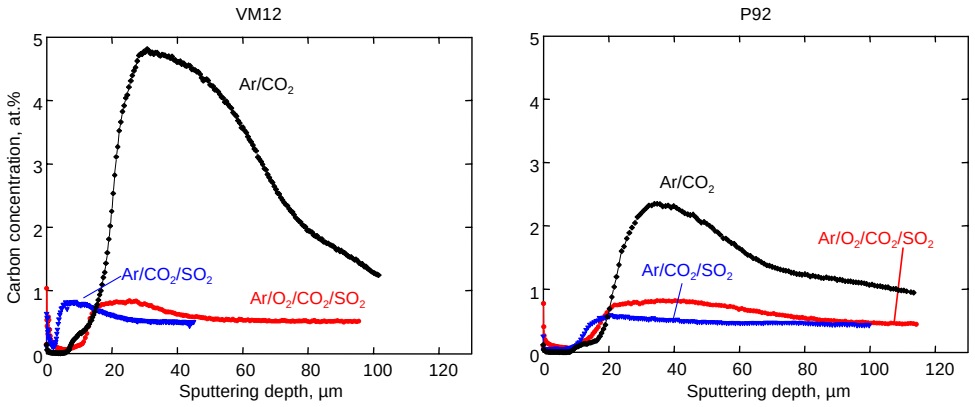

Figure 16.3: GDOES carbon profiles for VM12 (left) and P92 (right) after 250h isothermal oxidation in Ar/CO_2 (black), $Ar/CO_2/SO_2$ (blue) and $Ar/O_2/CO_2/SO_2$ at 550°C

The surface oxide scales on the 9-12% Cr steels after exposure to $Ar/CO_2/SO_2$ showed a duplex structure. The X-ray analysis revealed that both magnetite and iron sulfide had been formed on the metal surface. Additionally, a substantial fraction of voids within the outer scale was found (Figs. 16.4-6). The simultaneous formation of both sulfide and oxide in the outer scale indicates that no equilibrium was established between oxide surface and gas atmosphere. As suggested by McAdam and Young [165] the formation of FeS and Fe_3O_4 results from the following reaction:

$$\tfrac{5}{2}Fe + SO_2 = FeS + \tfrac{1}{2}Fe_3O_4 \qquad \text{(Eq. 16.1)}$$

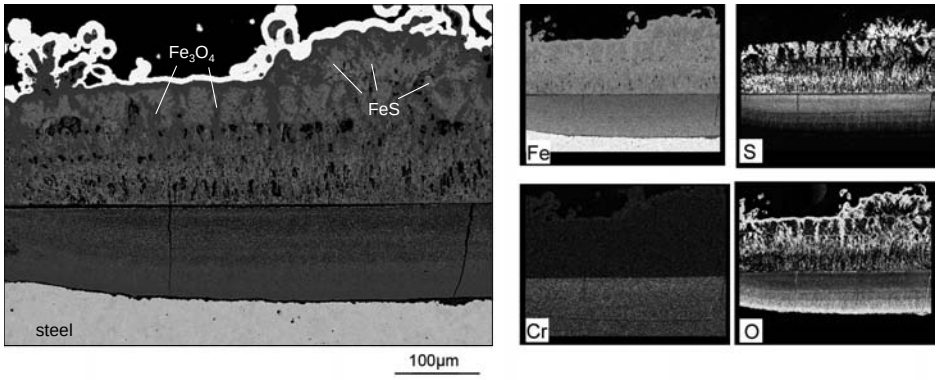

Fig. 16.4: SEM image of the cross section of 13CrMo4-4 and corresponding X-ray mapping after 250h isothermal oxidation in $Ar/CO_2/SO_2$ at 550°C

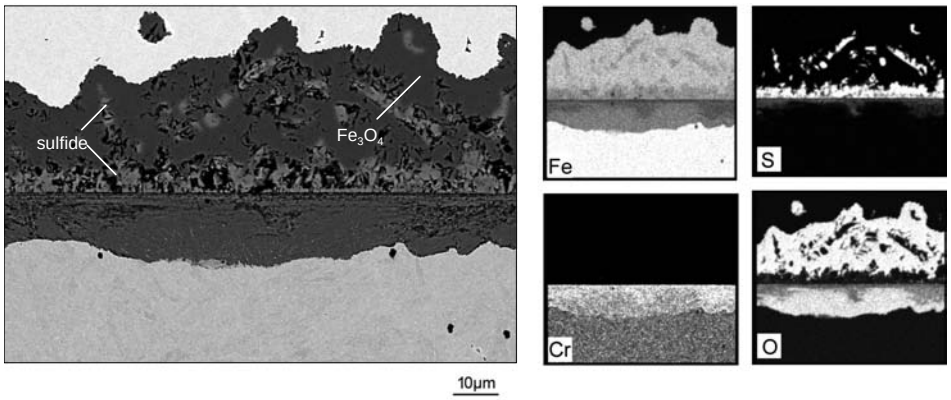

Fig. 16.5: SEM image of the cross section of P92 and corresponding X-ray mapping after 250h isothermal oxidation in $Ar/CO_2/SO_2$ at 550°C

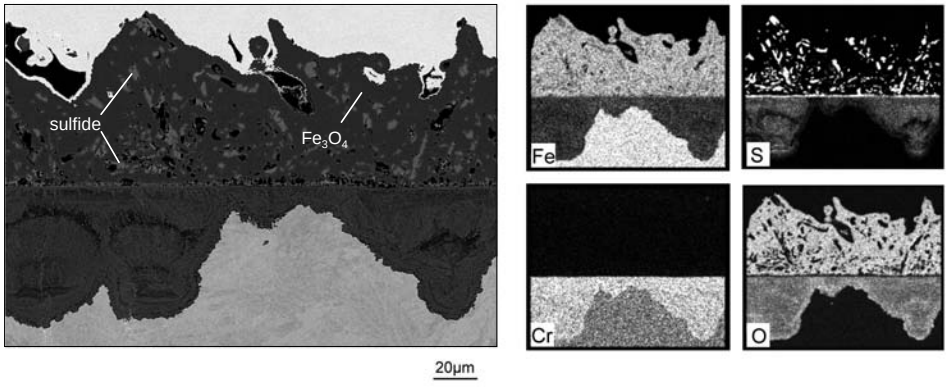

Fig. 16.6: SEM image of the cross section of VM12 and corresponding X-ray mapping after 250h isothermal oxidation in $Ar/CO_2/SO_2$ at 550°C

The composition of the formed sulfides varied from one alloy to another. A clear tendency was observed that among the formed sulfides the smallest atomic fraction of Fe was found for the steel containing the highest amount of Cr (Tab. 16.1).

This finding indicates that for high chromium steels outward cation diffusion from the bulk steel through the scale is significantly hampered and as a consequence the iron activity in the outer oxide scale is lower than in the case of steels containing smaller amounts of chromium. When the Cr concentration in the bulk steel is low, formation of a protective inner spinel layer is not possible, thus no barrier for fast iron diffusion exists. In fact, the X-ray mapping in Figs. 16.5-6 shows substantial chromium enrichment in the inner oxide scales of P92 and VM12. Based on data from Tab. 16.1 a rough estimation shows that the composition of the formed sulfides in the outer oxide scale varied from FeS to Fe_7S_8. The element mapping from Figs. 16.4-6 also shows some sulfur enrichment in the inner oxide scale, however, the chemical composition in this part of the scale has not been investigated.

	Fe	**S**	**O**
13CrMo4-4	50.0	50.0	0.0
	49.8	50.2	0.0
P92	45.6	54.4	0.0
	45.4	53.4	1.2
VM12	43.9	56.1	0.0
	42.9	57.1	0.0

Table 16.1: Chemical composition (in at.%) of analyzed sulfides in outer oxide scale from specimens in Figs. 16.4-6

The simultaneous formation of both oxide and sulfide at the scale-gas interface has been described in the literature to occur due to kinetic reasons [165-168]. The formation would occur when either the transport of the oxidant from the gas to the surface of the scale or the reaction at the scale/gas interface is the rate determining step in the overall oxidation process. An excess of metal ions reacts with the various gas species. Oxide and sulfide should then be intermixed and linear corrosion kinetics would be observed. In the case of the reaction of iron with SO_2 the presence of FeS in the scale facilitates the outward diffusion of iron which reacts with whichever partner is present on the surface of the scale [169]. This mechanism also explains the experimental observation that the formation of Fe_2O_3 was suppressed, although under

thermodynamic equilibrium conditions hematite should be stable at the gas/oxide interface, according to the Fe-S_2-O_2 stability diagram (Fig. 16.7).

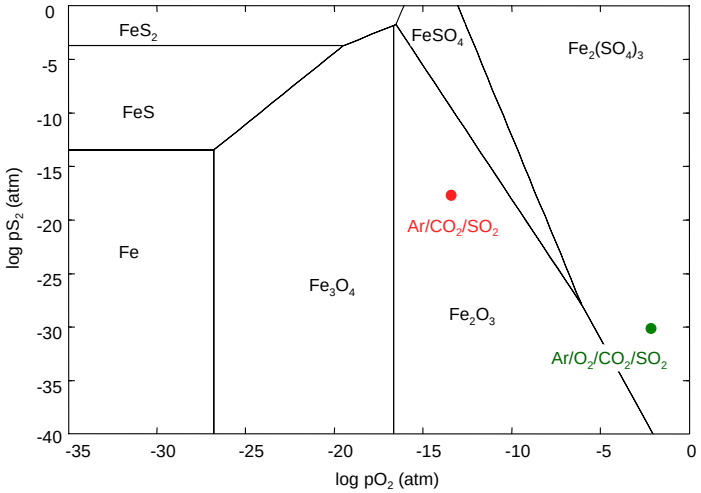

Figure 16.7: Fe-S_2-O_2 stability diagram at 550°C. Red and green points indicate location of test gases Ar/CO_2/SO_2 and Ar/O_2/CO_2/SO_2 in the case of thermodynamic equilibrium. Calculated using Factsage software

Considering the stability diagram for Fe-S_2-O_2, it is apparent that the equilibrium oxygen partial pressure of the gas in Ar/CO_2/SO_2 is sufficiently high for hematite formation. It is obvious that the stability diagram only describes the phase to be formed if equilibrium between gas atmosphere and the scale surface prevails. This equilibrium condition does not prevail in the early steps of reaction. Under these non-equilibrium conditions, e.g., oxides and sulfides may form simultaneously in an atmosphere containing oxygen and sulfur species. Such mixed scales commonly allow rapid cation transport from the scale/metal towards the scale/gas interface [165]. This implies that the metal activity at the scale surface remains high up to long exposure times and thus conditions for simultaneous oxide and sulfide formation are retained as observed, e.g., in Ar/CO_2/SO_2 (Figs. 16.4-6). Thus, the fact that after 250h exposure to Ar/CO_2/SO_2 at 550°C a mixture of Fe-base oxide and sulfides still prevailed is a clear proof that the scale surface and the gas atmosphere were not in thermodynamic equilibrium. The Fe activity at the scale surface is substantially higher and correspondingly the oxygen partial pressure is lower than would be the case if equilibrium prevailed. The oxygen activity is apparently lowered by the SO_2 addition to such an extent that it is below the dissociation pressure of hematite. A similar explanation was given by Young *et al.* [170] for the observation during oxidation of iron and manganese at 800°C in CO/CO_2/SO_2/N_2.

The suppression of carburization by an SO_2 addition was also found in $Ar/O_2/CO_2$. The obtained data for VM12 showed that the carbon ingress after 250h exposure to $Ar/O_2/CO_2/SO_2$ was 0.0086 mg/cm^2 which is a slightly higher value than that obtained for the low pO_2 atmosphere, i.e., $Ar/CO_2/SO_2$ (0.005 mg/cm^2). This might be surprising at first sight because in $Ar/O_2/CO_2/SO_2$ the carbon activity is several orders of magnitude lower than that in $Ar/CO_2/SO_2$; at 550°C it is $9x10^{-24}$ for $Ar/O_2/CO_2/SO_2$ and $2.2x10^{-13}$ for $Ar/CO_2/SO_2$. As already mentioned in Chapter 15, the extent of carburization is mainly governed by the gas permeability of the oxide scale rather than by the exact equilibrium carbon activity of the gas. The transfer of carbon to the alloy is affected by competitive adsorption at internal interfaces. Apparently the blocking of CO_2 (or CO) adsorption sites by H_2O and SO_2 is more substantial than that by oxygen.

Although the carburization rates of VM12 in $Ar/O_2/CO_2/SO_2$ and $Ar/CO_2/SO_2$ are quantitatively similar (comparing to those in the SO_2-free atmosphere), the morphology of the oxide scales formed in the two gases differ considerably. The GDOES profile of VM12 combined with the SEM cross section (Fig. 16.8) shows a sulfur enrichment in the inner oxide scale near the interface with the steel. The SEM cross section along with the X-ray mapping presented in Fig. 16.9 indicates that sulfur was not present in the outer oxide layer which was composed of magnetite and hematite exclusively.

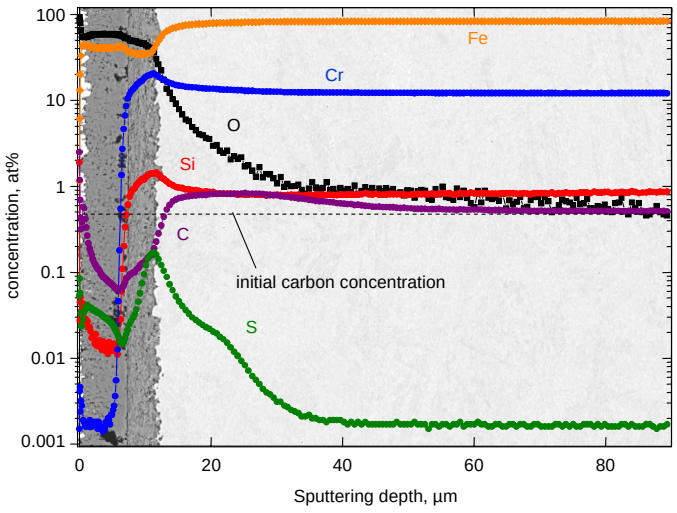

Figure 16.8: GDOES profiles of VM12 compared with SEM cross section after 250h isothermal oxidation in $Ar/O_2/CO_2/SO_2$ at 550°C

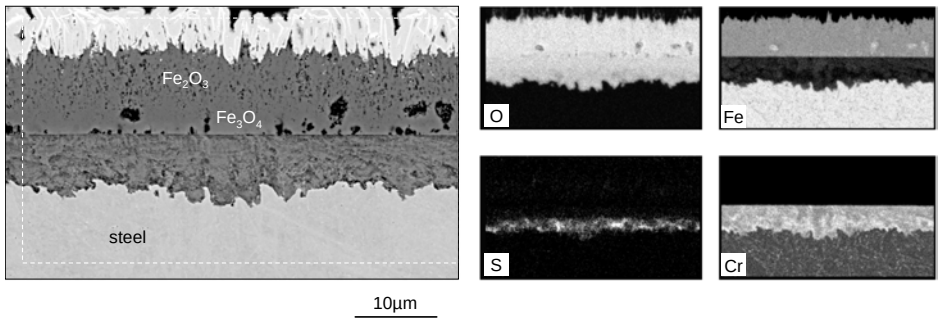

Fig. 16.9: SEM image of the cross section of VM12 and corresponding X-ray mapping after 250h isothermal exposure to $Ar/O_2/CO_2/SO_2$ at 550°C

It can be seen in Fig. 16.9 that a very low intensity of Fe was detected in the inner oxide scale where chromium and oxygen were enriched. A high content of S was also present in the inner oxide scale in the region close to the scale/steel interface. The EDX analysis did not allow to identify the exact nature of the sulfur containing phases in the inner oxide layer. However, based on the Cr-S_2-O_2 stability diagram (Fig. 16.10) it is believed that the sulfur enrichment was mainly related to the formation of CrS (most likely in equilibrium with Cr_2O_3). The quite low intensity of iron in the X-ray mapping together with oxygen suggests the existence of a minor amount of iron oxide, perhaps in the form of $(Fe,Cr)_3O_4$.

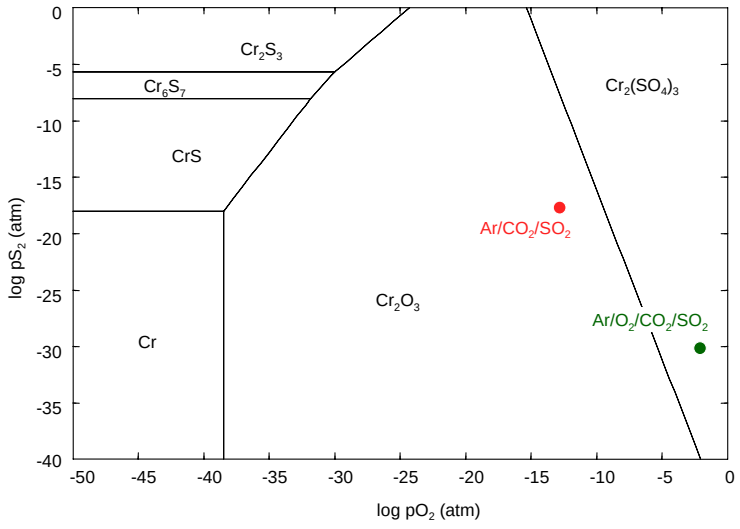

Fig. 16.10: Cr-S_2-O_2 stability diagram at 550°C. Red and green points indicate location of test gases $Ar/CO_2/SO_2$ and $Ar/O_2/CO_2/SO_2$ in the case of thermodynamic equilibrium. Calculated using Factsage software

As far as known to the author, no studies are available in the literature describing the effect of SO_2 on oxidation and especially carburization in CO_2 or O_2/CO_2. Investigations of the effect of minor SO_2 additions on the carburization process relate to atmospheres with high carbon activities, i.e., gases which are, e.g., rich in CO or CH_4. It is generally accepted that in such atmospheres a preferentially adsorbed layer of gaseous sulfur on an alloy surface reduces the ingress of carbon thus decreasing the carburization rate for, e.g., austenitic steels exposed to CH_4 or H_2/CH_4 with H_2S addition at temperatures of 950°C-1050°C [171]. This, however, cannot explain the observations made in the present study. The assumption of Flatley and Birks [172] additionally confirmed by McAddam and Young [165, 173] is that the SO_2 species reacts directly with the metal and does not dissociate first to provide O_2 and S_2 at the metal surface as the reactive species. The direct reaction of the SO_2 molecule with the metal has also been demonstrated by other authors [167, 169, 174, 175].

Considering the fact that in the present study, the sulfur activity was in all cases always extremely small (e.g., $pS_2=0.89x10^{-30}$ at 550°C in $Ar/O_2/CO_2/SO_2$), it might be difficult to give an easy explanation for such significant suppression of carbon uptake from the CO_2/SO_2-containing atmospheres (Fig. 16.3)

Nevertheless, a number of experiments performed by Young and Watson [170] with pure Cr at 900°C shows that a small addition of SO_2 (40ppm) to $CO/CO_2/N_2$ completely prevents nitrogen permeation through the scale and substantially decreases the rate of carbon ingress. The authors suggested that in $CO/CO_2/SO_2/N_2$ preferential adsorption of sulfur on oxide boundaries would be expected and the resultant blocking of internal surface sites could impede the surface diffusion of other species. The assumption was made that more reactive CO molecule can adsorb to some extent on the sulfur-poisoned grain boundaries, whereas the N_2 cannot. Since the $N_2^{(g)}$ and $CO_2^{(g)}$ molecules have the same size, it might be the case that CO_2 adsorption can also be significantly hampered by simple physical blockage of grain boundaries due to presence of SO_2.

Another possible explanation of the carburization reduction in CO_2/SO_2 atmospheres was proposed [170] that the rate of carbon diffusion in the alloy matrix, in the oxide or oxide + sulfide precipitation zone is decreased as a result of interactions between the dissolved oxidants. The thermodynamic interaction between sulfur and carbon can be described using an interaction coefficient, e_C^S given by Wagner:

$$e_C^S = \frac{\partial \log \gamma_C}{\partial (wt.\%S)} \qquad \text{(Eq. 16.2)}$$

where γ_C is the activity coefficient of carbon, and its dependence on solute sulfur concentration is explicit. Values for e_C^S have been estimated to be approximately 0.3. This implies a decrease in carbon solubility and also in diffusivity due to presence of sulfur. The latter explanation seems, however, not to be of great importance for the prevailing results because no clear indications of sulfur uptake into the alloy were found. Therefore, it is more likely that the suppression of carburization by presence of SO_2 is related to preferential adsorption of different gas species on the reacting external and internal surfaces.

17. Summary and conclusions

During exposure to the CO_2- and/or H_2O-containing atmospheres at temperatures in the range of 550-700°C the oxidation rate and scale composition of the low alloying steel 13CrMo4-4 was similar to those observed in steam environments. The 9-12% Cr ferritic/martensitic steels exhibited similar features that during oxidation in the mentioned test gases these steels tended to form multilayered Fe-base surface oxide scale, however, preceded by formation of a thin and protective Cr-base oxide. The time to breakaway of primarily formed scale depended mainly on the Cr content in the steel, microstructure and additions of minor alloying elements. It was found that silicon played an important role for improvement of the oxidation resistance.

The breakaway and failure of the initially formed protective chromia base scale was significantly reduced when 1% and especially 3% of oxygen was intentionally added to the Ar/CO_2 atmosphere. This effect was observed for all 9-12% Cr steels but was much more pronounced for materials with higher Cr content (VM12, HCM12). In contrast, oxygen addition in Ar/CO_2 did not significantly affect the oxidation rates of the low alloyed steel 13CrMo4-4. The oxidation behaviour of 13CrMo4-4 and the martensitic 9-12% Cr steels did not change substantially when 3% O_2 was introduced to the CO_2/H_2O test gas.

During exposure to the dry Ar/CO_2 and $Ar/O_2/CO_2$ test atmospheres the 9-12% Cr steels exhibited a so-called “bell shape” temperature dependence, i.e., the oxidation rates of these steels showed, above certain temperature, decrease of the scaling rate with increasing temperature. This effect was mainly related to the enhanced chromium mobility in the alloy at higher temperatures. This in turn resulted in higher Cr incorporation in the inner oxide layer so that a more protective oxide was formed to hamper Fe incorporation into the scale.

The Fe-base oxide scales formed on the ferritic/martensitic steels during exposure to the H_2O-containing atmospheres exhibited a strong tendency for the buckling of the outer oxide layer. This in turn, after prolonged exposure, frequently caused spallation and delamination from the outer oxide scale.

Enhanced Cr-rich carbide formation was observed for the 9-12% Cr steels exposed to CO_2-containing gases. The extent of carburization was reduced by the presence of water vapour. In the cases where Cr-rich oxide was formed on the metal surface, internal carburization could

not be detected. Therefore, it was assumed that Cr-base oxide scale was hardly permeable for CO_2 molecules. Carbide formation beneath the oxide scale was also observed in the case of austenitic alloys with lower Cr content. Presence of SO_2 in the CO_2-containing test atmospheres significantly reduced the extent of carbide formation.

The mechanisms responsible for breakaway of the initially formed Cr-base oxide scale and subsequent formation of the less protective Fe-rich oxide scales appeared to be similar in H_2O and CO_2-containing atmospheres. Although the dissolution of hydrogen and carbon in the steel, as a result of the reaction with H_2O or CO_2, respectively, had completely different effects on compound formation in the steel, the dissolution had the same effect on protective scale formation resulting in delayed transport of chromium towards the surface. In CO_2-containing atmospheres internal carbide formation was responsible for the decreased chromium transport towards the scale/metal interface. In H_2O-rich gases the incorporation of hydrogen in the steel resulted in higher oxygen solubility and/or diffusivity and consequently in enhanced internal oxidation of chromium.

The oxidation behaviour of austenitic steels strongly depended on the detailed alloy composition. The initial Cr concentration seemed to be a crucial factor determining the alloy oxidation resistance properties. At 550°C all studied austenitic steels exhibited very slow scale growth rates, while at and above 600°C steels with lower Cr content (<20%) started to form poorly protective Fe-base surface oxide scales. Depending on the atmosphere growth of separated oxide nodules due to local breakdown of the protective chromia scale or formation of a continuous oxide scale covering the entire metal surface was observed. In the latter case the outer oxide was prone to spallation upon thermal cycling. An increasing spallation rate was observed with increasing temperature.

Cold work applied by sandblasting significantly reduced the oxidation rate of austenitic alloys at temperatures up to 700°C by promoting the selective oxidation of chromium on the metal surfaces. Only a minor effect of cold work on the oxidation behaviour was observed at 700°C for the martensitic steels with lower Cr content (P92 and X20), whereas a significant improvement was found for VM12. At lower temperatures a positive effect of surface modification of the 9-12% Cr martensitic steels was not observed.

The high chromium austenitic steel 310N and the Ni-base alloy INCONEL 617 could, as a first approximation, be considered as chromia forming materials in the used temperature range up to 700°C. The presence of water vapour in combination with intentionally added oxygen led to the formation of volatile chromium oxyhydroxide. In the case of INCONEL 617 this resulted in a chromium loss which might become larger than the oxygen uptake by scale growth at 700°C, resulting in a net weight loss during prolonged exposure. For the austenitic steel 310N the additional loss of chromium by volatile oxyhydroxide formation resulted in a critical chromium depletion in the subscale zone, so that the pure chromia scale growth could no longer be sustained. Although the inner oxide was still Cr-rich, the outer scale consisted of Fe-base oxide resulting in higher growth rates than those found in the atmospheres which did not contain a combined addition of oxygen and water vapour.

18. References

1 IPCC Special Report on Carbon Dioxide Capture and Storage. Prepared by Working Group III of the Intergovernmental Panel on Climate Change, B. Metz, O. Davidson, H. C. de Coninck, M. Loos, L. A. Meyer (Eds.) Cambridge University Press, Cambridge, United Kingdom and New York, NY, USA (2005)

2 K. E. Zanganeh, A. Shafeen, C. Salvador, CO_2 Capture and Development of an Advanced Pilot-Scale Cryogenic Separation and Compression Unit, *Energ Procedia* (2009) **1**:247-252

3 E. Kakaras, A. Koumanakos, A. Doukelis, D. Giannakopoulos, I. Vorrias, Oxyfuel Boiler Design in a Lignite-Fired Power Plant, *Fuel* (2007) **86**:2144-2150

4 K. Natesan, Z. Zeng, Materials Performance In Advanced Steam Cycle and In Oxy-Fuel Combustion Systems, *Adv Sci Technol* (2010) **72**:1-11

5 B. J. P. Buhre, L. K. Elliott, C. D. Sheng, R. P. Gupta, T. F. Wall, Oxy-Fuel Combustion Technology for Coal-Fired Power Generation, *Prog Energ Combust* (2005) **31**:283-307

6 K. Jordal, M. Anheden, J. Yan, L. Strömberg, Oxyfuel Combustion for Coal-Fired Power Generation with CO_2 Capture – Opportunities and Challenges, Vattenfall Utveckling AB Stockholm- internal report

7 A Strategy for Developing Carbon Abatement Technologies for Fossil Fuel Use, Department for Trade & Industry, DTI/Pub URN 05/844, (2005)

8 D. W. Sturgeon, E. D. Cameron, F. D. Fitzgerald, Demonstration of an Oxyfuel Combustion System, *Energy Procedia* (2009) **1**:471-478

9 D. G. Chapel, C. L. Mariz, J. Ernest, Recovery of CO_2 from Flue Gases: Commercial Trends, Canadian Society of Chemical Engineers annual meeting, Saskatoon, Saskatchewan, Canada, (1999)

10 R. Bredesen, K. Jordal, O. Bolland, High-Temperature Membranes in Power Generation with CO_2 Capture, *Chem Eng Process* (2004) **43**:1129-1158

11 B. Bordenet, Influence of Novel Cycle Concepts on the High-Temperature Corrosion of Power Plants, *Mater Corros* (2008) **59**:361-366

12 A. Ellett, Oxygen Permeation and Thermo-Chemical Stability of Oxygen Separation Membrane Materials for the Oxyfuel Process, Report Forschungszentrum Jülich, Jülich FRG, *Energ Environ* (2009) **43** ISBN 978-3-89336-581-4

13 D. Singh, E. Croiset, P. L. Douglas, M. A. Douglas, Techno-Economic Study of CO_2 Capture from an Existing Coal-Fired Power Plant: MEA Scrubbing vs. O_2/CO_2 Recycle Combustion, *Energ Convers Manage* (2003) **44**:3073-3091

14 W. Blasiak, W. H. Yang, K. Narayanan, J. von Schéele, Flameless Oxyfuel Combustion for Fuel Consumption and Nitrogen Oxides Emissions Reductions and Productivity Increase, *J Energy Inst* (2007) **80**:3-11

15 F. Chatel-Pelage, M.Ovidiu, R. Carty, G. Philo, H. Farzan, S. Vecci, A Pilot Scale Demonstration of Oxy-Fuel Combustion with Flue Gas Recirculation in a Pulverized Coal-Fired Boiler, Proceedings 28th International Technical Conference on Coal Utilization & Fuel Systems, Clearwater, Florida, USA, (2003)

16 A. Kather, K. Mieske, C. Hermsdorf, M. Klostermann, D. Köpke, Oxyfuel Process for Hard Coal Power Plants with CO_2-Removal, 8th International Conference on Greenhouse Gas Control Technologies (GHGT-8), Trondheim, (2006)

17 Integrated Environmental Control Model (2005), Developed by Carnegie Mellon University for the U.S. DOE, National Energy Technology Laboratory. Publicly available at http://www.iecm-online.com/index.htm.

18 N. Otsuka, Fireside Corrosion, in: Shreir's Corrosion 4th Edition, Elsevier, Amsterdam, The Netherlands, (2010) **1**:457-481

19 J. R. Davis, Heat Resistant Materials, ASM Specialty Handbook, (1997) ISBN: 0871705966

20 N. Birks, G. H. Meier, F. S. Pettit, Introduction to The High-Temperature Oxidation of Metals, Cambridge University Press, Cambridge, UK, (2006)

21 B. Gleeson, Thermodynamics and Theory of External and Internal Oxidation of Alloys, in: Shreir's Corrosion 4th Edition, Elsevier, Amsterdam, The Netherlands, (2010) **1**:180-194

22 S. Chevalier, Mechanisms and Kinetics of Oxidation, , in: Shreir's Corrosion 4th Edition, Elsevier, Amsterdam, The Netherlands, (2010) **1**:132-152

23 P. Kofstad, High Temperature Corrosion, Elsevier Applied Science Publisher Ltd, London, UK, (1988)

24 C. Wagner, Beitrag zur Theorie des Anlaufvorgangs, *Zeitschrift für Physikalische Chemie* (1933) **B41:**25-41

25 G. Y. Lai, High-Temperature Corrosion And Materials Applications, ASM International, Materials Park, OH, USA, (2007)

26 D. J. Young, High Temperature Oxidation and Corrosion of Metals, Elsevier Linacre House, Oxford, UK, (2008)

27 N. Hussain, G. Schanz, S. Leistikow, K. A. Shahid, High-Temperature Oxidation and Spalling Behavior of Incoloy 825, *Oxid Met* (1989) **32**:405-431

28 B. Pujilaksono, T. Jonsson, H. Heidari, M. Halvarsson, J.-E. Svensson, L.-G. Johansson, Oxidation of Binary FeCr Alloys (Fe–2.25Cr, Fe–10Cr, Fe–18Cr and Fe–25Cr) in O_2 and in O_2 + H_2O Environment at 600°C, *Oxid Met* (2011) **75**:183–207

29 B. Pujilaksono, T. Jonsson, M. Halvarsson, I. Panas, J.-E. Svensson, L.-G. Johansson, Paralinear Oxidation of Chromium in O_2 + H_2O Environment at 600–700°C, *Oxid Met* (2008) **70**:163–188

30 E. J. Opila, D. L. Myers, N. S. Jacobson, I. M. B. Nielsen, D. F. Johnson, J. K. Olminsky, M. D. Allendorf, Theoretical and Experimental Investigation of the Thermochemistry of $CrO_2(OH)_2$(g), *J Phys Chem* A (2007) **111**:1971-1980

31 P. Y. Hou, Oxidation of Metals and Alloys, in: Shreir's Corrosion 4th Edition, Elsevier, Amsterdam, The Netherlands, (2010) **1**:195-239

32 L. W. Pinder, K. Dawson and G. J. Tatlock, High Temperature Corrosion of Low Alloy Steels, in: Shreir's Corrosion 4th Edition, Elsevier, Amsterdam, The Netherlands, (2010) **1**:195-239

33 G. H. Meier, K. Jung, N. Mu, N. M. Yanar, F. S. Pettit, J. P. Abellán, T. Olszewski, L. N. Hierro, W. J. Quadakkers, G. R. Holcomb, Effect of Alloy Composition and Exposure Conditions on the Selective Oxidation Behavior of Ferritic Fe-Cr and Fe-Cr-X Alloys, *Oxid Met* (2010) **74**:319-340

34 M. Schütze, Stress Effects in High Temperature Oxidation, in: Shreir's Corrosion 4th Edition, Elsevier, Amsterdam, The Netherlands, (2010) :153-179

35 H. Nickel, Y. Wouters, M. Thiele, W. J. Quadakkers, The Effect of Water Vapor on the Oxidation Behavior of 9% Cr Steels in Simulated Combustion Gases, *Fresenius J Anal Chem* (1998) **361**:540-544

36 N. K. Othman, J. Zhang • D. J. Young, Water Vapour Effects on Fe–Cr Alloy Oxidation, *Oxid Met* (2010) **73**:337-352

37 P.J. Ennis, W.J. Quadakkers, Mechanisms of Steam Oxidation in High Strength Martensitic Steels, *Int J Pres Ves Pip* (2007) **84**:75-81

38 W. J. Quadakkers, P. J. Ennis, J.Zurek, M. Michalik, Steam Oxidation of Ferritic Steels – Laboratory Test Kinetic Data, *Mater High Temp* (2005) **22**:47-60

39 A. Rahmel, J. Tobolski, Influence of Water Vapour and Carbon Dioxide on the Oxidation of Iron in Oxygen at High Temperatures, *Corros Sci* (1965) **5:**333-346

40 M. Schütze, P. F. Tortorelli, I. G. Wright, Development of a Comprehensive Oxide Scale Failure Diagram, *Oxid Met* (2010) **73**:389–418

41 B. J. Kooi, M. A. J. Somers, R. H. Jutte, E. J. Mittemeijer, On the Oxidation of α-Fe and ε-Fe_2N_{1-z}: II. Residual Strains and Blisters in the Oxide Layer, *Oxid Met* (1997) **48**:111-128

42 W. J. Quadakkers and J. Żurek, Oxidation in Steam and Steam/Hydrogen Environments, in: Shreir's Corrosion 4th Edition, Elsevier, Amsterdam, The Netherlands, (2010) **1**:407-456

43 G. R. Holcomb, Steam Oxidation and Chromia Evaporation in Ultrasupercritical Steam Boilers and Turbines, *J Electrochem Soc* (2009) **156**:292-297

44 M. R. Taylor, J. M. Calvert, D. G. Lees, D. B. Meadowcroft, The Mechanism of Corrosion of Fe-9% Cr Alloys in Carbon Dioxide, *Oxid Met* (1980) **14**:499-516

45 C. Gleave, J.M. Calvert, D.G. Lees, P.C. Rowlands, A Study of The Mechanism of Corrosion of Some Ferritic Steels In High-Pressure Carbon Dioxide with The Aid of Oxygen-18 as a Tracer. I Low-Silicon Mild Steel, *Proc R Soc Lond A.* (1982) **379**:409-427

46 J. Robertson, The Mechanism Of Carbon Deposition During The Breakaway Oxidation Of Steels In Carbon Dioxide, *Catal Today* (1990) **7**:267-276

47 C.S. Giggins, F.S. Pettit, Corrosion of Metals and Alloys in Mixed Gas Environments at Elevated Temperatures, *Oxid Met* (1980) **5:**363-413

48 G.H. Meier, W.C. Coons, R.A. Perkins, Corrosion of Iron- Nickel- and Cobalt-base Alloys in Atmospheres Containing Carbon and Oxygen. *Oxi Met* (1982) **17**:235-262

49 J.A. Colwell, R.A. Rapp, Reactions of Fe-Cr and Ni-Cr alloys in CO/CO_2 gases at 850 and 950 °C, *Metallurg Transact A* (1986) **17A**:1065-1074

50 P. Becker, D. J. Young, Carburization Resistance of Nickel-Base, Heat-Resisting Alloys, *Oxid Met* (2007) **67**:267-277

51 P. J. Ennis, K. P. Mohr, H. Schuster, Effect of Carburizing Service Environments on the Mechanical Properties of High-Temperature Alloys, *Nucl Technol* (1984) **66**:363-368

52 A. Schnaas, H. J. Grabke, High-Temperature Corrosion and Creep of Ni-Cr-Fe Alloys in Carburizing and Oxidizing Environments, *Oxid Met* (1978) **12**:387-404

53 H. M. Tawancy, N. M. Abbas, Mechanism of Carburization of High-Temperature Alloys, *J Mater Sci* (1992) **27**:1061-1069

54 C. T. Fujii, R. A. Meussner, Carburization of Fe-Cr Alloys During Oxidation in Dry Carbon Dioxide J *Electrochem Soc* (1967) **114**:435-442

55 H. J. Grabke, U. Gravenhorst, W. Steinkusch, Aufkohlung von Chrom-Nickel-Eisen-Stählen in der Kohlenstoffpackung *Werkst Korros* (1976) **27**:291-296

56 D. J. Young, Carburization and Metal Dusting, in: Shreir's Corrosion 4th Edition, Elsevier, Amsterdam, The Netherlands, (2010) **1**: 272-303

57 R. Viswanathan, W. T. Bakker, Materials for Ultra Supercritical Fossil Power Plants, EPRI, Palo Alto, CA: (2000) TR-114750

58 R. Viswanathan, J. Sarver, J. M. Tanzosh, Boiler Materials for Ultra-Supercritical Coal Power Plants-Steamside Oxidation, *J Mater Eng Perform* (2006) **15**:255-274

59 R. Viswanathan, W. Bakker, Materials for Ultrasupercritical Coal Power Plants-Boiler Materials: Part I, *J Mater Eng Perform* (2001) **10**:81-95

60 A. N. Hansson, M. Montgomery, M. A. J. Somers, Oxidation of X20 in Water Vapour: The Effect of Temperature and Oxygen Partial Pressure, *Oxid Met* (2009) **71**:201-218

61 J. Żurek, Oxidation and Oxidation Protection of Ferritic and Austenitic Steels in Simulated Steam Environments at Temperatures between 550 and 650°C. Dissertation, Rheinisch-Westfälische Technische Hochschule Aachen, 2004

62 Welding Filler Metals for Power Plant Engineering, Böhler Schweisstechnik Deutschland GmbH, Hamm, Germany

63 A. Duval, F. Miserque, M. Tabarant, J.-P. Nogier, A. Gédéon, Influence of the Oxygen Partial Pressure on the Oxidation of Inconel 617 Alloy at High Temperature, *Oxid Met* (2010) **74**:215-238

64 T. S. Jo, S.-H. Kim, D.-G. Kim, J. Y. Park, Y. D. Kim, Thermal Degradation Behavior of Inconel 617 Alloy, *Met Mater Int* (2008) **14**:739-743

65 W. J. Quadakkers, A. Elschner, H. Holzbrecher, K. Schmidt, W. Speier, H. Nickel, Analysis of Composition and Growth Mechanisms of Oxide Scales on High Temperature Alloys by SNMS, SIMS, and RBS, *Mikrochim Acta* (1992) **107**:197-206

66 W. J. Quadakkers, A. Elschner, W. Speier, H. Nickel, Composition and Growth Mechanisms of Alumina Scales on FeCrAl-Based Alloys Determined by SNMS, *Appl Surf Sci* (1991) **52**:271-28

67 D. H. Allen, J. E. Oakey, B. Scarlin, The New COST Action 522-Power Generation in the 21st Century: Ultra-Efficient, Low-Emission Plant, *in:* J. Lecomte-Beckers, F. Schubert, P. J. Ennis, (Eds.) Materials for Advanced Power Engineering, Forschungszentrum Jülich GmbH, Germany (1998) 1825-1839

68 K. Weinzierl, *VGB Kraftwerkstechnik* (1994) **74**:109-114

69 B. J. P. Buhre, L. K. Ellitot, C. D. Sheng, R. P. Gupta, T. F. Wall, Oxy-fuel Combustion Technology for Coal-Fired Power Generation, *Prog Energ Combust* (2005) **31**:283-307

70 K. Jordal, M. Anheden, J. Yan, L. Strömberg, Oxyfuel Combustion for Coal-Fired Power Generation with CO_2 Capture - Opportunities and Challenges. Proceedings of 7th International Conference on Greenhouse Gas Control Technologies (GHGT-7), Vancouver, Canada, (2004) 201-209

71 T. Pikkarainen, A. Tourunen, J. Hämäläinen, Oxyfuel Concept Development, *Energ Mater* (2007) **2:**78-83

72 B. Bordenet, F. Kluger, Thermodynamic Modelling of the Corrosive Deposits in Oxy-Fuel Fired Boilers, *Mater Sci Forum* (2008) **595-598**: 261-269.

73 P. J. Ennis, A. Zielinska-Lipiec, O. Wachter, A. Czyrska-Filemonowicz, Microstructural Stability and Creep Rupture Strength of the Martensitic Steel P92 for Advanced Power Plant, *Acta Materialia* (1997) **45**:4901-4907

74 P. J. Ennis, The Creep Rupture Behaviour and Steam Oxidation Resistance of P92 Weldments, *Mater High Temp* (2006) **23**:187-193

75 G. B. Holloway, Z. Zhang, A. W. Marshall, Properties of T/P92 CrMo Weld Metals For Ultra Super Critical (USC) Power Plant, Metrode Products Ltd, UK, Africa Fusion, (2008)

76 J. Żurek, E. Wessel, L. Niewolak, F. Schmitz, T.-U. Kern, L. Singheiser, W.J. Quadakkers, Anomalous Temperature Dependence of Oxidation Kinetics during Steam Oxidatin of Ferritic Steels in the Temperature Range 550-650°C, *Corros Sci* (2004) **46**:2301-2317

77 Z. Yue, M. Fu, X. Li, X. Tian, High Temperature Oxidation Behavior of TP304H Steel Coated with CeO_2 in Water Vapor, *Oxid Met* (2010) **74**:157-165

78 A. N. Hansson, H. Danielsen, F. B. Grumsen, M. Montgomery, Microstructural Investigation of the Oxide Formed on TP 347H FG during Long-Term Steam Oxidation, *Mater Corros* (2010) **61**:665-675

79 N. Otsuka, Y. Shida, H. Fujikawa, Internal-External Transition for the Oxidation of Fe-Cr-Ni Austenitic Stainless Steels in Steam, *Oxid Met* (1989) **32**:13-45

80 M. Sun, X. Wu, Z. Zhang, E.-H. Han, Oxidation of 316 Stainless Steel in Supercritical Water, *Corros Sci* (2009) **51**:1069-1072

81 R. Viswanathan, K. Coleman, J. Shingledecker, J. Sarver, G. Stanko, M. Borden, W. Mohn, S. Goodstine, I. Perrin, Boiler Materials for Ultrasupercritical Coal Power Plants, U.S. DOE NO.: DE-FG26-01NT41175

82 R. Uerlings, U. Bruch, H. Meyer, Investigations of the Operational Behaviour of Boiler Materials and their Welded Joints at Temperatures up to 650 °C, VGB Power Tech 3/2008

83 W. Przybilla, M. Schütze, Role of Growth Stresses on the Structure of Oxide Scales on Nickel at 800 and 900°C, *Oxid Met* (2002) **58**:103-145

84 M. Schütze, Deformation, Cracking Behavior of Protective Oxide Scales on Heat-Resistant Steels under Tensile Strain, *Oxid Met* (1985) **24**:199-232

85 H. Echsler, S. Ito, M. Schütze, Mechanical Properties of Oxide Scales on Mild Steel at 800 to 1000°C, *Oxid Met* (2003) **60**:241-269

86 R. Viswanathan, W. Bakker, Materials for Ultrasupercritical Coal Power Plants-Turbine Materials: Part II, *J Mater Eng Perf* (2001) **10**:96-101

87 M. Schwind, M. Hättestrand, H.-O. Andrén, Microstructural Stability of Creep Resistant Alloys for High Temperature Plant Applications, in: A. Strang, J. Cawley, G. W. Greenwood (Eds.) Microstructure of high temperature materials series, The Institute of Materials, London, UK, (1998) 197-214

88 R. Jayram, R. L. Klueh, Microstructural Characterization of 5 to 9 pct Cr-2 pct W-V-Ta Martensitic Steels, *Metall Mater A* (1998) **29**:1551-1558

89 A. Tohyama, Y. Minami, Development of the High Temperature Materials for Ultra Super Critical Boilers, *in*: R. Viswanathan, J. Nutting (Eds.) Advanced Heat Resistant Steel for Power Generation, The Institute of Materials, London, UK, (1999) 494-506

90 R. Y. Chen, W. Y. D. Yuen, Review of the High-Temperature Oxidation of Iron and Carbon Steels in Air or Oxygen, *Oxid Met* (2003) **59**:433-468

91 A. G. Evans, G. B. Crumley, and R. E. Demaray, On the Mechanical Behavior of Brittle Coatings and Layers, *Oxid Met* (1983) **20**:193-216

92 A. Norin, Mechanical Stresses Developed in Austenitic Fe-Cr-Ni Alloys by Oxidation in a CO_2 Atmosphere, *Oxid Met* (1975) **9**:259-274

93 W. K. Appleby, R.F. Tylecote, Stresses During The Gaseous Oxidation Of Metals, *Corros Sci* (1970) **10**:325-341

94 W. Jaenicke, S. Leistikow, A. Stadler, L. Albert, *Mem Sci Rev Metall* (1965) 62:231-239

95 M. Hänsel, W. J. Quadakkers, D. J. Young, Role of Water Vapor in Chromia-Scale Growth at Low Oxygen Partial Pressure, *Oxid Met* (2003) **59**:285-301

96 X. G. Zheng, D. J. Young, High-Temperature Corrosion of Cr_2O_3-Forming Alloys in CO-CO_2-N_2 Atmospheres, *Oxid Met* (1994) **42**:163-190

97 E. J. M. Verwey, The Crystal Structure of γ-Fe_2O_3 and γ-Al_2O_3, *Z Kristallogr* (1935) **91**:65-69

98 T. Sato, K. Nakatsuka, K. Toita, J. Shimoiizaka, Study on the artificial magnetite by wet method, *J JPN Soc Powder Powder Me* (1967) **14**:71-76

99 Ö. Özdemir, S. K. Banerjee, High Temperature Stability of Maghemite (γ-Fe_2O_3), *Geophys Res Lett* (1984) **11**:161-164

100 D. Hünert, Korrosionsprozesse und Aufkohlung von ferritisch-martensitischen Stählen in H_2O-CO_2 Atmosphären, BAM-Dissertationsreihe, Band 61 Berlin 2010, ISBN 978-3-9813550-4-8

101 G. M. Raynaud, R. A. Rapp, In situ Observation of Whiskers, Pyramids and Pits during High Temperature Oxidation of Metals, *Oxid Met* (1984) **21:**89-102

102 E. A. Polman, T. Fransen, P. J. Gellings, Oxidation Kinetics of Chromium and Morphological Phenomena, *Oxid Met* (1989) **32**:433-447

103 P. J. Grobner, C. C. Clark, P. V. Andreae, W. R. Sylvester, Steamside Oxidation and Exfoliation of Cr-Mo Superheater and Reheater Steels, The International Corrosion Forum Devoted Exclusively to the Protection and Performance of Materials, Chicago, (1980) **172**:1-19

104 E. A. Gulbransen, R. Ruka, Kinetics of Solid Phase Reactions in Oxide Films on Iron - The Reversible Transformation at or near 570°C, *J Met Trans AIME* (1950) **188**:1500-1508

105 L. W. Pinder, Oxide characterization for service failure investigations**,** *Corros Sci* (1981) **21**:749-763

106 S. Valette, S. Menecier, F. Goutier, P. Lefort, Kinetics of Some Iron-Based Alloys in Industrial CO_2: Formation of Wüstite Phase, *Mater Sci Forum* (2008) **595-598**:1153-1161

107 R. J. Ehlers, E. J. Smaardijk, H. J. Penkala, A. K. Tyagi, L. Singheiser, W. J. Quadakkers, Effect of Steel Composition on the Bell-Shape Temperature Dependence of Oxidation in Water Vapour Containing Environments, Proc. Int. Corr. Congress, Cape Town, South Africa, (1999), Proceedings, Paper 336

108 A. S. Khanna, P. Rodriguez, J. B. Gnanamoorthy, Oxidation Kinetics, Breakaway Oxidation, and Inversion Phenomenon in 9Cr-lMo Steels, *Oxid Met* (1986) **26**:171-200

109 J. Zurek, L. Nieto Hierro, J. Piron-Abellan, L. Niewolak L. Singheiser, W.J. Quadakkers, Effect of Alloying Additions in Ferritic 9-12% Cr Steels on the Temperature Dependence of the Steam Oxidation Resistance, *Mater Sci Forum* (2004) **461-464**:791-798

110 R. J. Ehlers, P. J. Ennis, L. Singheiser, W. J. Quadakkers, T. Link, Life Time Modelling of High Temperature Corrosion Processes, M. Schütze, W. J. Quadakkers, J. Nicholls (Eds.) European Federation of Corrosion Monograph, Nr. 34, The Institute of Materials, London, ISSN 1354-5116, 178-193

111 J. Ehlers, D. J. Young, E. J. Smaardijk, A. K. Tyagi, H. J. Penkalla, L. Singheiser, W. J. Quadakkers, Enhanced Oxidation of the 9% Cr Steel P91 in Water Vapour Containing Environments, *Corros Sci* (2006) **48**:3428-3454

112 H. E. Evans, A. T. Donaldson, T. C. Gilmour, Mechanisms of Breakaway Oxidation and Application to a Chromia-Forming Steel, *Oxid Met* (1999) **52**:379-402

113 E. Essuman, G. H. Meier, J. Żurek, M. Hänsel, L. Singheiser, W. J. Quadakkers, Enhanced Internal Oxidation as Trigger for Breakaway Oxidation of Fe-Cr Alloys in Gases Containing Water Vapor, *Scripta Mater* (2007) **57**:845–848

114 M. Schütze, W. J. Quadakkers, Cyclic Oxidation of High Temperature Materials, IOM Communications, London, UK, (1999)

115 H. Asteman, K. Segerdahl, J.-E. Svensson, L.-G. Johansson, The Influence of Water Vapour on the Corrosion of Chromia-Forming Steels, *Mater Sci Forum* (2001) **369-372**:277-286

116 H. Asteman, J.-E. Svensson, L.-G. Johansson, Oxidation of 310 Steel in H_2O/O_2 Mixtures at 600 °C: the Effect of Water-Vapour-Enhanced Chromium Evaporation, *Corros Sci* (2002) **44**:2635-2649

117 M. Halvarsson, J.E. Tang, H. Asteman, J.-E. Svensson, L.-G. Johansson, Microstructural Investigation of the Breakdown of the Protective Oxide Scale on a 304 Steel in the Presence of Oxygen and Water Vapour at 600°C, *Corros Sci* (2006) **48**:2014-2035

118 C. S. J. Tedmon, The Effect of Oxide Volatilization on the Oxidation Kinetics of Cr and Fe-Cr Alloys. *J Electrochem Soc* (1966) **113**:766-768

119 W. J. Quadakkers, T. Olszewski, J. P. Abellán, L. Singheiser, Oxidation of Metallic Materials in Simulated CO_2/H_2O-Rich Service Environments Relevant to an Oxyfuel Plant, VDI-Berichte (2010) **2102**:81-103

120 D. J. Young, B. A. Pint, Chromium Volatilization Rates from Cr_2O_3 Scales into Flowing Gases Containing Water Vapor, *Oxid Met* (2006) **66:**137-153

121 R. Trebbels, T. Markus, L. Singheiser, Investigation of Chromium Vaporization from Interconnector Steels with Spinel Coatings, *J Electrochem Soc* (2010) **157**:B490-B495

122 M. Stanislowski, E. Wessel, K. Hilpert, T. Markus, L. Singheiser, Chromium Vaporization from High-Temperature Alloys, I. Chromia-Forming Steels and the Influence of Outer Oxide Layers, *J Electrochem Soc* (2007) **154**:A295-A306

123 E. J. Opila, N. S. Jacobson, D. L. Myers, E. H. Copland, Predicting Oxide Stability in High-Temperature Water Vapor, *JOM* (2006) **58**:22-28

124 R. Trebbels, Report Forschungszentrum Jülich, Jülich FRG, Energy and Environment, (2009) **49** ISBN 978-3-89336-591-3

125 A. Galerie, Y. Wouters, The Kinetic Behaviour of Metals in Water Vapour at High Temperatures: Can General Rules be Proposed? *Mater Sci Forum* (2001) **231:**369-372

126 R. J. Ehlers, W. J. Quadakkers, Oxidation von ferritischen 9-12% Cr Stählen in wasserdampfhaltigen Atmosphären bei 500 bis 650°C, Report Forschungszentrum Jülich, Jül-3883, Jülich (2001) ISSN 0944-2952

127 H. Asteman, J.-E. Svensson, L.-G. Johansson, Evidence for Chromium Evaporation Influencing the Oxidation of 304L: The Effect of Temperature and Flow Rate, *Oxid Met* (2002) **57**:193-216

128 M. Schütze, D. Renusch, M. Schorr, Parameters Determining the Breakaway Oxidation Behaviour of Ferritic Martensitic 9% Cr Steels in Environments Containing H_2O, *Corros Eng Sci Tech* (2004) **39:**157-166

129 M. Michalik, M. Hänsel, W. J. Quadakkers, Effect of Water Vapour on Growth and Adherence of Chromia Scales on Pure Chromium, Report Forschungszentrum Jülich, Energy Technology, Jülich (2007) **67** ISSN 1433-5522

130 I. Langmuir, The Vapor Pressure of Metallic Tungsten. *Phys Rev* (1913) **2**:329-342

131 E. Essuman, G. H. Meier, J. Żurek, M. Hänsel, W. J. Quadakkers, The Effect of Water Vapor on Selective Oxidation of Fe-Cr Alloys, *Oxid Met* (2008) **69**:143-162

132 R. A. Rapp, The Transition from Internal to External Oxidation and the Formation of Interruption Bands in Silver-Indium Alloys, *Acta Met* (1961) **9**:730-741

133 V. Lepingle, G. Louis, D. Petelot, B. Lefebvre, B. Vandenberghe, Steam Corrosion Resistance of New 12% Cr Ferritic Boiler Steels, *Mater Sci Forum* (2004) **461-464**:1039-1040

134 L. Nieto Hierro, V. Rohr, P. J. Ennis, M. Schütze, W. J. Quaddakers, Steam Oxidation and its Potential Effects on Creep Strength of Power Station Materials, *Mater Corros* (2005) **56**:890-896

135 H. K. D. H. Bhadeshia, R. W. K Honeycombe, Steels Microstructure and Properties (3^{th} edition), Elsevier Ltd., Oxford, UK, (2006)

136 Y. Liu, W. Wie, L. Benum, M. Oballa, M. Gyorffy, W. Chen, Oxidation Behavior of Ni-Cr-Fe-Based Alloys: Effect of Alloy Microstructure and Silicon Content, *Oxid Met* (2010) **73**:207-218

137 K. Tamura, T. Sato, Y. Fukuda, K. Mitsuhata, H. Yamanouchi, High Temperature Strengths and Steam Oxidation Properties of New 9-12% Cr Ferritic Steel Pipes for USC Boilers, in: K. Natesan, P. Ganesan, G. Lai (Eds.) Heat Resistant Materials II, ASM International, Materials Park, OH, USA, (1995)

138 J. M. Francis, Structure of Surface Oxides Formed on A 20% Cr/25% Ni/Nb-Stabilised Steel in Carbon Dioxide at High Temperatures, *J British Corr* (1968) **3**:113-119

139 N. Sämann, M. Spiegel, H. J. Grabke, Influence of Surface Preparation on the Corrosion of Steels in Simulated Waste Incineration Environments, *Mater Sci Forum* (2001) **369-372**:963-970

140 L. Mikkelsen, S. Linderoth, J. B. Bilde-Sorensen, The Effect of Silicon Addition on the High Temperature Oxidation of a Fe-Cr Alloy, *Mater Sci Forum* (2004) **461-434**:117-122

141 A. M. Huntz, V. Bague, G. Beauple, C. Haut, C. Severac, P. Lecour, X. Longaygue, F. Ropital, Effect of Silicon on the Oxidation Resistance of 9% Cr Steels, *Appl Surf Sci* (2003) **207**:255-275

142 A. Rahmel, J. Tobolski, Einfluß von wasserdampf und kohlendioxyd auf die oxydation von eisen-silicium-legierungen in sauerstoff bei temperaturen von 750 bis 1050 °C, *Mater Corros* (1965) **16**:662-676

143 T. Ishitsuka, Y. Inoue, H. Ogawa, Effect of Silicon on the Steam Oxidation Resistance of a 9% Cr Heat Resistant Steel, *Oxid Met* (2004) **61**:125-142

144 Y. Murata, M. Morinaga, R. Hashiszume, Y. Sawaragi, M. Nakai, *in*: Proceedings of 3rd EPRI Conference on Advances in Materials Technology for Fossil Power Plants, Swansea, Wales, UK, (2001)

145 P. J. Ennis, W. J. Quadakkers, Materials for Advanced Power Engineering, *in*: J. Lecomte-Beckers, M. Carton, F. Schubert, P. Ennis (Eds.) *Energy Technology* (2002) **21**:1131-1142

146 H. E. Evans, D. A. Hilton, R. A. Holm, S. J. Webster, Influence of Silicon Additions on the Oxidation Resistance of a Stainless Steel, *Oxid Met* (1983) **19**:1-18

147 J. R. Davis, (Ed.) Nickel, Cobalt, and Their alloys. ASM Specialty Handbook, ASM International, Materials Park, OH, USA (2000)

148 S. Guan, J. Corkum,W. Smeltzer, Oxidation behaviour of Fe-Al-Si Alloys at 1073 and 1173K, *in:* Y. Saito, B. Önay and T. Maruyama (Eds.), High Temperature Corrosion of Advanced Materials and Protective Coatings, Elsevier Science Publishers B.V. (1992)

149 R. U. Husemann, Überlick Werkstoffentwicklungen für Komponenten des Dampferzeugers, FDBR Werkstofftagung, Düsseldorf 2004

150 H. Teranishi, Y. Sawaragi, M. Kubota, and Y. Hayase, Fine-Grained TP347H Steel Tubing with High Elevated-Temperature Strength and Corrosion Resistance for Boiler Applications, *The Sumitomo Search* (1989) **38**:63-74

151 H. Katsumi, H. Haruyama and F. Abe, Application of the Pre-Oxidation Treatment in Ar Gas for the NIMS High Strength Steels, *in*: R. Viswanathan, D. Gandy and K. Coleman (Eds.) Advances in Materials Technology for Fossil Power Plants, ASM International, Materials Park, OH, USA, (2005)

152 H. Matsuo, Y. Nishiyama, and T. Yamadera, Steam Oxidation of Fine-Grain Steels, *in:* R. Viswanathan, D. Gandy, and K. Coleman (Eds.) Advances in Materials Technology for Fossil Power Plants, ASM International, Materials Park, OH, USA, (2005) 441-451

153 F. Rouillard, G. Moine, M. Tabarant, J. C. Ruiz, Corrosion of 9Cr Steel in CO_2 at Intermediate Temperature II: Mechanism of Carburization, *Oxid Met* (2012) **77**:57-70

154 T. Gheno, D. Monceau, J. Zhang, D. J. Young, Carburisation of Ferritic Fe–Cr Alloys by Low Carbon Activity Gases, *Corros Sci* (2011) **53**:2767-2777

155 D. Hünert, G. Oder, W. Österle, R. Saliwan-Neumann, W. Schulz, I. Urban, A. Kranzmann, Ageing and Corrosion of Steels in CO_2 Rich Flue Gas, 1st Oxyfuel Combustion Conference, Cottbus, 2009

156 D. Hünert, A. Kranzmann, Impact of oxyfuel atmospheres $H_2O/CO_2/O_2$ and H_2O/CO_2 on the oxidation of ferritic-martensitic and austenitic steels, *Corros Sci* (2011) **53**:2306-2317

157 J. P. Abellán, T. Olszewski, H. J. Penkalla, G. H. Meier, L. Singheiser, W. J. Quadakkers, Scale Formation Mechanisms of Martensitic Steels in High CO_2/H_2O-Containing Gases Simulating Oxyfuel Environments, *Mater High Temp* (2009) **26**:63-72

158 W. F. Chu, A. Rahmel, The Conversion of Chromium Oxide to Chromium Carbide, *Oxid Met* (1981) **15**:331-337

159 J. P. Abellán, T. Olszewski, G. H. Meier, L. Singheiser, W. J. Quadakkers, The Oxidation Behaviour of the 9% Cr Steel P92 in CO_2- and H_2O-rich Gases Relevant to Oxyfuel Environments, *Int J Mat Res* (2010) **101**:1-13

160 K. Bongartz, D. F. Lupton, H. Schuster, A Model to Predict Carburization Profiles in High Temperature Alloys, *Metall Mater Trans A* (1980) **11**:1883-1893

161 K. Bongartz, W.J. Quadakkers, R. Schulten, H. Nickel, A Mathematical Model Describing Carburization in Multielement Alloy Systems, *Metall Mater Trans A* (1989) **20**:1021-1028

162 G. M. Smith, D. J. Young, D. L. Trimm, Carburization Kinetics of Heat-Resistant Steels, *Oxid Met* (1982) **18**:229-243

163 C. Anghel, E. Hörnlund, G. Hultquist, M. Limback, Gas Phase Analysis of CO Interactions with Solid Surfaces at High Temperatures, *Appl Surf Sci* (2004) **233**:392-401

164 H. J. Grabke, The Use of Isotope Exchange Reactions for the Study of Oxygen Transfer from H_2O and from CO_2 to Metals and Oxides, *Ann NY Acad Sci* (1973) **213**:110-129

165 G. McAdam, D. J. Young, Kinetic and Morphological Development of Oxide-Sulfide Scales on Iron at 1073 K, *Oxid Met* (1992) **37**:281-300

166 J. Unsworth, D. J. Young, Amounts and Distribution of Phases in Sulfide Plus Oxide Scales on Iron, *Oxid Met* (2003) **60**:447-465

167 J. Gilewicz-Wolter, Z. Żurek, Corrosion of Iron in Sulfur Dioxide at 0.1 MPa, *Oxid Met* (1996) **45**:469-486

168 F. Gesmundo, Mechanism of the Simultaneous Formation of Oxide and Sulfide at the Scale Surface During the Oxidation of a Pure Metal in Mixed Atmospheres, *Oxid Met* (1979) **13**:237-244

169 J. Gilewicz-Wolter, High-Temperature Corrosion of Iron in Sulfur Dioxide at Low Pressure, *Oxid Met* (1996) **46**:129-145

170 D. J. Young, S. Watson, High-Temperature Corrosion in Mixed Gas Environments, *Oxid Met* (1995) **44**:239-264

171 J. Barnes, J. Corish, J. F. Norton, Sulfur Effects on the Internal Carburization of Fe-Ni-Cr Alloys, *Oxid Met* (1986) **26**:333-350

172 T. Flatley, N. Birks, Oxidation of Iron in Atmospheres Containing Sulphur Dioxide, *J Iron Steel Inst* (1971) **209**:523-532

173 G. McAdam, D. J. Young, Kinetic and Morphological Development of Oxide-Sulfide Scales on Manganese at 1073 K, *Oxid Met* (1992) **37**:301-235

174 W. J. Quadakkers, A. S. Khanna, H. Schuster, and H. Nickel, Investigation of The Corrosion Mechanisms of Nickel and Nickel-based Alloys in SO_2-containing Environments Using an Evolved Gas Analysis Technique, *Mater Sci Eng* (1989) **A120-A121**:117-122

175 B. Gillot and M. Radid, Corrosion in SO_2 of Chromium and Manganese at High Temperature, *Oxid Met* (1990) **33**:279-299

		Fe	Cr	Ni	Mo	C	Nb	Al	W	N	V	Si	Mn	Co	Cu	Ti
Ferritic/ martensitic	**13CrMo4-4**	Bal.	0.92	0.13	0.46	0.11	-	0.03	-	0.01	-	0.17	0.49	-	0.29	-
	P92	Bal.	8.90	0.23	0.38	0.093	0.05	0.028	1.20	0.04	0.20	0.30	0.43	-	0.07	-
	P92-low Si	Bal.	8.96	0.06	0.47	0.106	0.07	0.007	1.84	-	0.20	0.04	0.45	-	-	-
	X20	Bal.	11.00	0.42	0.81	0.17	-	0.02	-	0.04	0.30	0.14	0.51	-	0.08	-
	HCM12	Bal.	12.00	-	1.00	0.10	0.05	-	1.00	-	0.25	0.3	0.55	-	-	-
	VM12 SHC	Bal.	11.40	0.20	0.27	0.11	0.05	0.02	1.50	0.04	0.22	0.44	0.17	1.50	0.07	-
	Crofer 22 APU	Bal.	23.00	0.16	-	0.05	-	0.10	-	0.011	-	0.10	0.40	-	-	0.05
Austenitic	**1.4910**	Bal.	16.49	12.34	2.23	0.02	-	-	-	0.12	-	0.38	1.28	-	-	-
	TP347H FG	Bal.	18.10	11.70	-	0.08	0.50	-	-	-	-	0.39	1.60	-	-	-
	Super 304H	Bal.	18.62	8.80	-	0.08	0.50	-	-	0.11	-	0.21	0.79	-	0.28	-
	DMV 310N	Bal.	24.60	20.80	-	0.066	0.43	-	-	0.02	-	0.33	1.20	-	-	-
Ni-base	**INCONEL 617**	1.14	21.90	Bal.	8.70	0.063	-	1.17	-	0.021	-	0.08	0.07	11.35	-	0.50
Binary alloys	**Fe-10Cr**	Bal.	10.1	-	-	0.0004	-	-	-	0.0008	-	-	-	-	-	-
	Ni-10Cr	-	9.9	Bal.	-	0.010	-	0.014	-	-	-	-	-	-	-	-
	Ni-20Cr	-	19.5	Bal.	-	0.001	-	-	-	-	-	-	-	-	-	-
	Ni-25Cr	-	24.9	Bal.	-	0.010	-	-	-	-	-	-	-	-	-	-

Table 19.1: Chemical composition (in wt.%) of metallic materials used in this study analyzed using ICP-OES

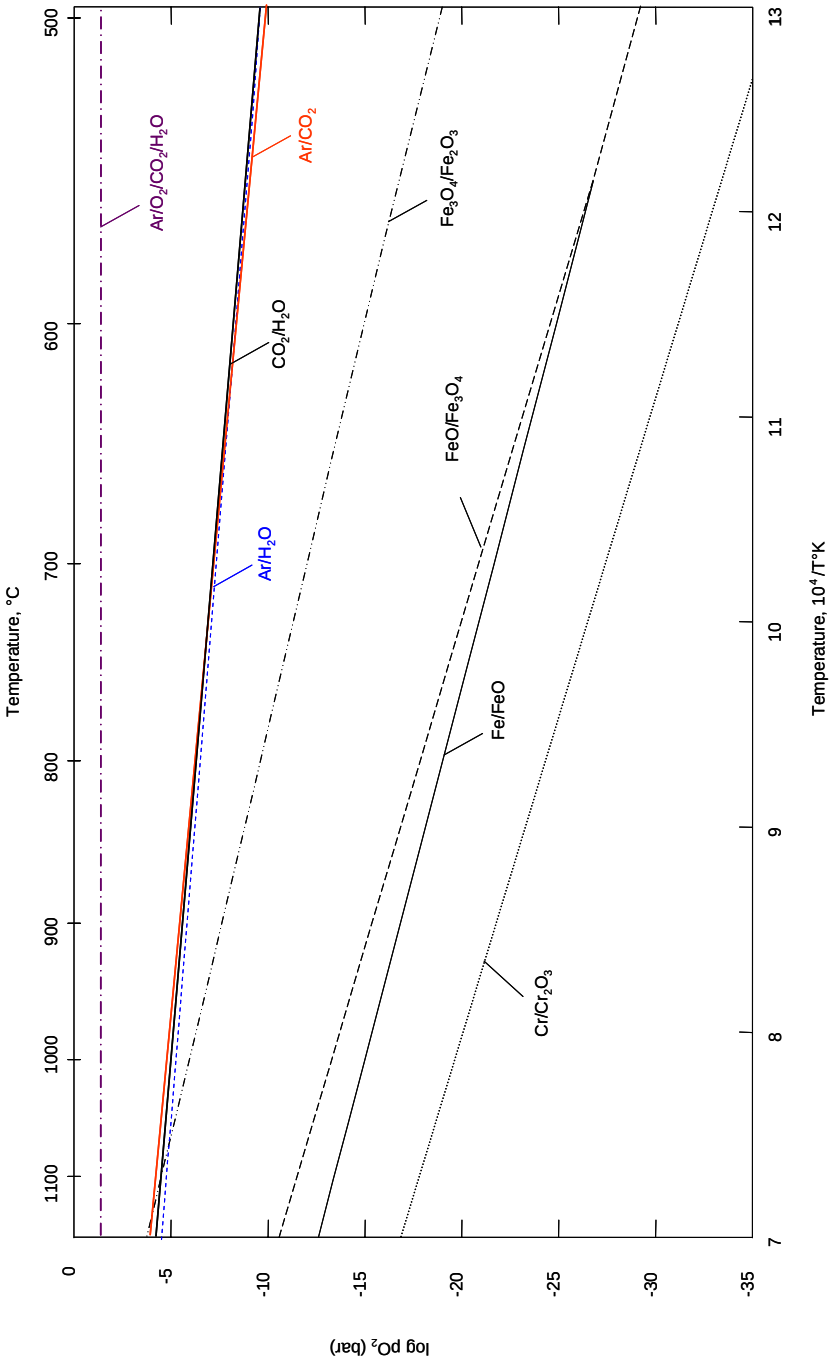

Figure. 19.1: Dissociation pressure of chromium and iron oxides as a function of reciprocal temperature compared with equilibrium oxygen partial pressure in atmospheres used in this study

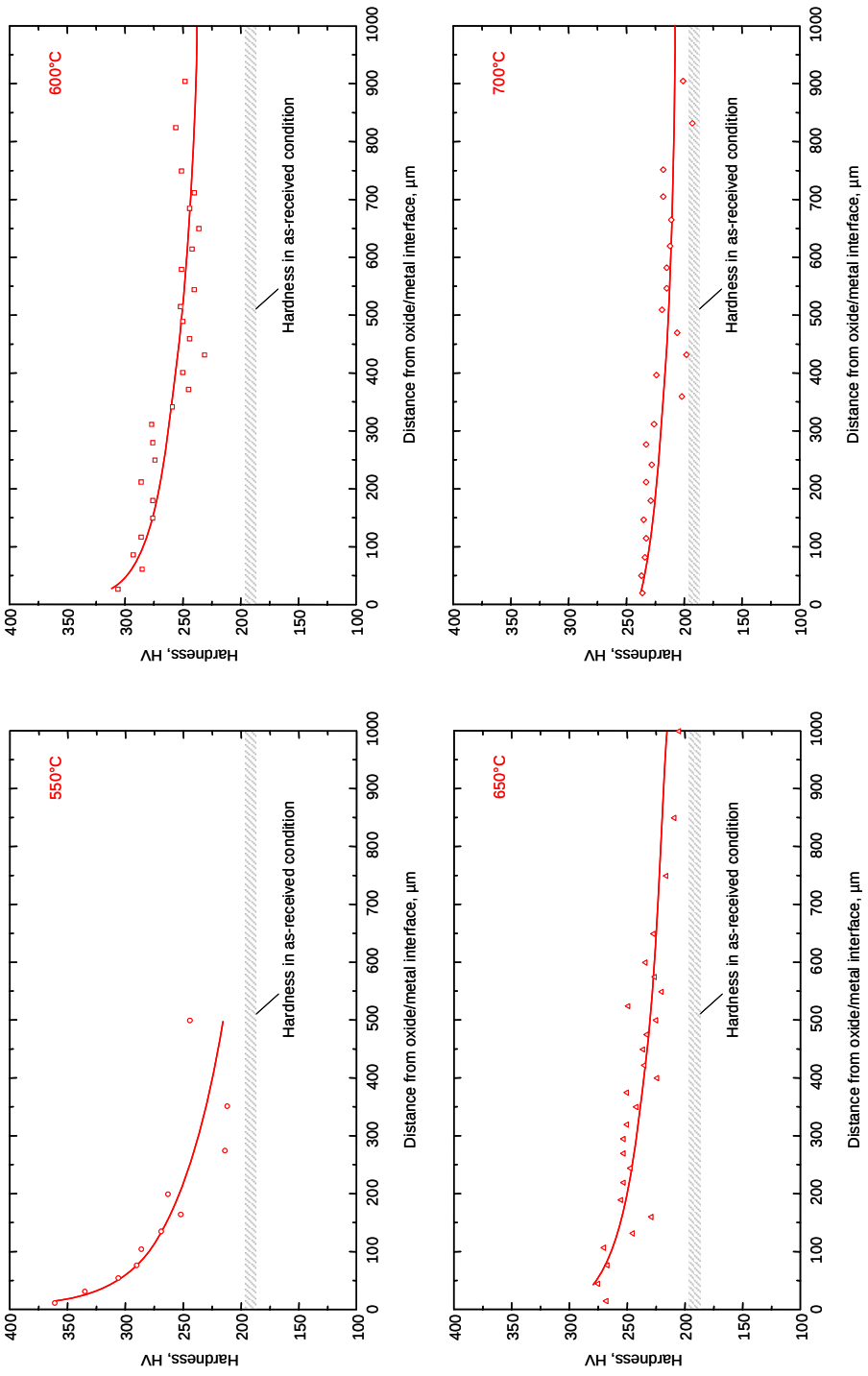

Figure 19.2: Hardness of P92 after oxidation in Ar/CO_2 at 550-700°C for 1000h

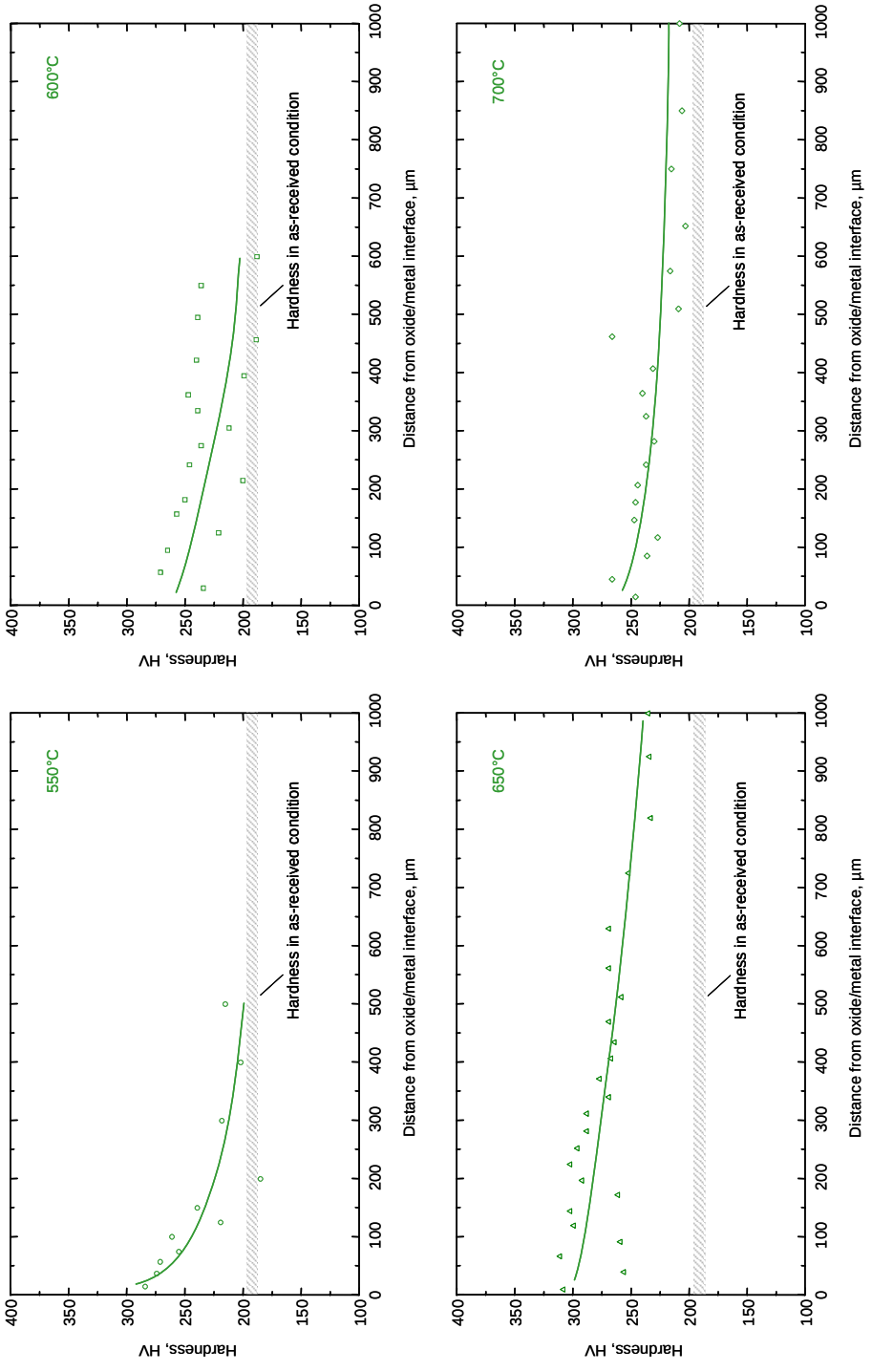

Figure 19.3: Hardness of P92 after oxidation in CO_2/H_2O at 550-700°C for 1000h

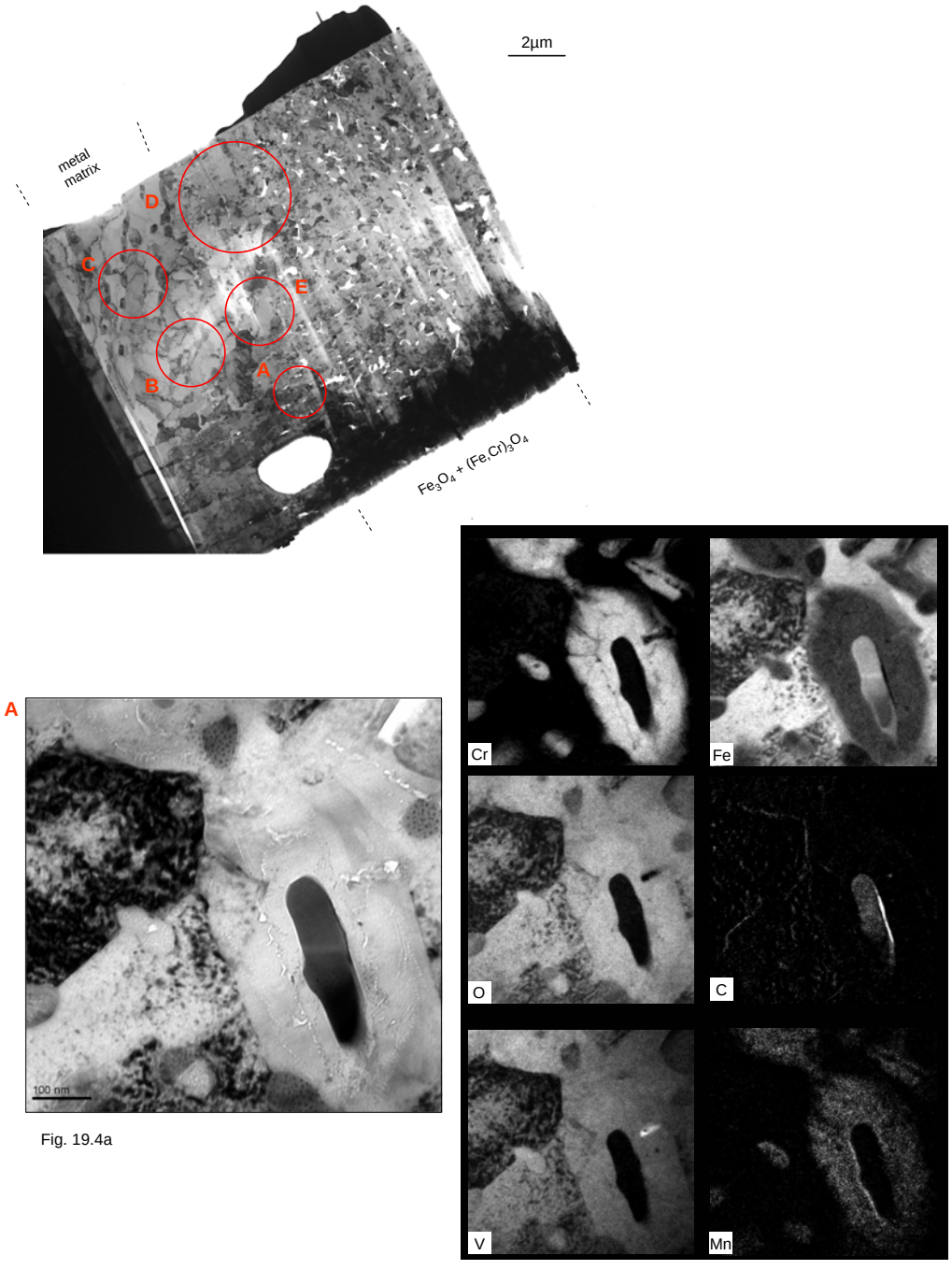

Fig. 19.4a

Figure 19.4: TEM lamella (up) from the inner part of the oxide scale formed on P92 after 100h isothermal exposure to CO_2/H_2O at 650°C. TEM images (Figs. 19.4a-e) and corresponding element mappings show the details of the steel microstructure close to the interface with inner oxide scale.

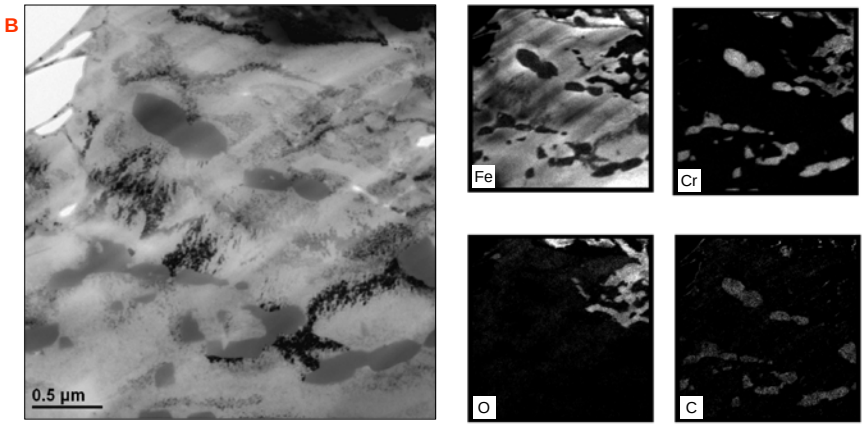

Fig. 19.4b

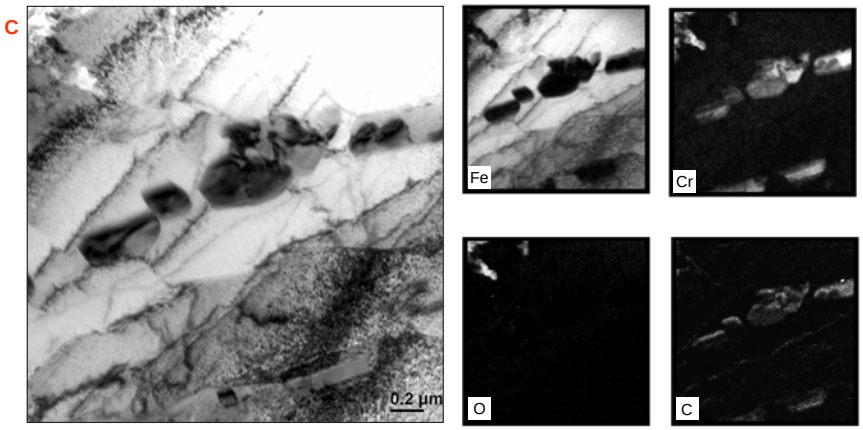

Fig. 19.4c

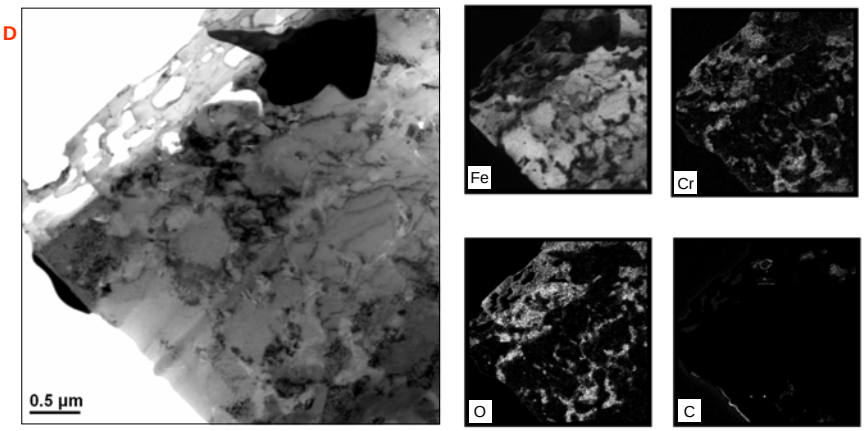

Fig. 19.4d

Figure 19.4: Continued

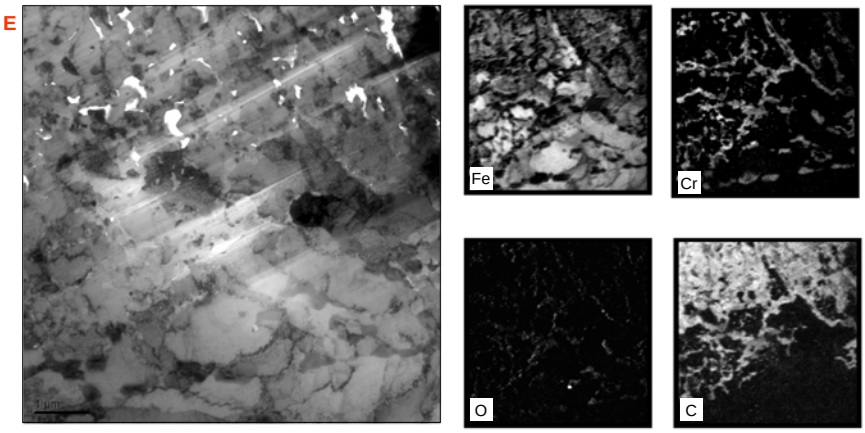

Fig. 19.4e

Figure 19.4: Continued

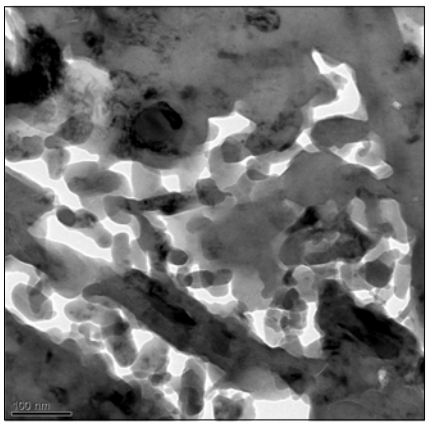

Fig. 19.5a

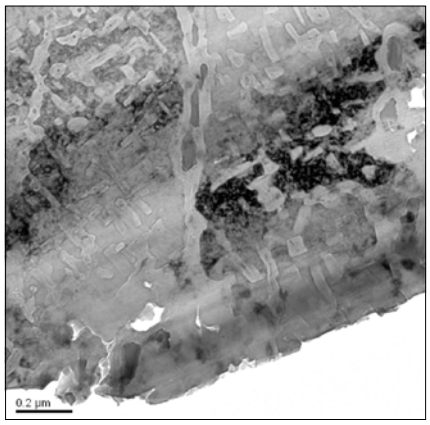

Fig. 19.5b

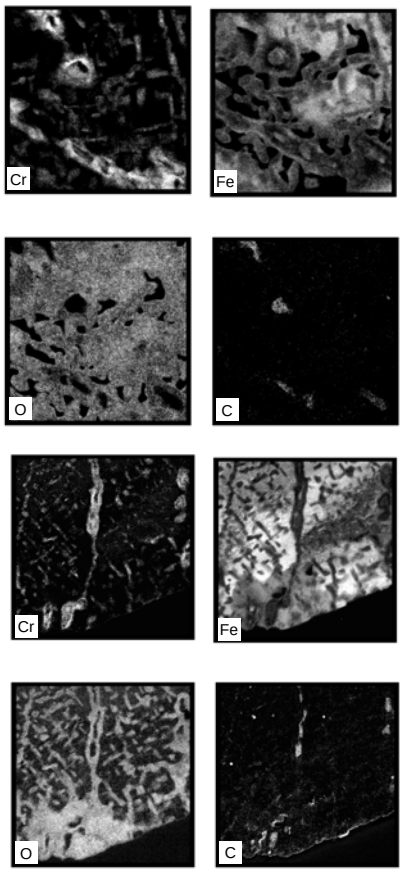

Figure 19.5: TEM cross sections from the inner part of the oxide scale formed on P92 after 100h isothermal exposure to CO_2/H_2O at 550°C. Both images (19.5a-b) show the details of the inner oxide scale microstructure close to the interface with internal oxidation zone

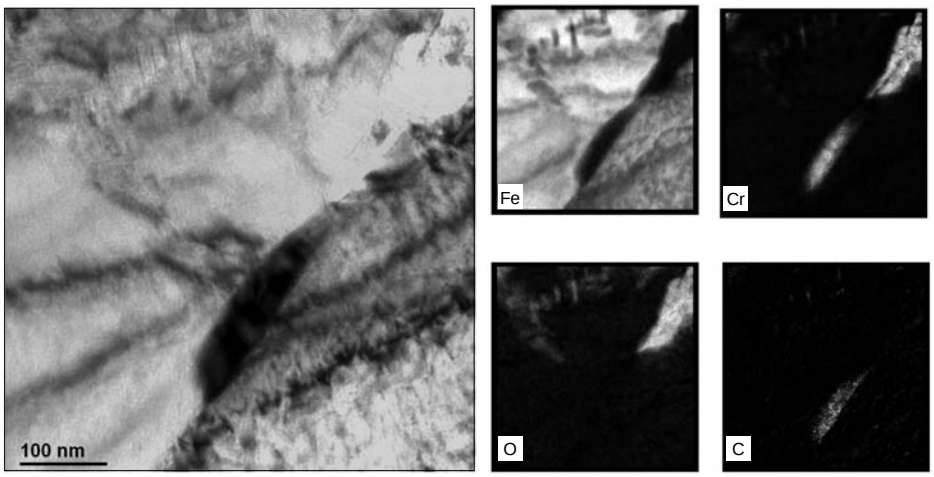

Fig. 19.6a

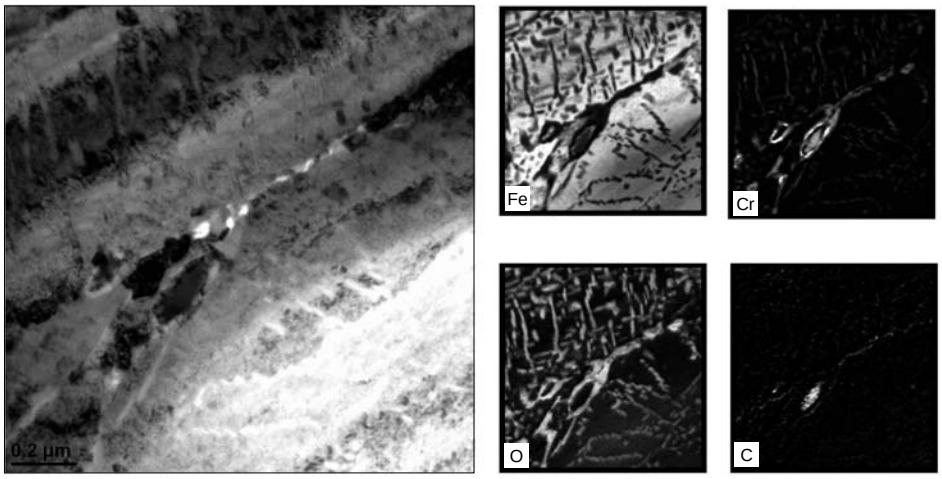

Fig. 19.6b

Figure 19.6: TEM cross sections from the inner part of the oxide scale formed on P92 after 100h isothermal exposure to Ar/H_2O at 550°C. Both images (19.6a-b) show the details of the internal oxidation zone

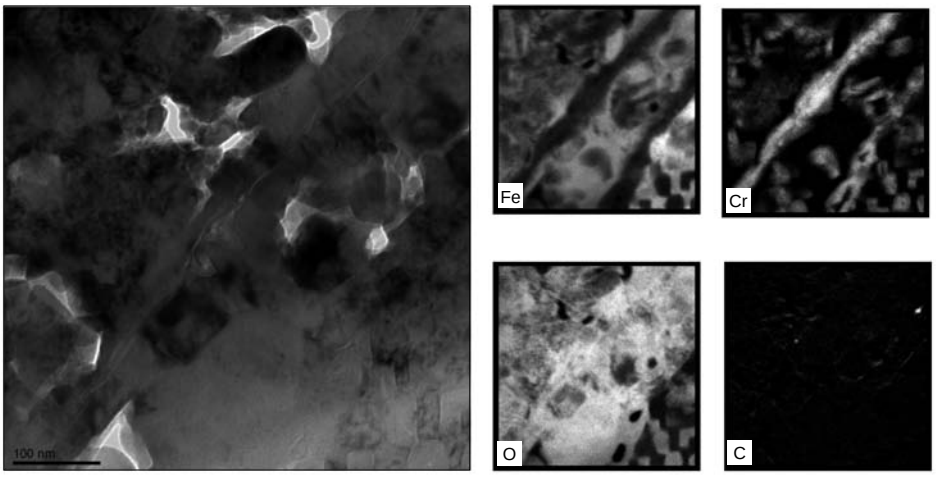

Fig. 19.7a

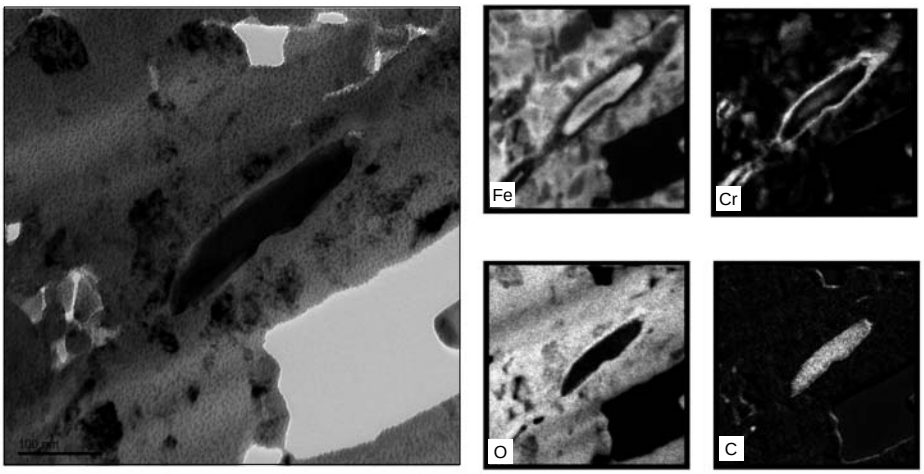

Fig. 19.7b

Figure 19.7: TEM cross sections from the inner part of the oxide scale formed on P92 after 100h isothermal exposure to Ar/H_2O at 550°C. Both images (19.7a-b) show the details of the inner oxide scale close to the internal oxidation zone

I would like to take this opportunity to express my gratitude and appreciation to the following people who have contributed in different ways towards the completion of this thesis:

First of all, I would like to extend my thanks to Prof. L. Singheiser for giving me the opportunity to complete this work.

I am grateful to Prof. W. J. Quadakkers for his patience, stimulating discussions and suggestions as well as his great contribution with analysis of the results contained in this work.

Many thanks to E. Wessel for performing the SEM analysis.

My gratitude goes to H. J. Penkala and D. Eβer for the TEM investigation.

I am grateful to A. Kick and H. Cosler for conducting the high temperature exposures and any other kind of help.

Great thanks to J. Bartsch and V. Gutzeit for assisting during the post-oxidation analysis.

The technical support of M. Felden is also acknowledged.

In addition, I am thankful to J. Pirón Abellán for being a good boss and supporting me at the very beginning.

Special thanks to all my present and former colleagues from the High Temperature Corrosion Group in IEK-2. Thank you for creating an enjoyable working atmosphere and also for your scientific support. In particular, I would like to express my gratitude to J. Żurek, P. Huczkowski and L. Niewolak who were always willing to help me on any subject.

Very special thanks to Wu Bei for her significant contribution to my work and constant support under any circumstances.

感谢你对我的论文修改提出的宝贵意见，
感谢你那诚挚的爱以及对我一直以来的支持，你是我的特别的好伴侣。

Band / Volume 145
Mechanistic studies on the OH-initiated atmospheric oxidation of selected aromatic hydrocarbons
S. Nehr (2012), viii, 129 pp.
ISBN: 978-3-89336-804-4

Band / Volume 146
Electron Spin Resonance Investigation of Semiconductor Materials for Application in Thin-Film Silicon Solar Cells
L. Xiao (2012), VIII, 147 pp.
ISBN: 978-3-89336-805-1

Band / Volume 147
Untersuchungen zum Sicherheits- und Transmutationsverhalten innovativer Brennstoffe für Leichtwasserreaktoren
O. Schitthelm (2012), V, 150 pp.
ISBN: 978-3-89336-806-8

Band / Volume 148
IEK-Report 2011. Klimarelevante Energieforschung
(2012), ca. 250 pp.
ISBN: 978-3-89336-808-2

Band / Volume 149
IEK-Report 2011. Climate-Relevant Energy Research
(2012), ca. 250 pp.
ISBN: 978-3-89336-809-9

Band / Volume 150
Netzintegration von Fahrzeugen mit elektrifizierten Antriebssystemen in bestehende und zukünftige Energieversorgungsstrukturen (2012)
ISBN: 978-3-89336-811-2

Band / Volume 151
Stratospheric ClOOCl chemistry at high solar zenith angles
O. Suminska-Ebersoldt (2012), VI, 126 pp
ISBN: 978-3-89336-817-4

Band / Volume 152
Keramiken und Keramikkombinationen zur Feinstpartikelabscheidung mit Hilfe thermisch induzierter Potentialfelder und Elektronenemissionen
D. Wenzel (2012), XXV, 155 pp
ISBN: 978-3-89336-820-4

Band / Volume 153
Bildung von sekundären Phasen bei tiefengeologischer Endlagerung von Forschungsreaktor-Brennelementen – Struktur- und Phasenanalyse
A. Neumann (2012), 329 pp
ISBN: 978-3-89336-822-8

Band / Volume 154
Coupled hydrogeophysical inversion for soil hydraulic property estimation from time-lapse geophysical data
M. Cho Miltin (2012), xi, 79 pp
ISBN: 978-3-89336-823-5

Band / Volume 155
Tiefentschwefelung von Flugturbinenkraftstoffen für die Anwendung in mobilen Brennstoffzellensystemen
Y. Wang (2012), 205 pp.
ISBN: 978-3-89336-827-3

Band / Volume 156
Self-consistent modeling of plasma response to impurity spreading from intense localized source
M. Koltunov (2012), V, 113 pp.
ISBN: 978-3-89336-828-0

Band / Volume 157
Phosphorsäureverteilung in Membran-Elektroden-Einheiten dynamisch betriebener Hochtemperatur-Polymerelektrolyt-Brennstoffzellen
W. Maier (2012), VI, 105 pp.
ISBN: 978-3-89336-830-3

Band / Volume 158
Modellierung und Simulation von Hochtemperatur-Polymerelektrolyt-Brennstoffzellen
M. Kvesic (2012), ix, 156 pp.
ISBN: 978-3-89336-835-8

Band / Volume 159
Oxidation Mechanisms of Materials for Heat Exchanging Components in CO_2/H_2O-containing Gases Relevant to Oxy-fuel Environments
T. Olszewski (2012), 200 pp.
ISBN: 978-3-89336-837-2

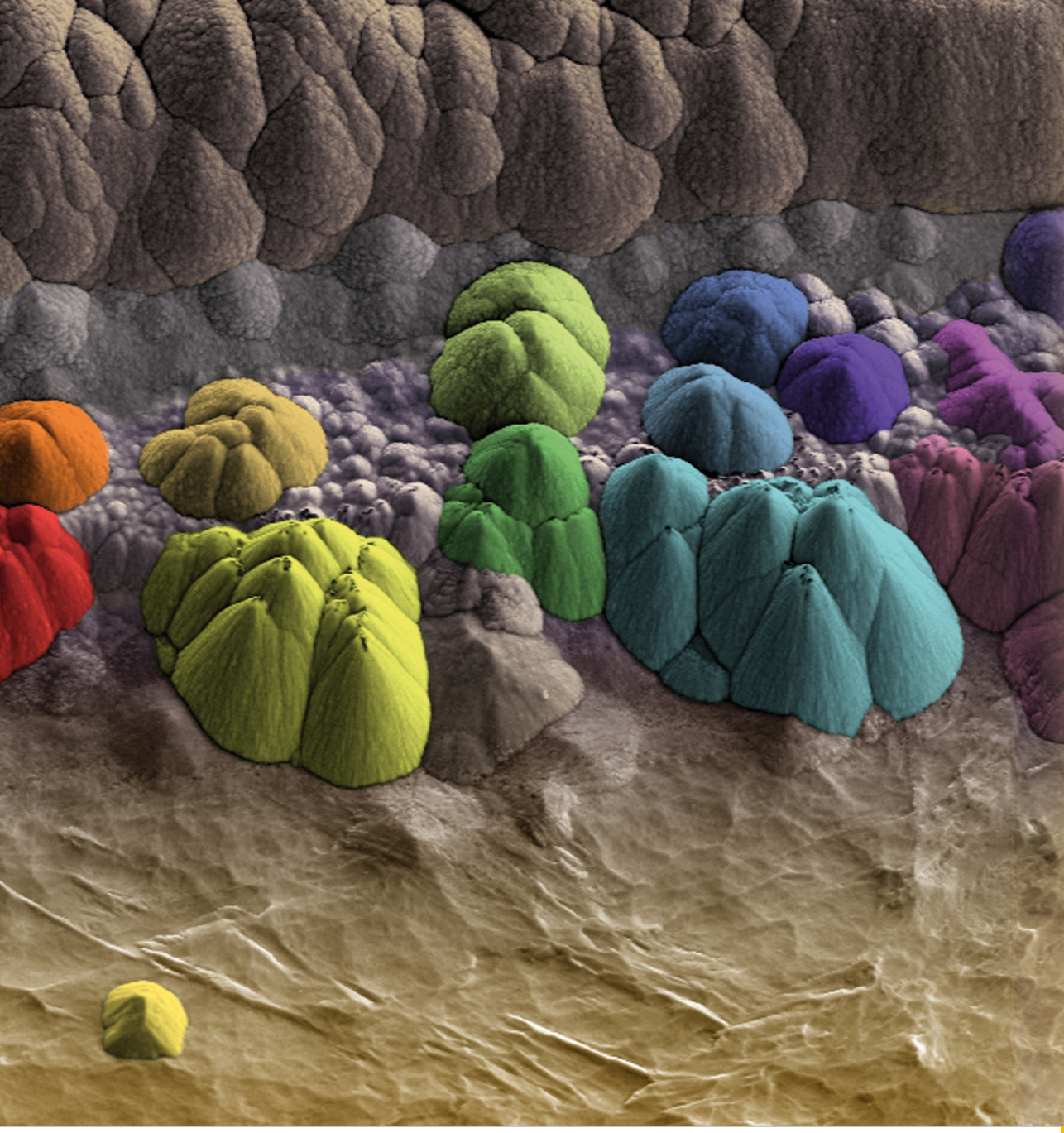

Energie & Umwelt / Energy & Environment
Band / Volume 159
ISBN 978-3-89336-837-2

JÜLICH
FORSCHUNGSZENTRUM